Aus der Klinik für Plastische, Ästhetische und Handchirurgie

der Medizinischen Fakultät

der Otto-von-Guericke-Universität Magdeburg

Abteilung Mikrogravitation und Translationale Regenerative Medizin

„The effects of low shear stress generated in simulated microgravity bioreactors on thyroid cancer cells and endothelial cells, and its role in the multicellular spheroid formation process"

Dissertation

zur Erlangung des Doktorgrades

Dr. med.

(doctor medicinae)

an der Medizinischen Fakultät

der Otto-von-Guericke-Universität Magdeburg

vorgelegt von **José Luis Cortés Sánchez**

aus **Torreón, Mexiko**

Magdeburg 2024

This work is dedicated to my wife, Esmeralda Martínez García, who accompanied me during this long journey in the distance and is now by my side. I am eternally grateful to you.

I am always grateful to my parents, José Luis Cortés Cárdenas and Margarita Sánchez Hinojosa. Because they always knew how to nourish and accompany my inner desire to become a scientist.

"At that point, the happiest thought of my life came to me in the following form: the gravitational field has only a relative existence. Thus, for an observer in free fall from the roof of a house, there exists, during his fall, no gravitational field." (1)

ALBERT EINSTEIN (1919)

Angefertigt von **März 2021 bis März 2024** in der Klinik für Plastische, Ästhetische und Handchirurgie, Abteilung Mikrogravitation und Translationale Regenerative Medizin von Frau Professorin Dr. med. Daniela Grimm.

Klinikdirektor:	**Herr Professor Dr. med. Manfred Infanger**
Betreuer:	**Frau Professorin Dr. med. Daniela Grimm** **Herr Dr. rer. nat. Marcus Krüger**

Bibliographical Description:

Cortes Sánchez, José Luis:
The effects of low shear stress generated in simulated microgravity bioreactors on thyroid cancer cells and endothelial cells, and its role in the multicellular spheroid formation process. – 2024. – 132 Pg., 11 Fig., 3 Appx.

Abstract

One in two persons will be diagnosed with cancer in their lifetime, and cancer will soon be the leading cause of death in Europe. New treatment options are needed, which only a deep understanding of the disease can provide. When exposed to microgravity conditions, cancer cells show changes in their malignant properties. However, an explanation for the differences observed is missing. Therefore, a new model explaining microgravity's molecular effects on human cells is necessary. This doctoral thesis discusses that the gravity vector does not directly affect cell physiology. The thesis also investigates the physiological role of ESA Ground-based facilities for microgravity simulation. Multiscale models of tissue mechanobiology are essential for understanding the role of microgravity in biological systems, as it seems that the immediate surroundings of a cell within a 3D environment override external gravitational stimuli. In this work, I investigated the effects of simulated microgravity on different thyroid cancer cell lines, such as epithelial thyroid cells and follicular thyroid cancer cell lines with metastatic origin. Endothelial cells are also important in this thesis, as they possess more mechanosensitive capabilities. Cancer cells exposed to the Random Positioning Machine (RPM) commonly cluster forming spheroids; however, an explanation for the formation process is unclear. In this thesis, a 2-step process is identified: 1) The cell detachment caused by fluid flow dynamics generated as a secondary effect in the RPM. 2) The free-fall obtained in simulated microgravity devices facilitates the aggregation process. Future cancer studies in microgravity conditions should be based on 3D tumor models to provide better insights into the role played by gravity unloading in cancer progression.

Schlüsselwörter:
simulierte Mikrogravitation, Mechanobiologie, Gravisensation, Schilddrüsenkarzinomzellen, Metastasierung, Sphäroide, Endothelzellen

Keywords:
simulated microgravity, mechanobiology, gravisensation, thyroid cancer cells, metastasis, spheroids, endothelial cells

This thesis is based on the following papers:

Melnik, D., **Cortés-Sánchez, J. L**., Sandt, V., Kahlert, S., Kopp, S., Grimm, D., & Krüger, M. (2023). Dexamethasone selectively inhibits detachment of metastatic thyroid cancer cells during random positioning. Cancers, 15(6), 1641.

Jokšienė, J., Sahana, J., Wehland, M., Schulz, H., **Cortés-Sánchez, J. L**., Prat-Duran, J., ... & Simonsen, U. (2023). Effects of High Glucose on Human Endothelial Cells Exposed to Simulated Microgravity. Biomolecules, 13(2), 189.

Cortés-Sánchez, J. L., Melnik, D., Sandt, V., Kahlert, S., Marchal, S., Johnson, I. R., ... & Krüger, M. (2023). Fluid and Bubble Flow Detach Adherent Cancer Cells to Form Spheroids on a Random Positioning Machine. Cells, 12(22), 2665.

The publication texts can be found in the appendix of this dissertation.

Table of contents

Abbreviations

Abbreviations	Meaning
2D	Two-dimensional
3D	Three-dimensional
A549	Adenocarcinoma human alveolar basal epithelial cells
AD	Adherent cells
ALL	Acute Lymphoblastic Leukemia
Appx.	Appendix
ARHGAP	Rho GTPase Activating Protein 1
ARHGEF	Rho Guanine Nucleotide Exchange Factor 1
BMI	Body Mass Index
CAF	Cancer-Associated Fibroblasts
CO_2	Carbon dioxide
CONAHCYT	Consejo Nacional de Humanidades, Ciencias y Tecnologías
DEX	Dexamethasone
DNA	Desoxyribonucleic Acid
dyn/cm2	Dynes per square centimeter
EA.hy926	Somatic hybrid cell line (fusion of A549 cancer cell line with Human umbilical vein endothelial cell line)
ECM	Extracellular matrix
FN1	Fibronectin 1 gene
FP	Filopodia
FTC-133	The metastatic cell line of a follicular thyroid carcinoma
GLUT3	Glucose transporter-3 gene
HIPPO	Salvador-Warts-Hippo pathway
HUVEC	Primary Human Umbilical Vein Endothelial Cells
ICU	Intensive Care Unit
CXCL8	Interleukin 8 gene
ISS	International Space Station
LATS	Large Tumor Suppressor Kinase 1
LINC	Linker of Nucleoskeleton and Cytoskeleton
LP	Lamellopodia
MCF-7	Michigan Cancer Foundation-7 breast cancer cell line
MCS	Multicellular Spheroid
ML-1	Human cell line derived from a dedifferentiated follicular thyroid carcinoma relapse
MLCK	Myosin-Light-Chain-Kinase
MLCP	Myosin-Light-Chain-Phosphatase
mPa	Millipascal
mRNA	Messenger RNA
mTOR	Mammalian target of rapamycin
MUC-1	Mucin-1 gene
NASA	National Aeronautics and Space Administration

NF-kB	Nuclear Factor Kappa B
NIH	National Health Institutes
nM	Nanomolar
NMII	Non-muscle myosin II
NOX4	NADPH oxidase 4 gene
p38	p38 mitogen-activated protein kinase
PDZ	Postsynaptic density protein (PSD95), Drosophila disc large tumor suppressor (DlgA), and zonula occludens-1 protein (ZO-1)
RCCS	Rotatory Cell Culture System
RhoA	Ras homolog family member A
RNA	Ribonucleic Acid
ROCK	Rho-associated protein kinase
ROS	Reactive oxygen species
RPM	Random Positioning Machine
RWV	Rotating Wall Vessel
SANS	Spaceflight associated Neuro-Ocular Syndrome
SRC	Proto-oncogene tyrosine-protein kinase Src
T25	T-25 square centimeter cell culture flask
TAZ	Transcriptional coactivator with PDZ-binding motif
US	United States
VEGF	Vascular Endothelial Growth Factor gene
WRO	Human follicular thyroid carcinoma cell line
YAP	Yes-associated protein 1
YLL	Years of Life Lost

1.- Preface

This thesis was made possible thanks to the Doctoral Scholarship provided by the Consejo Nacional de Humanidades, Ciencias y Tecnologias de Mexico (CONAHCYT) in cooperation with the Deutscher Akademischer Austauschdienst—a special thanks to all the tax contributors from Mexico who supported my stay in Germany.

The experiments performed for this thesis were realized from March 2021 to November 2023 in the Department of Microgravity and Translational Regenerative Medicine of the Otto-von-Guericke-University Magdeburg, Faculty of Medicine, under the supervision of Dr. rer. nat. Marcus Krüger and Prof. Dr. med. Daniela Grimm. The confocal microscopy imaging and shear stress experiments were done at the Institute of Anatomy of the University Clinic Magdeburg under the supervision of Dr. Stefan Kahlert in the laboratories of Prof. Dr. med. Hermann-Josef Rothkötter.

Supervisors:

Prof. Dr. med. Daniela Grimm
Head of the Department of Microgravity and Translational Regenerative Medicine
Otto-von-Guericke-University, Magdeburg, Germany

Dr. rer nat. Marcus Krüger
Group Leader of Environmental Cell Biology
Department of Microgravity and Translational Regenerative Medicine
Otto-von-Guericke-University, Magdeburg, Germany

2.- Hypothesis

The three main hypotheses for this doctoral thesis are:

- The fluid shear stress generated in simulated microgravity bioreactors, like the Random Positioning Machine (RPM) or 3D clinostats, can significantly impact the biological activity of an adherent cell population exposed to simulated microgravity.
- The spheroid formation process of cancer cells exposed to the RPM as an adherent cell population is a 2-step process: 1) First, some adherent cells detach and continue to grow in suspension; 2) Then, the suspension cell population starts to aggregate.
- Fluid shear stress is the most probable cause of cancer cell detachment from the adherent cell population exposed to the RPM. Microgravity exposure facilitates the cell aggregation process.

The experiments in real and simulated microgravity constantly showed changes in the cancer cells' malignancy features, and the observed effects are ascribed to the simulated microgravity condition. However, free fall is absent in the experiments performed with adherent cells on the RPM. The recent findings from the mechanobiology field can help to explain how our cells sense and adapt to mechanical forces in simulated microgravity devices.

3.- Aims and questions asked

This study aims to understand the physiological role of ESA ground-based facilities for simulated microgravity, particularly the RPM, for *in vitro* experiments with human cells and to define the best possible use for simulated microgravity bioreactors in human cells. Different research groups investigate its applications and use (2), but the results obtained in them are difficult to translate into space medicine applications. Those devices will continue to play a role in planning future space experiments; however, researchers need to understand the mechanism of action of these devices, including their disadvantages, to provide a correct interpretation of the results. Finally, a further goal of this thesis was to try to determine a gravisensor system for human mammalian cells.

In microgravity research, two open questions remain unsolved:

1) Why do metastatic cancer cell lines form spheroids when cultured under RPM conditions?

2) Can the exposure to microgravity explain all the effects observed in cells cultured on the RPM?

The integrative question is whether the cells cultured in the RPM as adherent cells feel simulated microgravity conditions.

Since the development of simulated microgravity bioreactors, it is assumed that when culturing a cell line on the RPM, the cells are in a state that approximates microgravity due to the randomization of the gravity vector. However, experiments performed with cancer cells in simulated microgravity bioreactors do not provide homogeneous results. Therefore, it is at least debatable that microgravity is the cause of all the changes observed in the cells. Therefore, a new model for the interpretation of results obtained in simulated microgravity bioreactors was investigated.

4.- Introduction

4.1. Cancer

The origin of the name "cancer" for this disease was ascribed to Hippocrates (ca. 460-ca. 370 BC), who used the word *carcinos* and *carcinoma*. Those words mean crab in Greek and probably refer to the shape the tumor can take with the finger-like spreading (3). Cancer is a disease affecting humans for over 200 million years (4). The first evidence of cancer treatment was found in an ancient Egyptian text more than 5,000 years old, which describes the cauterization of breast tumors, and it mentions that the disease was incurable (5). Nowadays, the 5-year survival rate of patients with breast cancer can reach up to 90% in highly developed countries.

Cancer does not consist of a single disease entity that can be treated in general, but is a group of diseases with some common characteristics (6). There are more than one hundred types of cancer, and the number of subtypes increases if molecular classification is considered. Therefore, there is no universal curative treatment for cancer. Molecular classification can also complicate the previous classification because tumors of different tissue origins may share similar genetic characteristics, and therefore, similar treatments can be implemented (7).

4.1.1. Epidemiology

Cancer will soon be the leading cause of death in Europe (8). In most countries, cancer is either the primary or second most common cause of premature mortality (9). As the world

population demographics are changing, the number of people who reach an older age increases as well as their risk of developing cancer. Around one in two people will be diagnosed with cancer during their lifetime (10). In 2022, the cancers with the highest incidences were lung cancer (2.48 million new cases per year worldwide), breast cancer (2.30 million cases), and prostate cancer (1.47 million cases). However, the most common causes of death by cancer are lung (1.82 million deaths per year worldwide), liver (759,000), and breast cancers (666,000) (11). There is a need to offer a better treatment to reduce mortality and provide an earlier diagnosis. Recent projections for the United States estimate that in 2024, there will be 2,001,140 new cancer cases and 611,720 cancer deaths, according to the American Cancer Society (12).

In the medical literature, cardiovascular diseases are commonly referred to as the leading cause of death; however, cancer has the most significant toll on society. A better representation of a disease's burden on society is the index years of life lost (YLL), which helps to describe how a particular disease shortens patients' lives. The most recent estimate for cancer is 15.2 YLL per person diagnosed with cancer in the US (13). In Germany, the YLL was estimated by the BURDEN 2020 project at the Robert Koch Institute, and of the total of years estimated to be lost in the population in 2017, tumor/neoplasms represented 35.2%, followed by cardiovascular diseases with 27.6% (14).

4.1.2. Cancer features

As cancer research expanded and consolidated, more features were discovered among the diverse types of tumors. Surprisingly, different tumor types shared some characteristics. Hanahan and Weinberg described the six hallmarks of cancer, where they provided principles that help understanding this complex disease (15). This work was further updated in 2011 (16) with eight hallmarks and two enabling characteristics, which are evading growth suppressors, avoiding immune destruction, enabling replicative immortality, tumor-promoting inflammation, activating invasion and metastasis, inducing or accessing vasculature, genome instability and mutation, resisting cell death, deregulating cellular metabolism, and sustaining proliferative signaling. In 2022, 4 enabling characteristics were added: no-mutational epigenetic reprogramming, polymorphic microbiomes, senescent cells, and unlocked phenotypic plasticity. (17)

4.1.3. Pathogenesis and Metastasis

The leading cause of death in cancer patients is metastasis (18). Metastasis is the growth of cancer cells in a site distant to the organ from which it originated (19). The metastatic outgrowth can affect different organs, and the tumor mass overwhelms the organ's functionality. Patients with metastatic disease are primarily incurable. However, metastasis formation is a multi-step process, and cancer cells must overcome a series of complicated challenges to colonize a distant organ (20).

There are two main ways for cancer cells to reach a distant organ: lymph nodes and blood vessels. Also, there is the option that cancer cells directly invade the adjacent tissues. In venous metastasis, the cell has to survive harsh conditions inside the circulation through the tumor vasculature and bloodstream; in fact, most cells succumb during this process, and only a few can expand and colonize distant body regions (21).

The typical steps for the formation of a cancer cell metastasis are: 1) Cancer cells from the primary tumor become motile and invade the adjacent extracellular environment. 2) Once inside the extracellular space, cancer cells must migrate and degrade the ECM to enter the lymphatic vessels. 3) Cancer cells must survive compression forces when entering the lymphatic vessels. 4) The cancer cell must adapt to the different nutrient compositions inside the lymphatic system (22), which differs from a blood vessel rich in nutrients. 5) Finally, the cancer cell must survive the shear forces on the lymph node in the range of 10-20 mPa (23), which is caused by the pumping of lymph fluid back into the central circulation. Human cells can feel and react to these small shear stress values, called “low-shear stress” and it has been reported, that it might increase the cell motility via an activation of the Piezo 1-YAP axis (24)

Lymph nodes constitute the most common metastatic site in cancer patients (25). In the lymph nodes, the cells of the immune system can detect cancer cells and, most of the time, eliminate them. The presence of metastatic lymph nodes is of great prognostic significance. For example, in patients with triple-negative breast cancer, the 5-year overall survival (OS) in node-negative patients is 80%, and this survival is reduced to 44% in patients with 10 or more positive nodes (26).

4.1.4. Cancer cell lines with metastatic origin

Cancer research involves the use of established cell lines. These cell lines have been isolated from cancer patients. It should be noted that a cell line isolated from a metastatic lymph node differs from a tumor cell line isolated directly from the primary tumor. The former

has undergone a selection process within the human body, enabling it to colonize the lymph node. The process involves the acquisition of new mutations and gene rearrangements that allow the cell line to survive in the new environment, and this cancer evolution theory was suggested as an explanation for how a tumor evades treatment (27).

4.1.5. Cancer cell microenvironment

Cancer cells are surrounded by the tumor microenvironment, which is composed of an extracellular matrix (ECM) and stromal cells. This cancer cell microenvironment can determine outcomes in cancer patients (28). In a tumor, the presence of cancer-associated fibroblasts exerts essential effects on the cancer cells, and a CAF-related gene signature was shown to be predictive of survival and drug response in patients with colorectal cancer (29). The microenvironment can regulate the cell behavior at the new metastatic site, especially the mechanical properties of the new colonized tissue (30). It can influence primary tumor growth, chemotherapy resistance, migration capabilities, and the potential to establish a secondary metastatic site (30).

4.1.6. Mechanobiology

Human cells are mechanosensitive and adapt to tissue stiffness. Cells do not translate mechanical signals into dedicated intracellular pathways but use the same pathways of other biochemical signaling. This leads to a crosstalk between metabolism and mechanobiology, which is of significant importance for the cancer cell metastasis process (31). Mechanobiological signaling can influence the cells up to the extent of hormones and cytokines, and the field of mechanobiology has been recently the focus of extensive research. One interesting application of mechanobiology involves mesenchymal stem cell research, where stem cells can be directed to differentiate into either bone or fat tissue depending on the stiffness of the matrix over which the cells are cultivated (32). Figure 1 shows the various degrees of stiffness of different body tissues in comparison to the typical materials used in cell culture laboratories (33).

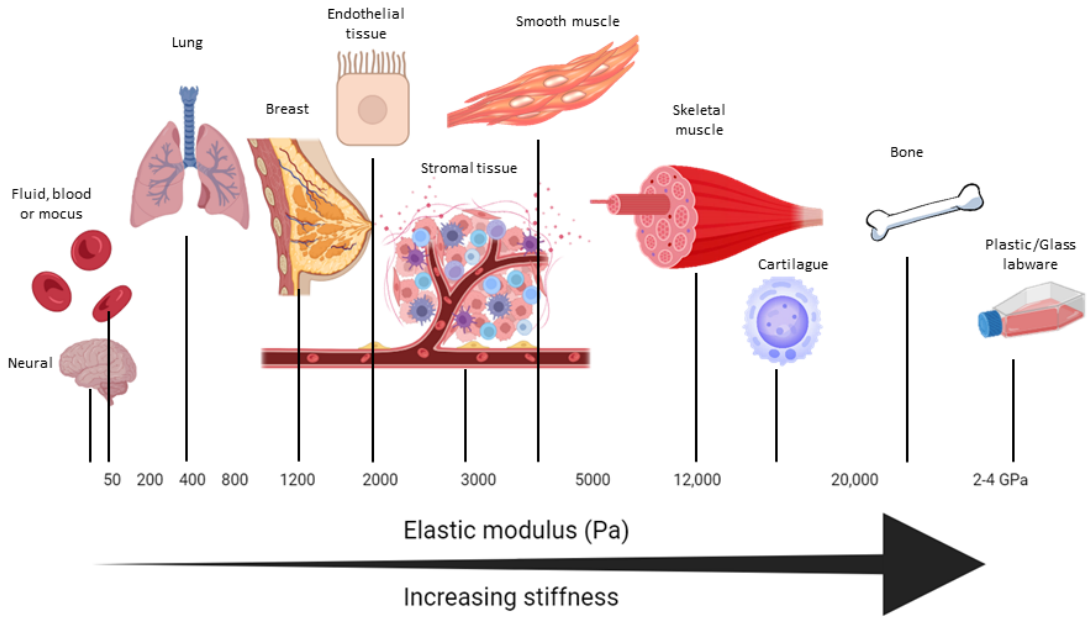

Figure 1.- *Mechanobiological properties of the different tissues, redrawn from Cox et al.* (33). *Pa: Pascals*

Mechanobiology plays a significant role in cancer. The mechanoreceptors can detect changes in mechanical inputs, influencing key pathways for cancer cell growth, survival, angiogenesis, invasion, and metastasis (34). Mechanobiology could be used to understand how dormant cancer metastases can survive by seeking environments characterized by softness. A soft ECM promotes the dormancy state of the cells, whereas a stiff microenvironment activates the proliferative state. This matrix-driven dormancy is a reversible process (35). Also, specific organs like the bone marrow can act as reservoirs for dormant cancer cells, which later provide further metastases to distant organs (36).

The cancer cell originates from a stiff tissue like the original tumor site, which is more metabolically active because of its rigid stiffness. Therefore, typical chemotherapeutic drugs can target them. However, once they are in the soft tissue, this metastasis is no longer metabolically active and therefore can evade chemotherapy. This difference explains why metastatic seeds are observed in soft organs like the lungs, brain, liver, and bone marrow and complements the cancer metastasis “soil and seed” hypothesis by Paget (37). Also, the stiffness of the ECM surrounding the cancer cells plays a critical role in cancer progression (38), and the cancer cells' ability to adapt to the stiffness of the ECM is related to the invasive potential of the cells (39).

4.1.7. Thyroid cancer

In cancer research in space, one of the most used cell lines is the thyroid cancer cell line FTC-133. Thyroid cancer is not a singular disease. Histologically, the classification divides

thyroid cancer into follicular, papillary, medullary, and anaplastic types. The classification also recognizes four stages for the disease, depending on the type of lymph node invasion and the presence of metastases. Until recently, a molecular classification of the disease was missing.

The FTC-133 cell line used in this work is a follicular thyroid cancer cell line isolated from the lymph nodes of a patient with stage IV disease. It is a highly advanced and specialized cell line. It may be considered that the FTC-133 cell line should not be referred to simply as a follicular thyroid cancer cell line, and according to a recent molecular classification, this cell line shares molecular characteristics of anaplastic thyroid cancer (40). The mutations can explain the more aggressive behavior (41). Thus, the term anaplastic-like cancer cell type better describes the FTC-133 cell line.

4.2. Microgravity

Because of Earth's mass of ~6×10^{24} kg, objects on the planet's surface are accelerated toward its center with a gravitational force of 9.81m/s² (42). Research in space represents the gold standard in microgravity research. However, astronauts aboard the International Space Station (ISS) in low Earth orbit at an altitude of about 350 km, are still exposed to 88.8% of Earth's gravitational field. Therefore, an alteration of the gravitational field is not the reason for all the observed changes in space travelers. What is then microgravity? In plain words from NASA, the state of microgravity occurs when an object is in free fall. Free fall is the movement of a body in which no forces other than gravity act on it (43). Therefore, weightlessness can be achieved by dropping objects in free fall in a vacuum environment.

4.2.1. ESA ground-based facilities for simulation of microgravity

Experiments in real microgravity are expensive and scarcely available. Different platforms have been developed to provide scientists on Earth with experimental conditions similar to real microgravity. This includes the clinostats, random positioning machines, and magnetic levitation. The ESA ground-based research program provides scientists access to experimental capabilities, aiming to serve as preparation for their space experiments (2).

The clinostat and the RPM are based on changing the perceived gravity vector direction over time by rotating the sample around one or more axes in space. This idea has been used to simulate the effects of microgravity on human cells or other systems, such as plants or bacteria (2). Researchers can simulate the free-fall effect on Earth using the correct

microgravity simulator. For example, using the Rotating Wall Vessel with a cell suspension inside, cells can experience microgravity. One of the best examples is the ClinoStar from CelVivo, for which researchers can optimize the speed of rotation according to the size and weight of the object, maintaining free-fall for a more extended period. Table 1 gives an overview of advantages and disadvantages of the simulated microgravity devices (figure 2):

Table 1.- *Comparison of different microgravity simulating devices.*

Device	Mechanism of action	Disadvantages
1.- Rotating Wall Vessel (RWV)	Constant rotation of the bioreactor allows the perpetual free fall of the cellular aggregate contained.	Constant flow of medium around the cells.
2.- ClinoStar by CelVivo	An improved version of RWV with control over speed depending on the size of the cell aggregate.	The bioreactors are small compared to a T25 cell culture flask.
3.- 3D Clinostat	Constant rotation in the 2 axes averages the gravity vector to microgravity levels.	High shear forces are generated according to the mathematical modeling of Wüest (44).
4.- Random Positioning Machine (RPM)	A 3D Clinostat with an improved algorithm that allows a random direction and speed of rotation.	Mimic microgravity responses for several but not all experimental conditions.(2)
5.- Magnetic levitation	A magnetic force is used to counterbalance the gravitational force (2).	Verification and final validation need comparable experiments in real microgravity.

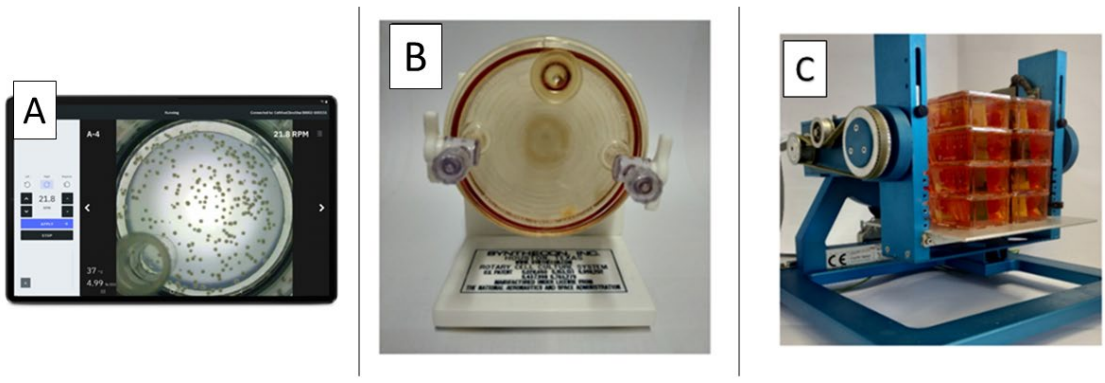

Figure 2.- *Simulated microgravity platforms. A. A Clinoreactor from the ClinoStar. B. An RWV. C: The RPM.*

The Bonn Criteria were developed to standardize simulated microgravity experiments (45).They define a minimum set of physical parameters of the culture device and cell culture conditions to be reported in clinostat and RPM experiments. The list of parameters is shown in Table 2 (45).

Table 2.- *Bonn Criteria [56]. Minimum set of parameters to be reported in clinostat and RPM experiments. The parameters marked with an * are exclusive for an RPM experiment.*

Properties of the culture vessel, culture media, and carrier beads.
Dimensions and rotation speed of vessel.
Chemical consistency including density and viscosity of media
Size, density, and porosity of beads and same features for the cells
Whether cells are motile or non-motile,
Density of beads with cells attached
Time of rotation and nature of controls
Operating temperature and Gas content
Angular velocity of rotation * and Highest angular acceleration *
Operating mode (random, centrifuge, clinostat in RPM or freely programmable mode) *

4.2.2. Cancer Research Under Microgravity Conditions

When exposed to microgravity, cancer cells show substantial alterations in genes and proteins related to the main features of cancer, such as adhesion, invasion, angiogenesis, and proliferation (42). In 2021, I attempted to adapt the "Hallmarks of Cancer" to cancer space studies and created figure 3, which summarizes the current knowledge about the effects of space conditions on cancer cells (46).

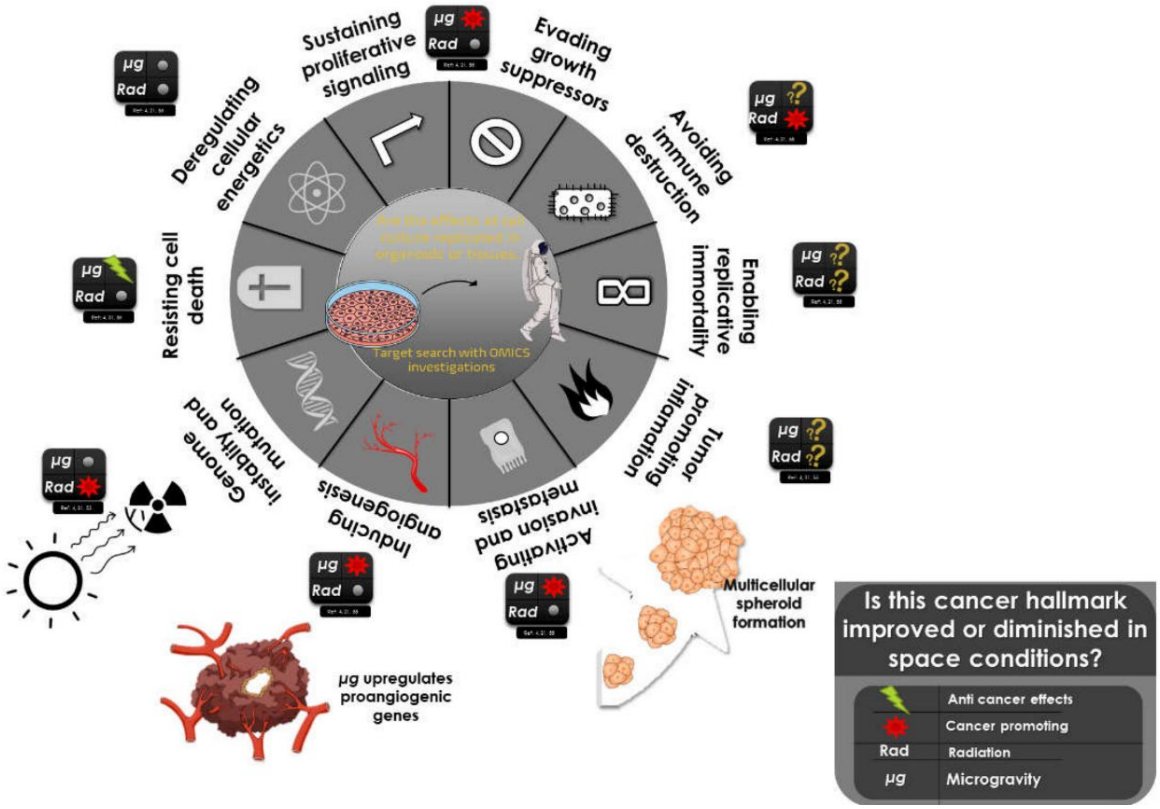

Figure 3.- *Summary of the features of cancer that are affected by space conditions (Taken from Cortés-Sanchez et al. [46]).*

However, it is exceedingly difficult to draw a general conclusion about the effects of microgravity on cancer progression because:

a) The general effect of microgravity on human cells has not been determined.

b) It is unknown which molecular mechanism explains the observed changes.

If a mechanism can be identified, such as the pathway responsible for the changes observed in cancer cell features, some new weaknesses in the cancer cell will be discovered and may be a potential target for a future drug.

A typical simulated microgravity RPM experiment with adherent cancer cells consists of:

1) An adherent population of cancer cells is cultivated in standard T25 cell culture flasks for 24 h. The cells grow as an adherent cell population and, after hours, are rigidly attached and start to proliferate.
2) After 24 h of seeding, the flasks are completely filled with cell culture medium and subjected to simulated microgravity exposure on the RPM.
3) After at least 24 h of rotation in the RPM, the initial adherent cells divide into two different cell populations: the original adherent cell population and some floating cell aggregate, called spheroids, of cancer cells growing in a 3D organization.

4) After gene expression and protein analyses, these two cell populations show apparent differences in molecular markers for cancer progression.

An explanation for the origin of the multicellular spheroids (MCS) is lacking in the current medical literature. Therefore, I investigated the possible causes for the MCS formation through the perspective of mechanobiology (figure 4).

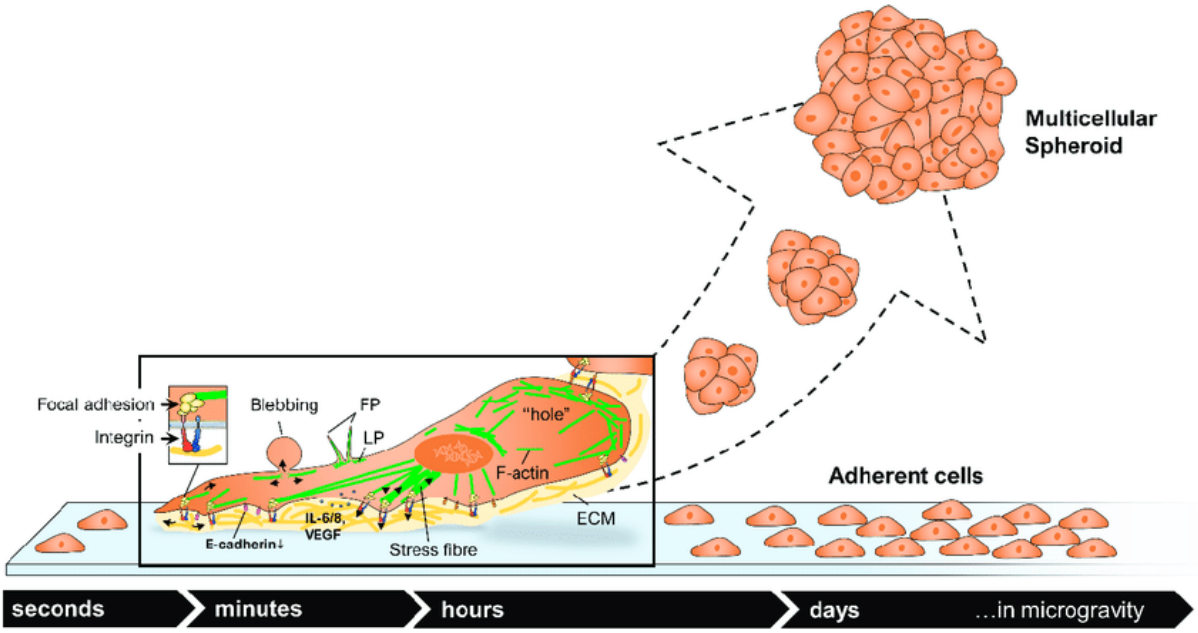

Figure 4.- *Representation of the MCS formation process on the RPM. FP: Filopodia, LP: Lamellopodia, VEGF: Vascular endothelial growth factor, ECM: Extracellular matrix. (Taken from [46].)*

The spheroids formation process occurring on the RPM is often presented as a metastasis model for cancer. Providing a good understanding of the environment, the RPM generates, this bioreactor represents a viable study model. In this work, it was attempted to contribute to the understanding of the primary signaling pathways cancer cells activate in the RPM experiments. Cells cultured in the RPM showed interesting changes regarding angiogenesis, invasion, and proliferation; however, the results are never homogeneous between the different cell types. Figure 5 shows the ClinoStar (A) and the iRPM (B). The spheroids obtained from a ClinoStar- and an RPM-exposure of FTC-133 follicular thyroid cancer cells are shown.

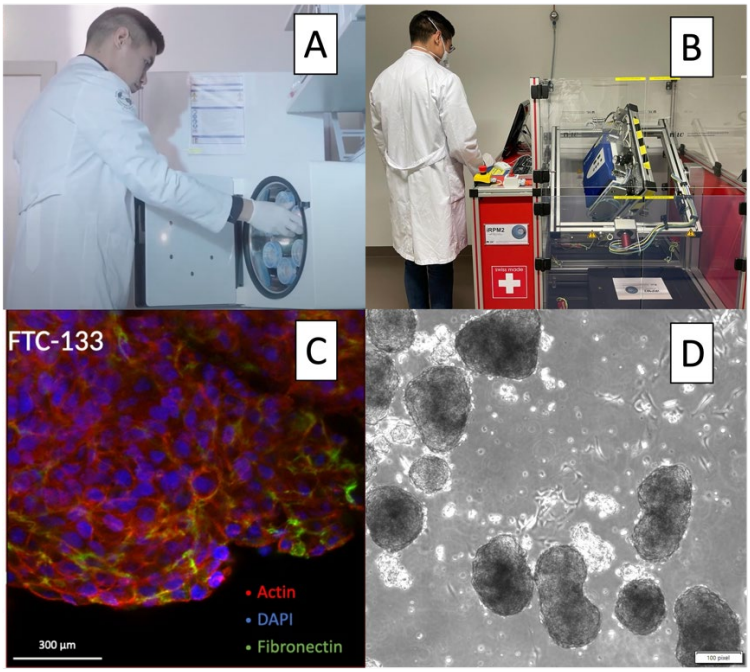

***Figure 5**.- A) Preparation of multicellular spheroids using the Celvivo Clinostar and B) the iRPM. C) Confocal laser scanning microscopy image of a multicellular spheroid obtained from FTC-133 cancer cells cultivated for 7 days in simulated microgravity; D) Brightfield microscopy of FTC-133 spheroids cultivated 7 days in the Clinostar.*

4.2.3. Endothelial cells under microgravity conditions

Endothelial cells are a vital part of the internal layer of a blood vessel. These cells cover the most internal layer of vessels and are part of its wall. They have a plain shape, and their diameter is adaptable according to the diameter of the vessel they cover. They also have an essential role in vascular regulation and the integrity of blood vessels, thanks to their specialized cell-cell adhesions. These junctions allow the cells to support and apply forces, affecting the endothelium's barrier function and response to stimuli. The endothelial cells are crucial in delivering nutrients and oxygen to the tissues and removing waste, and play a significant role in cancer metastasis and immune regulation (47).

Endothelial cells are also important in this thesis, as they possess more mechanosensitive properties. They are essential in space research, and it has been reported that astronauts suffer from cardiovascular problems, with a particular inflammation in the blood vessels during and after space-exposure. An increase in markers of endothelial dysfunction after long-duration space missions in astronauts with blood vessel damage has been observed, leading to a rise in endothelium procoagulant potential (48).

In vitro experiments have shown how microgravity alters the expression of inflammatory and vasoactive mediators in endothelial cells (49). For example, when using human umbilical vein endothelial cells (HUVEC) in a rotatory cell culture system (RCCS), researchers found growth inhibition after a return to normal gravity, which was mediated by

the mammalian target of rapamycin (mTOR) signaling and *miR-22* regulation (50). The endothelium is sensitive to unloading conditions, and space-flown endothelial cells show changes such as stress granules, reduced motility, mitochondrial senescence, telomere shortening, and increased apoptosis (51). EA.hy926 immortalized endothelial cells were exposed to real microgravity on the ISS for 12 days. Three different cell populations were observed: adherent cells, multicellular spheroids, and tubular-like structures. An enhanced collagen and laminin protein expression was observed in the 3D aggregates. The analysis of the cell culture supernatants revealed an alteration in the secretion of growth factors, cytokines, and ECM components of the space samples compared to the 1*g* or RPM group (52).

Furthermore, a drop in cell stiffness, where cortical rigidity experienced a significant decline, was observed in HUVEC cells exposed to simulated microgravity in the RPM for 24 h. Western blots demonstrated a reduction in the cytoskeletal components of the microgravity samples, and immunofluorescence staining showed disorganization of actin filaments and microtubules (53). Finally, one of the most important applications of the current knowledge gained from the exposure of endothelial cells to microgravity conditions is the future study of how these changes will affect wound healing and tissue response in case of traumatic injury or medical intervention in space (54).

4.2.4. Effect of microgravity on the human body

The present gold standard for research on human physiology under microgravity are studies conducted in real-microgravity on the ISS with astronauts. Astronauts suffer from bone and muscle loss during their stay on the ISS; however, sarcopenia is not homogenous in the entire body and focuses on weight-bearing structures, such as the so-called antigravitatory muscles, including the gastrocnemius and the musculoskeletal system of all the lower extremities. According to a meta-analysis, bone density remains unchanged for the thorax/upper limbs region relative to preflight levels, whereas a negative difference in the lumbar spine/pelvis and lower limbs is observed (55). The difference in the bone density changes can be explained by the position of these regions relative to the weight-bearing role they play in the body. Even when the whole body is in microgravity, the most significant changes are present in the body's lower part, which deals with the weight of the person on Earth. In microgravity, these structures are liberated from the constant load (figure 6).

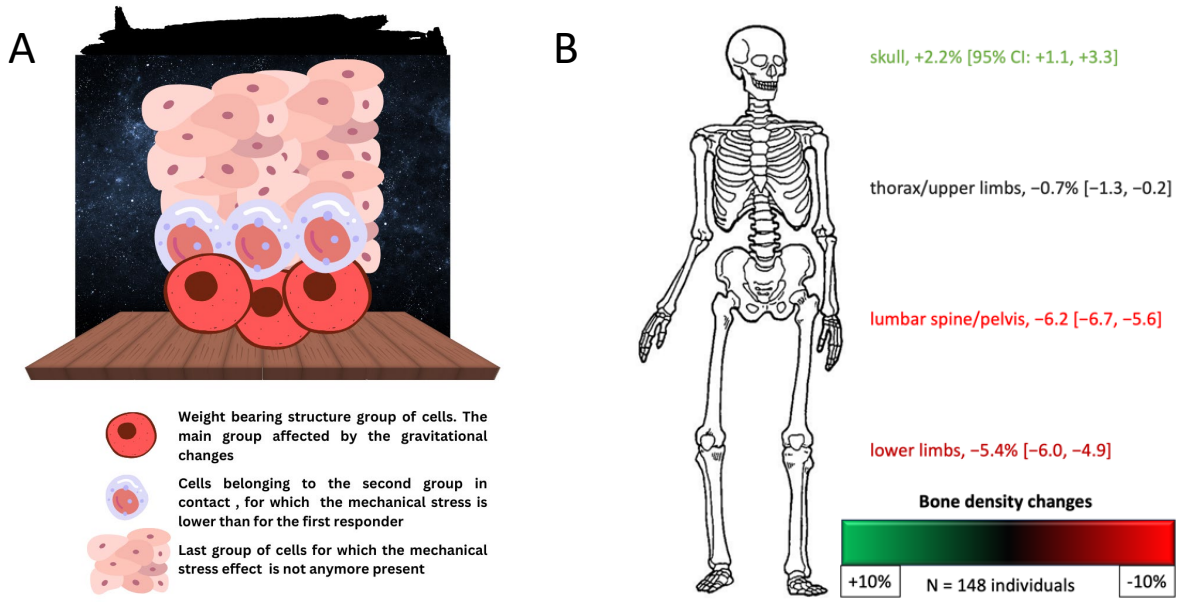

Figure 6.- *Model of the gravisensation for complex structures /multicellular organisms. A: Illustrates the proposed gravisensation in a complex multicellular structure. B: Summarizes the observed changes in the skeleton of astronauts (adapted from* (55)*)*

Researchers can understand the changes observed in the cells of our body once exposed to gravitational changes, only by considering all the relative forces acting on a cell. Cell in free fall as part of a 3D structure or embedded in a 3D matrix, are seemingly less prone to changes under the weightlessness/microgravity because they are now protected through this extracellular microenvironment and have less plasticity, therefore suffer less from the microgravity effects. Although a hypothesis, recent research observes this behavior. ElGindi *et al.* observed that the presence of a stiffer ECM during an RPM experiment attenuates the effects of microgravity simulation on the transcriptome of cells exposed to the RPM (56, 57).

4.2.5. Does our cells feel a gravity vector?

To explain the changes related to microgravity-exposure, we can take the bone and muscle alterations as an example. The human body is composed of different layers of organization: At first, the body systems carry specific physiological functions. Each system is composed of organs composed of tissues. The tissues are composed of many cell types and ECM, and finally, each cell is composed of organelles made of proteins and other macromolecules; at the end being formed by atoms and molecules. The interaction and coordination of the mechanisms of mechanotransduction across multiple hierarchies, from molecules to the whole-body level, have not been comprehensively investigated and deserve

further studies (58). Then, at which level of organization can our body perceive a gravity vector? If every cell can perceive the changes in the magnitude and direction gravity vector, then all the cells and corresponding systems in our body will experience the same sort of changes in microgravity. However, microgravity exposure does not affect every system in the body. Instead, first, the systems are affected, and then the cells composing those systems are subsequently altered. The following diagram will show this association (figure 7). As a recent paper states (59): "Some of the properties that emerge in the mesoscale are the results of phenomena happening at the microscale of our cell."

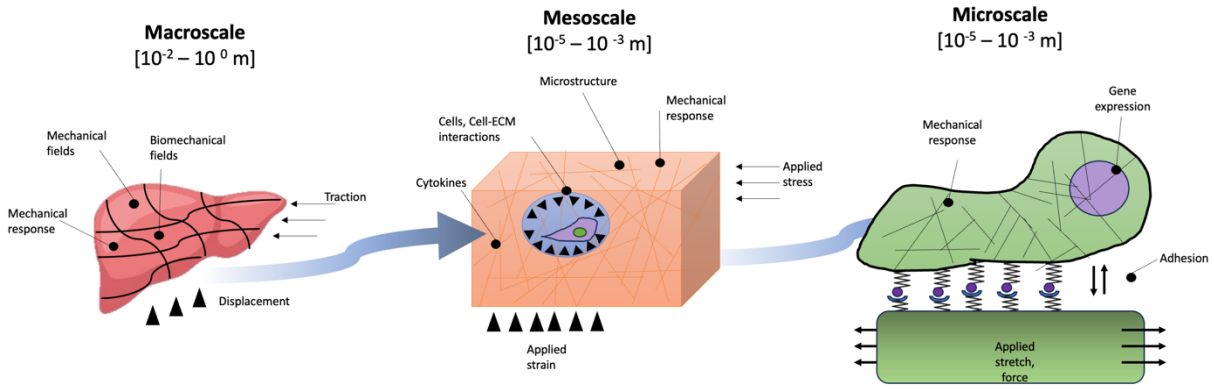

Figure 7.- *Explanation of the macroscale, mesoscale, and microscale forces. (Simplified version of the figure adapted from* (59)*.*

4.2.6. Gravisensation, in comparison to the other senses

The human body has organs to detect different stimuli and provide a sense of vision, hearing, proprioception, taste, smell, and tactile sensations. Our bodies perform this task at a system level. Different cells and tissues coordinate for each system to feel and interpret the stimuli (60). At the bottom of this chain, a specialized cell type is responsible for interpreting the signals and converting them into information that the nervous system integrates into the senses. However, there are no organs directly related to gravisensation (61, 62). The closest is the vestibular apparatus, which can detect acceleration in the three different axes of space, and this information helps to coordinate our movements.

This discussion led to a first conclusion about gravisensation: Human cells do not perceive the gravity vector directly, but the relative effects gravity has on bigger structures, which means our cells perceive gravity indirectly and not by a specific organelle. For an adherent cell inside a cell culture flask during the RPM experiments, the changes triggered by the gravity vector changes are relatively less important in comparison to the magnitude of other stimuli. Some authors argue that the mass of a single normal-sized cell is very small to allow a distinction in gravity vector changes (63). In comparison, the weight of the cell culture

medium surrounding the cell is much larger, and therefore the cells only indirectly perceive the gravity vector changes.

4.2.7. Mechanobiological perspective in microgravity

A mechanosensory unit in adherent cancer cells exposed to simulated microgravity conditions has been described by Sanyour *et al.* (46): Integrins are measuring the ECM stiffness constantly, and once microgravity creates mechanical unloading, the reaction force generated by the flask against the cells is lost and only the force generated by the stiffness is active. The cytoskeleton is then disorganized, as explained by the tensegrity model, and the tension in the actin stress fibers is lost. The cytoskeletal disorganization is transmitted to the nucleus by mechanosensory coactivators YAP/TAZ, which coordinate a countermeasure response to adapt the gene expression to the new tensional state of the cytoskeleton, for example, by upregulating genes from the *ARHGAP*/*ARHGEF* family, that upregulate Rho-GTPase activity, so the cytoskeleton regains its organization (figure 8).

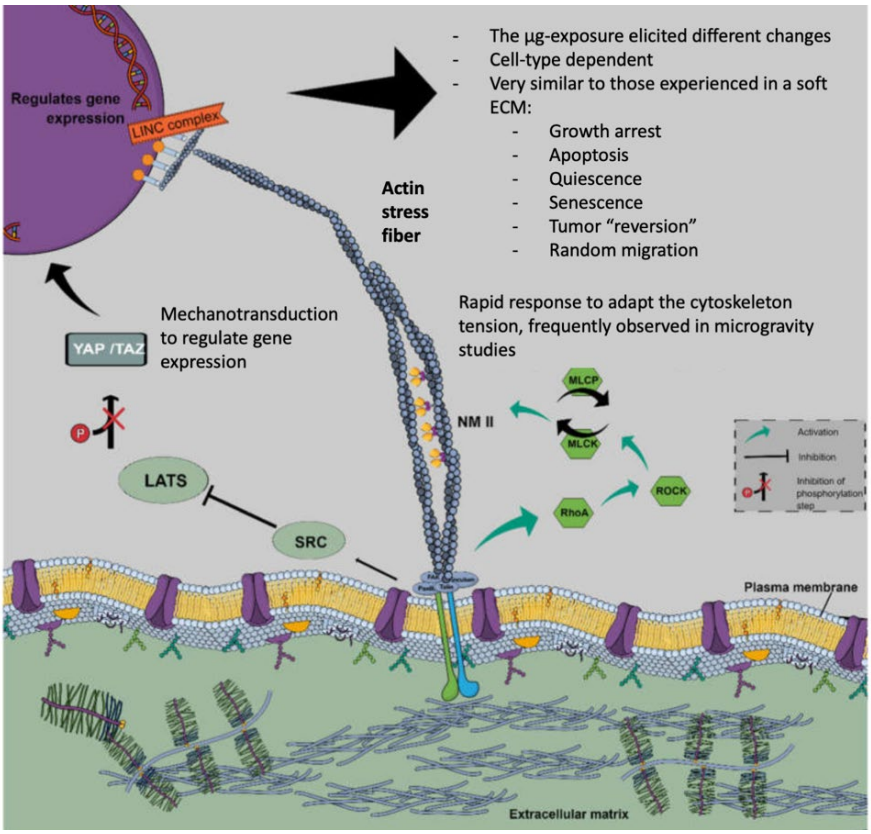

Figure 8.- *Diagram explaining the molecular pathway responsible for transduction of unloading conditions. Redrawn from [47]. ECM: Extracellular matrix, SRC: Proto-oncogene tyrosine-protein kinase Src. RhoA: Ras homolog family member A, ROCK: Rho-associated protein kinase, YAP: yes-associated protein, TAZ: transcriptional coactivator with PDZ-binding motif, LINC: Linker of Nucleoskeleton and Cytoskeleton, MLCK:*

Myosin light-chain kinase, MLCP: Myosin-light-chain phosphatase, LATS: Large tumor suppressor kinase, NMII: Non-muscle myosin II.

4.3. Discussion of the limitations and challenges of simulated microgravity devices

The analysis of experiments on the RPM is expected to compare the gene expression and protein results of the 1*g* static control with that of the RPM-spheroid population and the RPM-Adherent cell population. Critique can be made of this methodology because both cell populations are incomparable: an MCS is a 3D cell culture compared to a 1*g* flat culture, in which the cells are attached to the ground and form a 2D monolayer. MCSs are common in biomedical research and are not exclusive to microgravity research. There is an extensive range of possibilities for growing 3D aggregates that can even be composed of different cell types, for example, the non-adherent well plates, ECM modifications such as Matrigel, bioprinting, and the hanging drop technique (64). When grown in 3D structures, cells behave differently from those cultivated in the typical flat biology cell culture flasks (65).

The 3D cell culture of breast carcinoma MCF-7 cells possesses more than 50 times higher drug resistance than a 2D culture counterpart (66). The 3D culture resembles a cancer metastasis, and the tumor cells express efflux pumps to expel the chemotherapeutic compound outside of the cell (67); also, the 3D shape protects the cells in the center of the metastasis from the drug. Different cancer cell subpopulations with functional heterogeneity compose an MCS, such as the core *vs.* the outside growing ring of cells. For example, in MCF-7 spheroids, three different clusters of gene expression patterns were identified by single-cell RNA-seq, with one subgroup involved in proliferation, another serving the role of invading tissues, and the last serving as a reservoir cell population (68).

A better methodology would be to use a 1*g* static culture of spheroids obtained from a method distinct to the RPM, such as the hanging drop technique or a non-adherent surface plate. As this 1*g* spheroid control group is missing from previous simulated microgravity experiments, the microgravity generated spheroids group would be omitted from the discussion of the research articles. Recently, some authors have introduced this control group and provided a deeper understanding of the effects of microgravity on cancer progression (69).

4.3.1. Secondary effects produced inside the RPM

Shear stress is a secondary effect of culturing cells on the RPM. Mathematical modeling has established that it can reach up to 20 mPa for the adherent cell population in the flask (44). Such value may appear insignificant; however, it corresponds to the shear stress inside the lymphatic system (23). The first authors who demonstrated a biological significance for the

shear stress of the RPM were Hauslage *et al.*, who used an organism with a mechanosensitive bioluminescence as a biosensor and demonstrated biosensor activation by the shear forces generated inside the RPM (70). However, the biological role of shear stress by the RPM on human cells has not yet been determined. In this work, I aimed to determine the biological significance of this shear stress response.

Another consequence of the constant rotation of the RPM is that the cell culture medium increases its convection, providing a better mixture of its components, which improves the oxygen and CO_2 exchange (71). Poon suggests using an extra control group in the experiments with a shaking rocker (71), which increases the convection in the medium, so that the role of medium mixture in the RPM can be separated from microgravity. Using comparative transcriptomics, Kouznetsov (72) claims that the cell responses to simulated microgravity can be distinguished from the response to hydrodynamic stress. Such tests were also subject in this work, and the results are presented in the third paper of this dissertation (73).

4.3.2. 3D models and gravity alteration studies.

Using the correct experimental model when trying to extend conclusions in biomedical research is essential. A 2D cell culture does not accurately reflect physiological conditions, and the molecular pathways in an *in vivo* model are not represented in a 2D *in vitro* model(74). Culturing tumor spheroids can help to overcome such issues, as cells in a 3D environment possess characteristics typical of the tissue of origin (75). Similarly, an experiment using 3D models can provide a better understanding of gravisensation. One critical experiment to advance research on the role of microgravity in tumors is to expose 3D tumor models, such as organoids, spheroids, or cells embedded in an extracellular matrix to real microgravity. The experiments of Larose and colleagues will be taking tumor organoids to the ISS to probe whether microgravity will slow down or stop cancer growth (76). Progress has already been made in this direction in recent years, for example, using a cancer-on-a-chip model of glioblastoma under simulated microgravity conditions (77). The results from studying non-cancer cell lines will also help to understand the role of microgravity on 3D structures. For example, a skin model composed of skin and blood vessel cells was exposed to simulated microgravity conditions and reproduced the physiological changes of skin in space (78). In all the studies mentioned above, exposing a 3D structure to simulated microgravity allows us to draw conclusions that are closer to reality, as 3D culture conditions better resemble the physiological state of any organ or tissue.

4.4. Future directions for research and development of simulated microgravity devices

A limitation of cancer research in microgravity is that the conclusions about the effects of microgravity on cancer progression are extrapolations of only the molecular studies performed; however, a functional study is still missing in the field. It would be advantageous to expose tumor spheroids to simulated microgravity conditions and then, after microgravity exposure for at least seven days (the typical time frame after which cells have been shown to possess a molecular signature of reduced malignancy), inject the spheroids into mouse models on Earth. Spheroids obtained from a non-microgravity method represent the control group and will also be injected into another set of mouse models. After 30 days, which mice had more metastasis, or a more extensive disease progression could be quantified and measured. If mice injected with tumors that were exposed to microgravity showed a milder disease progression, this would prove that microgravity affected the capabilities of the tumor cells and made them less malignant. Interestingly, similar experiments were performed by Dr. Quinones-Hinojosa's group, which exposed cancer cells to real microgravity. After the weightlessness exposure, the cells were injected into a mouse model, and the tumor progressed faster in the microgravity group, so they concluded that microgravity selected more malignant cell phenotypes. However, the rocket only ascended to an altitude of about 26 km and the total time of microgravity was around 2 minutes, so these results cannot directly be compared to long-term experiments in space (79).

Other available tests that do not involve animal models are invasion, proliferation, radiosensitivity, and chemotherapeutic assays. For example, another possibility is to study invasion, one of the hallmarks of metastatic capabilities, using surrogate tests available (80), which have shown an excellent correlation with the invasive behavior of the tumor *in vivo*. Such functional studies are necessary to confirm the advantages of exposing the cells to the RPM or to space conditions on board the ISS.

5.- Discussion of the research publications.

5.1 Dexamethasone Selectively Inhibits Detachment of Metastatic Thyroid Cancer Cells during Random Positioning

The first paper reported novel data about the effects of dexamethasone (DEX) on metastatic low-differentiated follicular thyroid cancer cells (FTC-133 cell line). It is known that DEX inhibits MCS formation on the RPM (81), but the mechanism for this effect is still unclear. One of the goals of the research on MCS formation on the RPM is to identify a mechanism that inhibits MCS formation (42). Cancer researchers could later translate this knowledge into the development of new therapeutic approaches to inhibit metastasis formation in cancer patients.

Metastatic cancer cell lines tend to form spheroids when exposed to simulated microgravity. Based on previous data from cancer cell lines exposed to simulated microgravity conditions, NF-κB signaling was involved in MCS formation (82) and was altered in other cell lines exposed to real and simulated microgravity conditions (83). Therefore, we selected DEX to inhibit MCS formation through its interaction with the NF-κB pathway. In 2020, Melnik *et al*. (2020) showed that DEX can inhibit MCS formation dose-dependently (81). A 1000 nM concentration of DEX inhibited MCS formation, even after three days of RPM rotation. In this article, further experiments were performed to understand the inhibition of MCS formation.

The MCS formation is better understood as a 2-step process: First, the adherent cell population exposed to the RPM detaches from the surface of the flask. Second, the suspended cells start aggregating thanks to the free fall generated inside the RPM. In the first part of the article, it was demonstrated how the DEX effects are specific to the cell detachment step, the first step for the MCS formation (84). Different suspension cell populations were cultured on the RPM or non-adherent plates, a traditional method for MCS generation (64). Even in the presence of DEX, the cancer cells could form MCS. The results indicate that DEX interferes with the cell detachment process but not the cell aggregation process.

The specificity of this MCS inhibition during RPM-exposure was investigated using three different thyroid cancer cell lines with significant histological and molecular differences when exposed to DEX. Interestingly, the DEX-induced inhibition of MCS formation was observed only for metastatic cancer cell lines originating from lymph node metastases, such as FTC-133 and WRO. On the other hand, for the ML-1 cancer cell line, originating directly from the primary tumor, no MCS inhibition through DEX was found (84). Moreover, DEX did not affect the MCS formation for the non-carcinogenic thyroid cells Nthy-ori 3-1. From these results, it may be concluded that the mechanism for the DEX inhibition is related to a feature that only the metastatic cancer cell lines possess. The working hypothesis was as follows: During its cancer

progression background, a cancer cell must overcome many challenges to metastasize and colonize distant organs. This set of new features allowed the cells to detach once exposed to the RPM, (85), and the glucocorticoid DEX interferes with this process.

RPM-exposure activates stress signaling in cancer cells, specifically in FTC-133 cells, where gene and protein analyses showed the activation and nuclear translocation of p38. The p38 signaling is particularly vital in cancer progression and metastasis (86). Subsequently, the molecular mechanisms underlying this activation were investigated. In the article, it was also presented how DEX increased the adhesion properties of the cells, particularly to the flask surface. First, exposure to DEX causes cells to deposit more ECM factors, and this effect is higher with exposure to the RPM. This interplay between DEX and metastasis formation has important clinical implications: It has been previously reported that higher concentrations of DEX foster the progression of breast cancer (87).

During the RPM-exposure, the cells produced more mucin-1, an anti-adhesion molecule. We hypothesized that the cells secrete these factors to survive and resist the impact of the stress generated by the RPM shear stress rotation. Mucins provide a tumor-friendly microenvironment by ameliorating the inhospitable conditions in tumor-growing sites and allowing cancer cells to escape the immune system surveillance (88). Mucin production was higher in Nthy-ori 3-1 and ML-1 cells. The use of DEX in combination with a mucin inhibitor was surprisingly able to inhibit MCS formation also in Nthy-ori 3-1 and ML-1 cells. These results support the role of the anti-adhesion molecules in the MCS formation on microgravity.

In conclusion, in this research article, the molecular basis for the effects of DEX in preventing MCS formation on the RPM was clarified. Furthermore, a vital role for the cell adhesion molecules in the cell detachment process was established. A 2-step process for the MCS formation started to be elucidated and further explored in the following research articles.

5.2 Effects of High Glucose on Human Endothelial Cells Exposed to Simulated Microgravity.

The next step was to study a more mechanosensitive cell line. Therefore, the EA.hy926 endothelial cell line was cultured under simulated microgravity conditions using a 3D clinostat. This cell line originates from transformed human umbilical vein endothelial cells fused to clones of A549 lung carcinoma epithelial cell line (89). It is widely used as a model for endothelial cells in cardiovascular research (90) and possesses a cytoplasmic distribution of

Weibel-Palade bodies (91). It has properties of a differentiated endothelial cell and has been used in various vascular studies such as angiogenesis (92), homeostasis/thrombosis (93), hypertension (94), and inflammation (95). However, some contradictory data has appeared regarding its endothelial cell characteristics; for example, EA.hy926 cells do not align to the shear flow direction, contrary to their counterpart HUVEC, which do so (96).

The experiments used two distinct types of cell culture media on the 3D clinostat: one group with DMEM medium (low-glucose group) and the other using DMEM medium supplemented with 5 mM D-(+)-Glucose solution (high-glucose group). High glucose levels can damage the endothelial cell layer by producing ROS, leading to apoptosis and endothelial dysfunction (97). The effects of two different glucose concentrations in the experimental groups and the effects of shear stress in the 3D clinostat was compared to cells exposed to 1*g* static conditions. Gene expression analysis was realized, and protein characterization was performed by immunofluorescence and Western Blot analyses.

The results showed that clinostat-exposed endothelial cells modified the expression of FN1 protein, with a significant difference between the high- and low-glucose groups. The GLUT3 protein expression was also altered. It is crucial to notice that for the proteins and molecular pathways explored, culturing the cells on the clinostat was more significant than the effects of high glucose exposure. Finally, upregulation of *CXCL8* was observed, a typical observation in FTC-133 cells, MCF-7 cells, and other cancer cell lines exposed to simulated microgravity (98). We hypothesized that *CXCL8* belongs to a gene expression pathway responsible for inflammation and shear stress response in cancer cells.

This endothelial cell line also formed spheroid structures under simulated microgravity conditions, probably because of its cancer cell origin. Although the MCS and AD cell populations are grown under simulated microgravity conditions, they show different responses during the simulated microgravity exposure. An MCS control group obtained under 1*g* conditions would constitute a more suited comparison group for the microgravity-generated MCS.

Overall, the exposure to simulated microgravity had a stronger effect on the EA.hy926 cell line's gene and protein expression as opposed to hyperglycemia. Hyperglycemia had a stronger effect regarding a higher count and larger-sized MCS formation. We observed an elevated expression of NOX4 and CXCL8 due to simulated microgravity, suggesting an increased oxidative stress and inflammation. Finally, the hyperglycemia did not cause

significant changes in glucose metabolism, and changes occurred due to the exposure to the 3D clinostat.

5.3 Fluid and Bubble Flow Detach Adherent Cancer Cells to Form Spheroids on a Random Positioning Machine.

This publication reported new data about the physical effects of an RPM experiment. This article encompasses the thoughts and ideas that emerged from the Review paper: Cancer Cells in Space Conditions (46), in which there is a discussion of gravisensation. This earlier review proposed a set of experiments, which were performed in this research article.

First, the focus of the study was on the inverted gravity vector as a proof of concept, asking whether cells can feel the gravity vector. Random positioning is used to simulate a microgravity-environment through the nullification of gravity. This can be realized by disorientating the cells, or as 'vector-averaging' process. Therefore, it is necessary to evaluate the most extreme case for gravity vector alteration by exposing the adherent cells to a negative gravity vector.

According to the results in the article, although the cells feel an alteration of the gravity vector in the inverted flask experiment, they do not show the changes usually described with microgravity-exposure. The cells in the inverted experiments should have experienced a combination of both explanations: the gravity vector alteration might have impacted the cytoskeleton, but because of the period of the observations, cells had time to adapt. In addition, because of the cell size, the effect of inverting the gravity vector was negligible compared with other forces present (63), such as the hydrostatic pressure of the column of medium, material, and stiffness of the cell culture flask. This set of experiments suggested that the cells may not be interested in gravity vector alterations, and other stimuli may have a more significant impact on their biology.

5.3.1 Different rotational speeds yield average microgravity vector conditions over time; however, the gene expression results differ between different rotational speeds.

The theory behind the RPM experiments explains that by the constant rotation around the three axes in space, the RPM can generate a gravity vector nullification over time, which is in the range of microgravity levels. However, some results obtained in RPM experiments do not fit into a model where only the microgravity-exposure explains the changes observed in the cells in the RPM. For this reason, the following experiment was planned: the cancer cells

rotated in the RPM as part of a usual 3-day experiment. Three different experimental conditions were assessed. 1) One group of samples running at a slow speed (average of 30 degrees per second), a typical speed (average of 65 degrees per second), and a fast speed (average of 90 degrees per second). The FTC-133 cell line was used because it is one of the cell lines from which most simulated microgravity data has been obtained.

According to the average-vector theory, the three operating speeds resulted in a calculated time-averaged microgravity within a few hours. However, a different gene expression pattern was obtained, as well as different spheroid formation. These results concluded that the genes commonly reported to change under simulated microgravity conditions may not correspond to the microgravity-exposure but to another kind of stimulus, for example, shear stress. The faster the RPM rotation, the higher the shear stresses, with a similar trend for the gene expression changes. These results prove that the shear forces had a bigger-than-expected effect on the gene expression changes for cells cultured in the RPM. To further answer this question, the biological role of shear forces in the range generated by the RPM (between 10-20 mPa according to the study by Wüest) was investigated (44).

5.3.2. Role of shear stress in the cell detachment process.

FTC-133 cells were then exposed to low shear stress values. A peristaltic pump system connected to a cell culture in an Ibidi channel slide (figure 9) generated the shear stress environment. A regulated unidirectional flow generates a precise value for the shear stress by adjusting the flow speed according to a set of formulas specific to every slide. To obtain an accurate shear stress value, the value for the dynamical viscosity of the medium is added to the formula, which is multiplied by the flow rate. For example, in the case of a µ-Slide I $^{0.8}$ Luer Glass bottom slide (99), by using a 0.45 mL/min flow rate, a shear stress of 0.1 dyn/cm^2 is generated, and with a 0.90 mL/min flow rate, a shear stress of 0.2 dyn/cm^2 is generated. These values correspond to the calculated to be generated in the walls of the cell culture flask during a typical RPM experiment, according to the simulations by Wüest (44).

$$\boldsymbol{\tau = \eta \cdot factor\ (dependent\ on\ slide) \cdot \phi}$$

τ = shear stress

η = dynamical viscosity

ϕ = flow rate

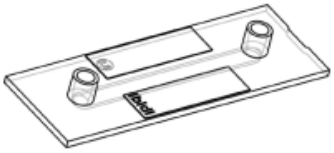

Figure 9.- *Formulas for calculating the shear stress rate in the Ibidi slides from [99].*

Live-cell visualization was done using an inverted microscope, and the following sequence of pictures shows how the cancer cells react to the shear flow and start to roll and detach from the cell culture flask (figure 10). Over an extended period and with specific analysis of the movement patterns, the cells' migration in the flow direction can be observed until they finally detached from the flask. The cells detached and rolled faster using a faster flow, providing 20 mPa of shear stress.

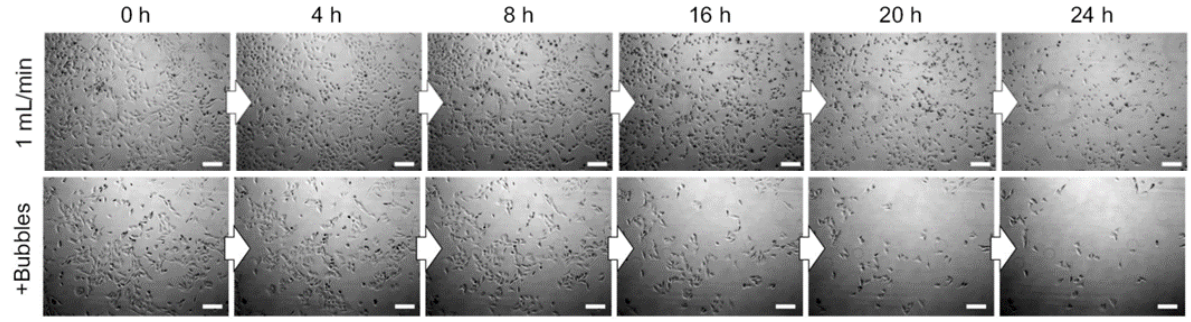

***Figure 10**.- In the top section, Live-cell microscopy pictures of cells exposed to fluid shear stress in the range generated by a normal RPM experiment during 24 h. The bottom row shows the effects of adding bubbles to the flow shear.*

Finally, bubbles had shown an impact on the cell detachment process from previous observations in the RPM. It was observed that those flasks with the giant and more numerous bubbles at the end of the experiment had more cancer spheroids and less adherent cell population remaining in the flask. Therefore, the role of bubbles in the cell detachment process in the RPM was investigated. Bubbles counteracted dexamethasone's inhibitory effects for spheroid formation and the cancer cells formed MCS even in the presence of dexamethasone. By using a different tubing configuration, bubbles were introduced into the fluid-shear experiment. The cells detached faster in the presence of bubbles, and almost no cells remained adhered to the flask at the end of the experiment (figure 10).

5.3.3. Molecular biology of the cell detachment process.

The cell detachment process observed in the RPM experiments can be simulated using a shear flow experiment. Gene and protein expression changes were investigated using qPCR and immunofluorescence microscopy, to determine if the same molecular pathways are activated in both cell detachment methods. It was observed that after 4 h of flow, the cell starts to roll and detach, so the 4-hour time point was used for the comparison. The gene expression changes in a 4-h RPM run were compared with the channel slide flow experiment at 20 mPa for 4 h. Surprisingly, similar changes in the gene expression were observed.

Regarding the immunofluorescence analysis, no clear pattern of transcription factor translocation was observed.

5.3.4. A new perspective in the RPM MCS formation for cancer studies

The experiments confirm how the MCS formation process in the RPM has two steps: the first step, cell detachment, has nothing to do with microgravity and is caused by the fluid shear stress, further compounded by the presence of bubbles in the medium. The spheroid formation occurs once fluid dynamics detach the cells, and the cells float freely in the culture medium. This cell-aggregation is facilitated by microgravity exposure. The figure 11 represents a visual summary of the findings.

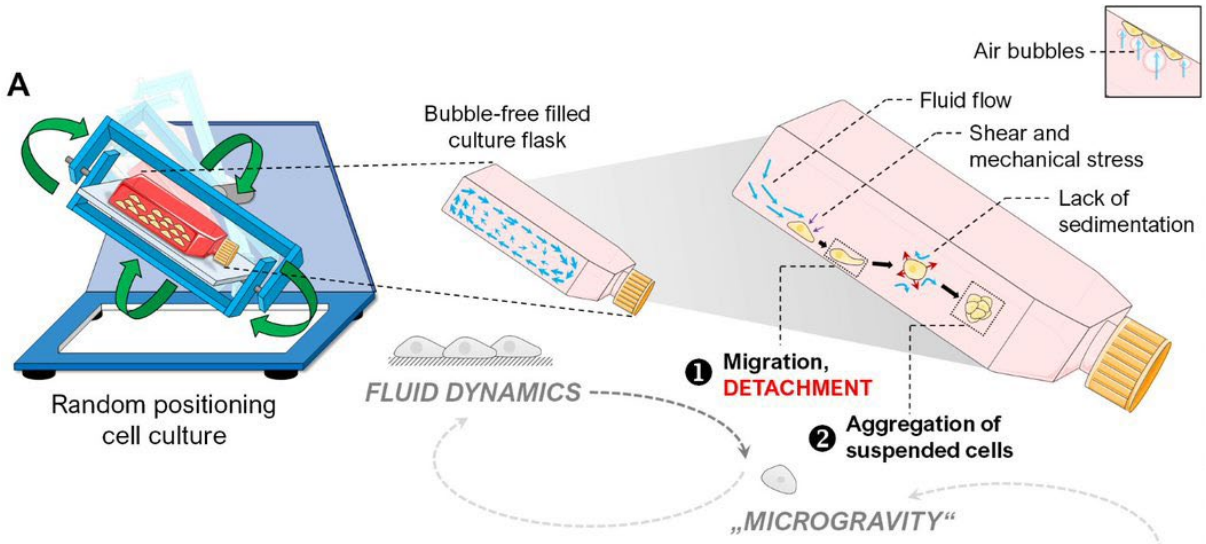

***Figure 11.**- Summary of the spheroid formation process in microgravity, taken from* (73).

5.4 Conclusions

To advance biological studies in microgravity for future space exploration, challenges associated with conducting experiments on the International Space Station (ISS) have led researchers to explore ground-based facilities simulating microgravity. The Random Positioning Machine and clinostats are such devices that aim to expose samples to simulated microgravity conditions. However, replicating experiments on these platforms is complex, partly due to a lack of understanding of how human cells perceive changes in gravity.

To address this challenge, a new model was proposed for testing gravisensation in human cells. When cancer cells are exposed to the RPM, MCS are formed, and this aggregation is attributed to a microgravity environment. However, this process is not completely understood. Our research revealed insights into cell detachment and aggregation, emphasizing the role of shear stress in the RPM experiments and molecular pathways involved in the gravisensation process.

Finally, the cells were actively subjected to shear stress in a controlled environment with regulated flow, which challenged the theory of averaged gravity vectors. Surprisingly, the adherent cell population could also detach from the flask when using shear stress in the range produced by the RPM. The RPM experiments identified shear stress as a significant factor influencing cells, gene expression, and protein profiles. The research proposes a two-step process for MCS formation on the RPM involving shear stress-induced detachment of the cells and subsequent “free fall” during random positioning.

From these data, a model for using ground-based facilities for microgravity experiments can be derived and transferred to other platforms. In addition, this model will help to understand gravisensation in human cells. The cells composing either a 3D structure or a multicellular organism are more concerned with the changes in the local microenvironment than with a gravity vector. The findings contribute to the long-standing question of how cells perceive changes in the gravity vector in microgravity platforms and provide valuable insights for future biological experiments in space.

5.5 Summary

Bioreactors to simulate microgravity are widely used in space research to prepare experiments in real microgravity conditions on the ISS. One of the most used simulation devices is the Random Positioning Machine, which can average the gravity vector at the microgravity level through constant rotation around all three spatial axes. These devices for simulating microgravity are among the ground-based facilities recommended by ESA.

However, recently there has been some discussion about the role of these devices in studying cells from multicellular organisms. This work investigates what role the modeled shear stress plays in the tumor cell lines cultured on the RPM and whether this shear stress can influence the observations made in the microgravity bioreactors. The results were summarized in the following three research articles.

The first article investigated various thyroid carcinoma cell lines exposed on the RPM, which were also subjected to a pharmacological intervention with dexamethasone as part of a follow-up study. The aim was to gain a better understanding of the mechanisms by which dexamethasone inhibits spheroid formation.

The second article examined the more mechanosensitive endothelial cell line EA.hy926. The cells were cultured on a 3D clinostat and exposed to or without a high glucose concentration.

Finally, the third article focused on the role of the secondary effects generated in the RPM. New control groups are introduced in simulated microgravity experiments, such as shear stress with a given fluid flow rate, the effects of bubbles, different gravity vector orientations, and the role of different RPM rotation speeds.

5.6 Zusammenfassung

Bioreaktoren zur Simulation von Mikrogravitation werden in der Weltraumforschung häufig verwendet, um Experimente unter realen Mikrogravitationsbedingungen, beispielsweise auf der ISS, vorzubereiten. Eines der am häufigsten verwendeten Simulationsgeräte ist die Random Positioning Machine, die durch eine konstante Rotation um alle drei Raumachsen den Schwerkraftvektor über die Zeit auf Mikrogravitationsniveau mitteln kann. Diese Geräte zur Simulation von Mikrogravitation zählen zu den von der ESA empfohlenen Bodenanlagen („ESA ground based facilities“).

In letzter Zeit sind unter Wissenschaftlern einige Zweifel über die Vergleichbarkeit der simulierten Mikrogravitation zu Weltraumexperimenten aufgekommen. Daher ist es wichtig, die genauen Effekte dieser Anlagen auf humane Zellkulturen zu studieren.

In dieser Arbeit wurde untersucht, welche Rolle der modellierte Scherstress bei den auf der RPM kultivierten Tumorzelllinien spielt und ob dieser Scherstress die in den Mikrogravitations-Bioreaktoren gemachten Beobachtungen beeinflussen kann. Die Ergebnisse wurden in den folgenden drei Forschungsartikeln zusammengefasst.

Der erste Artikel befasste sich mit verschiedenen auf der RPM exponierten Schilddrüsenkarzinomzelllinien, die im Rahmen einer Nachfolgestudie auch der pharmakologischen Intervention mit Dexamethason unterzogen wurden. Das Ziel war es ein besseres Verständnis der Mechanismen zu erlangen, durch die Dexamethason die Bildung von Tumor-Sphäroiden hemmt.

Der zweite Artikel untersuchte die mechanosensiblere, endotheliale Zelllinie EA.hy926. Die Zellen wurden auf einem 3D-Klinostaten und normaler bzw. erhöhter Glukosekonzentration (Diabetes-Modell) kultiviert.

Im dritten Artikel schließlich wird untersucht, welche Rolle die in der RPM erzeugten Sekundäreffekte bei der Sphäroidbildung spielen. Hierfür wurden neue Kontrollgruppen für simulierte Mikrogravitationsexperimente definiert, wie z.B. Scherstress mit einer bestimmten Durchflussrate, die Auswirkungen von Blasen sowie unterschiedliche Ausrichtungen des Schwerkraftvektors und die Rolle verschiedener Rotationsgeschwindigkeiten der RPM.

6. References

1. Einstein A.: Grundgedanken und Methoden der Relativitätstheorie in ihrer Entwicklung dargestellt. In: M. Janssen et al. (eds.): The Berlin Years: Writings. Princeton. Princeton University Press 1918.

2. Brungs S. et al.: Facilities for Simulation of Microgravity in the ESA Ground-Based Facility Programme.: Microgravity Sci. Technol. 28. 191–203 (2016)

3. Hajdu S.I.: A note from history: Landmarks in history of cancer, part 1.: Cancer 117. 1097–1102 (2011)

4. Hausman D.M.: What Is Cancer?: Perspect. Biol. Med. 62. 778–784 (2019)

5. Editorial: Advancing Cancer Therapy.: Nat Cancer 2. 245–246 (2021)

6. Nahleh Z. et al.: How to reduce your cancer risk: mechanisms and myths.: Int. J. Gen. Med. 4. 277 (2011)

7. Carbone A.: Cancer Classification at the Crossroads.: Cancers 12 (2020)

8. Schlemmer H.-P.: The Cancer Epidemic.: Radiologie (Heidelb.) 63. 49–56 (2023)

9. Soerjomataram I., F. Bray: Planning for tomorrow: global cancer incidence and the role of prevention 2020-2070.: Nat. Rev. Clin. Oncol. 18. 663–672 (2021)

10. Ahmad A.S. et al.: Trends in the lifetime risk of developing cancer in Great Britain: comparison of risk for those born from 1930 to 1960.: Br. J. Cancer 112. 943–947 (2015)

11. Ferlay J, Ervik M, Lam F, Laversanne M, Colombet M, Mery L, Piñeros M, Znaor A, Soerjomataram I, Bray F: Global Cancer Observatory: Cancer Today (version 1.1).: Lyon, France: International Agency for Research on Cancer. (2024). Available from: https://gco.iarc.who.int/today [last accessed April 7, 2024]

12. Siegel R.L. et al.: Cancer statistics, 2024.: CA Cancer J. Clin. 74. 12–49 (2024)

13. National Cancer Institute: Cancer Trends Progress Report. (2024). Available from: https://progressreport.cancer.gov. [last accessed January 4, 2024]

14. Wengler A. et al.: Years of life lost to death—A comprehensive analysis of mortality in Germany conducted as part of the BURDEN 2020 project.: Dtsch. Arztebl. Int. 118. 137–144 (2021)

15. Hanahan D., R.A. Weinberg: The hallmarks of cancer.: Cell 100. 57–70 (2000)

16. Hanahan D., R.A. Weinberg: Hallmarks of cancer: the next generation.: Cell 144. 646–674 (2011)

17. Hanahan D.: Hallmarks of Cancer: New Dimensions.: Cancer Discov. 12. 31–46 (2022)

18. Fares J. et al.: Molecular principles of metastasis: a hallmark of cancer revisited.: Signal Transduct Target Ther 5. 28 (2020)

19. Gerstberger S. et al.: Metastasis.: Cell 186. 1564–1579 (2023)

20. Bergers G., S.-M. Fendt: The metabolism of cancer cells during metastasis.: Nat. Rev. Cancer 21. 162–180 (2021)

21. Vanharanta S., J. Massagué: Origins of metastatic traits.: Cancer Cell 24. 410–421 (2013)

22. Lee C.-K. et al.: Tumor metastasis to lymph nodes requires YAP-dependent metabolic adaptation.: Science 363. 644–649 (2019)

23. Huang Q. et al.: Fluid shear stress and tumor metastasis.: Am. J. Cancer Res. 8. 763–777 (2018)

24. Zhu B. et al.: Piezo 1 activation facilitates cholangiocarcinoma metastasis via Hippo/YAP signaling axis.: Mol. Ther. Nucleic Acids 24. 241–252 (2021)

25. Zhou H. et al.: Progression of metastasis through lymphatic system.: Cells 10. 627 (2021)

26. Hernandez-Aya L.F. et al.: Nodal status and clinical outcomes in a large cohort of patients with triple-negative breast cancer.: J. Clin. Oncol. 29. 2628–2634 (2011)

27. Zhu X. et al.: Cancer evolution: A means by which tumors evade treatment.: Biomed. Pharmacother. 133. 111016 (2021)

28. Zhou R. et al.: A robust panel based on tumour microenvironment genes for prognostic prediction and tailoring therapies in stage I-III colon cancer.: EBioMedicine 42. 420–430 (2019)

29. Zhang L. et al.: Cancer-associated fibroblast-related gene signatures predict survival and drug response in patients with colorectal cancer.: Front. Genet. 13. 1054152 (2022)

30. Montagner M., S. Dupont: Mechanical Forces as Determinants of Disseminated Metastatic Cell Fate.: Cells 9 (2020)

31. Romani P. et al.: Crosstalk between mechanotransduction and metabolism.: Nat. Rev. Mol. Cell Biol. 22. 22–38 (2021)

32. Engler A.J. et al.: Matrix elasticity directs stem cell lineage specification.: Cell 126. 677–689 (2006)

33. Cox T.R., J.T. Erler: Remodeling and homeostasis of the extracellular matrix: implications for fibrotic diseases and cancer.: Dis. Model. Mech. 4. 165–178 (2011)

34. Papavassiliou K.A. et al.: The emerging promise of tumour mechanobiology in cancer treatment.: Eur. J. Cancer 190. 112938 (2023)

35. Kondapaneni R.V., S.S. Rao: Matrix stiffness and cluster size collectively regulate dormancy versus proliferation in brain metastatic breast cancer cell clusters.: Biomater Sci 8. 6637–6646 (2020)

36. Mukherjee A., J.J. Bravo-Cordero: Regulation of dormancy during tumor dissemination: the role of the ECM.: Cancer Metastasis Rev. 42. 99–112 (2023)

37. Langley R.R., I.J. Fidler: The seed and soil hypothesis revisited--the role of tumor-stroma interactions in metastasis to different organs.: Int. J. Cancer 128. 2527–2535 (2011)

38. Ishihara S., H. Haga: Matrix stiffness contributes to cancer progression by regulating transcription factors.: Cancers (Basel) 14. 1049 (2022)

39. Wullkopf L. et al.: Cancer cells' ability to mechanically adjust to extracellular matrix stiffness correlates with their invasive potential.: Mol. Biol. Cell 29. 2378–2385 (2018)

40. Baloch Z.W. et al.: Overview of the 2022 WHO classification of thyroid neoplasms.: Endocr. Pathol. 33. 27–63 (2022)

41. Landa I. et al.: Comprehensive genetic characterization of human thyroid cancer cell lines: A validated panel for preclinical studies.: Clin. Cancer Res. 25. 3141–3151 (2019)

42. Grimm D. et al.: The Fight against Cancer by Microgravity: The Multicellular Spheroid as a Metastasis Model.: Int. J. Mol. Sci. 23. 3073 (2022)

43. NASA: What is microgravity?: NASA (2009). Available from: https://www.nasa.gov/centers-and-facilities/glenn/what-is-microgravity/ [last accessed January 4, 2024]

44. Wuest S.L. et al.: Fluid Dynamics Appearing during Simulated Microgravity Using Random Positioning Machines.: PLoS One 12. e0170826 (2017)

45. Hammond T., P. Allen: The Bonn Criteria: Minimal Experimental Parameter Reporting for Clinostat and Random Positioning Machine Experiments with Cells and Tissues.: Microgravity Sci. Technol. 23. 271–275 (2011)

46. Cortés-Sánchez J.L. et al.: Cancer Studies under Space Conditions: Finding Answers Abroad.: Biomedicines 10. 25 (2021)

47. Locatelli L. et al.: From Cultured Vascular Cells to Vessels: The Cellular and Molecular Basis of Vascular Dysfunction in Space.: Front Bioeng Biotechnol 10. 862059 (2022)

48. Kuzichkin D.S. et al.: Endothelial dysfunction markers and immune response indices in cosmonauts' blood after long-duration space flights.: NPJ Microgravity 8. 1–9 (2022)

49. Maier J.A.M. et al.: The impact of microgravity and hypergravity on endothelial cells.: Biomed Res. Int. 2015. 1–13 (2015)

50. Xu D. et al.: The subsequent biological effects of simulated microgravity on endothelial cell growth in HUVECs.: Chin. J. Traumatol. 21. 229–237 (2018)

51. Barravecchia I., D. Angeloni: Microgravity inhibits autophagy in human capillary endothelial cells in space flight.: Autophagy Reports 1. 337–340 (2022)

52. Krüger M. et al.: Growth of Endothelial Cells in Space and in Simulated Microgravity - a Comparison on the Secretory Level.: Cell. Physiol. Biochem. 52. 1039–1060 (2019)

53. Janmaleki M. et al.: Impact of Simulated Microgravity on Cytoskeleton and Viscoelastic Properties of Endothelial Cell.: Sci. Rep. 6. 32418 (2016)

54. Morbidelli L. et al.: Effect of microgravity on endothelial cell function, angiogenesis, and vessel remodeling during wound healing.: Front. Bioeng. Biotechnol. 9 (2021)

55. Stavnichuk M. et al.: A systematic review and meta-analysis of bone loss in space travelers.: NPJ Microgravity 6. 13 (2020)

56. ElGindi M. et al.: Effects of an aged tissue niche on the immune potency of dendritic cells using simulated microgravity.: NPJ Aging 9. 14 (2023)

57. ElGindi M. et al.: 3D microenvironment attenuates simulated microgravity-mediated changes in T cell transcriptome.: Cell. Mol. Life Sci. 79. 508 (2022)

58. Cao R. et al.: A Hierarchical Mechanotransduction System: From Macro to Micro.: Adv. Sci. e2302327 (2023)

59. Guo Y. et al.: On modeling the multiscale mechanobiology of soft tissues: Challenges and progress.: Biophys. Rev. 3. 031303 (2022)

60. Frings S.: Sensory cells and sensory organs. In: Sensory Perception. pp. 5–21. Vienna. Springer Vienna 2012.

61. Takahashi K. et al.: Gravity sensing in plant and animal cells.: NPJ Microgravity 7. 2 (2021)

62. Häder D.-P. et al.: Gravireceptors in eukaryotes—a comparison of case studies on the cellular level.: npj Microgravity 3. 1–8 (2017)

63. Albrecht-Buehler G.: Possible mechanisms of indirect gravity sensing by cells.: ASGSB Bull. 4. 25–34 (1991)

64. Ryu N.-E. et al.: Spheroid culture system methods and applications for mesenchymal stem cells.: Cells 8. 1620 (2019)

65. Kapałczyńska M. et al.: 2D and 3D cell cultures - a comparison of different types of cancer cell cultures.: Arch. Med. Sci. 14. 910–919 (2018)

66. Gong X. et al.: Generation of multicellular tumor spheroids with microwell-based agarose scaffolds for drug testing.: PLoS One 10. e0130348 (2015)

67. Azharuddin M. et al.: Dissecting multi drug resistance in head and neck cancer cells using multicellular tumor spheroids.: Sci. Rep. 9. 20066 (2019)

68. Muciño-Olmos E.A. et al.: Unveiling functional heterogeneity in breast cancer multicellular tumor spheroids through single-cell RNA-seq.: Sci. Rep. 10. 12728 (2020)

69. Masini M.A. et al.: Prolonged exposure to simulated microgravity promotes stemness impairing morphological, metabolic and migratory profile of pancreatic cancer cells: a comprehensive proteomic, lipidomic and transcriptomic analysis.: Cell. Mol. Life Sci. 79. 226 (2022)

70. Hauslage J. et al.: Pyrocystis noctiluca represents an excellent bioassay for shear forces induced in ground-based microgravity simulators (clinostat and random positioning machine).: NPJ Microgravity 3. 12 (2017)

71. Poon C.: Factors implicating the validity and interpretation of mechanobiology studies in simulated microgravity environments.: Engineering Reports 2. e12242 (2020)

72. Kouznetsov N.V.: Cell responses to simulated microgravity and hydrodynamic stress can be distinguished by comparative transcriptomics.: International Journal of Translational Medicine 2. 364–386 (2022)

73. Cortés-Sánchez J.L. et al.: Fluid and Bubble Flow Detach Adherent Cancer Cells to Form Spheroids on a Random Positioning Machine.: Cells 12. 2665 (2023)

74. Brancato V. et al.: Could 3D models of cancer enhance drug screening?: Biomaterials 232. 119744 (2020)

75. El Harane S. et al.: Cancer spheroids and organoids as novel tools for research and therapy: State of the art and challenges to guide precision medicine.: Cells 12. 1001 (2023)

76. L. Larose T.: Tumors in space: Preparation for spaceflight. In: V. Pletser (ed.): Preparation of Space Experiments. London, England. IntechOpen 2020.

77. Silvani G. et al.: A 3D-bioprinted vascularized glioblastoma-on-a-chip for studying the impact of simulated microgravity as a novel pre-clinical approach in brain tumor therapy.: Adv. Ther. 4. 2100106 (2021)

78. Choi D.H. et al.: 3D cell culture using a clinostat reproduces microgravity-induced skin changes.: NPJ Microgravity 7. 20 (2021)

79. Garcia C.A. et al.: Behavior of glioblastoma brain tumor stem cells following a suborbital rocket flight: reaching the “edge” of outer space.: NPJ Microgravity 9. 1–7 (2023)

80. Shaw L.M.: Tumor Cell Invasion Assays. In: Cell Migration. pp. 097–106. New Jersey. Humana Press 2004.

81. Melnik D. et al.: Dexamethasone Inhibits Spheroid Formation of Thyroid Cancer Cells Exposed to Simulated Microgravity.: Cells 9 (2020)

82. Kopp S. et al.: The role of NFκB in spheroid formation of human breast cancer cells cultured on the Random Positioning Machine.: Sci. Rep. 8. 921 (2018)

83. Zhang Y. et al.: Transcriptomics, NF-κB pathway, and their potential spaceflight-related health consequences.: Int. J. Mol. Sci. 18. 1166 (2017)

84. Melnik D. et al.: Dexamethasone Selectively Inhibits Detachment of Metastatic Thyroid Cancer Cells during Random Positioning.: Cancers 15 (2023)

85. Klein C.A.: Cancer progression and the invisible phase of metastatic colonization.: Nat. Rev. Cancer 20. 681–694 (2020)

86. Igea A., A.R. Nebreda: The stress kinase p38α as a target for cancer therapy.: Cancer Res. 75. 3997–4002 (2015)

87. Pang J.M. et al.: Effects of synthetic glucocorticoids on breast cancer progression.: Steroids 164. 108738 (2020)

88. Wi D.-H. et al.: Mucin in cancer: a stealth cloak for cancer cells.: BMB Rep. 54. 344–355 (2021)

89. Edgell C.J. et al.: Permanent cell line expressing human factor VIII-related antigen established by hybridization.: Proc. Natl. Acad. Sci. U. S. A. 80. 3734–3737 (1983)

90. Targosz-Korecka M. et al.: Stiffness memory of EA.hy926 endothelial cells in response to chronic hyperglycemia.: Cardiovasc. Diabetol. 12 (2013)

91. Edgell C.J. et al.: Endothelium specific Weibel-Palade bodies in a continuous human cell line, EA.hy926.: In Vitro Cell. Dev. Biol. 26. 1167–1172 (1990)

92. Bauer J. et al.: In vitro model of angiogenesis using a human endothelium-derived permanent cell line: contributions of induced gene expression, G-proteins, and integrins.: J. Cell. Physiol. 153. 437–449 (1992)

93. Emeis J.J., C.J. Edgell: Fibrinolytic properties of a human endothelial hybrid cell line (Ea.hy 926).: Blood 71. 1669–1675 (1988)

94. Lee H.-G. et al.: Antihypertensive effects of IGTGIPGIW peptide purified from Hippocampus abdominalis: P-eNOS and p-AKT stimulation in EA.Hy926 cells and lowering of blood pressure in SHR model.: Mar. Drugs 20. 354 (2022)

95. Yuan H.-X. et al.: 5,2’-dibromo-2,4’,5’-trihydroxydiphenylmethanone attenuates LPS-induced inflammation and ROS production in EA.hy926 cells via HMBOX1 induction.: J. Cell. Mol. Med. 23. 453–463 (2019)

96. Macek Jilkova Z. et al.: CCM proteins control endothelial β1 integrin dependent response to shear stress.: Biol. Open 3. 1228–1235 (2014)

97. Ho F.M. et al.: High glucose-induced apoptosis in human endothelial cells is mediated by sequential activations of c-Jun NH(2)-terminal kinase and caspase-3.: Circulation 101. 2618–2624 (2000)

98. Corydon T.J. et al.: Current knowledge about the impact of microgravity on gene regulation.: Cells 12. 1043 (2023)

99. © ibidi GmbH: Application Note 11, Shear Stress and Shear Rates for ibidi µ-Slides Based on Numerical Calculations. © ibidi GmbH (2022)

7. Figure Index.

8.- Acknowledgements

I want to thank CONAHCYT for allowing me to obtain the Scholarship to pursue my doctoral studies in Germany and for your full support during this long journey. Thank you also to the DAAD for supporting me with the scholarship. Special thanks also go to Prof. Dr. med. Daniela Grimm for allowing me to perform my research at her lab and opening the doors to Research in Germany; I will always be grateful for her support during my studies. Thank you to Dr. rer. nat. Marcus Krüger, who also mentored me during my research, allowed me to develop my critical thinking and was always open to hearing new ideas and discussions. Thank you to Dr. rer. nat. Markus Wehland, for his valuable lessons in the art of academic writing. Thanks to Dr. rer. nat. Herbert Schulz, for his support as part of the AMCRIS project.

Thanks to my colleagues and friends in the Environmental Biology Group: M.Sc. Daniela Melnik, for all her teaching during my research, was always helpful and guided me in learning the different lab techniques. Thanks to our great lab technician, Vivann Sandt, who was always available to support us during the long experiments and was patient while teaching and instructing me. Thanks to M.Sc. Shannon Marschal, Anna Heinrich, and M.Sc. Jenny Graf, for their support during these three years. Thanks to M.Sc. Fernando Torres, M.Tech. Ashwini Mushunuri and Jakob Pfeiffer, thank you for their help with my research.

Thanks to my colleagues from the other departments and foreign universities, Dr. rer. nat. Christian Liemersdorf, Dr. Ian Johnson, Dr. Marco Calvaruso, and Dr. Simon L Wüest for their discussions and scientific input. At the OVGU, Dr. rer. nat. Sascha Kopp for fostering rational thinking and critical reasoning in me. Thank you to Dr. rer. nat. Stefan Kahlert, for his tremendous help with the Confocal Microscopy sessions and the Shear stress experiments, and to Prof. Dr. med. Hermann-Josef Rothkötter for supporting our research at the Anatomy Institute. Thanks to Dr. Jayashree Sahana and Dr. Justina Jokšienė at Aarhus University in Denmark for the collaboration during the endothelial cells experiments.

I want to express my gratitude to all my friends from the other laboratories in Magdeburg who helped to make the new city feel like home: Alberto Alcala, Marko Ristik, Christopher Funk, Marysol Segovia, Carlos Ernesto, Taynara Fernandes, Valeria Fárez, Sebastian Kleever, Jaqueline Zuñiga, Yi-Ting Shi, Jesus Espinosa, Sebastian García, Juan Nicolas, Bayan Awad and Nisreen.

I want to thank my mentors in México who motivated me to pursue my research career: Dr. Augusto Rojas Martínez, Dra. Rocio Ortiz López from the ITESM Monterrey; Dr. Rafael Argüello Astorga, who inspired me to perform my doctoral studies in Europe; Dr. Pablo Ruíz Flores and Dr. Jesús Muñiz Ugarte from the UAdeC, who gave me my first opportunities to do research as a medical student.

Finally, I would like to thank my wife, Dra. Esmeralda Martínez García, who joined me on this adventure in a new country, to my parents, José Luis Cortés Cárdenas and Margarita Sánchez Hinojosa, and to all my family in Mexico, who were always present, even at 9,334 km, each one of my achievements is your one and thanks to you.

9.- Eidesstattliche Erklärung

Ich erkläre, dass ich die der Medizinischen Fakultät der Otto-von-Guericke-Universität zur Promotion eingereichte Dissertation mit dem Titel:

„The effects of low shear stress generated in simulated microgravity bioreactors on thyroid cancer cells and endothelial cells, and its role in the multicellular spheroid formation process."

In der Klinik für Plastische, Ästhetische und Handchirurgie, der Medizinischen Fakultät der Otto-von-Guericke-Universität Magdeburg, Abteilung Mikrogravitation und Translationale Regenerative Medizin, ohne sonstige Hilfe durchgeführt und bei der Abfassung der Dissertation keine anderen als die dort aufgeführten Hilfsmittel benutzt habe.

Bei der Abfassung der Dissertation sind Rechte Dritter nicht verletzt worden.

Ich habe diese Dissertation bisher an keiner in- oder ausländischen Hochschule zur Promotion eingereicht. Ich übertrage der Medizinischen Fakultät das Recht, weitere Kopien meiner Dissertation herzustellen und zu vertreiben.

Magdeburg, den

José Luis Cortés Sánchez

Erklärung zur strafrechtlichen Verurteilung

Ich erkläre hiermit, nicht wegen einer Straftat verurteilt worden zu sein, die Wissenschaftsbezug hat.

Magdeburg, den

José Luis Cortés Sánchez

10.- Curriculum vitae.

Personal data

Name: José Luis Cortés Sánchez

Address: Raiffeisenstraße 8, 39112, Magdeburg

Nationality: Mexican

Civil status: Married

Telephone: +49 160 9219 9707

Email: jose.cortes@ovgu.de

Research indexes and profiles:

h-index: 6; Scopus Profile: 57386760300;

Forschungsportal Sachsen-Anhalt: ID = 117675 ORCID: 0000-0002-4646-9520

Work experience:

Position: Research Assistant

Date: Mai 2023 – currently

Research Area: AMCRIS (Artificial Intelligence Meets Cancer Research in Space)

Institution: Otto-von-Guericke-University Magdeburg, Faculty of Medicine, Department of Microgravity and Translational Regenerative Medicine, Group of Bioinformatics

Position: Doctoral student, DAAD-CONACYT Scholarship

Date: March 2021 – February 2024

Research Area: Cancer and Microgravity Research

Institution: Otto-von-Guericke-University, Faculty of Medicine, Department of Microgravity and Translational Regenerative Medicine, Group of Environmental Biology

Skills: -Cell culture (Celvivo, Biofloat, Ibidi Slides), 3D cancer cell culture (Breast, Thyroid, Lung cancer). Microfluidics and Shear stress cell culture. -Microgravity research: Ground-Based Simulated-Microgravity Platforms, Participation in 2 DLR Parabolic Flight Campaigns. -Microscopy techniques: Brightfield Microscopy, Confocal Microscopy, Immunofluorescence Staining. -Molecular Biology: RNA/DNA isolation, Real-time PCR. -Software: Fiji (ImageJ), ZEN Zeiss, LASX Leica, R studio (ggplot2, stats, tidyr, stringr, dplyr).

Position: Clinical Scientist

Date: March 2020 – February 2021

Project: SCOURGE (Spanish Coalition to Unlock Research on Host Genetics on Covid-19)

Institution: Hospital San Jose Tecnologico de Monterrey

Education

Title: Promotion „Dr. med"

Date: March 2021 – currently

University: Otto-von-Guericke University, Faculty of Medicine

Institute: Department of Microgravity and Translational Regenerative Medicine

Title: Research Assistant - Social Service Year:

Date: June 2019 – July 2020

Department: National Laboratory of Systems Medicine

Institution: Escuela de Medicina del Instituto Tecnólogico de Estudios Superiores de Monterrey

Title: Practical Year (Internship)

Internal Medicine, Surgery, Emergency Medicine, Pediatrics, Gynecology and Obstetrics.

Date: July 2018 – June 2019

Institution: Sanatorio Espanol de Torreon

University degree: Human Medicine

University: Faculty of Medicine of Torreón, Universidad Autónoma de Coahuila

Date: August 2013 – July 2020

2nd best student in the Generation

Coordination of the Poster Conference from the XVIII Medical Congress of Medicine "Cancer"

Language Certificates:

Deutsch Telc-B2, January 2023

Deutsch C1-Zertifikat (OVGU-Sprachenzentrum), August 2023

English TOEFL iBT: 100 pts C1, March 2020.

Publications:

2015

1.- Arellano, R. D. P. V., Argüello, J. R. A., Martínez, J. M., Marin, A. Y. G., Galarza, F. F. G., Guzman, D. G., & **Cortés-Sánchez, J.L.** (2015). Brief review of genomics in osteoarthritis. *International Journal of Orthopaedics*, *2*(4), 341-346.

2020

2.- **Cortes Sanchez, J. L**., Tovar Castaneda, A. C., Bustamante Sanchez, L. F., Espino Silva, P. K., Ruiz Flores, P., Peraza Martinez, L., & Muniz Ugarte, J. G. (2020, June). Molecular rearrangements of B-ALL and its prognosis associated in a Mexican cohort of patients. In *Pediatric Blood & Cancer* (vol. 67, pp. S166-s166). 111 River St, Hoboken 07030-5774, NJ USA: Wiley.

2021

3.- Martínez-García, E., **Cortés-Sánchez, J. L**., Ovalle-Escalera, C. N., González-Cortés, T., Haro-Santa Cruz, J., & Sarmiento-Martínez, H. I. (2021). Mammographic density patterns in women from Torreon, Coahuila. *Revista Medica del Instituto Mexicano del Seguro Social*, *59*(1), 65-72.

4.- **Cortés-Sánchez, J. L**., Callant, J., Krüger, M., Sahana, J., Kraus, A., Baselet, B., ... & Grimm, D. (2021). Cancer studies under space conditions: Finding answers abroad. *Biomedicines*, *10*(1), 25.

2022

5.- Grimm, D., Schulz, H., Krüger, M., **Cortés-Sánchez, J. L**., Egli, M., Kraus, A., ... & Wehland, M. (2022). The fight against cancer by microgravity: The multicellular spheroid as a metastasis model. *International Journal of Molecular Sciences*, *23*(6), 3073.

6.- Cruz, R., Diz-de Almeida, S., López de Heredia, M., Quintela, I., Ceballos, F. C., Pita, G., ..., **Cortés-Sánchez, J.L**., …, & Zeberg, H. (2022). Novel genes and sex differences in COVID-19 severity. *Human Molecular Genetics*, *31*(22), 3789-3806.

2023

7.- Sahana, J., **Cortés-Sánchez, J. L.,** Sandt, V., Melnik, D., Corydon, T. J., Schulz, H., ... & Wehland, M. (2023). Long-term simulation of microgravity induces changes in gene expression in breast cancer cells. *International Journal of Molecular Sciences*, *24*(2), 1181.

8.- Jokšienė, J., Sahana, J., Wehland, M., Schulz, H., **Cortés-Sánchez, J. L**., Prat-Duran, J., ... & Simonsen, U. (2023). Effects of High Glucose on Human Endothelial Cells Exposed to Simulated Microgravity. *Biomolecules*, *13*(2), 189.

9.- Melnik, D., **Cortés-Sánchez, J. L.,** Sandt, V., Kahlert, S., Kopp, S., Grimm, D., & Krüger, M. (2023). Dexamethasone selectively inhibits detachment of metastatic thyroid cancer cells during random positioning. *Cancers*, *15*(6), 1641.

10.- Pairo-Castineira, E., Rawlik, K., Bretherick, A. D., Qi, T., Wu, Y., Nassiri, I., ..., **Cortés-Sánchez, J.L.**, …, & ISARICC Investigators. (2023). GWAS and meta-analysis identifies 49 genetic variants underlying critical COVID-19. *Nature*, *617*(7962), 764.

11.- Alemany-Navarro, M., Diz-de Almeida, S., Cruz, R., Riancho, J. A., Rojas-Martínez, A., Lapunzina, P., ..., **Cortés-Sánchez, J.L**., …, & Carracedo, A. (2023). Psychiatric polygenic risk as a predictor of COVID-19 risk and severity: insight into the genetic overlap between schizophrenia and COVID-19. *Translational Psychiatry*, *13*(1), 189.

12.- Kanai, M., Andrews, S. J., Cordioli, M., Stevens, C., Neale, B. M., Daly, M., ..., **Cortés-Sánchez,** J.L., …, & Tiembe, N. (2023). A second update on mapping the human genetic architecture of COVID-19. *Nature*, *621*(7977), E7-E26.

13.- **Cortés-Sánchez, J. L.,** Melnik, D., Sandt, V., Kahlert, S., Marchal, S., Johnson, I. R., ... & Krüger, M. (2023). Fluid and Bubble Flow Detach Adherent Cancer Cells to Form Spheroids on a Random Positioning Machine. *Cells*, *12*(22), 2665.

14.- Castro-Santos, P., Rojas-Martinez, A., Riancho, J. A., Lapunzina, P., Flores, C., Carracedo, Á., ..., **Cortés-Sánchez, J.L**., …, & Fumadó, V. (2023). HLA-A* 11: 01 and HLA-C* 04: 01 are associated with severe COVID-19. *HLA*, *102*(6), 731-739.

2024

15.- Diaz-de Almeida, S., Cruz, R., Luchessi, A. D., Lorenzo-Salazar, J. M., de Heredia, M. L., Quintela, I., ..., **Cortés-Sánchez, J.L.,** …, & Carracedo, Á. (2024). Novel risk loci for COVID-19 hospitalization among admixed American populations. *eLife*, *13*

Preprints:

1.- Pérez-Jurado, L. A., Cáceres, A., Esko, T., López de Heredia, M., Quintela, I., Cruz, R., ..., **Cortés-Sánchez, J.L**., …, & Bustos, M. (2022). Clonal chromosomal mosaicism and loss of chromosome Y in men are risk factors for SARS-CoV-2 vulnerability in the elderly.

Conference abstracts and Presentations:

- "The role of YAP/TAZ in microgravity-induced bone loss. A literature review.", Congreso Mexicano de Medicina Espacial, Puebla, México, 05.10.2017.
- "Birth" of a multicellular spheroid– Implications for future RPM experiments. DLR 22. Gravimeeting Conference, Erlangen 24.04.2023.
- "Mechanobiological signaling of tumors cells in simulated microgravity bioreactors", MARS-Minisymposium, Magdeburg, 23.02.2024,
- "The role of AMCRIS in Flumias microscope-Workshop; Mammalian EB." AIMS-Meeting, Duisburg, 27.02.2024.

Grants:

- Travel grant for the Workshop: "Interdisciplinary research - Scientific dating – an encounter across disciplines". 05-06.10.2023. Belgium, Brussels. SCK-CEN Academy.
- CONAHCYT-DAAD, Doctoral Scholarship, March 2021 – February 2024.

Media mentions/features/appearances

- Research in Germany Campaign "From Space to Life": (25/09/2023) : José fights cancer in microgravity. " initiative by the Federal Ministry of Education and Research (BMBF) *youtu.be/MrpQ7kR7MB8?si=AFIcuUmbfPzxt6oi*

11.- Appendix.

11.1 Publication #1

Melnik, D., **Cortés-Sánchez, J. L**., Sandt, V., Kahlert, S., Kopp, S., Grimm, D., & Krüger, M. (2023). Dexamethasone selectively inhibits detachment of metastatic thyroid cancer cells during random positioning. Cancers, 15(6), 1641.

cancers

MDPI

Article

Dexamethasone Selectively Inhibits Detachment of Metastatic Thyroid Cancer Cells during Random Positioning

Daniela Melnik [1,2], José Luis Cortés-Sánchez [1], Viviann Sandt [1], Stefan Kahlert [2,3], Sascha Kopp [2,4], Daniela Grimm [1,2,5] and Marcus Krüger [1,2,*]

[1] Department of Microgravity and Translational Regenerative Medicine, Otto von Guericke University, 39106 Magdeburg, Germany
[2] Research Group "Magdeburger Arbeitsgemeinschaft für Forschung unter Raumfahrt- und Schwerelosigkeitsbedingungen" (MARS), Otto von Guericke University, 39106 Magdeburg, Germany
[3] Institute of Anatomy, Otto von Guericke University, 39120 Magdeburg, Germany
[4] Core Facility Tissue Engineering, Otto von Guericke University, 39106 Magdeburg, Germany
[5] Department of Biomedicine, Aarhus University, 8000 Aarhus, Denmark
* Correspondence: marcus.krueger@med.ovgu.de; Tel.: +49-391-6757471

Simple Summary: Metastasis is the most dangerous feature of advanced cancers. In vitro models of this process could help us to study and understand mechanisms that are not readily accessible in the human body. In our approach, we used random positioning cell cultures to induce cancer cells to spread and form tumor spheroids. In this experimental setup, we show that dexamethasone is able to specifically inhibit the detachment of metastatic thyroid cancer cells. Our results not only show how differently healthy and malignant thyroid cells act and react in this in vitro metastasis model system, but also provide valuable insights into its functioning, possibilities and limitations.

Abstract: We recently reported that synthetic glucocorticoid dexamethasone (DEX) is able to suppress metastasis-like spheroid formation in a culture of follicular thyroid cancer (FTC)-133 cells cultured under random positioning. We now show that this inhibition was selective for two metastatic thyroid carcinoma cells, FTC-133 and WRO, whereas benign Nthy-ori 3-1 thyrocytes and recurrent ML-1 follicular thyroid cancer cells were not affected by DEX. We then compare Nthy-ori 3-1 and FTC-133 cells concerning their adhesion and mechanosignaling. We demonstrate that DEX disrupts random positioning-triggered p38 stress signaling in FTC-133 cells, thereby antagonizing a variety of biological functions. Thus, DEX treatment of FTC-133 cells is associated with increased adhesiveness, which is mainly caused by the restored, pronounced formation of a normal number of tight junctions. Moreover, we show that Nthy-ori 3-1 and ML-1 cells upregulate the anti-adhesion protein mucin-1 during random positioning, presumably as a protection against mechanical stress. In summary, mechanical stress seems to be an important component in this metastasis model system that is processed differently by metastatic and healthy cells. The balance between adhesion, anti-adhesion and cell–cell connections enables detachment of adherent human cells on the random positioning machine—or not, allowing selective inhibition of thyroid in vitro metastasis by DEX.

Keywords: glucocorticoids; thyroid cancer; random positioning; in vitro metastasis; cell adhesion; anti-adhesion; tight junctions; cancer treatment

Citation: Melnik, D.; Cortés-Sánchez, J.L.; Sandt, V.; Kahlert, S.; Kopp, S.; Grimm, D.; Krüger, M. Dexamethasone Selectively Inhibits Detachment of Metastatic Thyroid Cancer Cells during Random Positioning. *Cancers* **2023**, *15*, 1641. https://doi.org/10.3390/cancers15061641

Academic Editor: David Wong

Received: 12 February 2023
Revised: 27 February 2023
Accepted: 6 March 2023
Published: 7 March 2023

1. Introduction

Cancer is considered one of the most life-threatening diseases due to its ability to metastasize. Metastasis is responsible for more than 90% of all cancer-related deaths [1]. The mechanism of cancer metastasis mainly involves six steps: (1) detachment from the primary tumor, (2) intravasation, (3) transport through the bloodstream, (4) entrapment in the endothelial walls of the distant organ, (5) extravasation into the parenchyma of the distant organ, and (6) formation of secondary tumors on the distant organ [2]. In most

cases, the initialization of the metastatic process is thought to be the result of a genetic [3] or epigenetic [4] trigger. However, there is increasing evidence that mechanical stimuli also contribute to metastasis through the interplay of physical forces and biochemical signals (reviewed in [5,6]). In this context, it is important to note that not all cancer cells have the ability to form metastases. It is generally believed that a process similar to epithelial-mesenchymal transition (EMT) is required for cancer cells to metastasize [7], which is associated with a loss of adhesion and stiffness [8]. Early on, Guck et al. [9] demonstrated that human breast cancer cell lines MCF-7 and especially the highly metastatic MDA-MB-231 are more deformable than their epithelial counterpart MCF-10A and opened the field for cancer biophysics. That the invasiveness of cancer cells is indeed correlated with their plastic response was recently reconfirmed by Cho et al. [10] using a novel microfluidic system. Interestingly, metastatic cancer cells seem to change their mechanical properties in response to passive and active mechanical stimuli to a much greater extent than normal cells [11–13].

The random positioning machine (RPM) is a rotating bioreactor originally developed for the study of gravitational biology in cells, tissues and organisms [14,15]. Unlike rotating clinostats, which are primarily designed to prevent sedimentation of suspension cells, the RPM generates shear forces as a side effect [16,17]. Computer simulations showed that the fluid motion inside the cell culture flasks on the RPM never reached or approached a steady state [18]. What is a disadvantage for some may be an advantage for others: adherent cells are stimulated by the RPM to detach from their surface, and in the case of tumor cells, this process mimics spreading in vivo in several aspects (Figure 1) [19–21]. Among the possible explanations for this in vitro metastasis model is that tumor cells respond differently and possibly more sensitively to mechanical stimuli. MDA-MB-231 cells with high metastatic potential were more susceptible to migration under fluid shear forces than the less metastatic MDA-MB-468. The benign MCF-10A cell line had the lowest migration potential under shear forces [22]. Fluid shear stress has also been described to promote invasion through increased secretion of matrix metalloproteinases (MMPs) [23], increased cell motility, and facilitated EMT of adherent tumor cells [24–26]. Ahn et al. [27] indicated that random positioning accelerates the migration of two types of adherent non-small cell lung cancer cells even in a floating environment. However, the exact mechanism of spheroid formation from 2D cultures on the RPM, which was also observed for several healthy cells [28–30], is still unclear.

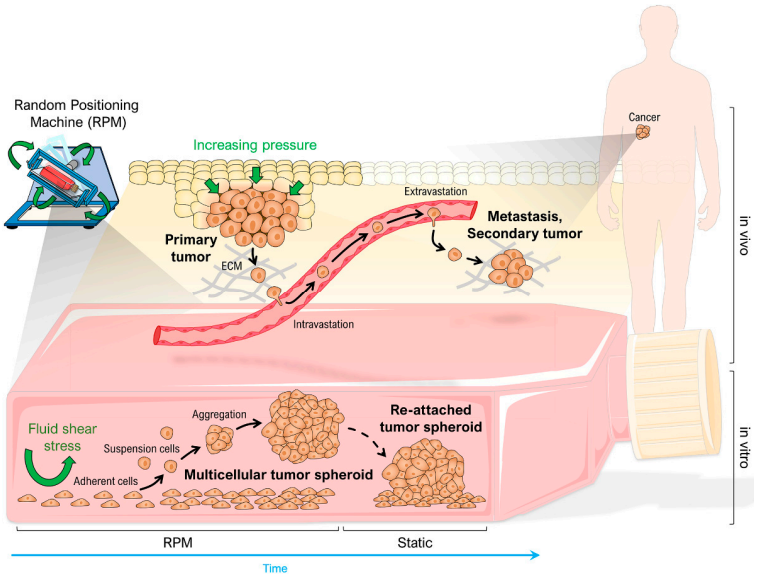

Figure 1. Comparison of metastasis in vivo and random positioning cell culture with adherent growing cancer cells in vitro. Modified from [19]. Parts of the figure were drawn by using pictures from Servier Medical Art, licensed under a Creative Commons Attribution 3.0 Unported License (https://creativecommons.org/licenses/by/3.0/, accessed on 12 February 2023).

Recently, we reported that RPM-induced spheroid formation of FTC-133 thyroid carcinoma cells was inhibited by dexamethasone (DEX) in a concentration-dependent manner and came across a complex regulation network of tumor spheroid formation under dynamic flow that may be influenced by glucocorticoids such as DEX [31]. With the current study, we aimed to reveal and explain the effects of DEX treatment on thyroid cancer cells cultured on the RPM and generally gain a better understanding of the behavior of human cells in a rotational culture.

2. Materials and Methods

2.1. Cell Lines and Cell Culture

The human follicular thyroid carcinoma cell lines FTC-133 (passages 17–25) and WRO (passages 10–16) and the noncancerous follicular epithelial cell line Nthy-ori 3-1 (passages 10–15) were purchased from Sigma-Aldrich (St. Louis, MO, USA). The human follicular thyroid carcinoma cell line ML-1 (passages 5–9) isolated from recurrence [32] was used from a laboratory stock. Cells were cultured in RPMI 1640 medium (Life Technologies, Carlsbad, CA, USA) supplemented with 10% fetal calf serum (FCS; Sigma-Aldrich, St. Louis, MO, USA), and 1% penicillin/streptomycin (Life Technologies) at 37 °C and 5% CO_2 until used for experiments. Twenty-four hours before each experiment, a cell density of 1×10^6 cells per flask were seeded in T25 cell culture flasks (Sarstedt, Nümbrecht, Germany) to allow cells to adhere. T25 flasks equipped with glass coverslips and a reduced cell density of 0.5×10^6 cells were used for immunofluorescence staining.

Breast epithelial cells (MCF-10A; ATCC, Manassas, VA, USA), mammary carcinoma cells (MCF-7; ATCC), and prostate carcinoma cells (PC-3, LnCAP; ATCC) for supplemental experiments were cultured accordingly. The MCF-10A cell line was cultured in DMEM/F12 medium supplemented with 0.5% Mammary Epithelial Growth Supplement (MEGS) (Life Technologies).

2.2. Dexamethasone and Drug Treatment

Ethanol-soluble DEX was purchased from Sigma-Aldrich. Twenty-four hours after seeding, cells were washed once with phosphate-buffered saline (PBS; Life Technologies), synchronized for four hours in RPMI 1640 with 0.25% FCS and 1% Penicillin/Streptomycin, following a cultivation with RPMI 1640 medium supplemented with 0–1000 nM DEX, as described in [31]. This procedure was applied before any drug treatment.

To investigate the selective effect of DEX on metastatic cell lines, we treated FTC-133 and WRO cells with the re-activator of mutant p53 activity, PRIMA-1^{Met} (2-(Hydroxymethyl)-2-(methoxymethyl)-1-azabicyclo [2.2.2]octan-3-one; Sigma-Aldrich). PRIMA-1^{Met} was dissolved in water. Cell cultures were supplemented with 10 µM PRIMA-1^{Met} or 10 µM PRIMA-1^{Met} combined with 1 µM DEX for three days.

To target GR signaling, we used the water-soluble GR antagonist Mifepristone (MIF, Sigma-Aldrich). Based on the highest DEX concentration of 1 µM, FTC-133 cells were cultured for three days in DEX:MIF ratios of 1:1, 1:10 and 1:20. Untreated cells, as well as cells treated with 1 µM DEX or 20 µM MIF, served as controls.

Moreover, we applied the D-amino acid cell-penetrating peptide inhibitor of MUC-1, GO-203 (Selleck Chemicals, Planegg, Germany). A GO-203 stock solution was prepared with sterile water. According to the manufacturer's instructions, we treated Nthy-ori 3-1 cells with 5 µM of GO-203 in combination with 1 µM DEX (Sigma-Aldrich) for three days. To exclude side effects of GO-203, controls supplemented with GO-203 and untreated controls were included.

2.3. Random Positioning

Cell cultures were randomly positioned on a desktop RPM (Dutch Space, Leiden, The Netherlands) inside an incubator or inside an incubator RPM (iRPM 2.0, designed and constructed by Prof. Jörg Sekler, University of Applied Sciences and Arts Northwestern Switzerland [33]), both operated in a real random mode. Before the run, all culture flasks

were filled bubble-free with medium supplemented with the corresponding drug concentrations. Corresponding static controls were each prepared in parallel under the same conditions and stored next to the device in an incubator.

2.4. Static Forced Floating Spheroid Formation

Cells were seeded in 96-well BIOFLOAT™ U-bottom plates (faCellitate, Mannheim, Germany) at a density of 2500 cells per well with culture medium supplemented with 0, 10, 100 and 1000 nM DEX at 37 °C and 5% CO_2. Images were acquired every 24 h for three days using an Invitrogen EVOS™ XL Core Imaging System (Thermo Fisher Scientific, Waltham, MA, USA).

2.5. Trypsin Digestion Adhesion Assay

To investigate the effect of DEX and random positioning on the "stickiness" of adherent FTC-133 and Nthy-ori 3-1 cells, we seeded 0.5×10^6 cells in a Slide Flask (Thermo Fisher Scientific). Cells were treated as described in Section 2.2. After a 24-h attachment period, the Slide Flasks were completely filled with RPMI 1640 medium supplemented with 1 µM DEX for the DEX treatment group and cultured for 24 h under static or RPM conditions. After 24 h, cells were photographed, washed once with PBS, and incubated for 9 min (Nthy-ori 3-1) or 5 min (FTC-133) in prewarmed 0.05% trypsin-EDTA (Life Technologies) at room temperature (RT). The Slide Flasks were moderately hit once, fresh medium was added and removed to stop the trypsin reaction, and the remaining cells were imaged under the microscope.

2.6. Phase Contrast Microscopy

Cells were observed and photographed using an OLYMPUS CKX53 inverted microscope (Olympus, Tokio, Japan) or an Invitrogen™ EVOS™ XL Core Imaging System (Thermo Fisher Scientific).

2.7. Immunofluorescence Microscopy

The adherent cells were washed twice with PBS and fixed by incubation for 30 min at 4 °C in 100% EtOH (Carl Roth, Karlsruhe, Germany), followed by 90 s in ice-cold acetone (Carl Roth) at RT. Cells were stored in 0.5 M sodium azide (Carl Roth) in 0.1 M PBS at 4 °C until observation. Fixed cells were blocked with 3% bovine serum albumin (BSA, Carl Roth) in 0.1 M PBS for 1 h at RT. Subsequently, the cells were labeled with the primary antibodies diluted in 1% BSA (listed in Table S1) overnight at 4 °C. The next day, the cells were washed three times with 0.1 M PBS and incubated with the secondary Alexa Fluor™ 488 (AF488)-conjugated anti-rabbit (Invitrogen, Life Technologies) or Alexa Fluor™ 647 (AF647)-conjugated anti-mouse (Invitrogen, Life Technologies) antibodies at a dilution of 1:500 or 1:1000 at RT for 1 h. Cells were washed again three times with 0.1 M PBS and mounted with Fluoroshield™ with DAPI (4′,6-diamidino-2-phenylindole) (Sigma-Aldrich). The next day, the slides were examined using a ZEISS LSM 800 confocal laser scanning microscope (Carl Zeiss, Oberkochen, Germany). To ensure comparability for intensity quantification, all images were acquired with the same settings using the ZEISS Airyscan detector and ZEN 3.4 software (Carl Zeiss). Images were normalized to the untreated FTC-133 samples cultured under static conditions. Airyscan processing settings were optimized for each antibody/wavelength combination and manually applied to corresponding samples. The resulting file was used in Fiji software v1.53t (ImageJ, imagej.net) to quantify the relative protein amount based on the fluorescence of the sample with the "Image Calculator" tool. Relative intensities were measured according to the method recently described by Shihan et al. [34]. To determine the ratio of protein localization between the nucleus and cytoplasm, the fluorescence intensities of the protein of interest were measured for the nuclear area and the cytoplasm. The nuclear area was determined before using the DAPI signal. For the co-localization measurement of assembled protein complexes, ImageJ image

calculation was used to combine the channels of interest and to subtract the DAPI channel. The amount of protein complexes/co-localization was indicated by the LUT fire setting.

2.8. mRNA Isolation and Quantitative Real-Time PCR

The adherent cells were washed once with PBS and fixed by addition of Invitrogen RNA*later*™ solution (Life Technologies). Cells were harvested using cell scrapers and samples were stored at −20 °C until mRNA extraction. mRNA isolation was performed by using the RNeasy Mini Kit (Qiagen, Venlo, The Netherlands), following the manufacturer's protocol. RNA concentration was determined with a NanoPhotometer® N60 (Implen, Munich, Germany) followed by cDNA synthesis using the High Capacity cDNA Reverse Transcription Kit (Life Technologies). To define the expression level of the genes of interest, quantitative real-time PCR was performed by using the Fast SYBR™ Green Master Mix (Life Technologies) and the QuantStudio™ 3 Real-Time PCR System (Thermo Fisher Scientific). Primer sequences used in the quantitative real-time PCR can be found in the Supplementary Materials (Table S2). The samples were measured in triplicates and evaluated by using the comparative threshold cycle ($\Delta\Delta C_T$) method with 18S rRNA as the housekeeper reference.

2.9. Protein Isolation and Western Blot Analysis

The adherent cells were placed on ice, washed once with ice-cold PBS, and then harvested with ice-cold PBS using cell scrapers. The suspensions were centrifuged at 3000× *g* for 10 min at 4 °C, then the PBS was discarded and the cell pellets were stored at −150 °C.

Proteins were isolated by performing incubation and centrifugation steps in RIPA lysis buffer (Sigma-Aldrich). Protein concentration was measured using the BCA protein assay (Carl Roth). First, 20 µg total protein were loaded onto an SDS-PAGE gel (8%, 10% or 12.5%, 1 mm), run for 20–30 min at 80 V, 90 min at 100 V, and transferred to a nitrocellulose membrane (Carl Roth; 90 min, 100 V). Membranes were blocked with 5% BSA (Carl Roth) in TBS-T for 1 h at RT. To detect proteins of interest, membranes were incubated overnight at 4 °C with a primary antibody diluted in TBS-T containing 5% BSA. GAPDH was used as a loading control. Afterwards, the membranes were washed three times with TBS-T for 5 min and incubated for 1 h at RT with a horseradish peroxidase (HRP)-linked secondary antibody (Invitrogen, Life Technologies) diluted in TBS-T containing 5% BSA. Before the protein bands were visualized by applying Clarity Western ECL Substrate (Bio-Rad, Hercules, CA, USA), the membrane was washed three times with TBS for 5 min. Images were acquired using the ChemiDoc™ XRS+ molecular imager (Bio-Rad) and analyzed using Image Lab™ 6.1 software (Bio-Rad).

For re-staining (e.g., to visualize loading controls of similar size to the protein of interest), membranes were stripped in some Western blots. To remove antibodies, membranes were incubated in stripping buffer (62.5 mM TRIS, 2% SDS, pH 6.8) at 50 °C for 15–20 min and then washed three times with TBS for 5 min.

All antibodies used for Western blot analyses can be found in the Supplementary Materials (Table S1).

2.10. Cell Culture Supernatant Analyses

Oxygen concentration was measured directly in the T25 cell culture flask by fiber-optic oxygen detection using a Microx TX3 transmitter equipped with a flat, broken-tip oxygen microsensor (PreSens, Regensburg, Germany). The sensor was calibrated according to the manufacturer's specifications. Temperature-compensated measurements (37 °C) were recorded using TX3v602 software (PreSens) over a period of 5 min.

2.11. Spheroid Measurement and Quantification

Spheroids were generated through the cultivation of adherent or suspended cells on the RPM. Images of spheroids were taken by using the microscopes described in Section 2.10. These were randomly selected and imaged with the 4× lens. The analysis was done with

ImageJ. First, the spheroids of five images were counted, then outlined with the ImageJ tool "freehand selections" and automatically measured.

2.12. Statistics

Statistical evaluation was performed using SPSS Statistics v28 (IBM, Armonk, NY, USA). The nonparametric Mann–Whitney U test or the independent *t*-test (for Western blot and O_2 saturation analyses due to the smaller number of samples) was used to compare samples from different culture conditions. All data are presented as mean ± standard deviation (SD) with a significance level of $p < 0.05$.

3. Results

As previously reported, FTC-133 spheroid formation was inhibited by DEX in a concentration-dependent manner (Figure 2A).

3.1. Dexamethasone Inhibits Formation but Not Stability of Multicellular Tumor Spheroids

To test spheroid integrity during DEX treatment, we added 1000 nM DEX to a culture of FTC-133 spheroids formed after three days on the RPM and continued random positioning. After three more days, we could see that the spheroids had not disassembled or shrunk, but continued growing in the presence of DEX (Figure 2B). DEX had no influence on the stability of preformed tumor spheroids on the RPM.

3.2. Dexamethasone Selectively Affects Spheroid Formation of Metastatic Thyroid Cancer Cells

In addition to FTC-133 cells, we tested spheroid formation of the normal Nthy-ori 3-1 thyroid epithelial cell line and recurrent ML-1 carcinoma cells derived from a dedifferentiated follicular thyroid carcinoma relapse (Figure 2D) in the presence of different DEX concentrations (0, 10, 100, 1000 nM). Both cell lines formed multicellular spheroids after 72 h on the RPM (Figure 2E). Although the Nthy-ori 3-1 and ML-1 spheroids were much smaller compared to the FTC-133 spheroids, formation was not inhibited by increasing DEX concentrations (Figure 2E). Furthermore, we tested a second metastasis-born thyroid cell line, WRO, that also showed a highly reduced formation of 3D aggregates in the presence of DEX (Figure 2E, bottom line).

The results suggested a selective effect of DEX on the RPM-triggered 3D growth of thyroid carcinoma cells isolated from metastases. Because both FTC-133 and WRO metastatic cell lines have *TP53* mutations, PRIMA-1^{Met} (APR-246) was used to restore mutant p53 activity, thus eliminating the possibility that the observed effect of DEX was due to p53 dysfunction. We demonstrated that the addition of 10 µM PRIMA-1^{Met} did not affect the DEX inhibition of spheroid formation in FTC-133 cells and could not completely reverse the effect in WRO cells (Figure 2F), ruling out the involvement of p53 in this process. Furthermore, PRIMA-1^{Met} alone had no effect on spheroid formation on the RPM.

3.3. Dexamethasone Supresses RPM-Induced Cell Detachment but Not 3D Growth in General

RPM-induced spheroid formation comprises two steps: The detachment of the actually adherent cells from their growth surface and the aggregation/growth of the detached and floating cells in the medium. To find out which step is influenced by DEX, we used ultra-low attachment multi-well plates for comparison, in which spheroids form automatically without mechanical action. After 72 h, spheroids of FTC-133 cells and Nthy-ori 3-1 cells have formed in the wells independently of the used DEX concentration (0–1000 nM) (Figure 2G). Furthermore, FTC-133 cells formed smaller spheroids in the presence of 1000 nM DEX when they were placed directly on the RPM without a prior attachment phase (Figure 2C). The number of these spheroids was comparable with those of the DEX-free samples. We also observed 3D growth when we cultured FTC-133 suspension cells together with DEX on a clinostat. Accordingly, DEX did not prevent the aggregation of the cells itself, but seems to impede the 'metastasis-like' detachment of thyroid cancer cells observed under random positioning.

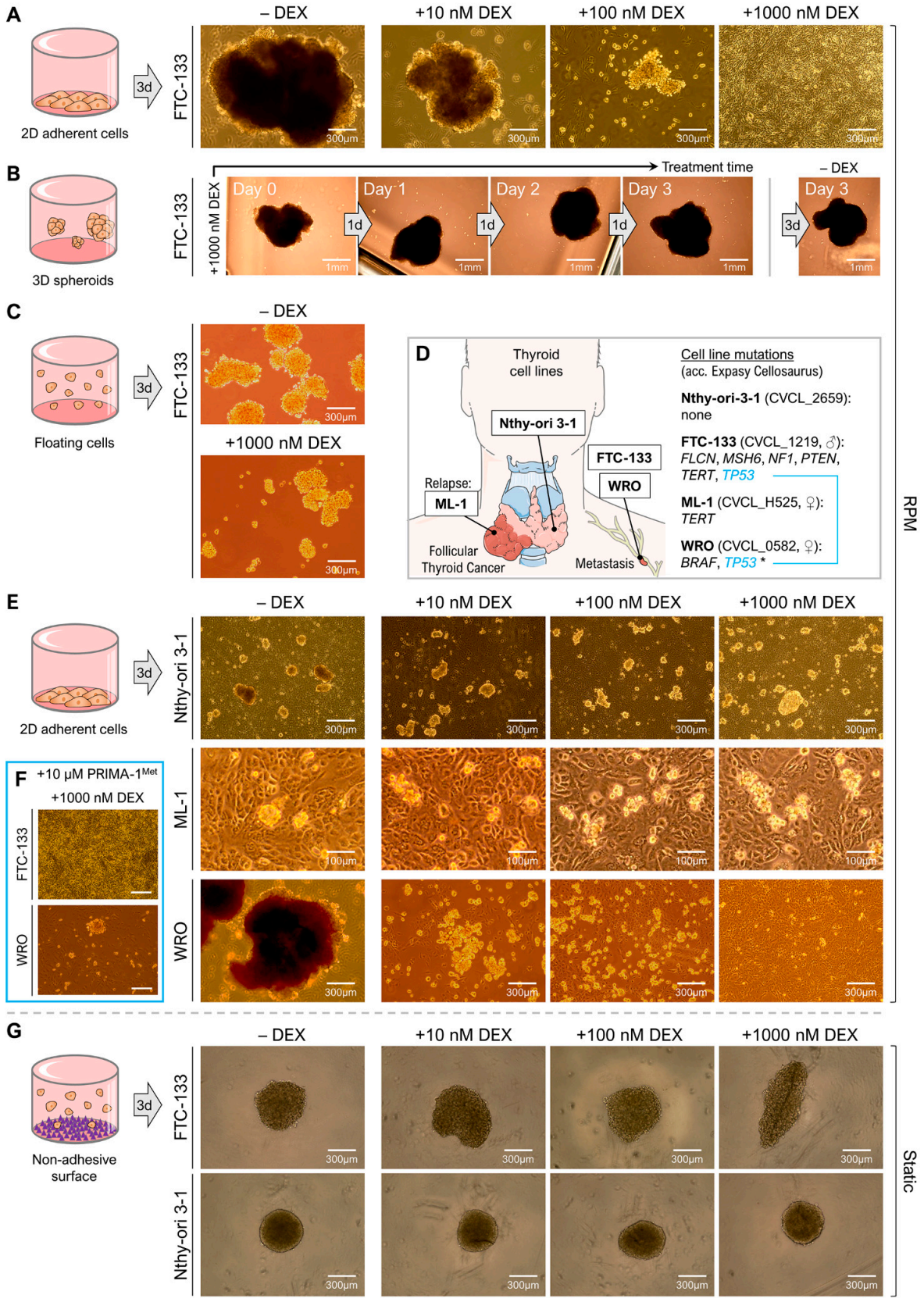

Figure 2. Impact of different DEX concentrations (0, 10, 100, 1000 nM) on spheroid formation and stability of different thyroid epithelial cells after 3 days. (**A**) Spheroid formation of adherent FTC-133 metastasized carcinoma cells after rotation on the RPM; (**B**) stability of preformed FTC-133 spheroids on the RPM in the presence of 1000 nM DEX; (**C**) spheroid formation of FTC-133 suspension

cells; (**D**) origins of the used thyroid cell lines and documented cell line mutations (https://www.cellosaurus.org; accessed on: 2 February 2023). ♂, ♀indicate the gender of the donor. * The *TP53 P223L* mutation in WRO cells is only reported by some authors; (**E**) spheroid formation of adherent Nthy-ori 3-1 thyroid epithelial, ML-1 recurrent and WRO metastasized thyroid carcinoma cells after 3d rotation on the RPM; (**F**) spheroid formation of FTC-133 and WRO cells in the presence of 10 µM of the p53 reactivator PRIMA-1^{Met} and 1000 nM DEX; (**G**) spheroid formation of FTC-133 and Nthy-ori 3-1 cells under static forced floating conditions in ultra-low attachment plates. Parts of subfigure D were drawn by using pictures from Servier Medical Art, licensed under a Creative Commons Attribution 3.0 Unported License (https://creativecommons.org/licenses/by/3.0/, accessed on 12 February 2023).

3.4. Dexamethasone Treatment Alters 'Stickiness' of the Cells

After showing specifically that the spheroid formation of FTC-133 cancer cells versus benign Nthy-ori 3-1 cells is affected by DEX (Figure 3A), we started to investigate the cause in these two cell lines. Considering the different forces of cell adhesion and shear forces on RPM (Figure 3B), DEX treatment of FTC-133 cells must result in adhesion forces being greater than shear forces leading to cell detachment. When treated with a DEX concentration of 1000 nM, spheroid formation of FTC-133 cells was completely suppressed in contrast to Nthy-ori 3-1 cells (Figure 3C, grey area). Spheroid size was also affected by DEX, but since the focus of this study was on the formation of spheroids rather than their later development, this aspect was not further explored here. A trypsinization assay showed that DEX increased the adhesiveness of both cell lines, and that random positioning deceased the adhesiveness of Nthy-ori 3-1 cells.

FTC-133 cells showed a more bipolar or multipolar shape with cellular bridging in the presence of DEX (Figure 3D, yellow arrows). Factors that may increase cell adhesion include extracellular matrix composition (ECM) proteins and cell–cell or cell–ECM junctions.

3.4.1. Extracellular Matrix

We examined the ECM composition based on the immunofluorescence of several major components, including fibronectin, collagen I/IV and laminin. Whereas DEX had no effect on fibronectin in FTC-133 cells, we found an 8-fold increase of fibronectin in DEX-treated Nthy-ori 3-1 cells. Moreover, we detected a decrease in fibronectin in RPM-grown FTC-133 cells, which was also present, although to a lesser extent, in Nthy-ori 3-1 cells (Figure 4A,B). In the RPM+DEX samples, the FTC-133 cells produced a slightly lower amount of fibronectin than the Nthy-ori 3-1 cells (Figure 4B).

Collagen I was more highly expressed in FTC-133 cells. Random positioning and DEX treatment alone increased collagen I levels in Nthy-ori 3-1 cells and decreased them simultaneously in FTC-133 (Figure 4C,D). Thus, collagen I levels of both cell lines were almost identical after 72 h of DEX treatment. Interestingly, DEX treatment during random positioning lead to a decrease in collagen I in both malignant and healthy cells (Figure 4D). Collagen IV was only detectable in significant amounts in FTC-133 cells after 72 h. It was less present after random positioning (Figure 4C).

Laminin was significantly reduced by DEX in FTC-133 cells, regardless of culture condition (Figure 4E,F). In Nthy-ori 3-1 cells there was a slight increase of laminin in the DEX-treated RPM group (Figure 4F).

While the amount of MMP-9 was not affected by either RPM or DEX, MMP-2 was decreased after DEX administration in both FTC-133 and Nthy-ori 3-1 cells. Nthy-ori 3-1 cells exhibited generally lower levels of MMP-2 and MMP-9. In particular, MMP-9 was increased 14-fold in FTC-133 cells (Figure 4G,H).

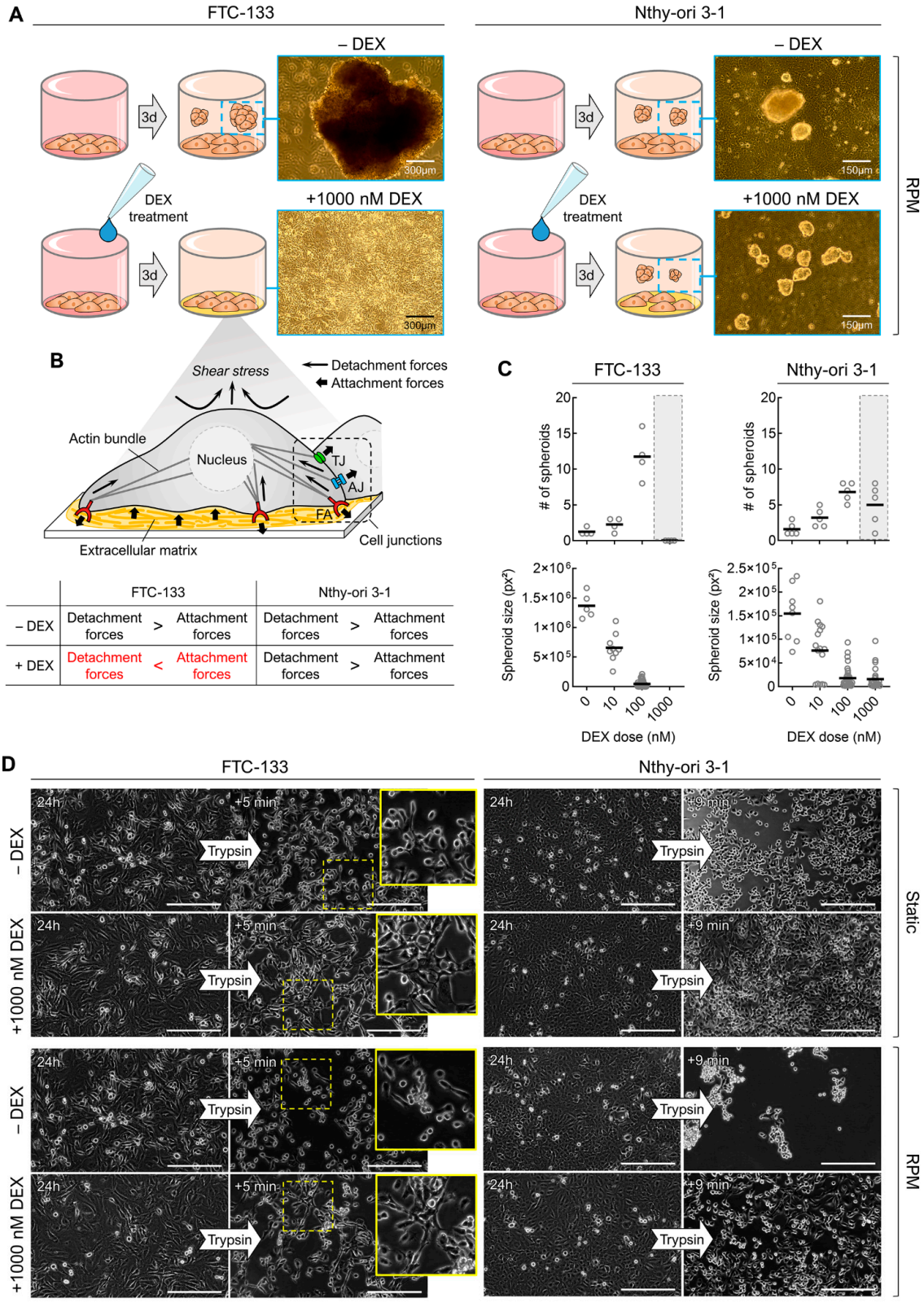

	FTC-133		Nthy-ori 3-1	
– DEX	Detachment forces	> Attachment forces	Detachment forces	> Attachment forces
+ DEX	Detachment forces	< Attachment forces	Detachment forces	> Attachment forces

Figure 3. (**A**) Observed effects of 1000 nM DEX on the RPM-induced spheroid formation of FTC-133 und Nthy-ori 3-1 cells after 3 days; (**B**) putative reasons for the different behavior of the two cell lines. AJ: adherens junction, FA: focal adhesion, TJ: tight junction; (**C**) number and size of spheroids formed after 3 days on the RPM depending on DEX concentration; (**D**) trypsin-based cell detachment assay reveals the general adhesiveness of cells after 24 h of culture in the presence and absence of DEX. The yellow boxes show an enlargement of the outlined section. Scale bars: 300 µm.

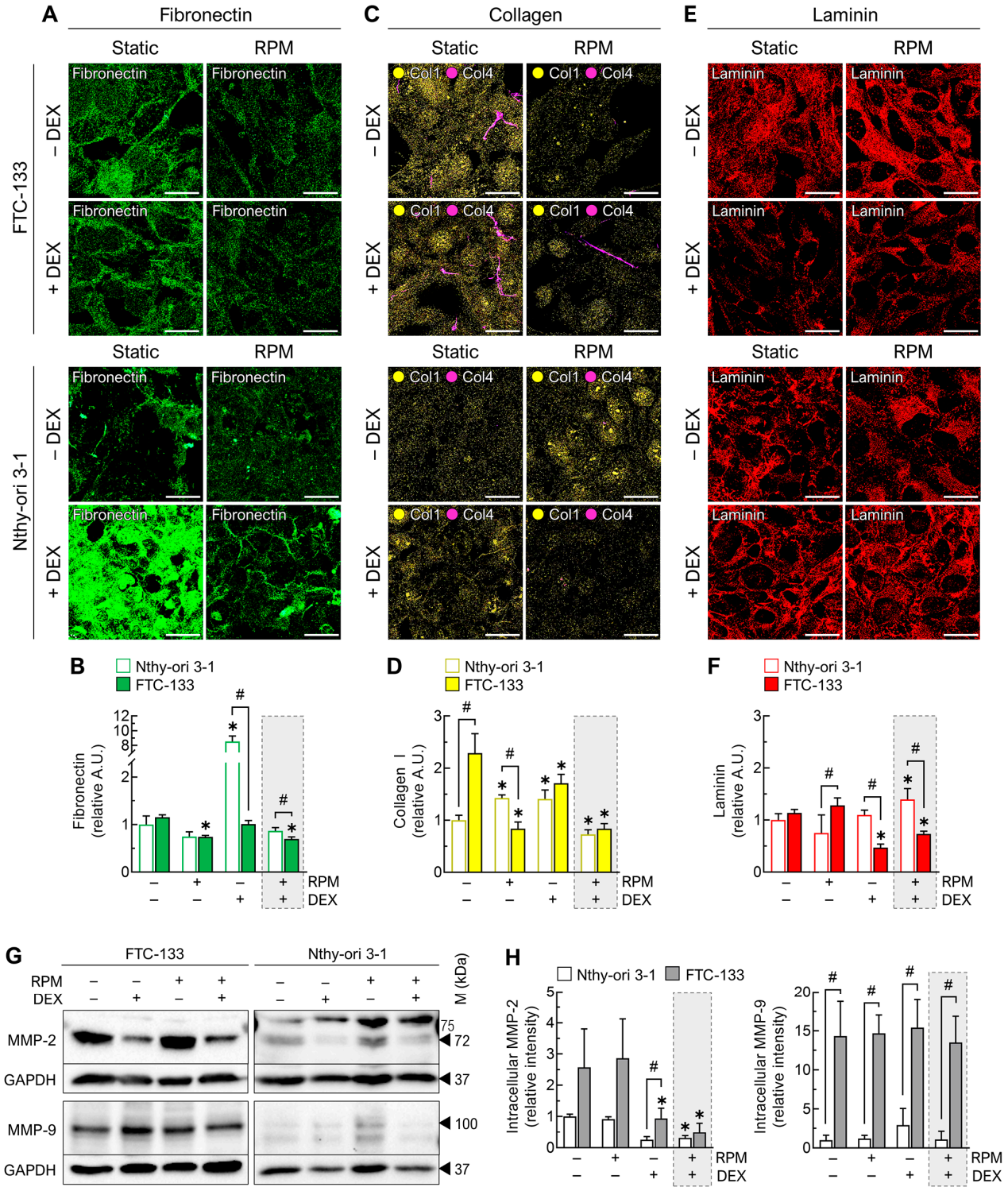

Figure 4. Effect of DEX (1000 nM) and random positioning on the ECM of FTC-133 and Nthy-ori 3-1 cells after 3 days. (**A**) Immunofluorescence of fibronectin; (**B**) fluorescence-based quantification of fibronectin under the different culture conditions (n = 5); (**C**) immunofluorescence of collagen I (yellow) and collagen IV (purple); (**D**) fluorescence-based quantification of collagen I under the different culture conditions (n = 5); (**E**) immunofluorescence of laminin; (**F**) fluorescence-based quantification of laminin under the different culture conditions (n = 5); (**G**) intracellular protein levels of matrix metallopeptidases MMP-2 and MMP-9 indicated by Western blot (see also Supplementary File S1); (**H**) densitometric quantification of Western blot proteins (n = 3). Scale bars: 300 µm. * $p < 0.05$ vs. control condition (−DEX/−RPM); # $p < 0.05$.

In summary, we showed that, in FTC-133 cells, three major ECM structural components were reduced by DEX treatment during random positioning. Compared with Nthy-ori 3-1 cells, the ECM components were even more reduced. In addition, FTC-133 cells produced many more collagenases. All this cannot explain the different response of the two cell lines to DEX treatment.

3.4.2. Cell Junctions

The expression of the tight junction (TJ) proteins claudin-1 and ZO-1 (zonula occludens 1) was significantly lower in FTC-133 cells than in Nthy-ori 3-1 cells under normal culture conditions. However, in both cell lines, the levels of the proteins were increased by both DEX and, to a lesser extent, by the RPM (Figure 5A,B). In particular, the expression of ZO-1 was increased 27-fold in FTC-133 in the presence of DEX and 20-fold after exposure to the RPM. In addition, FTC-133 cells showed increased nuclear localization of ZO-1 both on the RPM and after DEX treatment (Figure 5A), indicating the formation and maturation of TJs [35].

Co-localization analysis of claudin-1 and ZO-1 confirmed the enhanced formation of TJs by DEX, which reached the same amount in FTC-133 cells as in Nthy-ori 3-1 cells after 72 h, regardless of culture motion (Figure 5C). This increase in TJs could also explain the cellular bridging and altered shape of FTC-133 cells in the presence of DEX (Figure 3D). Another zonula occludens protein, ZO-2, showed similar regulation to ZO-1 in FTC-133 cells (Figure S1A). Overall, both FTC-133 cells and WRO cells showed very low baseline expression of claudin-1 under static cell culture and strong upregulation during DEX treatment on the RPM (Figure S1B). Therefore, TJ regulation might be related to the inhibition of spheroid formation of both cell lines by DEX (Figure S1C).

E-cadherin expression was generally lower in FTC-133 cells than in Nthy-ori 3-1 cells. Whereas E-cadherin was downregulated mainly by RPM in both cell lines, in FTC-133 cells, both DEX and RPM had a suppressive effect on β-catenin levels (Figure 5D,E). Overall, the amount of adherens junctions (AJs) was higher in FTC-133 cells in the RPM+DEX samples than in standard culture, but still significantly lower than in Nthy-ori 3-1 cells (Figure 5F).

Unlike the benign cells, there was an increase in focal adhesions (FAs) in FTC-133 cancer cells in response to the RPM (Figure 5G–I). In Nthy-ori 3-1 cells, a similar effect was detected in response to DEX. This is also reflected in the amount of the single components, FAK (focal adhesion kinase) and integrin-β1 (Figure 5H). Nevertheless, the combination RPM+DEX did not show any changes in the number of FAs in either cell line (Figure 5I).

In summary, although FTC-133 cells showed a significant increase in claudin-based TJs and cadherin-based AJs after DEX treatment on RPM, the number of cellular junctions examined in these experiments was not higher than that in Nthy-ori 3-1 cells.

3.4.3. Anti-Adhesion Molecules

Because neither the ECM composition nor the number of cellular junctions could explain the different response of the two cell lines to DEX treatment, we further investigated anti-adhesion effects. Thus, we examined the anti-adhesion molecule mucin-1 (MUC1), which is known to inhibit cell–cell and cell–ECM interactions [36,37].

According to the literature [38], the oncoprotein mucin-1 was more highly expressed in FTC-133 cells than in Nthy-ori 3-1 cells under static culture conditions. In FTC-133 cells, neither random positioning nor DEX treatment had any effect on mucin-1 levels (Figure 6A,B). However, immunofluorescence revealed a significant increase of mucin-1 in Nthy-ori 3-1 cells cultured on the RPM (Figure 6A,B). We also confirmed this effect for ML-1 cells (similar response to DEX as Nthy-ori 3-1), but not for WRO cells (similar response to DEX as FTC-133) (Figure S2A). Treatment with 5 μM of the MUC1-inhibitor GO-203 showed that DEX could also suppress RPM-induced spheroid formation of Nthy-ori 3-1 cells after inhibition of mucin-1 (Figure 6D). In addition, we found an attenuated ability for spheroid formation when we cultured Nthy-ori 3-1 cells in the presence of GO-203 on the RPM (Figure 6E,F). Moreover, the amount of mucin-1 in the presence of GO-203 was decreased after 72 h on the RPM (Figure 6G).

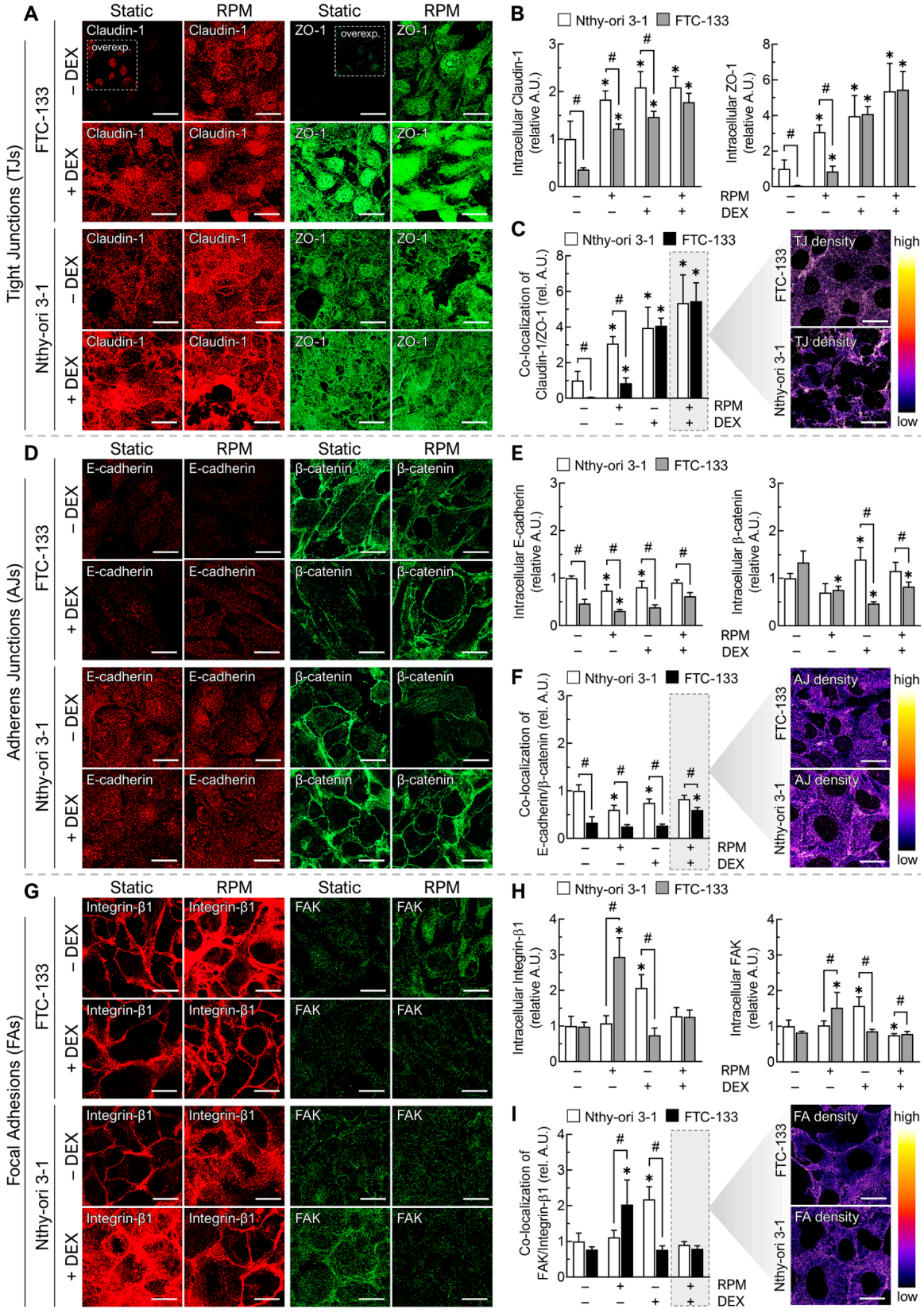

Figure 5. Effect of DEX (1000 nM) and random positioning on the cell junctions of FTC-133 and Nthy-ori 3-1 cells after 3 days. (**A**) Immunofluorescence of claudin-1 (red) and ZO-1 (green). The small inserts show low signal pictures with higher brightness; (**B**) fluorescence-based quantification

of claudin-1 and ZO-1 under the different culture conditions (n = 5); (**C**) co-localization of claudin-1 and ZO-1; (**D**) immunofluorescence of E-cadherin (red) and β-catenin (green); (**E**) fluorescence-based quantification of E-cadherin and β-catenin under the different culture conditions (n = 5); (**F**) co-localization of E-cadherin and β-catenin; (**G**) immunofluorescence of integrin-β1 (red) and FAK (green); (**H**) fluorescence-based quantification of integrin-β1 and FAK under the different culture conditions (n = 5); (**I**) co-localization of integrin-β1 and FAK. Scale bars: 300 µm. * $p < 0.05$ vs. control condition (−DEX/−RPM); # $p < 0.05$.

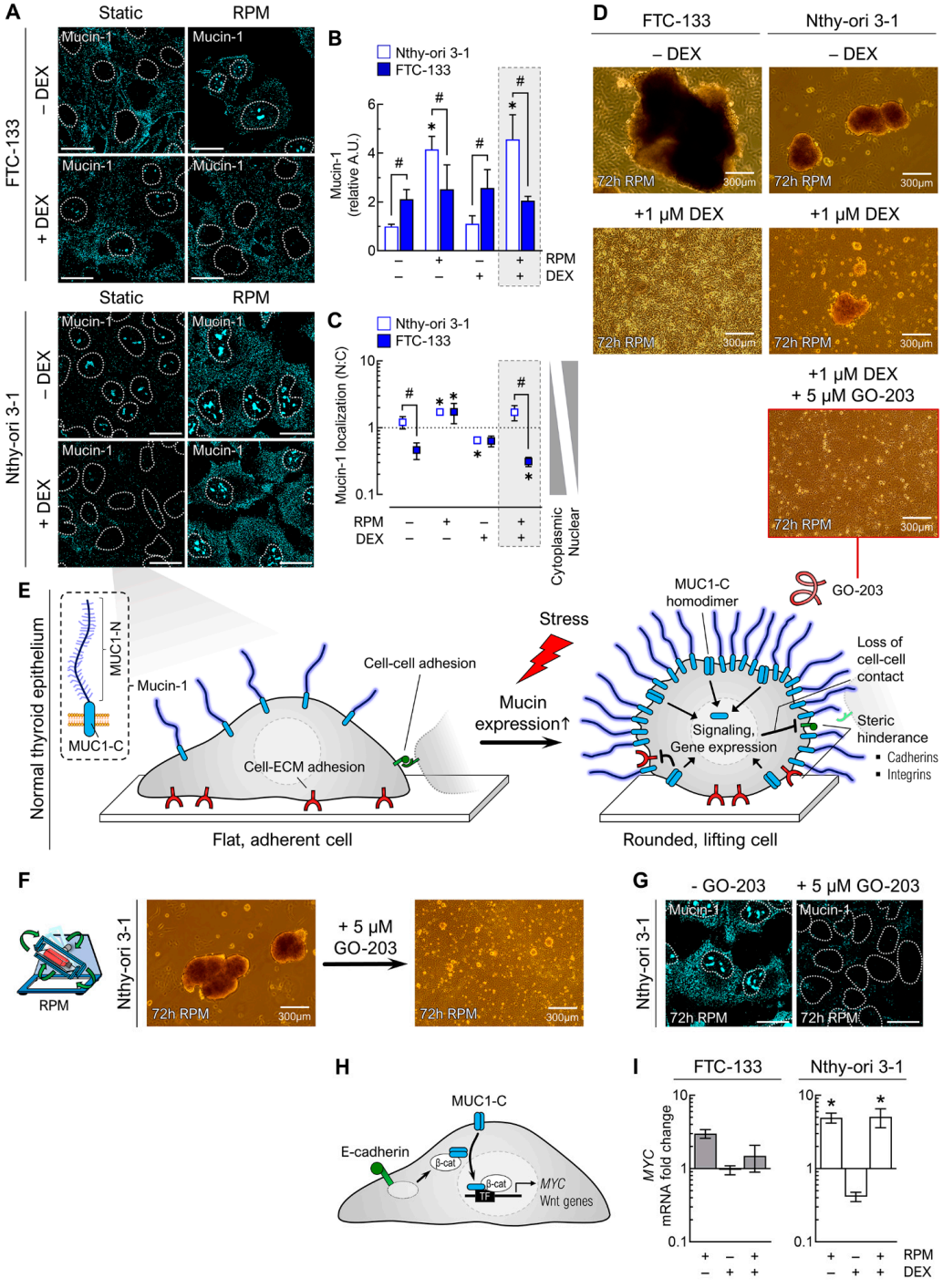

Figure 6. Effect of DEX (1 µM) and random positioning on mucin-1 in FTC-133 and Nthy-ori 3-1 cells after 3 days. (**A**) Mucin-1 immunofluorescence in adherently growing cells. Mucin-1 is shown in turquoise, with the outlines of the nuclei as dashed lines; (**B**) fluorescence-based quantification of

mucin-1 under the different culture conditions (n = 5); (**C**) nuclear localization of mucin-1 (n = 5); (**D**) spheroid formation of FTC-133 and Nthy-ori 3-1 cells in the presence of 1 µM DEX and 5 µM of the MUC1-inhibitor GO-203; (**E**) hypothetical model that could explain the anti-adhesion of Nthy-ori 3-1 cells during RPM-induced increased mucin-1 expression. Mucin-1 is a transmembrane glycoprotein consisting of two subunits, an extracellular, N-terminal highly glycosylated subunit (MUC1-N) and a C-terminal transmembrane subunit (MUC1-C). MUC1-C can form homodimers that affect cellular signaling pathways and gene expression; (**F**) spheroid formation of Nthy-ori 3-1 cells in the presence of 5 µM GO-203; (**G**) MUC-1 immunofluorescence (turquoise) of adherently growing Nthy-ori 3-1 cells in absence and presence of 5 µM GO-203. (**H**) MUC1-C activates the Wnt/β-catenin pathway and induces *MYC* expression. TF: transcription factor. (**I**) Expression levels (mRNA) of the *MYC* gene (n = 5). Scale bars: 300 µm. * $p < 0.05$ vs. control condition (−DEX/−RPM); # $p < 0.05$.

The C-terminal transmembrane subunit of mucin-1 (MUC1-C) can activate the Wnt/β-catenin pathway and induce expression of *MYC* and other Wnt genes (Figure 6H). Consistent with the immunofluorescence data of Nthy-ori 3-1 cells (Figure 6A–C), the expression of *MYC* was significantly increased on the RPM (Figure 6I).

3.5. Dexamethasone Influences Signal Transduction Pathways

3.5.1. Glucocorticoid Receptor Signaling

The main actions of DEX occur through the activation of the glucocorticoid receptor (GR, gene symbol: *NR3C1*), which is activated by phosphorylation and can actively shuttle between cytoplasm and nucleus, where it acts as a transcription factor (Figure 7C) [39]. To verify whether GR effects were responsible for the observed spheroid suppression in FTC-133 cells, we used the competitive GR inhibitor mifepristone (MIF). We found that increasing amounts of MIF (1–20 µM) in the presence of DEX (1 µM) indeed facilitated the (re-)formation of small tumor spheroids.

However, the spheroids in the presence of MIF were smaller than in the vehicle samples (Figure 7A), maybe due to its known anti-proliferative effect. Quantification of the spheroids showed very well the competitive principle of MIF and DEX: with increasing MIF concentration, the number of spheroids formed approaches of the untreated control group (Figure 7B).

With this information, we took a closer look at GR activity under random positioning and DEX treatment. Under static cell culture conditions, expression of the *NR3C1* gene was lower in FTC-133 cells (68.3%) compared to Nthy-ori 3-1 (Figure 7D). Moreover, *NR3C1* transcription in the two cell lines was affected differently by external conditions: While *NR3C1* mRNA levels in FTC-133 cells were increased by DEX, they were decreased in Nthy-ori 3-1 cells by random positioning (Figure 7E).

Western blot showed an increased GR amount in FTC-133 cells on the RPM in the absence of DEX. We also observed a generally lower amount of "activated" p-GR (Ser211) in Nthy-ori 3-1 cells and a strong increase in p-GR after the addition of DEX in both cell lines (Figure 7F,G).

In the absence of DEX, GR was mainly located in the cytoplasm near the nucleus of FTC-133 cells (Figure 7H, yellow arrows). In the presence of DEX, the amount of GR was reduced, but little was translocated to the nucleus (Figure 7H,I). GR translocation was not significantly altered by random positioning after 72 h, suggesting that the RPM has no major influence on normal GR behavior in FTCs. In Nthy-ori 3-1 cells, GR was significantly translocated to the nucleus during DEX treatment (Figure 7H,I).

At the gene expression level, the GR target genes *FKBP5* and *DUSP1* were found to be upregulated in both cell lines in the presence of DEX under both rotational and static conditions (Figure 7J).

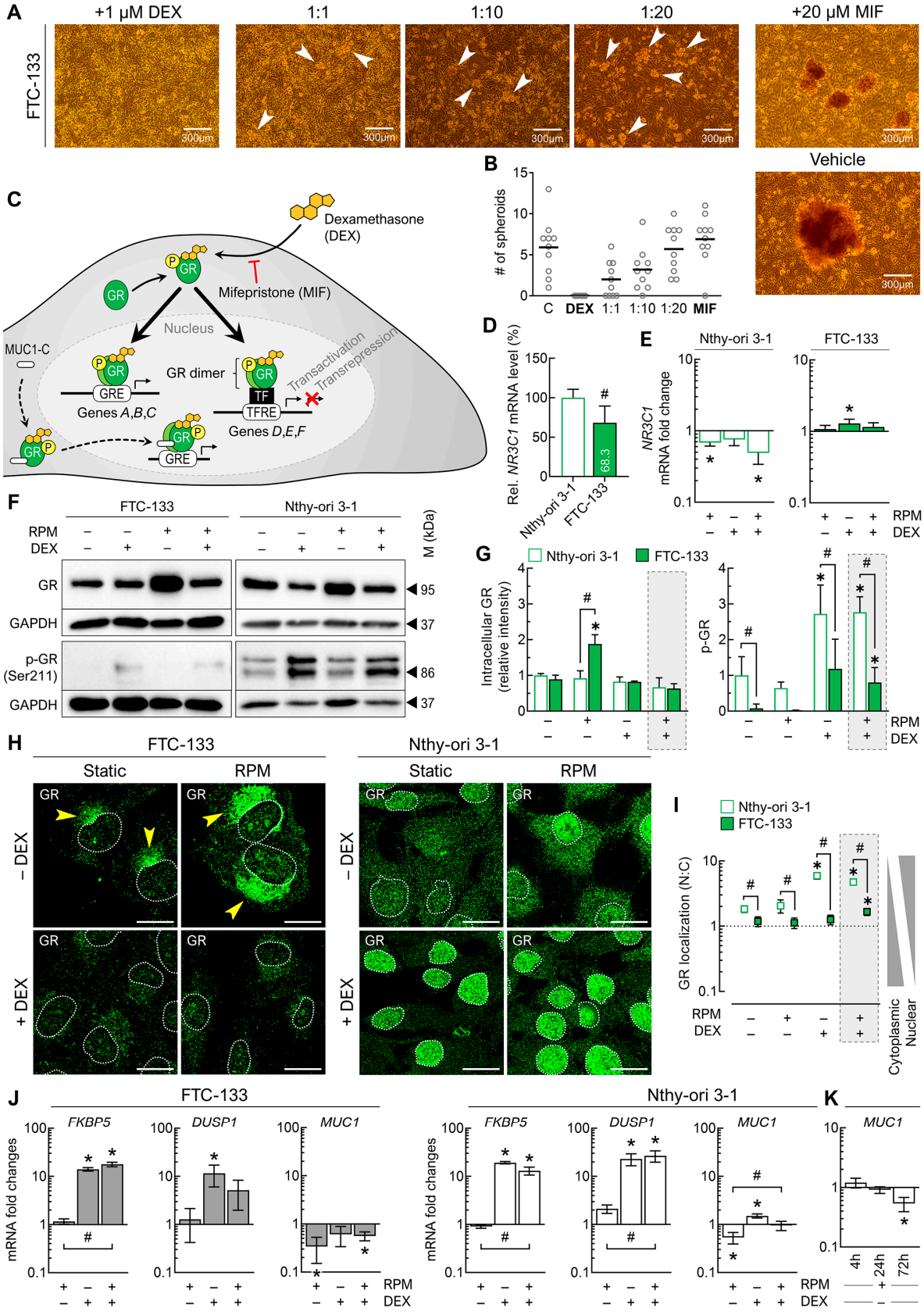

Figure 7. Effect of DEX on the glucocorticoid receptor (GR) and GR signaling in FTC-133 and Nthy-ori 3-1 cells after 3 days. (**A**) Spheroid formation (white arrows) of FTC-133 cells in the presence of 1 µM DEX and different concentrations (1–20 µM) of the competitive GR inhibitor mifepristone (MIF); (**B**) number of FTC-133 spheroids formed on the RPM in the presence of DEX and MIF

(n = 10). (**C**) Simplified schematic representation GR's mechanism of action. The genomic effects of DEX occur through its binding to GR and the movement of DEX-GR to the nucleus, where they can regulate the transcription of genes. GRE: glucocorticoid response element, TF: transcription factor, TFRE: transcription factor response element. (**D**) Expression levels (mRNA) of the *NR3C1* gene (n = 5); (**E**) fold changes of *NR3C1* expression under the different culture conditions (n = 5); (**F**) intracellular protein levels of GR and phosphorylated GR (p-GR) indicated by Western blot (see also Supplementary File S1); (**G**) densitometric quantification of Western blot proteins (n = 3); (**H**) GR immunofluorescence in adherently growing cells. GR is shown in green, with the outlines of the nuclei as dashed lines. In DEX-free FTC-133 cultures, GR is located near the nucleus (yellow arrows). (**I**) Nuclear localization of GR (n = 5); (**J**) fold changes in the expression of some signature genes of the GR pathway under the different culture conditions (n = 5); (**K**) fold changes in *MUC1* expression on the RPM after different time points (n = 5). Scale bars: 300 µm. * $p < 0.05$ vs. control condition (−DEX/−RPM); $^{\#}$ $p < 0.05$.

However, the upregulation of *DUSP1* (encoding dual specificity protein phosphatase 1) in FTC-133 cells on the RPM was lower than in the static cell culture. In addition, one other mutual target gene of GR, *MUC1* (encoding mucin-1), was downregulated in FTC-133 cells primarily by the RPM, whereas in Nthy-ori 3-1 cells it was decreased by random positioning but also upregulated by DEX (Figure 7J). The observed overexpression of mucin-1 protein in Nthy-ori 3-1 cells on the RPM (Figure 6A) could be explained by a transient upregulation of *MUC1* and subsequent negative feedback after 72 h (Figure 7K).

Since a large percentage of GR binding sites is known to be hypoxia-specific [40–42] and we needed to work with completely filled cell culture flasks for random positioning, we also checked whether there was a gene expression response to hypoxia via hypoxia-inducible factor 1α (HIF1A). We found that *HIF1A* expression was upregulated only in Nthy-ori 3-1 cells when the culture flasks were completely filled (Figure S3). This change was independent of RPM exposure or DEX treatment.

3.5.2. Cell Stress Signaling

A crosstalk between GR and p38 mitogen-activated protein kinase (MAPK) was reported earlier [43–45]. p38 (gene symbol: *MAPK14*) can be activated by phosphorylation through mechanical forces [46] and then either accelerates the activation of GR or migrates to the nucleus, where it can itself affect various transcription factors and thus control the expression of numerous genes (Figure 8A). *MAPK14* was expressed about three-fold higher in the cancer cells (Figure 8B), and transcription was upregulated by DEX treatment in both FTC-133 cells and Nthy-ori 3-1 cells. However, downregulation of *MAPK14* by random positioning was also observed in FTCs (Figure 8C).

The p38 protein levels were generally higher in Nthy-ori 3-1 cells compared with FTC-133 cells and were not significantly affected by DEX treatment or the RPM. Phosphorylated p-p38 (Thr180, Tyr182), which can be transferred to the nucleus, was significantly increased in FTC-133 cells on the RPM without DEX and significantly decreased after DEX treatment. In Nthy-ori 3-1 cells, p-p38 levels were not altered by DEX or by random positioning (Figure 8D,E).

Under static cell culture conditions, p38 was mainly located in the cytoplasm of FTC-133 cells, whereas on the RPM, p38 was shifted into the nucleus. This translocation did not occur in the presence of DEX. In contrast, in Nthy-ori 3-1 cells, p38 was shifted into the nucleus only in the presence of DEX (Figure 8F). Thus, we found a strong activation of the p38 pathway during random positioning in FTC-133 cells without DEX and a slight activation of this pathway in Nthy-ori 3-1 cells with DEX (Figure 8G).

Genes under the control of p38 include *IL6*, *CXCL8* and *IL1B*. Consistent with the nuclear localization of p38, all three genes were upregulated on the RPM in FTC-133 cells, and for *IL6* and *CXCL8* we found attenuation of the mRNA levels on the RPM in the presence of DEX. In Nthy-ori 3-1 cells, gene expression was not affected by the RPM alone, but *IL6* and *IL1B* were downregulated on the RPM in the presence of DEX (Figure 8H).

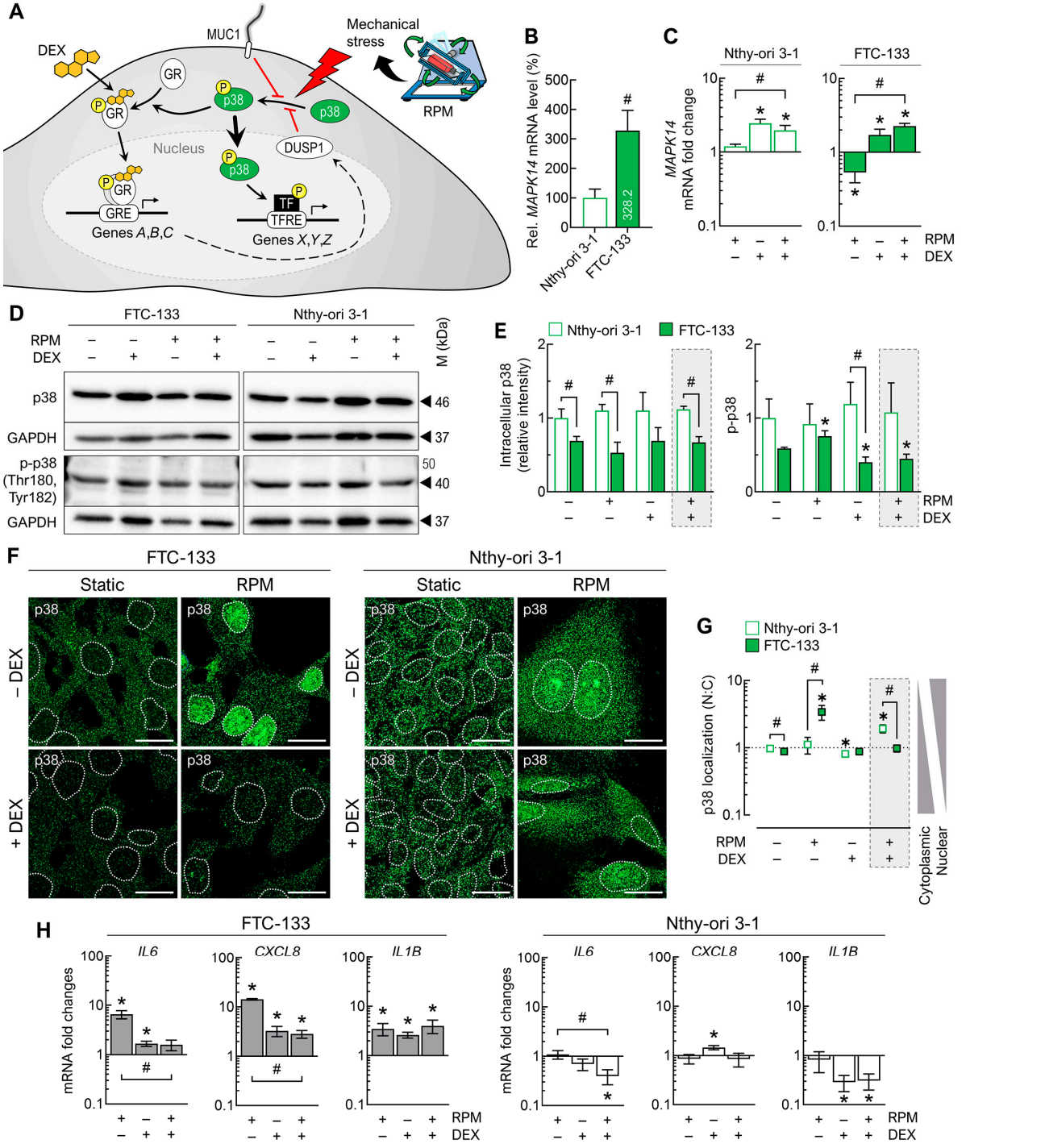

Figure 8. Effect of DEX on p38 MAPK and p38 signaling in FTC-133 and Nthy-ori 3-1 cells after 3 days. (**A**) Simplified schematic representation of p38′s mechanism of action. GRE: glucocorticoid response element, TF: transcription factor, TFRE: transcription factor response element. (**B**) Expression levels (mRNA) of the *MAPK14* gene ($n = 5$); (**C**) fold changes of *MAPK14* expression under the different culture conditions ($n = 5$); (**D**) intracellular protein levels of p38 and phosphorylated p38 (p-p38) indicated by Western blot (see also Supplementary File S1); (**E**) densitometric quantification of Western blot proteins ($n = 3$); (**F**) p38 immunofluorescence in adherently growing cells. p38 is shown in green, with the outlines of the nuclei as dashed lines. (**G**) Nuclear localization of p38 ($n = 5$); (**H**) fold changes in the expression of some mutual signature genes of the p38 pathway under the different culture conditions ($n = 5$). Scale bars: 300 µm. * $p < 0.05$ vs. control condition (−DEX/−RPM); $^{\#}$ $p < 0.05$.

4. Discussion

In this study, we showed that DEX is not only able to suppress RPM-induced spheroid formation of FTC-133 follicular thyroid cancer cells, but this inhibition was selective for two metastatic thyroid carcinoma cells, WRO and FTC-133, whereas benign Nthy-ori 3-1 cells and recurrent ML-1 thyroid cancer cells were not affected by DEX.

4.1. Effects of Dexamethasone

DEX is commonly used in clinical practice to treat side effects such as nausea and vomiting caused by chemotherapy. Wu et al. [47] pointed out that DEX itself is able to inhibit tumor cells in vitro and in vivo. That DEX may also have an anti-metastatic effect is supported by several findings. In a recent study, DEX not only decreased the viability of T47D human breast cancer cells in a time- and dose-dependent manner, but also reduced their cell adhesion and migration. This effect was explained by the altered expression of α-/β-integrin, E-/N-cadherin and MMP-2/-9 in response to DEX treatment [48]. Other authors described a disruption of dynamic cytoskeletal organization in these cells when they were treated with DEX [49]. Lin et al. [50,51] previously observed suppression of ovarian cancer metastasis by DEX. In human bladder cancer cells, suppression of MMP-2, MMP-9 and IL-6 expression, as well as induction of mesenchymal-to-epithelial transition (MET were found in the presence of DEX [52]. Therefore, the described effects of DEX on the RPM metastasis model are not entirely unfounded.

Control of GR by PTEN (phosphatase and tensin homolog) appears to be a fail-safe mechanism for tumor suppression [53]. The loss of PTEN activity in FTC-133 cells might affect GR levels, which could explain the lower translocation of GR into the nucleus of FTC-133 cells in the presence of DEX. In endothelial cells, shear stress led to nuclear localization of GR and consequent expression from the GRE promoter [54,55]. This we could not detect with our thyroid cells on the RPM. While the RPM seems to play a rather minor role in YAP1/Hippo signaling in the adherent cell population, FTC-133 cells responded to random positioning with strong activation of p38. This p38 stress signaling in FTC-133 cells could be inactivated by DEX, maybe due to the kinase activity of GR-induced DUSP1, which was upregulated after DEX treatment. In comparison, Nthy-ori 3-1 cells also activated p38 on the RPM but to a lesser extent and without sensitivity to DEX. Thus, DEX directly interferes with RPM-induced stress signaling via p38 in FTC-133 cells and antagonizes a variety of gene expressions and cell functions according to the multiple transcriptional substrates of p38 [56].

4.2. RPM-Induced Spheroid Formation and Its Inhibition by Dexamethasone

It has been previously reported in the literature that both healthy (Nthy-ori 3-1) and low-differentiated follicular thyroid cancer cells (ML-1, FTC-133, and WRO) form spheroids on the RPM within 24 h [57–62]. All these cells required a lag time of several hours before some of the cells detached from the bottom of the culture flask and assembled into 3D aggregates, while others remained attached. According to the latest comparison by Warnke et al. [58], no striking difference was found between healthy and cancer cells with respect to morphological changes induced by random positioning. It was therefore even more surprising that DEX specifically inhibits the spheroid formation of metastatic thyroid carcinoma cells on the RPM. This suggests that the RPM-induced spheroid formation of the different cell types may not be identical. To date, very few studies have addressed the question of how spheroid formation on the RPM is affected by drugs or the targeted blocking of functional proteins (Table 1). Therefore, it is very difficult to obtain insightful data from this works.

Table 1. Other studies on targeting RPM-induced spheroid formation of cancer cells.

Cell Line	Drug	Main Findings	Reference
FTC-133	Dexamethasone	Inhibition of spheroid formation.	[31]
MCF-7	Dexamethasone Rolipram Olaparib	Reduced spheroid formation. No effects. No effects.	[63]
MCF-7	PP2 anti-E-cadherin	Inhibition of spheroid formation. Increased spheroid formation.	[64]

Some years ago, Lin and Wang [65] summarized the use of glucocorticoids in cancer treatment. In their literature review, they found different effects, in particular that glucocorticoid treatment could promote the growth of malignant solid tumors in certain cancers, while playing a suppressive role in tumor progression and metastasis in other cancers. They concluded that simple cellular experimental models are not sufficient to accurately predict therapeutic outcome in vivo [65]. According to the current literature, space science-derived RPM [66,67] enables a complex, though not yet fully understood, in vitro model for adherent cancer cell metastasis [19–21,68]. Since RPM also promotes 3D growth of other benign cells, it is understandable that there must be some differences between spheroid and tumor spheroid formation, although the visible result is the same in the end. Comparisons between FTC-133 and Nthy-ori 3-1 RPM cell cultures have been performed in the past. Kopp et al. [57] suggested that growth and angiogenic factors may be responsible for the differences in RPM-induced spheroid formation between malignant and healthy thyroid cells. Warnke et al. [58,59] confirmed the involvement of cytokines and focal adhesion proteins during the RPM culture of both cell lines. However, these comparisons were primarily related to gene and protein expression of markers with a focus on the response to altered gravity conditions. In this study, we took a more functional phenotypic approach to explain why benign thyroid cells respond differently to DEX on the RPM treatment than the corresponding carcinoma cells. In this way, we could determine that the adhesion of tumor and healthy thyroid cells on the RPM is affected differently.

We observed, under normal culture conditions, that DEX increased the adhesion of both cell types. This can be explained, on the one hand, by the increased expression of fibronectin (only in Nthy-ori 3-1 cells) and, on the other hand, by an increased formation of TJs, which was particularly observed in metastatic FTC-133 and WRO cells. Glucocorticoid-induced TJ formation and re-organization has been previously described and studied in mouse mammary epithelial cells [69,70] and in preclinical human intestinal models (summarized in [71]). In our experiments, the RPM also increased the expression of TJ proteins claudin-1 and ZO-1, as well as the formation of TJs, which had an enhancing effect when combined with DEX treatment. In a clinorotation experiment with MCF-7 breast cancer cells, Adamian et al. [72] recently observed similar increases in claudin-1 and claudin-3 after 72 h.

It is known that changes in the expression and/or distribution of TJ proteins can lead to a loss of cohesion of the TJ structure. This, in turn, gives cancer cells the ability to invade and ultimately metastasize [73]. In general, low expression of TJs is observed in highly metastatic cancer cells [74], and dedifferentiation of thyroid carcinomas is associated with a decrease in claudin-1, -4, and -7 expression [75]. In FTC-133 cells, our data confirmed low TJ protein expression. However, intracellular localization of claudins is also important, as pure overexpression of non-junctional nuclear claudin-1 in FTC-133 cells led to increased cell migration and invasion [76].

In addition, we also found an increase in AJs in FTC-133 when the cells were treated with DEX on the RPM. AJs have a similar structural organization to TJs: cadherins form contacts with catenins, and these complexes connect the cell surface to the cytoskeleton. In particular, decreased expression or loss of cadherins has been associated with epithelial tumor development, invasion and metastasis [77]. In addition, for the RPM metastasis

model, Sahana et al. [64] found that blocking E-cadherin with an antibody increased the tumor spheroid formation of MCF-7 cells. In thyroid cancer, E-cadherin expression is considered a potential predictive factor for clinical disease progression [78]. Huang et al. [79] reported that the loss of cell adhesion in CGTH W-2 thyroid cancer cells compared with healthy thyrocytes may be due to the incomplete assembly of the cadherin–catenin complexes at the cell membrane. Thus, an increase in assembled AJs, as we have seen from the co-localization of E-cadherin and β-catenin, could also lead to enhanced cell adhesion.

Therefore, it is reasonable to speculate that the increased number of TJs and AJs, especially in FTC-133 cells, could cause a reduction in cell migration after DEX treatment on the RPM, which then leads to the inhibition of tumor spheroid formation. In addition, it would be important to clarify whether the increased occurrence of cell–cell junctions influences the detachment behavior of the cancer cells. It is possible that coherent aggregates of cells, rather than individual cells, detach. For this investigation, an RPM microscope would have to be available, which is currently not the case. Furthermore, this alone does not answer the question of why RPM-induced spheroid formation of healthy Nthy-ori 3-1 cells is not inhibited by DEX, where the amount of ECM proteins and cell junctions is as high or higher than in FTC-133 cells.

4.3. Spheroids from Healthy Cells on the RPM—A Question of Anti-Adhesion?

Cell surface-associated mucins such as mucin-1 are involved in the protection of epithelial surfaces from mechanical stress [80]. This protection program seems to be activated in adherent Nthy-ori 3-1 and ML-1 cells on the RPM, but not in FTC-133 and WRO cells. Because mucin-1 was upregulated in Nthy-ori 3-1 cells only in the RPM samples (not by DEX alone), a hypoxia-induced effect, which has been described in other epithelial cells for other mucins [81], can be excluded here. One possibility could be RPM-induced expression of *MUC1* via STAT3, as recently described in chondrocytes [82]. Due to steric hindrance of mucin-1 and adhesion proteins, overexpressed mucin-1 has an anti-adhesion effect on cells [83]. Intracellularly, it leads to loss of cell–cell contact and induces anchorage-independent growth including resistance to anoikis [84,85]. Both effects could favor the detachment of Nthy-ori 3-1 cells during random positioning, which show much stronger adhesion than metastatic FTC-133 cells under normal culture conditions (Figure 3D). They could even allow the formation of spheroids from cells that would otherwise not detach during random positioning, or undergo anoikis after detachment. Indeed, the absence of such an unexpected mucin-1 increase may explain why not all benign or primary human cells readily form 3D structures on the RPM. Spheroid formation on the RPM is more frequently observed in tumor cells, which tend to spread or migrate and generally have higher mucin expression [86]. One of the best-known example pairs studied so far on the RPM is probably MCF-7 mammary tumor cells and MCF-10A mammary epithelial cells. Monti et al. [86] showed that only MCF-7 cells formed spheroids on the RPM after 72 h. In addition, we found by immunofluorescence analysis that MCF-10A cells expressed very little mucin-1 protein (Figure S2B). Triple-negative MDA-MB-231 cells, which also have very low levels of mucin-1 [87], tend to adhere to culture flasks on the RPM rather than detach (unpublished data). It is also known that *MUC1* gene expression in prostate cancer cells is inhibited by the androgen receptor (AR) [88]. In some of our preliminary experiments, AR-positive LnCAP cells detached less from the growth surface after administration of dihydrotestosterone. Mucin-1 immunofluorescence staining confirmed a decrease in protein amount in the presence of dihydrotestosterone (Figure S2C). In addition, RPM-induced spheroid formation was observed to be absent in some primary endothelial cells. While human umbilical vein endothelial cells (HUVECs) are able to form 3D aggregates, this does not work for human saphenous vein endothelial cells (HSVECs) under RPM conditions [89]. At least for HUVECs, it was demonstrated that mucin-1 is expressed and can be released from the cell membrane [90]. However, we could not find any information about mucin-1 in HSVECs so far.

In this study, we attempted to target mucin-1 pharmaceutically. Although GO-203 is primarily an inhibitor of MUC1-C and thus blocks its intracellular signaling, an auto-inductive effect that has been described for mucin-1 [91] could explain the reduction of (surface) mucin-1 observed after supplementation of GO-203 (Figure 6G).

In summary, it seems important to note that not only adhesion proteins play a role in RPM-induced spheroid formation, but also anti-adhesion proteins.

5. Conclusions

For gravitational biologists, the RPM offers a good platform to study tumor progression or metastasis in vitro and to uncover special targets for cancer therapy [19–21,68]. In this study, we could show that RPM-grown thyroid cancer cells behave differently than corresponding benign epithelial cells when treated with DEX. Comparative analyses showed that the cell detachment process (which is often referred to as 'in vitro metastasis') during random positioning is selectively suppressed by DEX in metastatic cancer cells; on the one hand, due to massive formation of TJs in these cells, and, on the other hand, due to the upregulation of anti-adhesive mucin-1 in their non-metastasis-derived relatives by the RPM. The overall picture of an initially hypothesized anti-metastasis effect of DEX in vitro emerged from an interplay of different effects of the cells, all of which responded differently to RPM cell culture. The balance between adhesion and anti-adhesion appears to allow detachment of adherent human cells on an RPM. This depends on the origin of the cells, their development, and their consequent susceptibility to stress. Therefore, it will continue to be very important to study exactly how human cells behave in rotating bioreactors in order to derive the maximum benefit from these model systems for translational medicine.

Supplementary Materials: The following supporting information can be downloaded at: https://www.mdpi.com/article/10.3390/cancers15061641/s1, Figure S1: Effect of DEX (1000 nM) and random positioning on tight junction proteins after 3 days; Figure S2: Mucin-1 expression in relation to cell adhesion of different cell lines in RPM experiments; Figure S3: Oxygen saturation and hypoxia-induced expression of *HIF1A* in completely filled cell culture flasks; Table S1: Antibodies used for immunofluorescence and Western blot analyses; Table S2: Primer sequences for quantitative real-time PCR. File S1: Full-size Western blots.

Author Contributions: Conceptualization, D.M. and M.K.; methodology, D.M., V.S., J.L.C.-S. and M.K.; software, J.L.C.-S., D.M. and S.K. (Stefan Kahlert); validation, D.M., S.K. (Sascha Kopp) and M.K.; formal analysis, D.M. and J.L.C.-S.; investigation, D.M., V.S. and J.L.C.-S.; resources, D.G.; data curation, D.M. and M.K.; writing—original draft preparation, D.M. and M.K.; writing—review and editing, M.K. and D.G.; visualization, D.M., J.L.C.-S. and M.K.; supervision, M.K.; funding acquisition, D.G. All authors have read and agreed to the published version of the manuscript.

Funding: This research was funded by the German Space Agency at DLR (Deutsches Zentrum für Luft- und Raumfahrt) under grant numbers 50WB1924 and 50WB2219. J.L.C.-S. received financial support from the CONACyT-DAAD scholarship.

Institutional Review Board Statement: Not applicable.

Informed Consent Statement: Not applicable.

Data Availability Statement: The data presented in this study are available in the electronic Supplementary Material. The complete raw data are available on request.

Acknowledgments: We would like to thank Jenny Graf for further insights into mucin-1 expression in additional cell lines.

Conflicts of Interest: The authors declare no conflict of interest. The funders had no role in the design of the study; in the collection, analyses, or interpretation of data; in the writing of the manuscript, or in the decision to publish the results.

References

1. Steeg, P.S. Targeting metastasis. *Nat. Rev. Cancer* **2016**, *16*, 201–218. [CrossRef] [PubMed]
2. Hapach, L.A.; Mosier, J.A.; Wang, W.; Reinhart-King, C.A. Engineered models to parse apart the metastatic cascade. *NPJ Precis. Oncol.* **2019**, *3*, 20. [CrossRef]
3. Lara, O.D.; Wang, Y.; Asare, A.; Xu, T.; Chiu, H.-S.; Liu, Y.; Hu, W.; Sumazin, P.; Uppal, S.; Zhang, L.; et al. Pan-cancer clinical and molecular analysis of racial disparities. *Cancer* **2020**, *126*, 800–807. [CrossRef]
4. Galle, E.; Thienpont, B.; Cappuyns, S.; Venken, T.; Busschaert, P.; Van Haele, M.; Van Cutsem, E.; Roskams, T.; van Pelt, J.; Verslype, C.; et al. DNA methylation-driven EMT is a common mechanism of resistance to various therapeutic agents in cancer. *Clin. Epigenet.* **2020**, *12*, 27. [CrossRef]
5. Wirtz, D.; Konstantopoulos, K.; Searson, P.C. The physics of cancer: The role of physical interactions and mechanical forces in metastasis. *Nat. Rev. Cancer* **2011**, *11*, 512–522. [CrossRef]
6. Northcott, J.M.; Dean, I.S.; Mouw, J.K.; Weaver, V.M. Feeling Stress: The Mechanics of Cancer Progression and Aggression. *Front. Cell Dev. Biol.* **2018**, *6*, 17. [CrossRef]
7. Kumar, S.; Weaver, V.M. Mechanics, malignancy, and metastasis: The force journey of a tumor cell. *Cancer Metastasis Rev.* **2009**, *28*, 113–127. [CrossRef] [PubMed]
8. Kalluri, R.; Weinberg, R.A. The basics of epithelial-mesenchymal transition. *J. Clin. Investig.* **2009**, *119*, 1420–1428. [CrossRef]
9. Guck, J.; Schinkinger, S.; Lincoln, B.; Wottawah, F.; Ebert, S.; Romeyke, M.; Lenz, D.; Erickson, H.M.; Ananthakrishnan, R.; Mitchell, D.; et al. Optical deformability as an inherent cell marker for testing malignant transformation and metastatic competence. *Biophys. J.* **2005**, *88*, 3689–3698. [CrossRef] [PubMed]
10. Yan, Z.; Xia, X.; Cho, W.C.; Au, D.W.; Shao, X.; Fang, C.; Tian, Y.; Lin, Y. Rapid Plastic Deformation of Cancer Cells Correlates with High Metastatic Potential. *Adv. Healthc. Mater.* **2022**, *11*, 2101657. [CrossRef]
11. Baker, E.L.; Lu, J.; Yu, D.; Bonnecaze, R.T.; Zaman, M.H. Cancer Cell Stiffness: Integrated Roles of Three-Dimensional Matrix Stiffness and Transforming Potential. *Biophys. J.* **2010**, *99*, 2048–2057. [CrossRef] [PubMed]
12. Wullkopf, L.; West, A.-K.V.; Leijnse, N.; Cox, T.R.; Madsen, C.D.; Oddershede, L.B.; Erler, J.T. Cancer cells' ability to mechanically adjust to extracellular matrix stiffness correlates with their invasive potential. *Mol. Biol. Cell* **2018**, *29*, 2378–2385. [CrossRef]
13. Gensbittel, V.; Kräter, M.; Harlepp, S.; Busnelli, I.; Guck, J.; Goetz, J.G. Mechanical Adaptability of Tumor Cells in Metastasis. *Dev. Cell* **2021**, *56*, 164–179. [CrossRef] [PubMed]
14. Borst, A.G.; van Loon, J.J.W.A. Technology and Developments for the Random Positioning Machine, RPM. *Microgravity Sci. Technol.* **2008**, *21*, 287. [CrossRef]
15. van Loon, J.J.W.A. Some history and use of the random positioning machine, RPM, in gravity related research. *Adv. Space Res.* **2007**, *39*, 1161–1165. [CrossRef]
16. Hauslage, J.; Cevik, V.; Hemmersbach, R. Pyrocystis noctiluca represents an excellent bioassay for shear forces induced in ground-based microgravity simulators (clinostat and random positioning machine). *NPJ Microgravity* **2017**, *3*, 12. [CrossRef] [PubMed]
17. Leguy, C.A.D.; Delfos, R.; Pourquie, M.J.B.M.; Poelma, C.; Westerweel, J.; van Loon, J.J.W.A. Fluid dynamics during Random Positioning Machine micro-gravity experiments. *Adv. Space Res.* **2017**, *59*, 3045–3057. [CrossRef]
18. Wuest, S.L.; Stern, P.; Casartelli, E.; Egli, M. Fluid Dynamics Appearing during Simulated Microgravity Using Random Positioning Machines. *PLoS ONE* **2017**, *12*, e0170826. [CrossRef]
19. Cortés-Sánchez, J.L.; Callant, J.; Krüger, M.; Sahana, J.; Kraus, A.; Baselet, B.; Infanger, M.; Baatout, S.; Grimm, D. Cancer Studies under Space Conditions: Finding Answers Abroad. *Biomedicines* **2021**, *10*, 25. [CrossRef]
20. Krüger, M.; Melnik, D.; Kopp, S.; Buken, C.; Sahana, J.; Bauer, J.; Wehland, M.; Hemmersbach, R.; Corydon, T.J.; Infanger, M.; et al. Fighting Thyroid Cancer with Microgravity Research. *Int. J. Mol. Sci.* **2019**, *20*, 2553. [CrossRef]
21. Grimm, D.; Schulz, H.; Krüger, M.; Cortés-Sánchez, J.L.; Egli, M.; Kraus, A.; Sahana, J.; Corydon, T.J.; Hemmersbach, R.; Wise, P.M.; et al. The Fight against Cancer by Microgravity: The Multicellular Spheroid as a Metastasis Model. *Int. J. Mol. Sci.* **2022**, *23*, 3073. [CrossRef]
22. Riehl, B.D.; Kim, E.; Lee, J.S.; Duan, B.; Yang, R.; Donahue, H.J.; Lim, J.Y. The Role of Fluid Shear and Metastatic Potential in Breast Cancer Cell Migration. *J. Biomech. Eng.* **2020**, *142*, 101001. [CrossRef] [PubMed]
23. Qazi, H.; Palomino, R.; Shi, Z.D.; Munn, L.L.; Tarbell, J.M. Cancer cell glycocalyx mediates mechanotransduction and flow-regulated invasion. *Integr. Biol.* **2013**, *5*, 1334–1343. [CrossRef] [PubMed]
24. Rizvi, I.; Gurkan, U.A.; Tasoglu, S.; Alagic, N.; Celli, J.P.; Mensah, L.B.; Mai, Z.; Demirci, U.; Hasan, T. Flow induces epithelial-mesenchymal transition, cellular heterogeneity and biomarker modulation in 3D ovarian cancer nodules. *Proc. Natl. Acad. Sci. USA* **2013**, *110*, E1974–E1983. [CrossRef] [PubMed]
25. Liu, S.; Zhou, F.; Shen, Y.; Zhang, Y.; Yin, H.; Zeng, Y.; Liu, J.; Yan, Z.; Liu, X. Fluid shear stress induces epithelial-mesenchymal transition (EMT) in Hep-2 cells. *Oncotarget* **2016**, *7*, 32876–32892. [CrossRef] [PubMed]
26. Choi, H.Y.; Yang, G.M.; Dayem, A.A.; Saha, S.K.; Kim, K.; Yoo, Y.; Hong, K.; Kim, J.H.; Yee, C.; Lee, K.M.; et al. Hydrodynamic shear stress promotes epithelial-mesenchymal transition by downregulating ERK and GSK3β activities. *Breast Cancer Res.* **2019**, *21*, 6. [CrossRef]
27. Ahn, C.B.; Lee, J.-H.; Han, D.G.; Kang, H.-W.; Lee, S.-H.; Lee, J.-I.; Son, K.H.; Lee, J.W. Simulated microgravity with floating environment promotes migration of non-small cell lung cancers. *Sci. Rep.* **2019**, *9*, 14553. [CrossRef]

28. Wehland, M.; Steinwerth, P.; Aleshcheva, G.; Sahana, J.; Hemmersbach, R.; Lützenberg, R.; Kopp, S.; Infanger, M.; Grimm, D. Tissue Engineering of Cartilage Using a Random Positioning Machine. *Int. J. Mol. Sci.* **2020**, *21*, 9596. [CrossRef]
29. Grimm, D.; Infanger, M.; Westphal, K.; Ulbrich, C.; Pietsch, J.; Kossmehl, P.; Vadrucci, S.; Baatout, S.; Flick, B.; Paul, M.; et al. A Delayed Type of Three-Dimensional Growth of Human Endothelial Cells Under Simulated Weightlessness. *Tissue Eng. Part A* **2009**, *15*, 2267–2275. [CrossRef]
30. Buken, C.; Sahana, J.; Corydon, T.J.; Melnik, D.; Bauer, J.; Wehland, M.; Krüger, M.; Balk, S.; Abuagela, N.; Infanger, M.; et al. Morphological and Molecular Changes in Juvenile Normal Human Fibroblasts Exposed to Simulated Microgravity. *Sci. Rep.* **2019**, *9*, 11882. [CrossRef]
31. Melnik, D.; Sahana, J.; Corydon, T.J.; Kopp, S.; Nassef, M.Z.; Wehland, M.; Infanger, M.; Grimm, D.; Krüger, M. Dexamethasone Inhibits Spheroid Formation of Thyroid Cancer Cells Exposed to Simulated Microgravity. *Cells* **2020**, *9*, 367. [CrossRef] [PubMed]
32. Schönberger, J.; Bauer, J.; Spruss, T.; Weber, G.; Chahoud, I.; Eilles, C.; Grimm, D. Establishment and characterization of the follicular thyroid carcinoma cell line ML-1. *J. Mol. Med.* **2000**, *78*, 102–110. [CrossRef] [PubMed]
33. Benavides Damm, T.; Walther, I.; Wüest, S.L.; Sekler, J.; Egli, M. Cell cultivation under different gravitational loads using a novel random positioning incubator. *Biotechnol. Bioeng.* **2014**, *111*, 1180–1190. [CrossRef]
34. Shihan, M.H.; Novo, S.G.; Le Marchand, S.J.; Wang, Y.; Duncan, M.K. A simple method for quantitating confocal fluorescent images. *Biochem. Biophys. Rep.* **2021**, *25*, 100916. [CrossRef] [PubMed]
35. Gottardi, C.J.; Arpin, M.; Fanning, A.S.; Louvard, D. The junction-associated protein, zonula occludens-1, localizes to the nucleus before the maturation and during the remodeling of cell-cell contacts. *Proc. Natl. Acad. Sci. USA* **1996**, *93*, 10779–10784. [CrossRef]
36. Wesseling, J.; van der Valk, S.W.; Hilkens, J. A mechanism for inhibition of E-cadherin-mediated cell-cell adhesion by the membrane-associated mucin episialin/MUC1. *Mol. Biol. Cell* **1996**, *7*, 565–577. [CrossRef]
37. Wesseling, J.; van der Valk, S.W.; Vos, H.L.; Sonnenberg, A.; Hilkens, J. Episialin (MUC1) overexpression inhibits integrin-mediated cell adhesion to extracellular matrix components. *J. Cell Biol.* **1995**, *129*, 255–265. [CrossRef]
38. Nath, S.; Mukherjee, P. MUC1: A multifaceted oncoprotein with a key role in cancer progression. *Trends Mol. Med.* **2014**, *20*, 332–342. [CrossRef]
39. Scheschowitsch, K.; Leite, J.; Assreuy, J. New insights in glucocorticoid receptor signaling—More than just a ligand binding receptor. *Front. Endocrinol.* **2017**, *8*, 16. [CrossRef]
40. Vanderhaeghen, T.; Timmermans, S.; Watts, D.; Paakinaho, V.; Eggermont, M.; Vandewalle, J.; Wallaeys, C.; Van Wyngene, L.; Van Looveren, K.; Nuyttens, L.; et al. Reprogramming of glucocorticoid receptor function by hypoxia. *EMBO Rep.* **2022**, *23*, e53083. [CrossRef]
41. Vanderhaeghen, T.; Beyaert, R.; Libert, C. Bidirectional Crosstalk Between Hypoxia Inducible Factors and Glucocorticoid Signalling in Health and Disease. *Front. Immunol.* **2021**, *12*, 684085. [CrossRef]
42. Yang, N.; Berry, A.; Sauer, C.; Baxter, M.; Donaldson, I.J.; Forbes, K.; Donn, R.; Matthews, L.; Ray, D. Hypoxia regulates GR function through multiple mechanisms involving microRNAs 103 and 107. *Mol. Cell. Endocrinol.* **2020**, *518*, 111007. [CrossRef] [PubMed]
43. Lea, S.; Li, J.; Plumb, J.; Gaffey, K.; Mason, S.; Gaskell, R.; Harbron, C.; Singh, D. P38 MAPK and glucocorticoid receptor crosstalk in bronchial epithelial cells. *J. Mol. Med.* **2020**, *98*, 361–374. [CrossRef]
44. Szatmáry, Z.; Garabedian, M.J.; Vilček, J. Inhibition of Glucocorticoid Receptor-mediated Transcriptional Activation by p38 Mitogen-activated Protein (MAP) Kinase. *J. Biol. Chem.* **2004**, *279*, 43708–43715. [CrossRef]
45. Irusen, E.; Matthews, J.G.; Takahashi, A.; Barnes, P.J.; Chung, K.F.; Adcock, I.M. p38 Mitogen-activated protein kinase–induced glucocorticoid receptor phosphorylation reduces its activity: Role in steroid-insensitive asthma. *J. Allergy Clin. Immunol.* **2002**, *109*, 649–657. [CrossRef]
46. Hoffman, L.; Jensen, C.C.; Yoshigi, M.; Beckerle, M. Mechanical signals activate p38 MAPK pathway-dependent reinforcement of actin via mechanosensitive HspB1. *Mol. Biol. Cell* **2017**, *28*, 2661–2675. [CrossRef]
47. Wu, Y.; Xia, R.; Dai, C.; Yan, S.; Xie, T.; Liu, B.; Gan, L.; Zhuang, Z.; Huang, Q. Dexamethasone inhibits the proliferation of tumor cells. *Cancer Manag. Res.* **2019**, *11*, 1141–1154. [CrossRef] [PubMed]
48. Mohammadi, L.; Mosayyebi, B.; Imani, M.; Rahmati, M. Dexamethasone Reduces Cell Adhesion and Migration of T47D Breast Cancer Cell Line. *Anticancer Agents Med. Chem.* **2022**, *22*, 2494–2501. [CrossRef] [PubMed]
49. Meng, X.G.; Yue, S.W. Dexamethasone disrupts cytoskeleton organization and migration of T47D Human breast cancer cells by modulating the AKT/mTOR/RhoA pathway. *Asian Pac. J. Cancer Prev.* **2014**, *15*, 10245–10250. [CrossRef] [PubMed]
50. Lin, K.-T.; Sun, S.-P.; Wu, J.-I.; Wang, L.-H. Low-dose glucocorticoids suppresses ovarian tumor growth and metastasis in an immunocompetent syngeneic mouse model. *PLoS ONE* **2017**, *12*, e0178937. [CrossRef]
51. Lin, K.-T.; Yeh, Y.-M.; Chuang, C.-M.; Yang, S.Y.; Chang, J.-W.; Sun, S.-P.; Wang, Y.-S.; Chao, K.-C.; Wang, L.-H. Glucocorticoids mediate induction of microRNA-708 to suppress ovarian cancer metastasis through targeting Rap1B. *Nat. Commun.* **2015**, *6*, 5917. [CrossRef]
52. Zheng, Y.; Izumi, K.; Li, Y.; Ishiguro, H.; Miyamoto, H. Contrary Regulation of Bladder Cancer Cell Proliferation and Invasion by Dexamethasone-Mediated Glucocorticoid Receptor Signals. *Mol. Cancer Ther.* **2012**, *11*, 2621–2632. [CrossRef]
53. Yip, H.Y.K.; Chee, A.; Ang, C.-S.; Shin, S.-Y.; Ooms, L.M.; Mohammadi, Z.; Phillips, W.A.; Daly, R.J.; Cole, T.J.; Bronson, R.T.; et al. Control of Glucocorticoid Receptor Levels by PTEN Establishes a Failsafe Mechanism for Tumor Suppression. *Mol. Cell* **2020**, *80*, 279–295.e8. [CrossRef] [PubMed]

54. Ji, J.Y.; Jing, H.; Diamond, S.L. Shear Stress Causes Nuclear Localization of Endothelial Glucocorticoid Receptor and Expression From the GRE Promoter. *Circ. Res.* **2003**, *92*, 279–285. [CrossRef] [PubMed]
55. Nayebosadri, A.; Christopher, L.; Ji, J.Y. Bayesian Image Analysis of Dexamethasone and Shear Stress-Induced Glucocorticoid Receptor Intracellular Movement. *Ann. Biomed. Eng.* **2012**, *40*, 1508–1519. [CrossRef] [PubMed]
56. Whitmarsh, A.J. A central role for p38 MAPK in the early transcriptional response to stress. *BMC Biology* **2010**, *8*, 47. [CrossRef] [PubMed]
57. Kopp, S.; Warnke, E.; Wehland, M.; Aleshcheva, G.; Magnusson, N.E.; Hemmersbach, R.; Corydon, T.J.; Bauer, J.; Infanger, M.; Grimm, D. Mechanisms of three-dimensional growth of thyroid cells during long-term simulated microgravity. *Sci. Rep.* **2015**, *5*, 16691. [CrossRef]
58. Warnke, E.; Pietsch, J.; Kopp, S.; Bauer, J.; Sahana, J.; Wehland, M.; Krüger, M.; Hemmersbach, R.; Infanger, M.; Lützenberg, R.; et al. Cytokine Release and Focal Adhesion Proteins in Normal Thyroid Cells Cultured on the Random Positioning Machine. *Cell. Physiol. Biochem.* **2017**, *43*, 257–270. [CrossRef]
59. Warnke, E.; Pietsch, J.; Wehland, M.; Bauer, J.; Infanger, M.; Görög, M.; Hemmersbach, R.; Braun, M.; Ma, X.; Sahana, J.; et al. Spheroid formation of human thyroid cancer cells under simulated microgravity: A possible role of CTGF and CAV1. *Cell Commun. Signal.* **2014**, *12*, 32. [CrossRef]
60. Svejgaard, B.; Wehland, M.; Ma, X.; Kopp, S.; Sahana, J.; Warnke, E.; Aleshcheva, G.; Hemmersbach, R.; Hauslage, J.; Grosse, J.; et al. Common Effects on Cancer Cells Exerted by a Random Positioning Machine and a 2D Clinostat. *PLoS ONE* **2015**, *10*, e0135157. [CrossRef]
61. Grosse, J.; Wehland, M.; Pietsch, J.; Schulz, H.; Saar, K.; Hübner, N.; Elles, C.; Bauer, J.; Abou-El-Ardat, K.; Baatout, S.; et al. Gravity-sensitive signaling drives 3-dimensional formation of multicellular thyroid cancer spheroids. *FASEB J.* **2012**, *26*, 5124–5140. [CrossRef]
62. Grimm, D.; Bauer, J.; Kossmehl, P.; Shakibaei, M.; Schöberger, J.; Pickenhahn, H.; Schulze-Tanzil, G.; Vetter, R.; Eilles, C.; Paul, M.; et al. Simulated microgravity alters differentiation and increases apoptosis in human follicular thyroid carcinoma cells. *FASEB J.* **2002**, *16*, 604–606. [CrossRef]
63. Kopp, S.; Sahana, J.; Islam, T.; Petersen, A.G.; Bauer, J.; Corydon, T.J.; Schulz, H.; Saar, K.; Huebner, N.; Slumstrup, L.; et al. The role of NFκB in spheroid formation of human breast cancer cells cultured on the Random Positioning Machine. *Sci. Rep.* **2018**, *8*, 921. [CrossRef]
64. Sahana, J.; Nassef, M.Z.; Wehland, M.; Kopp, S.; Krüger, M.; Corydon, T.J.; Infanger, M.; Bauer, J.; Grimm, D. Decreased E-Cadherin in MCF7 Human Breast Cancer Cells Forming Multicellular Spheroids Exposed to Simulated Microgravity. *Proteomics* **2018**, *18*, 1800015. [CrossRef]
65. Lin, K.T.; Wang, L.H. New dimension of glucocorticoids in cancer treatment. *Steroids* **2016**, *111*, 84–88. [CrossRef]
66. Calvaruso, M.; Militello, C.; Minafra, L.; La Regina, V.; Torrisi, F.; Pucci, G.; Cammarata, F.P.; Bravatà, V.; Forte, G.I.; Russo, G. Biological and Mechanical Characterization of the Random Positioning Machine (RPM) for Microgravity Simulations. *Life* **2021**, *11*, 1190. [CrossRef]
67. Wuest, S.L.; Richard, S.; Kopp, S.; Grimm, D.; Egli, M. Simulated microgravity: Critical review on the use of random positioning machines for mammalian cell culture. *Biomed. Res. Int.* **2015**, *2015*, 971474. [CrossRef] [PubMed]
68. Nassef, M.Z.; Melnik, D.; Kopp, S.; Sahana, J.; Infanger, M.; Lützenberg, R.; Relja, B.; Wehland, M.; Grimm, D.; Krüger, M. Breast Cancer Cells in Microgravity: New Aspects for Cancer Research. *Int. J. Mol. Sci.* **2020**, *21*, 7345. [CrossRef] [PubMed]
69. Zettl, K.S.; Sjaastad, M.D.; Riskin, P.M.; Parry, G.; Machen, T.E.; Firestone, G.L. Glucocorticoid-induced formation of tight junctions in mouse mammary epithelial cells in vitro. *Proc. Natl. Acad. Sci. USA* **1992**, *89*, 9069–9073. [CrossRef] [PubMed]
70. Woo, P.L.; Cercek, A.; Desprez, P.Y.; Firestone, G.L. Involvement of the helix-loop-helix protein Id-1 in the glucocorticoid regulation of tight junctions in mammary epithelial cells. *J. Biol. Chem.* **2000**, *275*, 28649–28658. [CrossRef]
71. Tena-Garitaonaindia, M.; Arredondo-Amador, M.; Mascaraque, C.; Asensio, M.; Marin, J.J.G.; Martínez-Augustin, O.; Sánchez de Medina, F. Modulation of intestinal barrier function by glucocorticoids: Lessons from preclinical models. *Pharmacol. Res.* **2022**, *177*, 106056. [CrossRef]
72. Adamian, M.; Hekmat, A.; Hajebrahimi, Z. The Impacts of Simulated Microgravity on The Cell Viability and Claudin-1 and Claudin-3 Expression of MCF-7 Breast Cancer Cells. *J. Sci. Islam. Repub. Iran* **2021**, *32*, 105–114. [CrossRef]
73. Martin, T.A. The role of tight junctions in cancer metastasis. *Semin. Cell Dev. Biol.* **2014**, *36*, 224–231. [CrossRef] [PubMed]
74. Salvador, E.; Burek, M.; Förster, C.Y. Tight Junctions and the Tumor Microenvironment. *Curr. Pathobiol. Rep.* **2016**, *4*, 135–145. [CrossRef] [PubMed]
75. Tzelepi, V.N.; Tsamandas, A.C.; Vlotinou, H.D.; Vagianos, C.E.; Scopa, C.D. Tight junctions in thyroid carcinogenesis: Diverse expression of claudin-1, claudin-4, claudin-7 and occludin in thyroid neoplasms. *Mod. Pathol.* **2008**, *21*, 22–30. [CrossRef] [PubMed]
76. Zwanziger, D.; Badziong, J.; Ting, S.; Moeller, L.C.; Schmid, K.W.; Siebolts, U.; Wickenhauser, C.; Dralle, H.; Fuehrer, D. The impact of CLAUDIN-1 on follicular thyroid carcinoma aggressiveness. *Endocr.-Relat. Cancer* **2015**, *22*, 819–830. [CrossRef] [PubMed]
77. Na, T.-Y.; Schecterson, L.; Mendonsa, A.M.; Gumbiner, B.M. The functional activity of E-cadherin controls tumor cell metastasis at multiple steps. *Proc. Natl. Acad. Sci. USA* **2020**, *117*, 5931–5937. [CrossRef]
78. Zhou, C.; Yang, C.; Chong, D. E-cadherin expression is associated with susceptibility and clinicopathological characteristics of thyroid cancer: A PRISMA-compliant meta-analysis. *Medicine* **2019**, *98*, e16187. [CrossRef]

79. Huang, S.H.; Wu, J.C.; Chang, K.J.; Liaw, K.Y.; Wang, S.M. Distribution of the cadherin-catenin complex in normal human thyroid epithelium and a thyroid carcinoma cell line. *J. Cell. Biochem.* **1998**, *70*, 330–337. [CrossRef]
80. Singh, P.K.; Hollingsworth, M.A. Cell surface-associated mucins in signal transduction. *Trends Cell Biol.* **2006**, *16*, 467–476. [CrossRef] [PubMed]
81. Zhou, X.; Tu, J.; Li, Q.; Kolosov, V.P.; Perelman, J.M. Hypoxia induces mucin expression and secretion in human bronchial epithelial cells. *Transl. Res.* **2012**, *160*, 419–427. [CrossRef]
82. Nakamura, Y.; Saitou, M.; Komura, S.; Matsumoto, K.; Ogawa, H.; Miyagawa, T.; Saitou, T.; Imamura, T.; Imai, Y.; Takayanagi, H.; et al. Reduced dynamic loads due to hip dislocation induce acetabular cartilage degeneration by IL-6 and MMP3 via the STAT3/periostin/NF-κB axis. *Sci. Rep.* **2022**, *12*, 12207. [CrossRef]
83. van Putten, J.P.M.; Strijbis, K. Transmembrane Mucins: Signaling Receptors at the Intersection of Inflammation and Cancer. *J Innate Immun.* **2017**, *9*, 281–299. [CrossRef]
84. Hollingsworth, M.A.; Swanson, B.J. Mucins in cancer: Protection and control of the cell surface. *Nat. Rev. Cancer* **2004**, *4*, 45–60. [CrossRef] [PubMed]
85. Wi, D.H.; Cha, J.H.; Jung, Y.S. Mucin in cancer: A stealth cloak for cancer cells. *BMB Rep.* **2021**, *54*, 344–355. [CrossRef] [PubMed]
86. Monti, N.; Masiello, M.G.; Proietti, S.; Catizone, A.; Ricci, G.; Harrath, A.H.; Alwasel, S.H.; Cucina, A.; Bizzarri, M. Survival Pathways Are Differently Affected by Microgravity in Normal and Cancerous Breast Cells. *Int. J. Mol. Sci.* **2021**, *22*, 862. [CrossRef] [PubMed]
87. Wu, G.; Kim, D.; Kim, J.N.; Park, S.; Maharjan, S.; Koh, H.; Moon, K.; Lee, Y.; Kwon, H.J. A Mucin1 C-terminal Subunit-directed Monoclonal Antibody Targets Overexpressed Mucin1 in Breast Cancer. *Theranostics* **2018**, *8*, 78–91. [CrossRef]
88. Rajabi, H.; Joshi, M.D.; Jin, C.; Ahmad, R.; Kufe, D. Androgen receptor regulates expression of the MUC1-C oncoprotein in human prostate cancer cells. *Prostate* **2011**, *71*, 1299–1308. [CrossRef]
89. Krüger, M.; Kopp, S.; Wehland, M.; Bauer, J.; Baatout, S.; Moreels, M.; Egli, M.; Corydon, T.J.; Infanger, M.; Grimm, D. Growing blood vessels in space: Preparation studies of the SPHEROIDS project using related ground-based studies. *Acta Astronaut.* **2019**, *159*, 267–272. [CrossRef]
90. Porowska, H.; Paszkiewicz-Gadek, A.; Wosek, J.; Wnuczko, K.; Rusak, M.; Szczepański, M. Expression of MUC1 mucin in human umbilical vein endothelial cells (HUVEC). *Folia Histochem. Cytobiol.* **2010**, *48*, 417–424. [CrossRef]
91. Kufe, D.W. MUC1-C oncoprotein as a target in breast cancer: Activation of signaling pathways and therapeutic approaches. *Oncogene* **2013**, *32*, 1073–1081. [CrossRef] [PubMed]

11.2 Publication #2

Jokšienė, J., Sahana, J., Wehland, M., Schulz, H., **Cortés-Sánchez, J. L**., Prat-Duran, J., ... & Simonsen, U. (2023). Effects of High Glucose on Human Endothelial Cells Exposed to Simulated Microgravity. Biomolecules, 13(2), 189.

biomolecules

MDPI

Article

Effects of High Glucose on Human Endothelial Cells Exposed to Simulated Microgravity

Justina Jokšienė [1,2], Jayashree Sahana [2], Markus Wehland [3], Herbert Schulz [3], José Luis Cortés-Sánchez [3], Judit Prat-Duran [2], Daniela Grimm [2,3,4,†] and Ulf Simonsen [2,*,†]

1 Laboratory of Preclinical Drug Investigation, Institute of Cardiology, Lithuanian University of Health Sciences, Sukileliu Ave. 15, LT-50162 Kaunas, Lithuania
2 Department of Biomedicine, The Faculty of Health, Aarhus University, Ole Worms Allé 4, 8000 Aarhus, Denmark
3 Department of Microgravity and Translational Regenerative Medicine, Medical Faculty, Otto von Guericke University, Universitätsplatz 2, 39106 Magdeburg, Germany
4 Research Group "Magdeburger Arbeitsgemeinschaft für Forschung unter Raumfahrt- und Schwerelosigkeitsbedingungen" (MARS), Otto von Guericke University, 39106 Magdeburg, Germany
* Correspondence: us@biomed.au.dk; Tel.: +45-60202613
† These authors contributed equally to this work.

Abstract: A diabetogenic state induced by spaceflight provokes stress and health problems in astronauts. Microgravity (μ*g*) is one of the main stressors in space causing hyperglycaemia. However, the underlying molecular pathways and synergistic effects of μ*g* and hyperglycaemia are not fully understood. In this study, we investigated the effects of high glucose on EA.hy926 endothelial cells in simulated μ*g* (s-μ*g*) using a 3D clinostat and static normogravity (1*g*) conditions. After 14 days of cell culture under s-μ*g* and 1*g* conditions, we compared the expression of extracellular matrix (ECM), inflammation, glucose metabolism, and apoptosis-related genes and proteins through qPCR, immunofluorescence, and Western blot analyses, respectively. Apoptosis was evaluated via TUNEL staining. Gene interactions were examined via STRING analysis. Our results show that glucose concentrations had a weaker effect than altered gravity. μ*g* downregulated the ECM gene and protein expression and had a stronger influence on glucose metabolism than hyperglycaemia. Moreover, hyperglycaemia caused more pronounced changes in 3D cultures than in 2D cultures, including bigger and a greater number of spheroids, upregulation of NOX4 and the apoptotic proteins NF-κB and CASP3, and downregulation of fibronectin and transglutaminase-2. Our findings bring new insights into the possible molecular pathways involved in the diabetogenic vascular effects in μ*g*.

Keywords: microgravity; endothelial cells; hyperglycaemia; 3D cell culture; apoptosis; extracellular matrix; interleukin-8

Citation: Jokšienė, J.; Sahana, J.; Wehland, M.; Schulz, H.; Cortés-Sánchez, J.L.; Prat-Duran, J.; Grimm, D.; Simonsen, U. Effects of High Glucose on Human Endothelial Cells Exposed to Simulated Microgravity. *Biomolecules* **2023**, *13*, 189. https://doi.org/10.3390/biom13020189

Academic Editor: Viswanathan Natarajan

Received: 23 December 2022
Revised: 14 January 2023
Accepted: 15 January 2023
Published: 17 January 2023

1. Introduction

Space travel, including the near-future expeditions to the Moon, Mars, and other planets and an increase in space tourism, sounds exciting and adventurous, but it possesses many health-related hazards. Stressors, such as noise, isolation, hypoxia, disrupted circadian rhythms, exposure to ionizing radiation, and microgravity (μ*g*), induce a cumulative and significant effect on health [1,2]. Prolonged exposure to the space environment causes alterations in glucose and lipid metabolism [3], and telomeric, epigenetic, ocular, and cognitive changes [4]. It has been suggested that, in particular, μ*g* causes subclinical diabetogenic changes. These manifest as insulin secretion and sensitivity alterations, decreased glucose tolerance and increased plasma glucose [5].

Glucose and insulin intolerance is a common complication during spaceflight [6] and its terrestrial s-μ*g* analogues, such as head-down tilt bed rest [7] or dry immersion [8]. Understanding how hyperglycaemic conditions in space affect astronauts' health during long-term missions is crucial, and it is important to know and address all the subsequent

health hazards during and after spaceflight. For instance, μ*g*, hyperglycaemia, and persistent low-grade inflammation are linked to chronic non-healing wounds. They are another relevant concern for space agencies [9]. Hyperglycaemia can trigger oxidative stress and inflammation via the AGE–RAGE axis by increasing TNFα, IL-6, and endothelin, and decreasing nitric oxide levels. Increased glucose availability generates more reactive oxygen species (ROS) and diminishes antioxidant surveillance, increasing oxidative stress. This, in turn, activates nonoxidative glucose pathways that further increase ROS production, stimulating the vicious metabolic cycle [10].

The exposure of endothelial cells to hyperglycaemia is linked with endothelial dysfunction and apoptosis [11]. High glucose also induces aerobic glycolysis and transglutaminase-2 (TG2) activity [12] and can trigger apoptosis via intracellular Ca^{2+} and ROS-induced activation of TG2 [13]. Another important fact is that endothelial cells are sensitive to mechanical forces as they are constantly influenced by shear stress, extracellular matrix (ECM) stiffness, mechanical stretch, and gravity. It was detected that endothelial cell apoptosis could be regulated via such mechanical forces [14]. However, the molecular mechanisms underlying the synergistic effects of μ*g* and hyperglycaemia are not fully understood.

The principal aim of this study was to investigate the effects of hyperglycaemia on endothelial cells' behaviour and key gene and protein expression in s-μ*g* using a 3D clinostat and static normogravity (1*g*) conditions. After 14 days of cell cultivation under s-μ*g* and 1*g* conditions, we harvested the cell material and measured the gene expression of ECM, inflammatory, glycolysis, glucose transport, and apoptosis-related genes. Apoptosis was further evaluated through TUNEL assay staining. Additionally, a Search Tool for the Retrieval of Interacting Genes/Proteins (STRING) analysis was performed to investigate the overall interactions among the genes and proteins of interest.

2. Materials and Methods

2.1. Cell Culturing

The immortalised cell line EA.hy926 (CRL-2922; ATCC, Manassas, VA, USA) was used in this study. It is a somatic cell hybrid type with endothelial cell morphology, displaying Weibel–Palade bodies that are specific to vascular endothelium, as previously described [15]. This cell line was derived by fusing primary human umbilical vein cells with a lung carcinoma A549 cell line. EA.hy926 cells (deposited by CS. Edgell) were purchased from ATCC (CRL-2922™).

The EA.hy926 cells were seeded into T25 flasks (Sarstedt, Nümbrecht, Germany) or slide flasks (Nunc™ Lab-Tek™ SlideFlask; Thermo Fisher Scientific, Waltham, MA, USA) for immunofluorescence staining and cultured using DMEM medium (D4947, Merck), supplemented with 10% FBS (F7524, Merck, Damstadt, Germany) and 1% penicillin/streptomycin solution (P4333, Merck, Damstadt, Germany), corresponding to low glucose (LG) medium. Half of the flasks were grown in hyperglycaemic conditions with high glucose (HG) medium, which was pre-made by supplementing regular 5 mM DMEM medium with D-(+)-Glucose solution (G8769, Merck, Damstadt, Germany). The cells were cultured either in 1*g* or s-μ*g* conditions with either LG or HG medium for 2 weeks. The medium was changed once after seven days. The experimental length was selected to recreate real μ*g* experiments in space, where good cell viability was demonstrated for at least 14 days [16].

2.2. Three-Dimensional Clinostat

Microgravity conditions were simulated using a custom-built 3D clinostat, which was designed and constructed by the German Space Agency (Deutsches Zentrum für Luft-und Raumfahrt, DLR, Cologne, Germany) and later revised by Aarhus University, Denmark [17].

The clinostats are the so-called National Aeronautics and Space Administration's (NASA) and European Space Agency's (ESA) acknowledged ground-based facilities and simulated μ*g* (s-μ*g*) on Earth [18]. These devices minimise the influence of gravity by rotating the biological sample around all three axes.

To prepare the flasks for cultivation in s-μ*g* using the custom-built 3D clinostat, EA.hy926 cells were seeded at 5×10^5 density into T25 flasks (n = 6 for each experimental condition) or at 3×10^5 density into slide flasks (n = 6 for each experimental condition) in LG medium. Cell counting was performed using Corning® Cell Counter (CLS6749, Merck, Darmstadt, Germany), and cell viability was assessed via staining with Trypan blue 0.4% solution (T8154, Sigma-Aldrich, Burlington, MA, USA). The cells were kept in 1*g* conditions (37 °C, 5% CO_2) for 24 h to let the cells adhere. Then, serum starvation was implemented for another 24 h. Afterward, the FBS-free medium was removed, and the flasks were filled to the top with either LG or HG growth medium. The bubbles floating on top were removed through suction, and the lids were carefully screwed to avoid the formation of new air bubbles. In addition, the bottle caps were wrapped with sterilised parafilm and enclosed in sterilised sachets to prevent contamination. Then, half of the flasks were transferred from the laminar flow cabinet to the clinostat (37 °C) and mounted as close to the centre of rotation as possible. Another half of the flasks were used as static 1*g* controls and were placed in the incubator. The point of cell transfer to either clinorotation or incubator was considered the 1st day of the experiment.

The morphological evaluation of cell growth was performed using a light microscope (Leica DM IL LED, Germany) on the 1st, 7th, and 14th days of cell culture.

After seven days, half of the LG and HG medium from each flask was removed and replaced with complete fresh medium before allowing s-μ*g* flasks to stand vertically for 30 min to avoid sucking out the multicellular structures (MCS) and allowing them to settle down. After an additional week of cultivation in 1*g* and μ*g*, the cells, including adherent cells (AD) and MCS from s-μ*g* flasks, were collected. The spheroid count (n = 5) and spheroid area (n = 6) were calculated from the images obtained on day 14 with an EVOS M5000 microscope from s-μ*g* flasks (Thermo Scientific, Waltham, MA, USA).

2.3. Sample Collection and Protein Extraction

After 14 days, the cell samples for qPCR and Western blot experiments were collected. Media from 1*g* flasks were discarded, and media from s-μ*g* flasks were poured into 50 mL tubes to collect s-μ*g*-MCS. Each flask surface was washed three times with 5 mL of phosphate-buffered saline (PBS) and mechanically detached with cell scrapers (Sarstedt, Nümbrecht, Germany). The cell suspensions were collected in new 50 mL tubes (for 1*g* and s-μ*g*-AD cells). Then, all tubes containing the cells were centrifuged at 1000 rpm for 10 min at 4 °C. Supernatants (leaving approx. 1 mL) were removed, resuspended, and transferred to Eppendorf tubes. The Eppendorf tubes were centrifuged at 1000 rpm for 10 min at 4 °C, and the supernatant was fully removed.

The pellets for qPCR experiments were loosened up in a small amount (100–200 μL) of RNAlater Stabilization Solution (Invitrogen by Thermo Fischer), resuspended in a total of 1 mL of RNAlater, transferred to Eppendorf tubes, and put into a −20 °C freezer until further use.

The pellets for Western blot experiments were lysed with lysis buffer (RIPA with Halt protease and phosphatase inhibitor cocktail (78841, ThermoFisher Scientifics Waltham, MA, USA)) and protease/phosphatase inhibitor (1:100) by adding half the amount to pellet size, vortexed for 30 s and kept on ice for 30 min. During that time, the tubes were vortexed every 10 min for 30 s, followed by a sonification of 45 s using a Branson 2210 Ultrasonic bath (Buch & Holm, Herlev, Denmark). Then, the samples were centrifuged (10 min, 4 °C, 13,000 rcf), and the supernatants were transferred into new Eppendorf tubes. Protein concentration was determined using Lowry's method.

2.4. Western Blot Analysis

The protein samples were boiled at 95 °C for 5 min. The wells of the Criterion TGX Stain-Free Gel (5678084, Bio-Rad, Hercules, CA, USA) were rinsed twice with 200 μL of the running buffer (1610772, Bio-Rad). Then, the samples were loaded, dedicating a few wells for a molecular weight marker (161-0373, Bio-Rad, Hercules, CA, USA). The gel

ran for 30 min at 250 V with the running buffer. After the run, the gel was removed from the plastic and exposed to UV light to activate the gel and obtain an image for total protein quantification and normalization. During the gel UV scan, the polyvinylidene difluoride membrane (1620177, Bio-Rad, Hercules, CA, USA) was activated with ethanol 99.9% for 5 min, followed by washing the membrane with transfer buffer (10026938, Bio-Rad, Hercules, CA, USA). The filter papers were soaked in the transfer buffer for a few minutes before the transfer. The gel, the membranes, and the filter papers were stacked and put into the Trans-Blot Turbo Transfer System (Bio-Rad, Hercules, CA, USA) for 30 min at 100 V.

The membrane was read with UV light to show the total protein transferred and washed for 10 min with Tris-buffered saline-Tween 20 (TBST) to remove the excess transfer buffer. Then, the membrane was incubated for 5 min with the EveryBlot blocking buffer (12010020, Bio-Rad, Hercules, CA, USA). After blocking, the membrane was incubated with the primary antibody (Table A1) in a blocking buffer for 2 h at RT or overnight at 4 °C. Then the membrane was washed for 10–15 min 4 times with TBST, followed by incubation with the secondary antibody diluted in a blocking buffer for 2 h at RT. After appropriate washing steps, the membrane was developed using Clarity Western ECL Substrate (1705061, Bio-Rad, Hercules, CA, USA) solution according to the manufacturer's instructions. Both reagents were mixed in a 1:1 ratio and spread on the membrane surface in the dark for 5 min. The images were obtained with Syngene PXi Touch (Syngene by Synoptics Group) and analyzed with the Syngene Gene Tools analysis software. Data are relative to total protein and expressed as % of control; n = 4 for NF-κB p65 and CASP-3 analysis, n = 5 for TG2, NOX4, and FN1. An overview of the used antibodies is given in Table A1.

2.5. Immunofluorescence Staining and Terminal Deoxynucleotidyl Transferase dUTP Nick End Labelling (TUNEL) Assay

Slide flasks after 14 days of cultivation were used for immunofluorescence staining. Media from 1*g* and s-μ*g* slide flasks were discarded. The cells were fixed with 4% PFA at room temperature (RT) for 20 min, then washed 3 times with PBS (3 min/wash). The permeabilization was performed with Triton-X 0.1% solution in PBS for 10 min, followed by a washing step. Then, the cells were blocked with 5% BSA in PBS for 30 min at RT. After the blocking step, the blocking solution was discarded, and the flask was detached from the slide with a special tool.

The cell surface area was covered with corresponding primary antibody solutions and diluted in 1% BSA in PBS. The samples with the primary antibodies were kept in a humidified, light-protected box at 4 °C overnight. The next day, the cells were washed and incubated with the secondary antibodies for 1 h at RT in a humidified dark box. Then, the slides were rinsed with deionized water, preserved, and counterstained with Fluoroshield™ with DAPI (F6057, Sigma-Aldrich, Burlington, MA, USA) mounting medium. The slides were sealed with cover glass and allowed to dry for 1–2 h before visualisation. The slides were stored at 4 °C protected from light. A list of antibodies and dilutions used is presented in Table A1.

To evaluate the level of apoptosis, some slide flasks were analysed with Click-iT™ TUNEL Alexa Fluor Imaging Assay for Microscopy & HCS (C10245, Invitrogen by Thermo Fischer, Waltham, MA, USA), which was performed according to the manufacturer's recommendations. This method was published in detail previously [19].

Immunofluorescence and TUNEL assay staining were analysed with an inverted confocal laser scanning microscope with super-resolution (LSM 800 Airyscan, Zeiss, Oberkochen, Germany). Images of TUNEL staining, triosephosphate isomerase 1, and fibronectin were obtained with a 40× air objective; all other images were acquired with a 40× oil immersion objective. Excitation and emission wavelengths were as follows: λ_{exc} = 495 nm and λ_{em} = 519 nm for FITC; λ_{exc} = 493 nm and λ_{em} = 517 nm for AF488; λ_{exc} = 557 nm and λ_{em} = 572 nm for AF546. All samples were analysed with the image analysis program

ZEN 3.5 (Blue Edition). At least five fields of view were captured for TUNEL and each antibody staining (n = 5).

2.6. RNA Isolation and Quantitative Polymerase Chain Reaction (qPCR)

The RNeasy Mini Kit (Qiagen, Hilden, Germany) was used to isolate RNA according to the manufacturer's instructions. RNA concentrations and quality were assessed spectrophotometrically at 260 nm using an Implen™ NanoPhotometer™ N60. The A260/280 ratio of isolated RNA was 1.5 or higher. The cDNA for quantitative real-time PCR (qPCR) was obtained using the High-Capacity cDNA Reverse Transcription Kit (Applied Biosystems, Darmstadt, Germany) using 1 µ*g* of total RNA in a 20-µL reaction mixture at RT.

The qPCR method was used to determine the expression levels of selected genes after 14 d of incubation under s-µ*g* compared to the static control group (1*g*). The method was previously described in detail [20]. The primers were designed using NCBI Primer Blast, and they were selective for cDNA by spanning exon–exon junctions and had a Tm of around 60 °C. The primers were synthesised by TIB Molbiol (Berlin, Germany) and are listed in Table A2. All assays were run on an Applied Biosystems 7500 Fast Real-Time PCR System using the Fast SYBR™ Green PCR Master Mix (both Applied Biosystems, Darmstadt, Germany).

For qPCR, there were 3 technical and 5 biological replicates. The reaction volume was 20 µL, including 1 µL of template cDNA and a final primer concentration of 500 nM. PCR conditions were as follows: 20 s at 95 °C, 40 cycles of 30 s at 95 °C and 30 s at 60 °C, followed by a melting curve analysis step (temperature gradient from 60 to 95 °C with +0.3 °C/cycle). All samples were measured in triplicate, and 18S rRNA was used as a housekeeping gene to normalise the expression data. The comparative Ct (ΔΔCt) method was used for the relative quantification of transcription levels, and the 1*g* control group was defined as 100% for reference.

2.7. STRING Analysis

To analyse the interaction network of genes used in qPCR, we used the STRING V11.5 tool [21] (available at https://string-db.org/, accessed on 5 December 2022) with a minimum interaction score of 0.4. The method was earlier published by Nassef et al. [19].

2.8. Statistical Analyses

All data are presented as mean ± standard deviation (SD). Statistical evaluation was performed using IBM SPSS Statistics 24 software (IBM, Armonk, NY, USA). Grubbs' test was used to identify and remove statistical outliers. An unpaired two-tailed *t*-test was performed for analysis between 2 groups (spheroid count and spheroid area). The Mann–Whitney U Test was used to compare groups for qPCR and Western blot. Statistical significance was assumed when $p < 0.05$.

3. Results

3.1. Hyperglycaemia in Microgravity Induces the Formation of Bigger and a Greater Number of Multicellular Structures

Images of the cells were taken on the 1st day before randomising them to the different gravity conditions, and on the 14th day after the cultivation in 1*g* and s-µ*g*. On day 1, in both LG and HG treatment groups, the cells were confluent and exhibited the same morphology as typically elongated endothelial cells (Figure 1a,d). After 14 days, distinctive differences were observed between the 1*g* and s-µ*g* groups, as the cells in the 1*g* were over-confluent and grew in layers on top of each other (Figure 1b,e), whereas the cells in the s-µ*g* samples formed MCS that floated freely in the supernatant and were detached from adherent cells (Figure 1c,f). In addition, s-µ*g* contained adherently growing cells on the bottom of the culture flasks. Tubular structures were seen in some of the s-µ*g* flasks, as shown in Figure 1f.

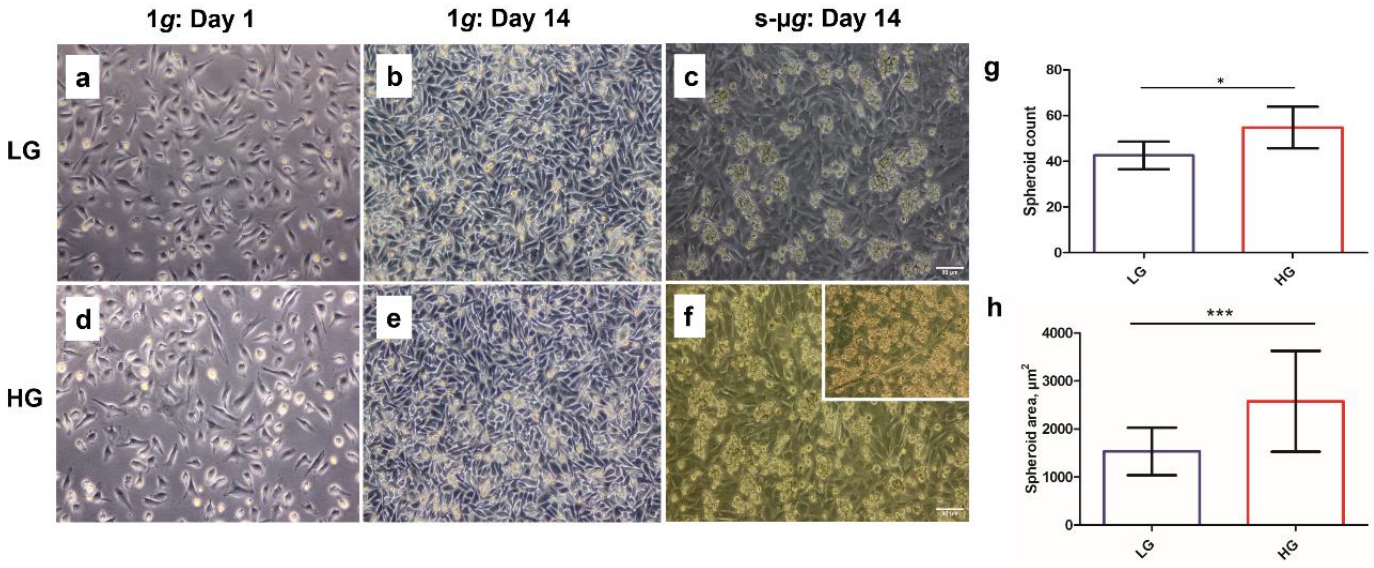

Figure 1. Morphological characteristics of EA.hy926 cells after exposure to low (LG) and high glucose (HG) media, and static normogravity (1*g*) or simulated microgravity (s-µ*g*) through phase contrast microscopy (**a**–**f**). Adherent cells (s-µ*g*-AD) and multicellular structures (s-µ*g*-MCS) in s-µ*g* samples can be observed (**c**,**f**). The insert in (**f**) shows another sample with a tubular structure. The scale bar represents 90 µm. The quantification of the spheroid number (**g**) and the relative spheroid size (**h**) are displayed. The spheroid size was determined via the spheroid area (µm^2). Significant changes in spheroid number or spheroid size are indicated by * ($p < 0.05$) or *** ($p < 0.001$), respectively.

Evaluation of the number and size of spheroids in LG and HG s-µ*g* samples revealed that there were significantly more spheroid structures in the HG group compared to the LG group. Additionally, the spheroid size was significantly increased in the HG s-µ*g* samples as opposed to the LG s-µ*g* samples (Figure 1g,h).

3.2. Extracellular Matrix Proteins Collagen IV and Fibronectin Are Downregulated in Microgravity

Collagen IV was more pronounced in 1*g* LG (Figure 2a) as opposed to 1*g* HG (Figure 1d); however, it seemed more expressed in s-µ*g* HG samples (Figure 2e,f) contrary to s-µ*g* LG (Figure 2b,c). Small collagen deposits had a punctate pattern in 1*g* HG (Figure 2d), whereas they showed a more fibrous pattern in s-µ*g*-AD HG and s-µ*g*-MCS HG samples (Figure 2e,f). s-µ*g*-AD and s-µ*g*-MCS samples cultured in hyperglycaemic conditions (Figure 2e,f) appeared to have a denser pattern and higher expression of collagen IV than the corresponding LG samples (Figure 2b,c).

The relative gene expression for *COL4A6* was significantly downregulated in both the s-µ*g*-MCS LG and s-µ*g*-MCS HG groups compared to the corresponding 1*g* and s-µ*g*-AD groups (Figure 2g). There was no difference between LG and HG conditions regarding gene expression.

Fibronectin was sparse in the confocal microscopy images and was seen as small dots in the visual field in all LG samples (Figure 2h–j). In contrast, in the 1*g* HG sample, fibronectin was much more pronounced and had a fibrous mesh-forming appearance (Figure 2k). In the HG s-µ*g*-AD and s-µ*g*-MCS groups, the staining was reduced and had a pale and dusty appearance, more similar to the LG samples.

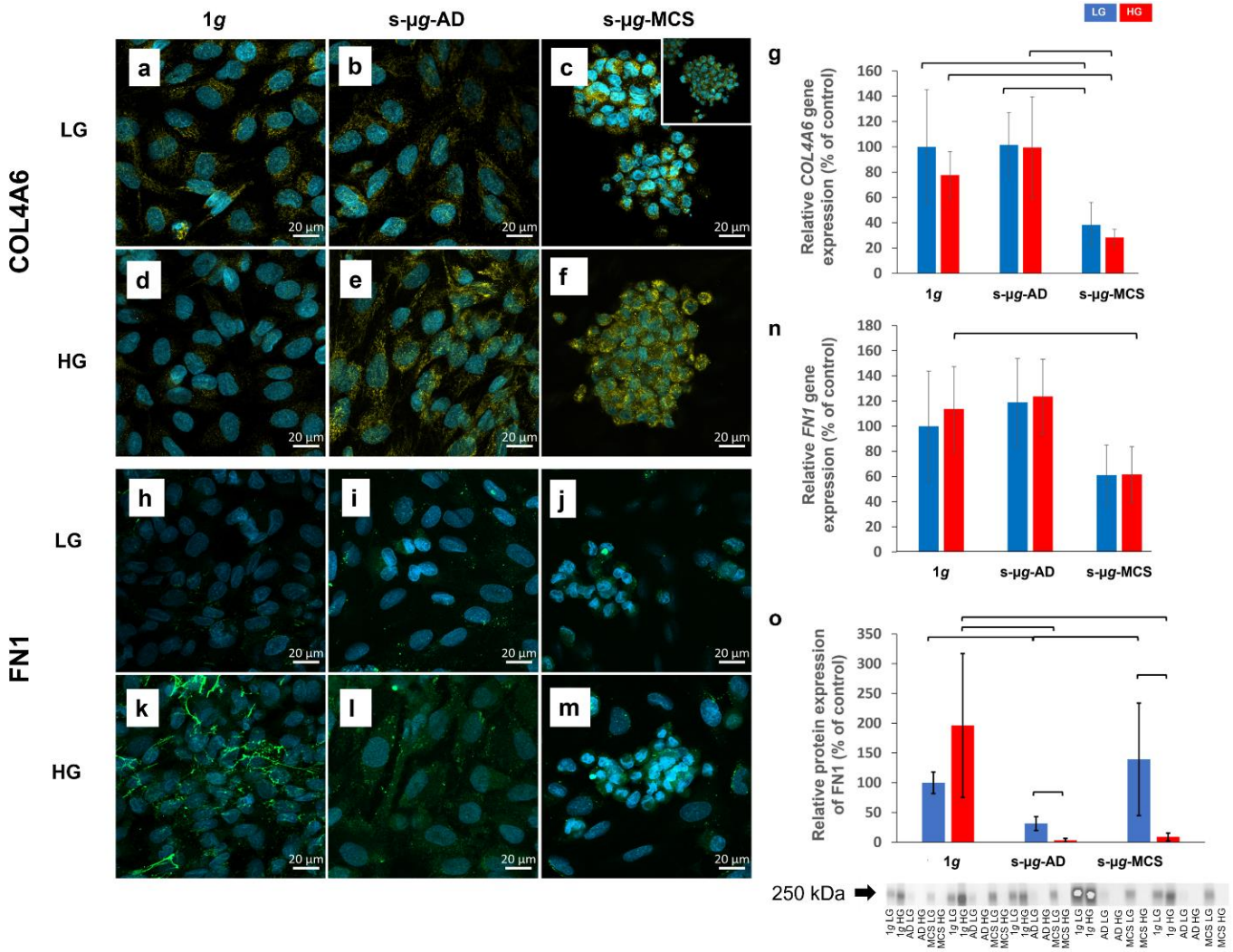

Figure 2. Analysis of the ECM proteins collagen IV (**a**–**g**) and fibronectin (**h**–**o**) after 14 days of cultivation either at 1*g* or s-µ*g* and either using low (LG) or high (HG) glucose medium. In the presentation of the s-µ*g* samples, a differentiation was made between AD and MCS. The data were detected via immunostaining (**a**–**f**,**h**–**m**), qPCR (**g**,**n**), and Western blot techniques (**o**). The brackets represent a significance level of $p < 0.05$.

The *FN1* gene expression was significantly decreased in s-µ*g*-MCS HG compared to 1*g* HG (Figure 2n). Western blot data showed a significant decrease in the protein expression of fibronectin in s-µ*g*-AD HG and s-µ*g*-MCS HG compared to the 1*g* HG control samples (Figure 2o). In contrast, only a significant depletion of FN1 protein expression in adherent cells was observed under LG conditions. Additionally, significantly lower FN1 protein expression was measured in s-µ*g*-HG groups compared to s-µ*g*-LG groups. Full blots are represented as supplementary materials in Figures S1–S5.

3.3. Microgravity Has a Stronger Effect on Glucose Metabolism Than Hyperglycaemia

3.3.1. Glucose Transporters

GLUT1 (Figure 3a–f) and GLUT3 (Figure 3h–m) were present in all cells, and GLUT1 showed a pattern of perinuclear accumulation in all groups. GLUT3 seemed to have a similar pattern and intensity in all treatment groups. GLUT1 levels were slightly elevated in both s-µ*g*-LG and s-µ*g*-HG samples.

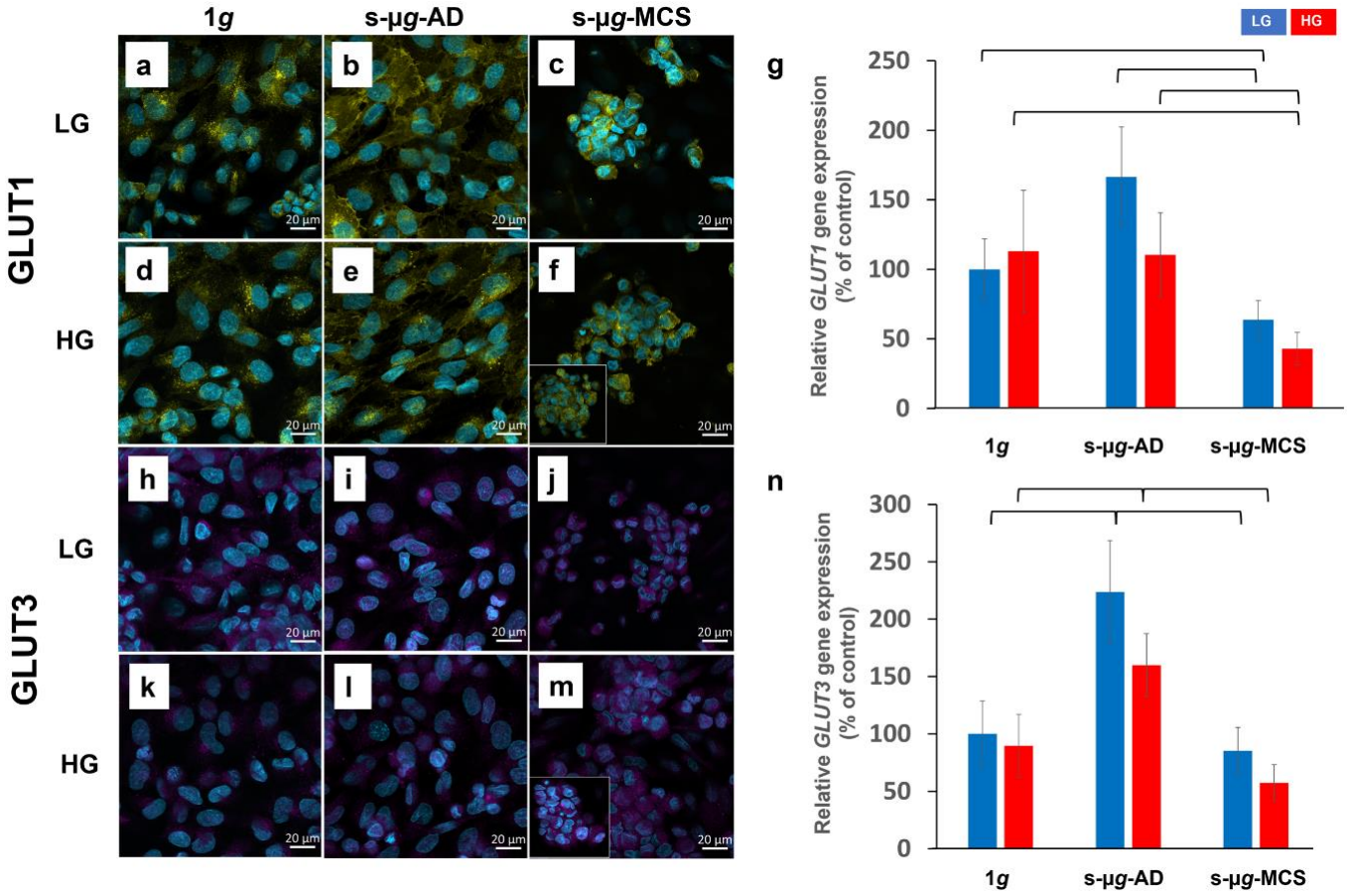

Figure 3. Analysis of glucose transporters GLUT1 and GLUT3 after 14 days of cultivation either at 1*g* or s-µ*g* and either using low (LG) or high (HG) glucose medium. Immunostaining (**a**–**f**,**h**–**m**) and qPCR (**g**,**n**) results are represented. The brackets represent a significance level of $p < 0.05$.

qPCR results of the *GLUT1* gene expression exhibited a significant downregulation of *GLUT1* between 1*g* control and s-µ*g*-MCS and between s-µ*g*-AD and s-µ*g*-MCS in both LG and HG. Irrespective of the glucose concentration, we observed a significant *GLUT3* increase between 1*g* control and s-µ*g*-AD and a considerable decrease in control levels between s-µ*g*-AD and s-µ*g*-MCS samples (Figure 3n).

3.3.2. Triosephosphate Isomerase 1

The fluorescence intensity of triosephosphate isomerase 1 was higher in the s-µ*g*-AD LG and s-µ*g*-MCS LG samples compared to 1*g* LG (Figure 4a–c). It was also lower in the s-µ*g*-AD HG and s-µ*g*-MCS HG samples compared to 1*g* HG (Figure 4d–f). The *TPI1* gene expression was significantly downregulated in s-µ*g*-MCS LG samples compared to s-µ*g*-AD LG.

3.4. Transglutaminase-2 Expression Is Modulated by Microgravity and Hyperglycaemia

TG2 was present in all cells and showed a pattern of perinuclear accumulation in all groups (Figure 5a–f). Both LG and HG 1*g* samples exhibited a lower intensity and a much higher distribution in the corresponding s-µ*g*-AD and s-µ*g*-MCS samples. *TGM2* gene expression was significantly downregulated in HG s-µ*g*-MCS compared to both HG 1*g* control and HG s-µ*g*-AD cells (Figure 5g). In LG cells, only LG s-µ*g*-MCS vs. LG s-µ*g*-AD *TGM2* gene expression was significantly decreased. Relative protein levels were significantly elevated in LG s-µ*g*-MCS compared to the LG s-µ*g*-AD and LG 1*g* groups (Figure 5h). In addition, TG2 was more expressed in LG s-µ*g*-MCS than in the respective HG group (see also Figure S1).

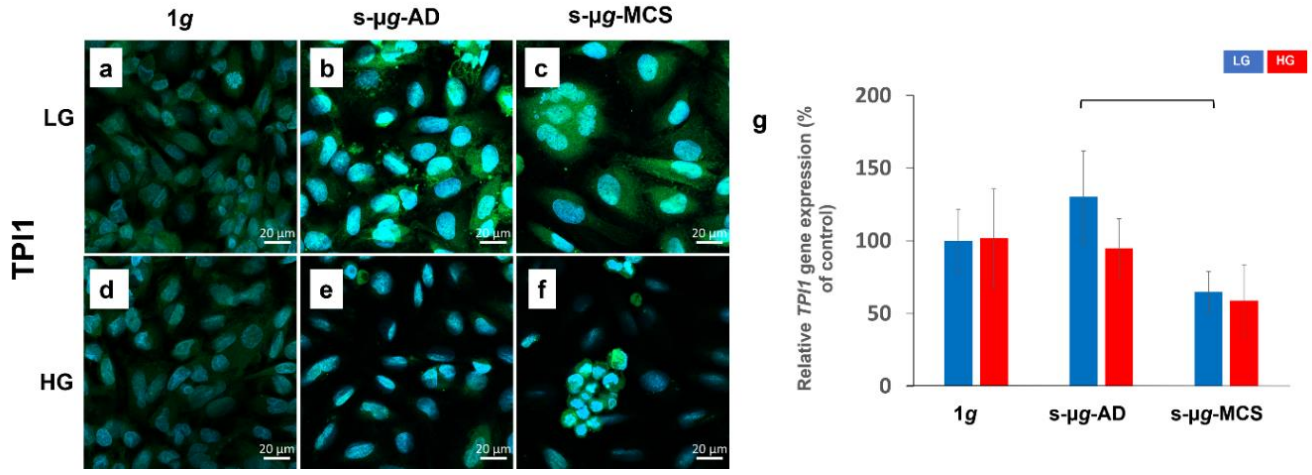

Figure 4. Analysis of TPI1 after 14 days of cultivation either at 1*g* or s-µ*g* and either using low (LG) or high (HG) glucose medium. Data were obtained through immunostaining (**a**–**f**) and qPCR (**g**). The bracket stands for a significance level of $p < 0.05$.

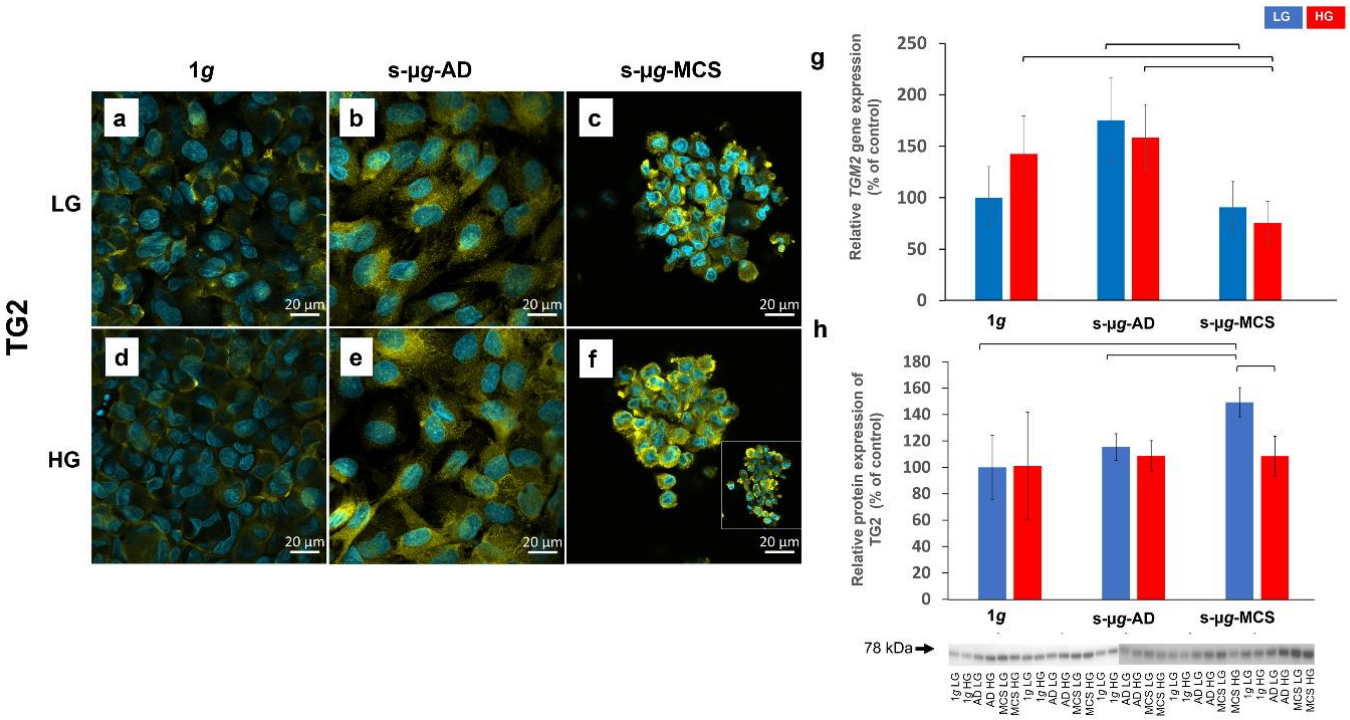

Figure 5. Analysis of TG2 after 14 days of cultivation either at 1*g* or s-µ*g* and either using low (LG) or high (HG) glucose medium. Data were obtained via immunostaining (**a**–**f**), qPCR (**g**), and Western blot (**h**) techniques. The brackets represent a significance level of $p < 0.05$.

3.5. NADPH Oxidase 4 and Interleukin-8 Are Upregulated on the Clinostat

3.5.1. NADPH Oxidase 4

The NADPH oxidase 4 (NOX4) protein was detectable in all three groups, with increasing intensity from 1*g* control samples over s-µ*g*-AD to s-µ*g*-MCS cells, irrespective of glucose concentration (Figure 6a–f). Co-localisation with nuclei is observed due to two dyes overlapping and giving a greener colour around the nuclei area in s-µ*g*-AD and s-µ*g*-MCS samples. The s-µ*g*-AD groups showed a stronger fluorescence intensity compared with 1*g* samples. s-µ*g*-MCS exhibited overall the most intense and denser NOX4 deposits.

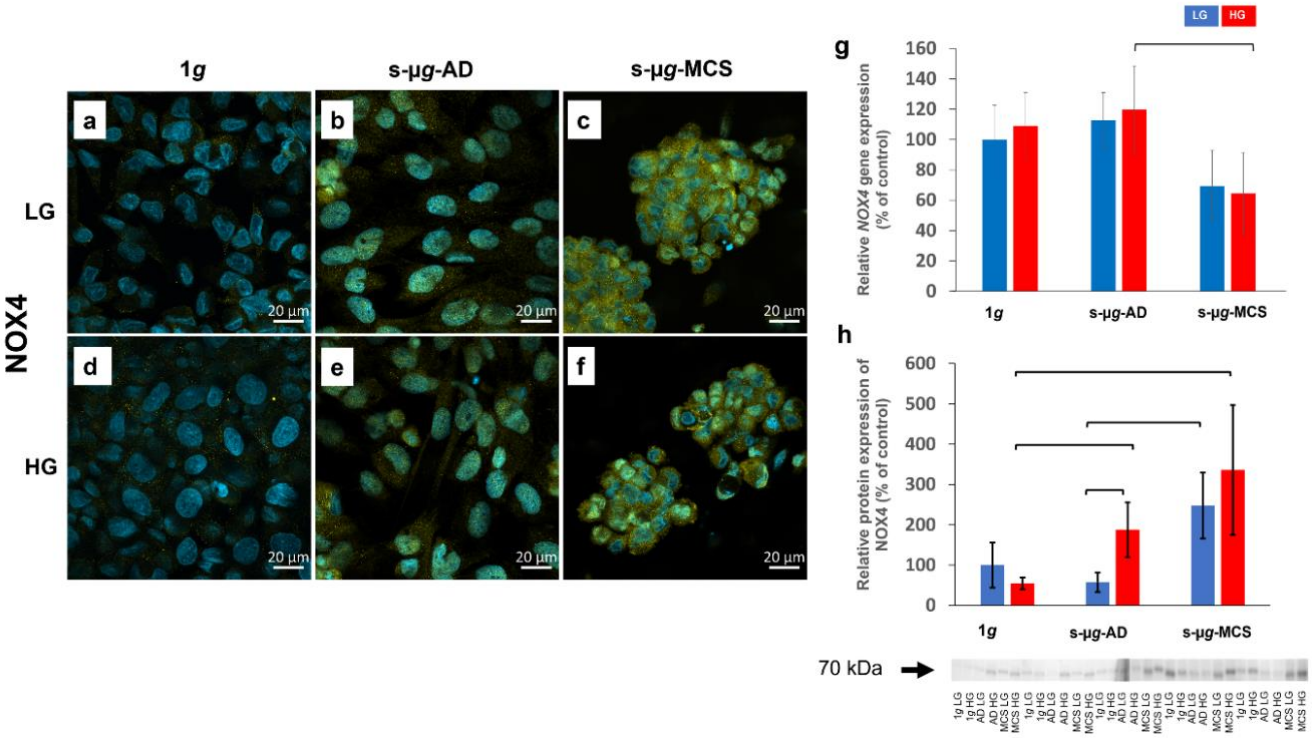

Figure 6. Analysis of NOX4 after 14 days of cultivation either at 1*g* or s-µ*g* and either using low (LG) or high (HG) glucose medium. Data were obtained via immunostaining (**a**–**f**), qPCR (**g**), and Western blot (**h**) techniques. The bracket stands for a significance level of $p < 0.05$.

Relative gene expression of *NOX4* was downregulated in s-µ*g*-MCS, showing a statistically significant decrease in s-µ*g*-MCS HG compared to s-µ*g*-AD HG (Figure 6g). Increased protein expression was observed in HG s-µ*g*-AD, LG s-µ*g*-MCS, and HG s-µ*g*-MCS samples (Figure 6h). In addition, protein levels were significantly higher in HG compared to LG s-µ*g*-AD (see also Figure S5).

3.5.2. Interleukin-8

After the 14-day clinostat exposure, the interleukin-8 (CXCL-8) protein was detected either distributed in the cytoplasm (Figure 7, red arrows) or around the nucleus (Figure 7, yellow arrows). The signal intensities were lower in all LG samples compared to HG. Moreover, 1*g* LG and s-µ*g*-AD LG samples stored CXCL8 in dense deposits on cell edges, while corresponding HG groups had more intracellular granules distributed across the cytoplasm. Both LG and HG MCS showed higher CXCL8 fluorescence intensities.

qPCR results for *CXCL-8* revealed a significant upregulation in both LG and HG s-µ*g* groups compared to the respective 1*g* samples (Figure 7g). The *CXCL8* gene expression in s-µ*g*-AD LG was approximately two-fold higher and more than four-fold higher in s-µ*g*-MCS LG compared to the corresponding 1*g* groups. In HG samples, the expression was almost four-fold higher in both clinorotated AD and MCS groups.

3.6. Endothelial Cells Undergo Apoptosis on the Clinostat

3.6.1. Osteopontin

Using confocal laser scanning microscopy (CLSM), osteopontin was visible in the cytoplasm of all samples (Figure 8a–f). The staining area had a lower fluorescence intensity in s-µ*g*-AD cells compared to s-µ*g*-MCS and 1*g*.

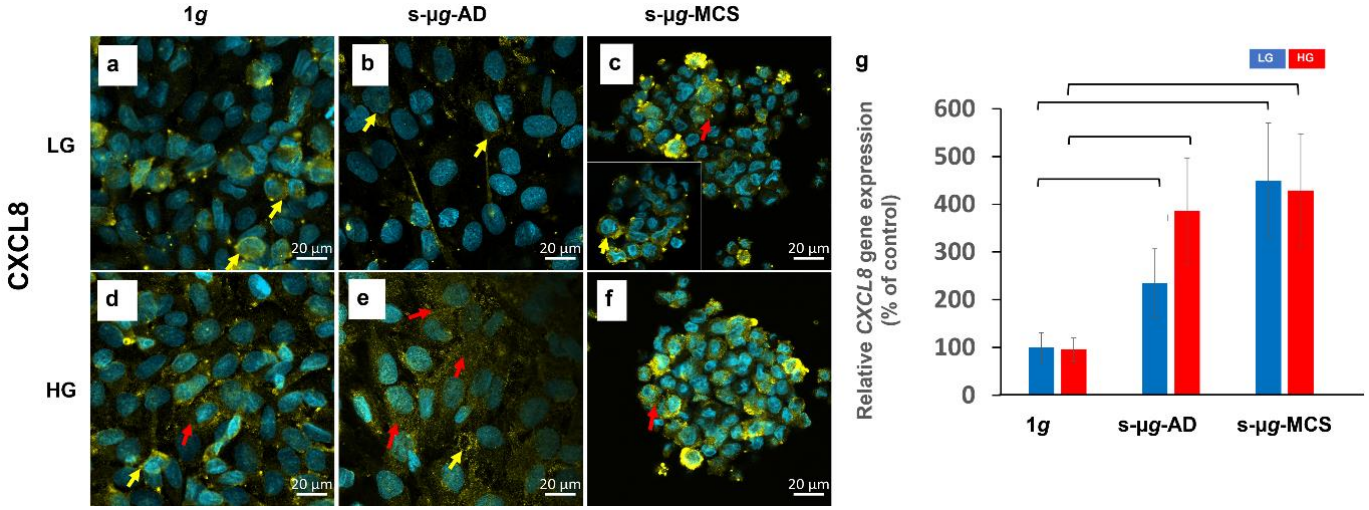

Figure 7. Analysis of CXCL8 after 14 days of cultivation either at 1*g* or s-µ*g* and either using low (LG) or high (HG) glucose medium. Data were obtained via immunostaining (**a**–**f**) and qPCR (**g**). The brackets stand for a significance level of $p < 0.05$.

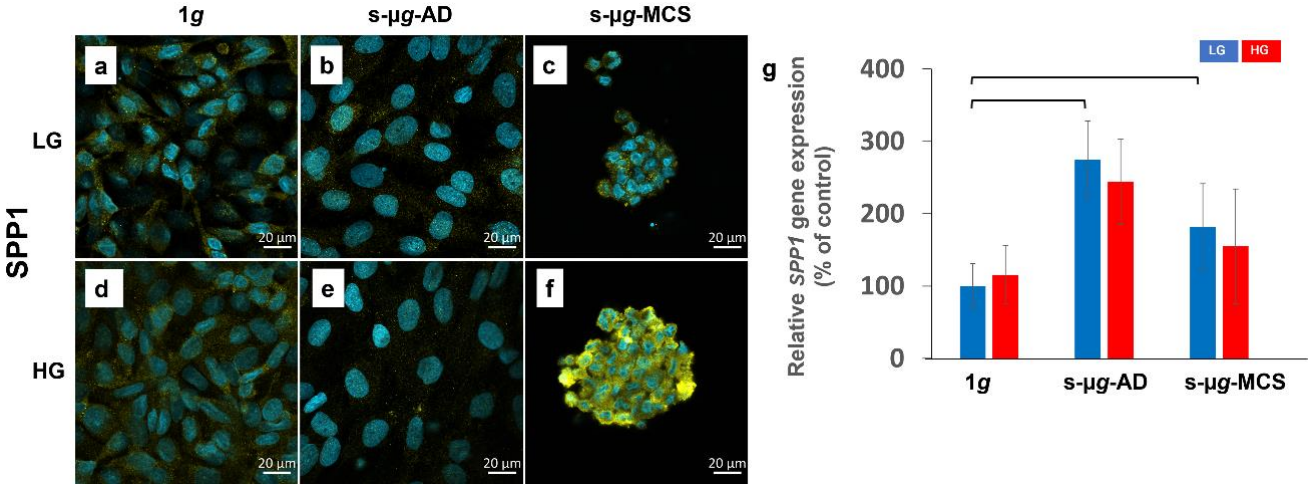

Figure 8. Analysis of SPP1 after 14 days of cultivation either at 1*g* or on the clinostat, either using low (LG) or high (HG) glucose medium. Data were obtained by immunostaining (**a**–**f**) and qPCR (**g**). The two brackets stand for a significance level of $p < 0.05$.

Osteopontin is encoded by the *SPP1* gene. The qPCR results for *SPP1* (Secreted Phosphoprotein 1) revealed a significant upregulation between LG groups: a heightened elevation in clinorotated AD and MCS compared to 1*g*. The tendency for a similar increase was observed in HG samples.

3.6.2. NF-κB p65

NF-κB p65-positive cells were found in all cells. Staining for NF-κB p65 and visualising through CLSM revealed that in all adherent cells in both LG and HG groups, the protein was highly stored in the cytosol (Figure 9, red arrows). Some translocations of NF-κB p65 to the nucleus were detected in s-µ*g*-AD cells and a large number in the s-µ*g*-MCS group (Figure 9, yellow arrows).

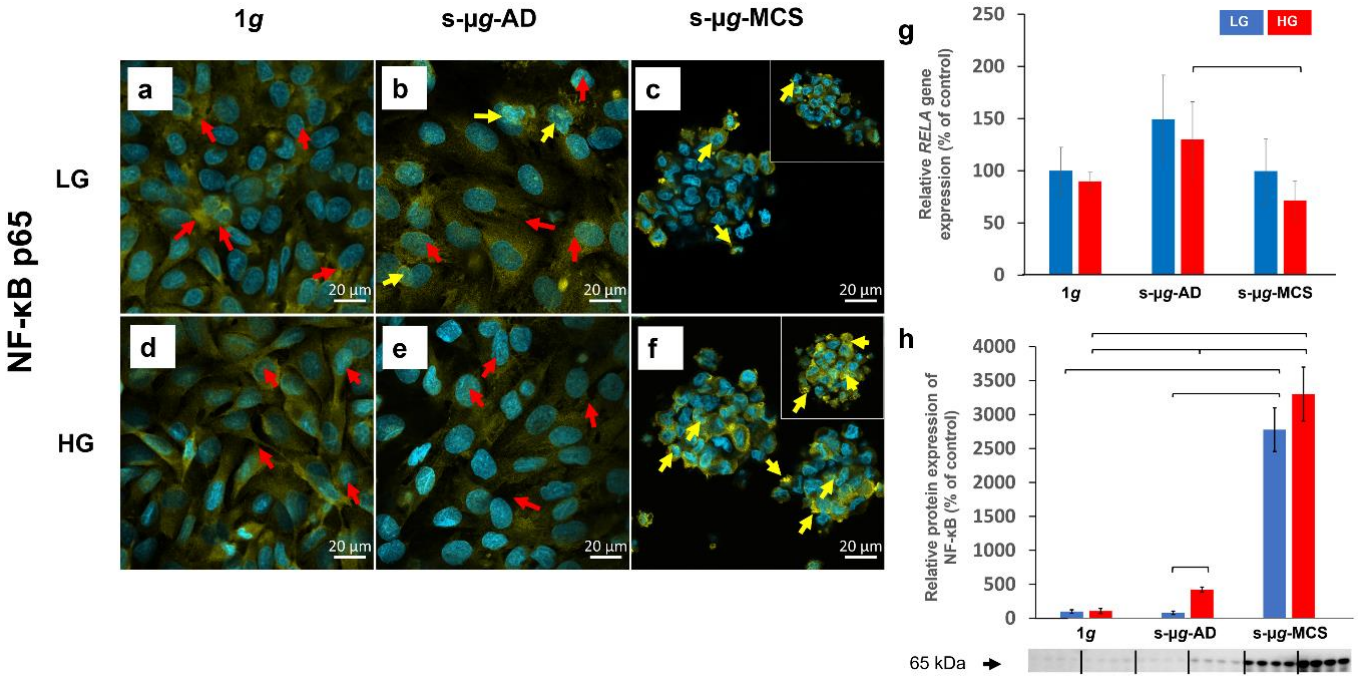

Figure 9. Analysis of NF-κB p65 after 14 days of cultivation either at 1*g* or on the clinostat, either using low (LG) or high (HG) glucose medium. Data were obtained via immunostaining (**a**–**f**), qPCR (**g**), and Western blot (**h**). The brackets stand for a significance level of $p < 0.05$.

qPCR of the NF-κB p65 coding gene *RELA* showed significant downregulation of s-µ*g*-MCS HG compared with s-µ*g*-AD HG cells (Figure 9g). Western blot analysis revealed a significant and very high increase in all s-µ*g*-MCS samples compared to 1*g*. In addition, s-µ*g*-AD cells were influenced by the glucose concentration, which had an impact on the protein expression as a significant upregulation was observed in HG compared to LG (Figures 9h and S4).

3.6.3. Caspase-3

Caspase-3 positive cells were found in all samples (Figure 10, red arrows). Regarding the *CASP3* gene expression, significant up-regulations were detected in s-µ*g*-AD HG and s-µ*g*-MCS HG samples (Figure 10g). The Western blot analysis of cleaved CASP-3 revealed an upregulation in clinorotated AD HG compared to 1*g* HG and a downregulation to baseline levels in s-µ*g*-MCS HG compared to s-µ*g*-AD HG. A clear impact of hyperglycaemia was observed between s-µ*g*-AD samples, with a significant increase in the HG group (Figures 10h and S3).

3.6.4. TUNEL Staining

TUNEL assay and DAPI staining revealed a co-localisation of staining in the nucleus, which indicated the occurrence of apoptosis. As represented in Figure 11 (red arrows), a higher incidence of apoptotic cells was observed in cells cultivated on the clinostat.

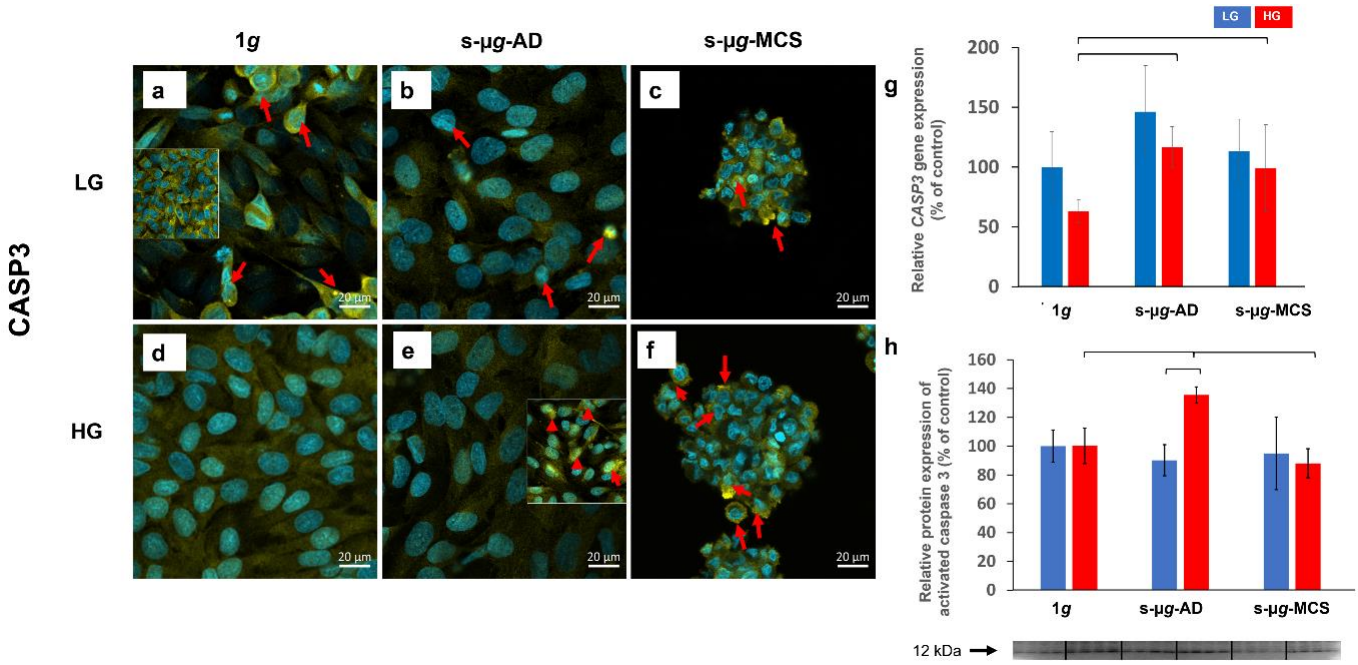

Figure 10. Analysis of CASP3 after 14 days of cultivation either at 1*g* or s-µ*g*, either using low (LG) or high (HG) glucose medium. Data were obtained via immunostaining (**a**–**f**), qPCR (**g**), and Western blot (**h**). The brackets represent a significance level of $p < 0.05$.

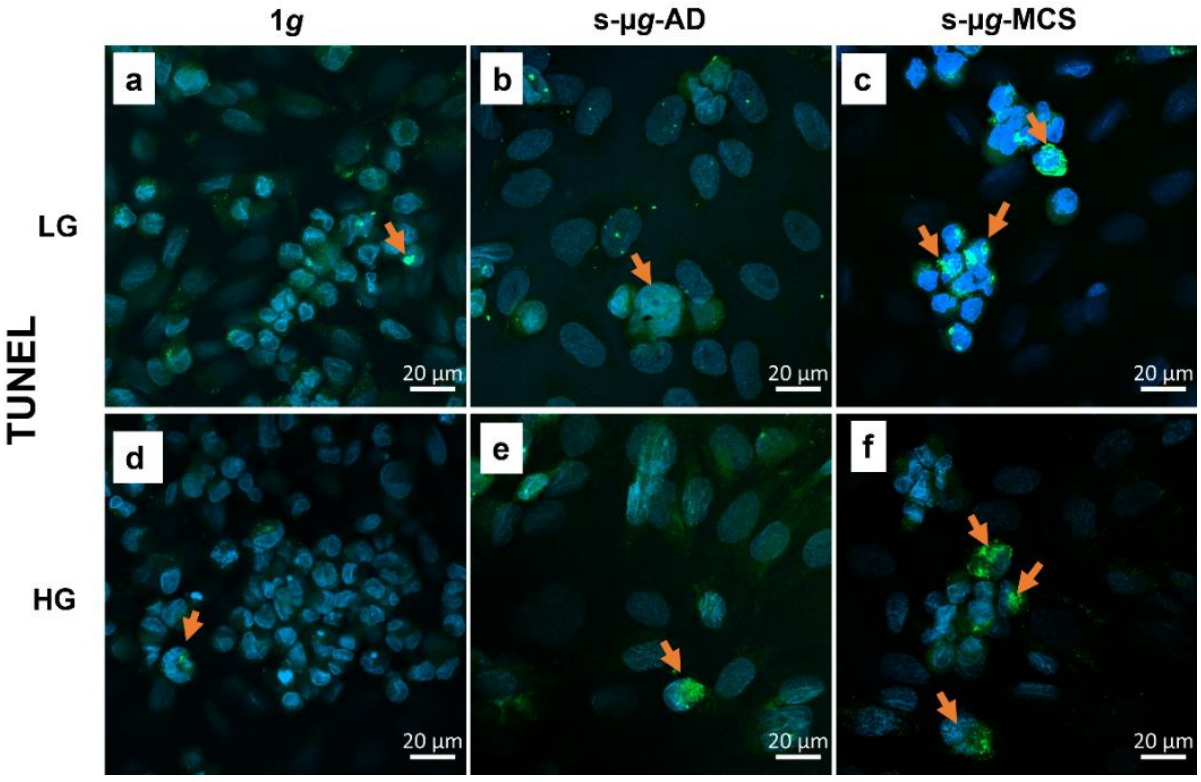

Figure 11. TUNEL assay after 14 days of cultivation, either at 1*g* or on the clinostat and either using low (LG) or high (HG) glucose medium. (**a**) 1*g* in LG; (**b**) s-µ*g* adherent cells in LG; (**c**) s-µ*g* multicellular structures in LG; (**d**) 1*g* in HG; (**e**) s-µ*g* adherent cells in HG; (**f**) s-µ*g* multicellular structures in HG.

4. Discussion

Endothelial cells are heterogenous mechanosensitive cells that undergo morphological, functional, and biochemical changes in μ*g*-conditions [22]. Exposure to real μ*g* (r-μ*g*) can only be achieved using parabolic flights, sounding rockets, space crafts, or space labs, as available on the International Space Station (ISS) [23]. However, high costs and the infrequency of missions limit the performance of such experiments [24]. In addition, a short duration of r-μ*g* in space missions limits the possibility of studies to investigate many lengthy and complex biological processes. Regarding parabolic flight experiments, rapid cycling between 1*g*, 1.8*g*, and μ*g* might also disrupt and interfere with the actual μ*g*-measurements [25]. Various methods to simulate μ*g* on Earth have been established to overcome these limitations, including 2D and 3D clinostats, random positioning machines, rotating wall vessels, and diamagnetic levitation [26]. However, only some aspects of r-μ*g* are mimicked [22]. In μ*g* analogues the extent of the Earth's gravity vector cannot be removed; only its influence or effect can be reduced by randomising the direction of gravity over time (clinostat and random positioning machine) or by counteracting the gravitational force with another force (magnetic levitation). s-μ*g* analogues can only generate similar effects of μ*g* on physiological responses [27].

In the present study, we hypothesised that a high glucose concentration would affect the EA.hy926 cells cultured at 1*g* and μ*g* differently, including their behaviour and key gene and protein expression. Our data indicate that μ*g* had a stronger effect on gene and protein expression than hyperglycaemia. We observed a tendency for downregulation of the ECM genes *FN1* and *COL4A6* in s-μ*g*-MCS, irrespective of HG treatment. No change in *COL1A1* was observed (Figure A1). The fibronectin protein was also downregulated in s-μ*g* groups. Not so many studies have been conducted to investigate the ECM as a complementary counterpart of the gravireception system that consists of the cytoskeleton, ECM, and nucleoskeleton [28]. Our ECM findings differ from the previous similar study [29], though they correspond to the results obtained from r-μ*g* [30]. The variance may be due to different exposure times to μ*g* and the different μ*g*-simulating devices.

Endothelial cells rely on glycolysis to produce energy for cellular metabolism [31]. Triosephosphate isomerase 1 (TPI1) is a key glycolytic enzyme that converts dihydroxyacetone phosphate to glyceraldehyde-3-phosphate [32]. In the study published by Bertelli et al. [33], a transcriptomic analysis revealed a downregulation of TPI1 after 4 weeks of culture in 25 mM D-glucose in comparison with controls. Similarly, the downregulation of glucose transporters is expected under the influence of HG treatment. Even though some studies did not indicate downregulations of glucose transporters in retinal capillary endothelial cells [34] or rat heart endothelial cells [35], vascular endothelial cells exposed to hyperglycaemia usually downregulate the rate of glucose transport by reducing *GLUT1* and *GLUT3* mRNAs and their protein expression. These regulations could be adaptive changes to protect endothelial cells from the damage caused by an excessive glucose influx [36,37]. Interestingly, our findings indicate no significant downregulation of the *GLUT1*, *GLUT3*, and *TPI1* gene expression due to hyperglycaemia. Downregulation of these genes was only caused by the change in gravity. Suppression of the glucose transport might have a connection with suppressed glucose metabolism in general, as was revealed in the study with EA.hy926 cells exposed to r-μ*g* on board the SJ-10 satellite, where the cells displayed a suppressed energy metabolism and glucose uptake [30].

Our study results show that the *TGM2* gene was downregulated and the TG2 protein was upregulated in μ*g*. There are no other studies that provide similar comparable data, but there is evidence that TG2, also known as tissue transglutaminase, is a cross-linking enzyme for fibronectin and mediates adhesion [38]. TG2 is a multifunctional enzyme, and its function in endothelial cell behaviour under μ*g* is unclear. It is known, for instance, that NF-κB activation depends on TG2 cross-linking of IκBα and subsequent proteasomal degradation, which suggests possible TG2 association with inflammation [39]. There is evidence that TG2's function in endothelial cells depends on its location [40]. We observed

a higher perinuclear intracellular TG2 accumulation in clinorotated samples, which might indicate its involvement in endothelial cell proliferation and apoptosis [40].

It has been shown previously that exposure to μ*g* upregulated NOX4 in some other cell types, such as blood mononuclear cells [41]. Some studies found that 4-week hindlimb unloading increased the levels of the pro-oxidative enzymes NOX2 and NOX4 in cerebral arteries but not in mesenteric arteries [42,43]. Our results indicate that NOX4 was significantly increased in s-μ*g*, which corresponds to other studies regarding μ*g* and ROS correlation [44]. The cytokine *CXCL8* was significantly elevated in s-μ*g*-AD and s-μ*g*-MCS, irrespective of HG treatment. These findings agree with earlier results from long-term s-μ*g* and r-μ*g* space missions with other cell types and seem to constitute a central reaction to μ*g*-exposure [45,46].

RELA encodes the ubiquitous transcription factor NF-κB and has a central position in the STRING protein–protein interaction profile of gene expressions studied using qPCR (Figures 9g and 12b). The differential gene expression of *RELA* between adherent cells and spheroids under s-μ*g* in high glucose medium is accompanied by significant upregulation of the chemokine interleukin-8 which encodes the *CXCL8* gene. It should be noted that *CXCL8* regulation by s-μ*g* is independent of the medium composition and aggregation state of the cells (Figure 12b). Recently it could be shown that in non-small cell lung carcinoma cells but not in A549 adenocarcinoma human alveolar basal epithelial cells, the interleukin-8 secretion is influenced by TNF-related apoptosis-inducing ligand (TRAIL) receptors [47]. In A549 cells, *CXCL8* gene expression is regulated by JNK or MEK MAP kinases and ATF4, in addition to NF-κB [47]. In EA.hy926, interestingly, the mitogen-activated protein kinase 8 encoding *MAPK8* is also significantly upregulated in adherent cells compared to spheroids (Figures 12b and A1), just like in NF-κB.

In general, the activation of programmed cell death was observed in this study. The TUNEL assay showed a higher incidence of apoptotic cells in s-μ*g* groups. Additionally, cleaved caspase-3 and the NF-κB protein were elevated in clinorotation groups. The NF-κB protein was also translocated to the nucleus in s-μ*g* samples; thus, the linkage between apoptosis and the pro-apoptotic NF-κB pathway is predicted. In addition, Kang et al. found that the s-μ*g* environment induced microvascular endothelial cell apoptosis and correlated with an increased expression of NF-κB [48]. The osteopontin levels were increased under s-μ*g*, similar to previous studies [49]. The overexpression of the cell adhesion molecule osteopontin is associated with cytoskeletal remodelling and the transition from 2D to 3D growth of endothelial cells under s-μ*g* [50,51]. It has been demonstrated previously that osteopontin has protective effects against apoptosis in endothelial cells [51]. No μ*g*-effects were observed in the regulation of other apoptotic genetic markers, including *CASP8*, *CASP9*, and *PARP1* (Figure A1).

Based on our results, hyperglycaemia had no effect on gene and protein expression in normogravity conditions. In μ*g*-conditions resulting in detached cellular structures, including spheroids and multicellular structures, hyperglycaemia increased the size and the number of spheroid structures, decreased fibronectin and transglutaminase-2, and increased NF-κB, NOX4, and caspase-3.

These findings are in accordance with other studies. It was found that spheroids from human dermal-derived microvascular endothelial cells of healthy donors were smaller and more compact, while spheroids from the cells of diabetic patients were larger in diameter and produced more sprouts [52]. Additionally, the activation of NF-κB signalling (NF-κB/miR-425-5p/MCT4 axis) showed a subsequent induction of apoptosis in endothelial cells under hyperglycaemic conditions [31], and caspase-3 was involved in high glucose-induced apoptosis, as demonstrated by Ho et al. [53]. On the other hand, contrary to our results, other studies found an increase in fibronectin and transglutaminase-2 in hyperglycaemic conditions in endothelial cells [13,54]. This suggests that μ*g* might interfere with hyperglycaemia-triggered pathways.

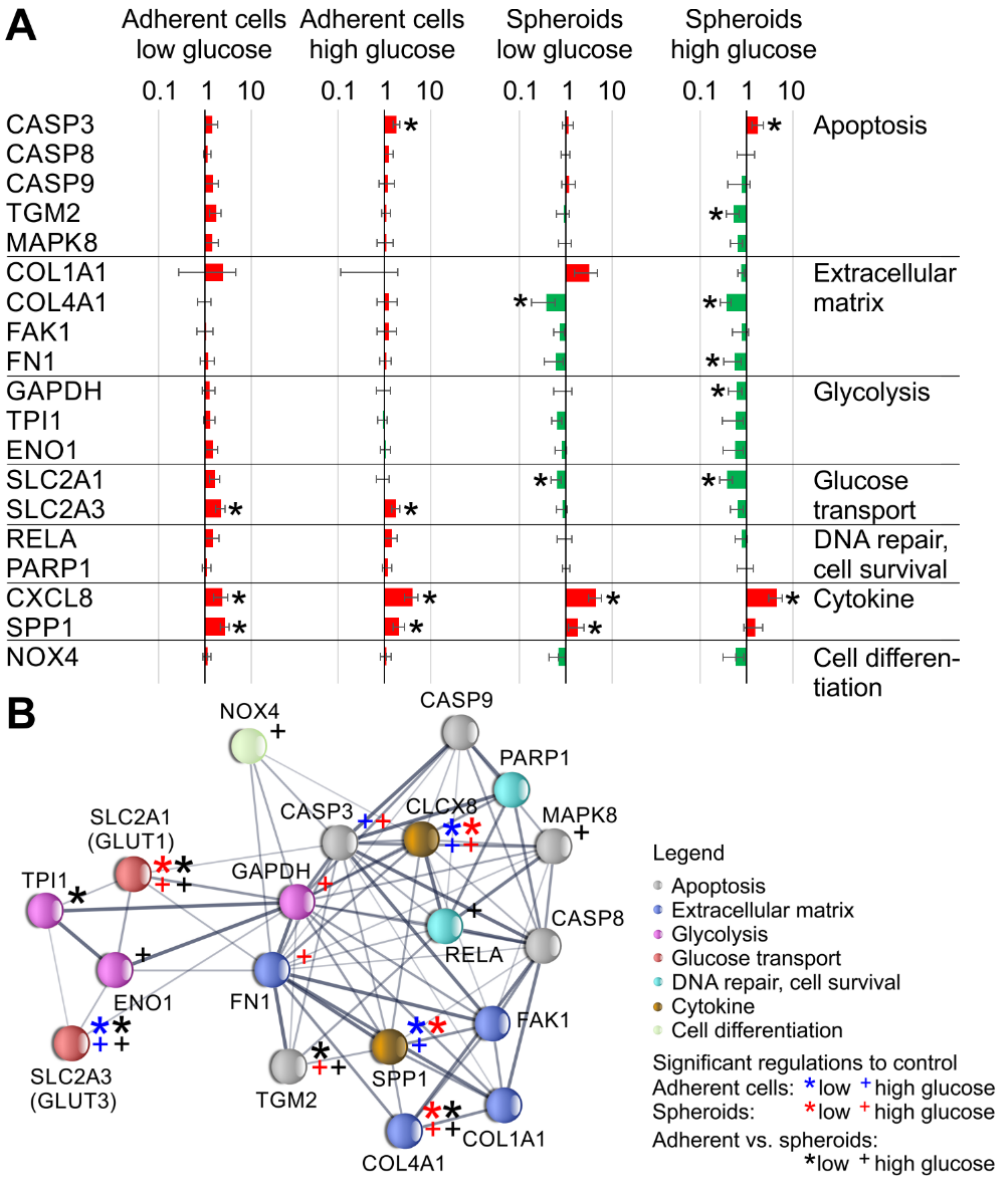

Figure 12. Overview of gene expression changes in the 19 genes quantified through qPCR. (**A**) Gene expression ratios. Significant regulations ($p < 0.05$) are indicated with an asterisk; upregulations or downregulations compared to the 1*g* control are indicated in red and green, respectively. (**B**) EMBL STRING protein–protein interaction of the 19 genes examined. Medium confidence interactions (0.4) with the colour-coded area of protein action are shown.

Overall, our findings show that hyperglycaemia has marked effects in s-µ*g* but not in 1*g*. An overview of all other qPCR results not shown in the results section, including *COL1A1*, *CASP8*, *CASP9*, *PARP1*, and others, is given in Figure A1.

The current study had some limitations, including the evaluation at a fixed time point after 14 days. It is unclear how HG and µ*g* would gradually affect the cell behaviour and phenotype over time. In addition, the study was performed only for 14 days. Long-term effects lasting over 1–2 months in length might be required in future studies. Some of the HG effects may be lost due to the weaker sensitivity to the permanent EA.hy926 cell line stressor compared to primary cells [55]. To better understand the interactions of HG and µ*g*, it might be necessary to evaluate these factors in primary cells or in vivo and co-culture spheroids to make future findings more in vivo-relevant. Diabetogenic states induced in µ*g* might also be related to multisystemic effects. For instance, there might be a connection between skeletal muscle [56] and bone loss [5] or skeletal muscle

glycogen synthesis [57]. Possible bone loss and hyperglycaemia connections in μ*g* might be due to increased glucocorticoids [58]. Increased skeletal muscle glycogen synthesis and overcompensation mean blood glucose depletion that might trigger a higher glucose intake or liver release. In addition, compromised liver carbohydrate metabolism might play a role [59]. These interconnections are not apparent and could be further examined in future studies.

5. Conclusions

Overall, μ*g* revealed a stronger effect on the EA.hy926 cell line's gene and protein expression as opposed to hyperglycaemia. Though, in some cases, a significant effect of hyperglycaemia in μ*g* was observed, such as the stimulation of a higher count and larger-sized MCS formation, the upregulation of the expression of the pro-oxidative enzyme NOX4 and the apoptotic proteins NF-κB and CASP3, and a more pronounced downregulation of fibronectin and transglutaminase-2. We observed an elevated expression of *NOX4* and *CXCL8* due to μ*g*, indicating increased oxidative stress and inflammation. Hyperglycaemia did not cause significant changes in glucose metabolism, and the changes occurred only due to the change in gravity. Our findings bring new insights into the diabetogenic vascular effects of μ*g* and their underlying mechanisms.

Supplementary Materials: The following supporting information can be downloaded at: https://www.mdpi.com/article/10.3390/biom13020189/s1, Figure S1: transglutaminase-2 (TG2); Figure S2: fibronectin (FN1); Figure S3: caspase-3 (CASP3); Figure S4: NF-κB p65; Figure S5: NADPH oxidase 4 (NOX4).

Author Contributions: Conceptualisation, D.G. and U.S.; methodology, J.J., J.S., J.P.-D., M.W. and H.S.; software, H.S.; validation, D.G., M.W., U.S. and H.S.; formal analysis, J.J. and M.W.; investigation, J.J., J.S., M.W., H.S., J.P.-D. and J.L.C.-S.; resources, D.G. and U.S.; data curation, M.W.; writing—original draft preparation, J.J.; writing—review and editing, J.J., D.G., U.S., H.S. and J.P.-D.; visualisation, J.J., J.S., D.G., M.W. and J.P.-D.; supervision, D.G., U.S. and M.W.; project administration, D.G. and U.S.; funding acquisition, D.G. and U.S. All authors have read and agreed to the published version of the manuscript.

Funding: This research was funded by Deutsches Zentrum für Luft- und Raumfahrt (DLR), BMWi projects 50WB1924 and 50WB2219 (D.G.) and by the ESA-WHISPER project (D.G.). U.S. was supported by the NovoNordisk Foundation (NNF20OC0065767).

Institutional Review Board Statement: Not applicable.

Informed Consent Statement: Not applicable.

Data Availability Statement: Not applicable.

Acknowledgments: The authors would like to thank AU Bioimaging Core Facility (Aarhus University, Denmark) for access and guidance in image acquisition. Special thanks to Susie Mogensen (Department of Biomedicine, Aarhus University, Denmark), for her thorough technical support.

Conflicts of Interest: The authors declare no conflict of interest.

Appendix A

Table A1. Overview of the antibodies used for immunocytochemistry and Western blot analyses.

Antibody	Host Animal	Dilution for ICC	Dilution for WB	Supplier, Cat. No.
NOX4	rabbit	1:250	1:4000	Abcam, Cambridge, UK, ab133303
GLUT-1	rabbit	1:200	-	Sigma-Aldrich, 07-1401
GLUT3	rabbit	1:250	-	Abcam, ab41525
TIM	rabbit	1:250	-	Santa Cruz Biotechnology, Dallas, TX, USA, sc-30145

Table A1. *Cont.*

Antibody	Host Animal	Dilution for ICC	Dilution for WB	Supplier, Cat. No.
TG2	mouse	1:250	1:1000	Zedira, Darmstadt, Germany, A033
COL4A6	rabbit	1:250	-	ThermoFischer, PA5-50939
Anti-Fibronectin	rabbit	1:250	1:800	Abcam, ab2413
CASP3	rabbit	1:250	-	Cell Signaling Technology, Danvers, MA, USA, 9662S
Activated CASP3	rabbit	-	1:1000	
OPN	mouse	1:250	-	Sigma-Aldrich, C8487 Sigma-Aldrich, SAB4200018
CXCL8 (IL-8)	mouse	1:250	-	ThermoFischer, AHC0762
NF-κB p65	rabbit	1:200	-	Cell Signaling Technology, 4764S
Anti-Rabbit (Alexa Fluor® 488)	goat	1:500	-	Abcam, ab150077
Anti-Rabbit (Alexa Fluor® 594)	goat	1:500	-	Abcam, ab150080
Anti-Mouse (Alexa Fluor® 488)	goat	1:500	-	Invitrogen™, A11029
Anti-mouse IgG, HRP-linked	horse	-	1:4000	Cell Signaling Technology, 7076S
Anti-rabbit IgG (H+L) Cross-Adsorbed, HRP	goat	-	1:4000	Invitrogen™, G21234

Table A2. Overview of the primers used for qPCR analysis.

Gene Name	Primer Name	Sequence *
18S-rRNA	18S-F	GGAGCCTGCGGCTTAATTT
	18S-R	CAACTAAGAACGGCCATGCA
CASP3	CASP3-F	AACTGCTCCTTTTGCTGTGATCT
	CASP3-R	GCAGCAAACCTCAGGGAAAC
CASP8	CASP8-F	TGCAAAAGCACGGGAGAAAG
	CASP8-R	CTCTTCAAAGGTCGTGGTCAAAG
CASP9	CASP9-F	CTCCAACATCGACTGTGAGAAGTT
	CASP9-R	GCGCCAGCTCCAGCAA
COL1A1	COL1A1-F	CGATGGATTCCCGTTCGAGT
	COL1A1-R	GAGGCCTCGGTGGACATTAG
COL4A6	COL4-F	GGTACCTGTAACTACTATGCCAACTCCTA
	COL4-R	CGGCTAATTCGTGTCCTCAAG
CXCL8	CXCL8-F	TGGCAGCCTTCCTGATTTCT
	CXCL8-R	GGGTGGAAAGGTTTGGAGTATG
ENO1	ENO1-F	TGGGAAAGATGCCACCAATGT
	ENO1-R	GCAGCTCCAGGCCTTCTTTA
FAK1	FAK1-F	TGTGGGTAAACCAGATCCTGC
	FAK1-R	CTGAAGCTTGACACCCTCGT
FN1	FN1-F	AGATCTACCTGTACACCTTGAATGACA
	FN1-R	CATGATACCAGCAAGGAATTGG
GAPDH	GAPDH-F	CCACATCGCTCAGACACCAT
	GAPDH-R	GCAACAATATCCACTTTACCAGAGTTAA
GLUT1	GLUT1-F	TTCACTGTCGTGTCGCTGTT
	GLUT1-R	TGAGTATGGCACAACCCGC
GLUT3	GLUT3-F	ACATTTTGAAGGTTTTGTTGGCTG
	GLUT3-R	TCAGAGCTGGGGTGACCTTC
JNK1	JNK1-F	TCTCCTTTAGGTGCAGCAGTG
	JNK1-R	CAGAGGCCAAAGTCGGATCT

Table A2. *Cont.*

Gene Name	Primer Name	Sequence *
NOX4	NOX4-F	ACCCTCACAATGTGTCCAAC
	NOX4-R	CTCGAAATCGTTCTGTCCAGTC
PARP1	PARP1-F	CGAGTCGAGTACGCCAAGAG
	PARP1-R	CATCAAACATGGGCGACTGC
RELA	RELA-F	ACTGCCGGGATGGCTTCT
	RELA-R	CGCTTCTTCACACACTGGATTC
SPP1	SPP1-F	CCGAGGTGATAGCTTGGCTT
	SPP1-R	TGTGGCATCAGGATACTGTTCA
TGM2	TGM2-F	AAGAGGAGCGGCAGGAGTATG
	TGM2-R	GCCCAAAATTCCAAGGTATGTTC
TPI1	TPI1-F	CAAGGTCGTCCTGGCCTATG
	TPI1-R	TGTACTTCCTGGGCCTGTTG

* All sequences are given in 5′-3′direction.

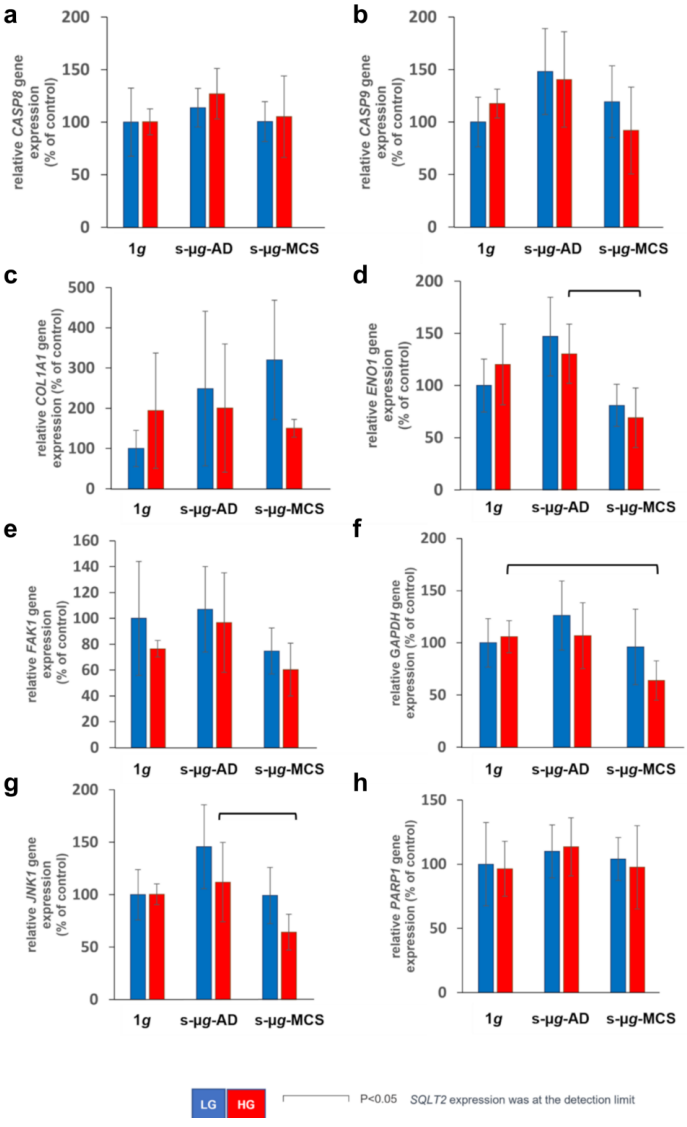

Figure A1. qPCR analysis for other genes assessed in this study. The gene expression of (**a**) *CASP8*, (**b**) *CASP9*, (**c**) *COL1A1*, (**e**) *FAK1*, and (**h**) *PARP1*, was not significantly altered during the 14-day clinostat exposure and HG treatment. (**d**) *ENO1* and (**g**) *JNK1* were significantly downregulated in high-glucose s-µ*g*-MCS cells compared to high-glucose s-µ*g*-AD cells. (**f**) *GAPDH* was mostly not regulated during the 14-day s-µ*g*-exposure and HG treatment, except for HG 1*g* control vs. HG MCS.

References

1. Grimm, D. Microgravity and space medicine. *Int. J. Mol. Sci.* **2021**, *22*, 6697. [CrossRef] [PubMed]
2. Löbrich, M.; Jeggo, P.A. Hazards of human spaceflight. *Science* **2019**, *364*, 127–128. [CrossRef]
3. Wang, Y.; Zhao, W.; Shi, J.; Wang, J.; Hao, J.; Pang, X.; Huang, X.; Chen, X.; Li, Y.; Jin, R.; et al. Intestinal microbiota contributes to altered glucose metabolism in simulated microgravity mouse model. *FASEB J.* **2019**, *33*, 10140–10151. [CrossRef]
4. Garrett-Bakelman, F.E.; Darshi, M.; Green, S.J.; Gur, R.C.; Lin, L.; Macias, B.R.; McKenna, M.J.; Meydan, C.; Mishra, T.; Nasrini, J.; et al. The NASA twins study: A multidimensional analysis of a year-long human spaceflight. *Science* **2019**, *364*, eaau8650. [CrossRef]
5. Tobin, B.W.; Uchakin, P.N.; Leeper-Woodford, S.K. Insulin secretion and sensitivity in space flight: Diabetogenic effects. *Nutrition* **2002**, *18*, 842–848. [CrossRef] [PubMed]
6. Hughson, R.L.; Robertson, A.D.; Arbeille, P.; Shoemaker, J.K.; Rush, J.W.E.; Fraser, K.S.; Greaves, D.K. Increased postflight carotid artery stiffness and inflight insulin resistance resulting from 6-mo spaceflight in male and female astronauts. *Am. J. Physiol. Heart Circ. Physiol.* **2016**, *310*, H628–H638. [CrossRef] [PubMed]
7. Yang, C.; Chen, J.; Wu, F.; Li, J.; Liang, P.; Zhang, H.; Wang, H.; Li, Y.; Wan, Y.; Qin, L.; et al. Effects of 60-day head-down bed rest on osteocalcin, glycolipid metabolism and their association with or without resistance training. *Clin. Endocrinol.* **2014**, *81*, 671–678. [CrossRef] [PubMed]
8. de Abreu, S.; Amirova, L.; Murphy, R.; Wallace, R.; Twomey, L.; Gauquelin-Koch, G.; Raverot, V.; Larcher, F.; Custaud, M.A.; Navasiolava, N. Multi-System Deconditioning in 3-Day Dry Immersion without Daily Raise. *Front. Physiol.* **2017**, *8*, 799. [CrossRef]
9. Strollo, F.; Gentile, S.; Pipicelli, A.M.V.; Mambro, A.; Monici, M.; Magni, P. Space Flight-Promoted Insulin Resistance as a Possible Disruptor of Wound Healing. *Front. Bioeng. Biotechnol.* **2022**, *10*, 868999. [CrossRef]
10. Mapanga, R.F.; Essop, M.F. Damaging effects of hyperglycemia on cardiovascular function: Spotlight on glucose metabolic pathways. *Am. J. Physiol. Heart Circ. Physiol.* **2016**, *310*, H153–H173. [CrossRef]
11. Allen, D.A.; Yaqoob, M.M.; Harwood, S.M. Mechanisms of high glucose-induced apoptosis and its relationship to diabetic complications. *J. Nutr. Biochem.* **2005**, *16*, 705–713. [CrossRef]
12. Bhedi, C.D.; Nasirova, S.; Toksoz, D.; Warburton, R.R.; Morine, K.J.; Kapur, N.K.; Galper, J.B.; Preston, I.R.; Hill, N.S.; Fanburg, B.L.; et al. Glycolysis regulated transglutaminase 2 activation in cardiopulmonary fibrogenic remodeling. *FASEB J.* **2020**, *34*, 930–944. [CrossRef] [PubMed]
13. Bhatt, M.P.; Lim, Y.-C.; Hwang, J.; Na, S.; Kim, Y.-M.; Ha, K.-S. C-Peptide Prevents Hyperglycemia-Induced Endothelial Apoptosis Through Inhibition of Reactive Oxygen Species–Mediated Transglutaminase 2 Activation. *Diabetes* **2013**, *62*, 243. [CrossRef] [PubMed]
14. Zeng, Y.; Du, X.; Yao, X.; Qiu, Y.; Jiang, W.; Shen, J.; Li, L.; Liu, X. Mechanism of cell death of endothelial cells regulated by mechanical forces. *J. Biomech.* **2022**, *131*, 110917. [CrossRef]
15. Edgell, C.J.S.; Haizlip, J.E.; Bagnell, C.R.; Packenham, J.P.; Harrison, P.; Wilbourn, B.; Madden, V.J. Endothelium specific Weibel-Palade bodies in a continuous human cell line, EA.hy926. *In Vitro Cell. Dev. Biol.* **1990**, *26*, 1167–1172. [CrossRef] [PubMed]
16. Pietsch, J.; Gass, S.; Nebuloni, S.; Echegoyen, D.; Riwaldt, S.; Baake, C.; Bauer, J.; Corydon, T.J.; Egli, M.; Infanger, M.; et al. Three-dimensional growth of human endothelial cells in an automated cell culture experiment container during the SpaceX CRS-8 ISS space mission—The SPHEROIDS project. *Biomaterials* **2017**, *124*, 126–156. [CrossRef]
17. Baran, R.; Marchal, S.; Campos, S.G.; Rehnberg, E.; Tabury, K.; Baselet, B.; Wehland, M.; Grimm, D.; Baatout, S. The Cardiovascular System in Space: Focus on In Vivo and In Vitro Studies. *Biomedicines* **2022**, *10*, 59. [CrossRef]
18. Grimm, D.; Schulz, H.; Krüger, M.; Cortés-Sánchez, J.L.; Egli, M.; Kraus, A.; Sahana, J.; Corydon, T.J.; Hemmersbach, R.; Wise, P.M.; et al. The Fight against Cancer by Microgravity: The Multicellular Spheroid as a Metastasis Model. *Int. J. Mol. Sci.* **2022**, *23*, 3073. [CrossRef]
19. Nassef, M.Z.; Kopp, S.; Melnik, D.; Corydon, T.J.; Sahana, J.; Krüger, M.; Wehland, M.; Bauer, T.J.; Liemersdorf, C.; Hemmersbach, R.; et al. Short-Term Microgravity Influences Cell Adhesion in Human Breast Cancer Cells. *Int. J. Mol. Sci.* **2019**, *20*, 5730. [CrossRef]
20. Nassef, M.Z.; Kopp, S.; Wehland, M.; Melnik, D.; Sahana, J.; Krüger, M.; Corydon, T.J.; Oltmann, H.; Schmitz, B.; Schütte, A.; et al. Real Microgravity Influences the Cytoskeleton and Focal Adhesions in Human Breast Cancer Cells. *Int. J. Mol. Sci.* **2019**, *20*, 3156. [CrossRef]
21. Snel, B.; Lehmann, G.; Bork, P.; Huynen, M.A. STRING: A web-server to retrieve and display the repeatedly occurring neighbourhood of a gene. *Nucleic Acids Res.* **2000**, *28*, 3442. [CrossRef] [PubMed]
22. Cotrupi, S.; Ranzani, D.; Maier, J.A.M. Impact of modeled microgravity on microvascular endothelial cells. *Biochim. Biophys. Acta-Mol. Cell Res.* **2005**, *1746*, 163–168. [CrossRef] [PubMed]
23. Maier, J.A.M.; Cialdai, F.; Monici, M.; Morbidelli, L. The Impact of Microgravity and Hypergravity on Endothelial Cells. *Biomed Res. Int.* **2015**, *2015*, 434803. [CrossRef]
24. Grimm, D.; Wehland, M.; Pietsch, J.; Aleshcheva, G.; Wise, P.; Van Loon, J.; Ulbrich, C.; Magnusson, N.E.; Infanger, M.; Bauer, J. Growing tissues in real and simulated microgravity: New methods for tissue engineering. *Tissue Eng. Part B Rev.* **2014**, *20*, 555–566. [CrossRef] [PubMed]

25. van Loon, J.J.W.A. Centrifuges for Microgravity Simulation. The Reduced Gravity Paradigm. *Front. Astron. Sp. Sci.* **2016**, *3*, 21. [CrossRef]
26. Herranz, R.; Anken, R.; Boonstra, J.; Braun, M.; Christianen, P.C.M.; De Geest, M.; Hauslage, J.; Hilbig, R.; Hill, R.J.A.; Lebert, M.; et al. Ground-Based Facilities for Simulation of Microgravity: Organism-Specific Recommendations for Their Use, and Recommended Terminology. *Astrobiology* **2013**, *13*, 1–17. [CrossRef]
27. Oluwafemi, F.A.; Neduncheran, A. Analog and simulated microgravity platforms for life sciences research: Their individual capacities, benefits and limitations. *Adv. Sp. Res.* **2022**, *69*, 2921–2929. [CrossRef]
28. Andreeva, E.; Matveeva, D.; Zhidkova, O.; Zhivodernikov, I.; Kotov, O.; Buravkova, L. Real and Simulated Microgravity: Focus on Mammalian Extracellular Matrix. *Life* **2022**, *12*, 1343. [CrossRef]
29. Dittrich, A.; Grimm, D.; Sahana, J.; Bauer, J.; Kröger, M.; Infanger, M.; Magnusson, N.E. Key Proteins Involved in Spheroid Formation and Angiogenesis in Endothelial Cells After Long-Term Exposure to Simulated Microgravity. *Cell. Physiol. Biochem.* **2018**, *45*, 429–445. [CrossRef]
30. Li, N.; Wang, C.; Sun, S.; Zhang, C.; Lü, D.; Chen, Q.; Long, M. Microgravity-Induced Alterations of Inflammation-Related Mechanotransduction in Endothelial Cells on Board SJ-10 Satellite. *Front. Physiol.* **2018**, *9*, 1025. [CrossRef]
31. Luo, E.; Wang, D.; Yan, G.; Qiao, Y.; Zhu, B.; Liu, B.; Hou, J.; Tang, C. The NF-κB/miR-425-5p/MCT4 axis: A novel insight into diabetes-induced endothelial dysfunction. *Mol. Cell. Endocrinol.* **2020**, *500*, 110641. [CrossRef]
32. Daniel, B.; Livne, A.; Cohen, G.; Kahremany, S.; Sasson, S. Endothelial Cell–Derived Triosephosphate Isomerase Attenuates Insulin Secretion From Pancreatic Beta Cells of Male Rats. *Endocrinology* **2021**, *162*, bqaa234. [CrossRef] [PubMed]
33. Bertelli, P.M.; Pedrini, E.; Hughes, D.; McDonnell, S.; Pathak, V.; Peixoto, E.; Guduric-Fuchs, J.; Stitt, A.W.; Medina, R.J. Long term high glucose exposure induces premature senescence in retinal endothelial cells. *Front. Physiol.* **2022**, *13*, 929118. [CrossRef]
34. Fernandes, R.; Suzuki, K.; Kumagai, A.K. Inner blood-retinal barrier GLUT1 in long-term diabetic rats: An immunogold electron microscopic study. *Investig. Ophthalmol. Vis. Sci.* **2003**, *44*, 3150–3154. [CrossRef] [PubMed]
35. Hirsch, B.; Rösen, P. Diabetes mellitus induces long lasting changes in the glucose transporter of rat heart endothelial cells. *Horm. Metab. Res.* **1999**, *31*, 645–652. [CrossRef] [PubMed]
36. Riahi, Y.; Sin-Malia, Y.; Cohen, G.; Alpert, E.; Gruzman, A.; Eckel, J.; Staels, B.; Guichardant, M.; Sasson, S. The Natural Protective Mechanism Against Hyperglycemia in Vascular Endothelial CellsRoles of the Lipid Peroxidation Product 4-Hydroxydodecadienal and Peroxisome Proliferator–Activated Receptor δ. *Diabetes* **2010**, *59*, 808–818. [CrossRef] [PubMed]
37. Leão, L.L.; Tangen, G.; Barca, M.L.; Engedal, K.; Santos, S.H.S.; Machado, F.S.M.; de Paula, A.M.B.; Monteiro-Junior, R.S. Does hyperglycemia downregulate glucose transporters in the brain? *Med. Hypotheses* **2020**, *139*, 109614. [CrossRef]
38. Akimov, S.S.; Krylov, D.; Fleischmana, L.F.; Belkin, A.M. Tissue Transglutaminase Is an Integrin-Binding Adhesion Coreceptor for Fibronectin. *J. Cell Biol.* **2000**, *148*, 825. [CrossRef]
39. Eckert, R.L.; Kaartinen, M.T.; Nurminskaya, M.; Belkin, A.M.; Colak, G.; Johnson, G.V.W.; Mehta, K. Transglutaminase Regulation of Cell Function. *Physiol. Rev.* **2014**, *94*, 383. [CrossRef]
40. Nadalutti, C.; Viiri, K.M.; Kaukinen, K.; Mäki, M.; Lindfors, K. Extracellular transglutaminase 2 has a role in cell adhesion, whereas intracellular transglutaminase 2 is involved in regulation of endothelial cell proliferation and apoptosis. *Cell Prolif.* **2011**, *44*, 49–58. [CrossRef]
41. Bisserier, M.; Shanmughapriya, S.; Rai, A.K.; Gonzalez, C.; Brojakowska, A.; Garikipati, V.N.S.; Madesh, M.; Mills, P.J.; Walsh, K.; Arakelyan, A.; et al. Cell-free mitochondrial DNA as a potential biomarker for astronauts' health. *J. Am. Heart Assoc.* **2021**, *10*, 22055. [CrossRef] [PubMed]
42. Peng, L.; Ran, H.H.; Zhang, Y.; Zhao, Y.; Fan, Y.Y.; Peng, L.; Zhang, R.; Cao, F. NADPH Oxidase Accounts for Changes in Cerebrovascular Redox Status in Hindlimb Unweighting Rats. *Biomed. Environ. Sci.* **2015**, *28*, 799–807. [CrossRef] [PubMed]
43. Zhang, R.; Ran, H.H.; Peng, L.; Xu, F.; Sun, J.F.; Zhang, L.N.; Fan, Y.Y.; Peng, L.; Cui, G. Mitochondrial regulation of NADPH oxidase in hindlimb unweighting rat cerebral arteries. *PLoS ONE* **2014**, *9*, e95916. [CrossRef]
44. Takahashi, K.; Okumura, H.; Guo, R.; Naruse, K. Effect of Oxidative Stress on Cardiovascular System in Response to Gravity. *Int. J. Mol. Sci.* **2017**, *18*, 1426. [CrossRef]
45. Dietrichs, D.; Grimm, D.; Sahana, J.; Melnik, D.; Corydon, T.J.; Wehland, M.; Krüger, M.; Vermeesen, R.; Baselet, B.; Baatout, S.; et al. Three-Dimensional Growth of Prostate Cancer Cells Exposed to Simulated Microgravity. *Front. Cell Dev. Biol.* **2022**, *10*, 234. [CrossRef]
46. Kopp, S.; Krüger, M.; Bauer, J.; Wehland, M.; Corydon, T.J.; Sahana, J.; Nassef, M.Z.; Melnik, D.; Bauer, T.J.; Schulz, H.; et al. Microgravity Affects Thyroid Cancer Cells during the TEXUS-53 Mission Stronger than Hypergravity. *Int. J. Mol. Sci.* **2018**, *19*, 4001. [CrossRef] [PubMed]
47. Favaro, F.; Luciano-Mateo, F.; Moreno-Caceres, J.; Hernández-Madrigal, M.; Both, D.; Montironi, C.; Püschel, F.; Nadal, E.; Eldering, E.; Muñoz-Pinedo, C. TRAIL receptors promote constitutive and inducible IL-8 secretion in non-small cell lung carcinoma. *Cell Death Dis.* **2022**, *13*, 1046. [CrossRef]
48. Kang, C.Y.; Zou, L.; Yuan, M.; Wang, Y.; Li, T.Z.; Zhang, Y.; Wang, J.F.; Li, Y.; Deng, X.W.; Liu, C.T. Impact of simulated microgravity on microvascular endothelial cell apoptosis. *Eur. J. Appl. Physiol.* **2011**, *111*, 2131–2138. [CrossRef]
49. Infanger, M.; Kossmehl, P.; Shakibaei, M.; Baatout, S.; Witzing, A.; Grosse, J.; Bauer, J.; Cogoli, A.; Faramarzi, S.; Derradji, H.; et al. Induction of three-dimensional assembly and increase in apoptosis of human endothelial cells by simulated microgravity: Impact of vascular endothelial growth factor. *Apoptosis* **2006**, *11*, 749–764. [CrossRef]

50. Buravkova, L.B.; Rudimov, E.G.; Andreeva, E.R.; Grigoriev, A.I. The ICAM-1 expression level determines the susceptibility of human endothelial cells to simulated microgravity. *J. Cell. Biochem.* **2018**, *119*, 2875–2885. [CrossRef]
51. Mamazhakypov, A.; Sartmyrzaeva, M.; Sarybaev, A.S.; Schermuly, R.; Sydykov, A. Clinical and Molecular Implications of Osteopontin in Heart Failure. *Curr. Issues Mol. Biol.* **2022**, *44*, 3573–3597. [CrossRef] [PubMed]
52. Vorwald, C.E.; Murphy, K.C.; Leach, J.K. Restoring Vasculogenic Potential of Endothelial Cells from Diabetic Patients Through Spheroid Formation. *Cell. Mol. Bioeng.* **2018**, *11*, 267–278. [CrossRef] [PubMed]
53. Ho, F.M.; Liu, S.H.; Liau, C.S.; Huang, P.J.; Lin-Shiau, S.Y. High glucose-induced apoptosis in human endothelial cells is mediated by sequential activations of c-Jun NH(2)-terminal kinase and caspase-3. *Circulation* **2000**, *101*, 2618–2624. [CrossRef]
54. Roy, S.; Sala, R.; Cagliero, E.; Lorenzi, M. Overexpression of fibronectin induced by diabetes or high glucose: Phenomenon with a memory. *Proc. Natl. Acad. Sci. USA* **1990**, *87*, 404–408. [CrossRef]
55. Uruski, P.; Mikuła-Pietrasik, J.; Drzewiecki, M.; Budkiewicz, S.; Gładki, M.; Kurmanalina, G.; Tykarski, A.; Książek, K. Diverse functional responses to high glucose by primary and permanent hybrid endothelial cells in vitro. *J. Mol. Cell. Cardiol.* **2021**, *156*, 1–6. [CrossRef] [PubMed]
56. Stuart, C.A.; Shangraw, R.E.; Prince, M.J.; Peters, E.J.; Wolfe, R.R. Bed-rest-induced insulin resistance occurs primarily in muscle. *Metabolism.* **1988**, *37*, 802–806. [CrossRef]
57. Hirose, M.; Kaneki, M.; Sugita, H.; Yasuhara, S.; Martyn, J.A.J. Immobilization depresses insulin signaling in skeletal muscle. *Am. J. Physiol. Endocrinol. Metab.* **2000**, *279*, 1235–1241. [CrossRef]
58. Yang, J.; Yang, Z.; Li, W.; Xue, Y.; Xu, H.; Li, J.; Shang, P. Glucocorticoid: A potential role in microgravity-induced bone loss. *Acta Astronaut.* **2017**, *140*, 206–212. [CrossRef]
59. Vinken, M. Hepatology in space: Effects of spaceflight and simulated microgravity on the liver. *Liver Int.* **2022**, *42*, 2599–2606. [CrossRef]

11.3 Publication #3

Cortés-Sánchez, J. L., Melnik, D., Sandt, V., Kahlert, S., Marchal, S., Johnson, I. R., ... & Krüger, M. (2023). Fluid and Bubble Flow Detach Adherent Cancer Cells to Form Spheroids on a Random Positioning Machine. Cells, 12(22), 2665.

cells

MDPI

Article

Fluid and Bubble Flow Detach Adherent Cancer Cells to Form Spheroids on a Random Positioning Machine

José Luis Cortés-Sánchez [1], Daniela Melnik [1,2], Viviann Sandt [1], Stefan Kahlert [3], Shannon Marchal [1], Ian R. D. Johnson [4], Marco Calvaruso [5], Christian Liemersdorf [6], Simon L. Wuest [7], Daniela Grimm [1,2,8] and Marcus Krüger [1,2,*]

1 Department of Microgravity and Translational Regenerative Medicine, Otto-von-Guericke University, 39106 Magdeburg, Germany; jose.cortes@ovgu.de (J.L.C.-S.); daniela.melnik@med.ovgu.de (D.M.); viviann.sandt@med.ovgu.de (V.S.); shannon.marchal@med.ovgu.de (S.M.); daniela.grimm@med.ovgu.de (D.G.)
2 Research Group "Magdeburger Arbeitsgemeinschaft für Forschung unter Raumfahrt- und Schwerelosigkeitsbedingungen" (MARS), Otto-von-Guericke University, 39106 Magdeburg, Germany
3 Institute of Anatomy, University Hospital Magdeburg, 39120 Magdeburg, Germany; stefan.kahlert@med.ovgu.de
4 Research in Space Environments Group, UniSA Clinical and Health Sciences, University of South Australia, Adelaide, SA 5000, Australia; ian.johnson@unisa.edu.au
5 Institute of Bioimaging and Molecular Physiology, National Research Council (IBFM-CNR), 90015 Cefalù, Italy; marco.calvaruso@ibfm.cnr.it
6 Department of Gravitational Biology, Institute of Aerospace Medicine, German Aerospace Center, 51147 Cologne, Germany; christian.liemersdorf@dlr.de
7 Institute of Medical Engineering, Lucerne University of Applied Sciences and Arts, 6052 Hergiswil, Switzerland; simon.wueest@hslu.ch
8 Department of Biomedicine, Aarhus University, 8000 Aarhus C, Denmark
* Correspondence: marcus.krueger@med.ovgu.de; Tel.: +49-391-67-57471

Citation: Cortés-Sánchez, J.L.; Melnik, D.; Sandt, V.; Kahlert, S.; Marchal, S.; Johnson, I.R.D.; Calvaruso, M.; Liemersdorf, C.; Wuest, S.L.; Grimm, D.; et al. Fluid and Bubble Flow Detach Adherent Cancer Cells to Form Spheroids on a Random Positioning Machine. *Cells* **2023**, *12*, 2665. https://doi.org/10.3390/cells12222665

Academic Editor: Alexander E. Kalyuzhny

Received: 30 October 2023
Revised: 10 November 2023
Accepted: 17 November 2023
Published: 20 November 2023

Abstract: In preparing space and microgravity experiments, the utilization of ground-based facilities is common for initial experiments and feasibility studies. One approach to simulating microgravity conditions on Earth is to employ a random positioning machine (RPM) as a rotary bioreactor. Combined with a suitable low-mass model system, such as cell cultures, these devices simulating microgravity have been shown to produce results similar to those obtained in a space experiment under real microgravity conditions. One of these effects observed under real and simulated microgravity is the formation of spheroids from 2D adherent cancer cell cultures. Since real microgravity cannot be generated in a laboratory on Earth, we aimed to determine which forces lead to the detachment of individual FTC-133 thyroid cancer cells and the formation of tumor spheroids during culture with exposure to random positioning modes. To this end, we subdivided the RPM motion into different static and dynamic orientations of cell culture flasks. We focused on the molecular activation of the mechanosignaling pathways previously associated with spheroid formation in microgravity. Our results suggest that RPM-induced spheroid formation is a two-step process. First, the cells need to be detached, induced by the cell culture flask's rotation and the subsequent fluid flow, as well as the presence of air bubbles. Once the cells are detached and in suspension, random positioning prevents sedimentation, allowing 3D aggregates to form. In a comparative shear stress experiment using defined fluid flow paradigms, transcriptional responses were triggered comparable to exposure of FTC-133 cells to the RPM. In summary, the RPM serves as a simulator of microgravity by randomizing the impact of Earth's gravity vector especially for suspension (i.e., detached) cells. Simultaneously, it simulates physiological shear forces on the adherent cell layer. The RPM thus offers a unique combination of environmental conditions for in vitro cancer research.

Keywords: rotating bioreactor; simulated microgravity; cancer cell; shear stress; cell detachment; in vitro metastasis

1. Introduction

One of the most exciting aspects of biomedical research using microgravity provided by real microgravity platforms, such as International Space Station (ISS), is the formation of three-dimensional spheroids or organoids that seem to be enhanced under microgravity conditions lacking sedimentation [1–4]. These 3D cell cultures are more relevant to an organism's complex biology than traditional two-dimensional monocultures of cells and provide a potential means to minimize animal experiments. Cancer cells exposed to microgravity may also provide models for metastasis events [5,6]. Whilst orbital labs such as the ISS provide the gold standard for microgravity research, the logistics and extensive costs prohibit easy access to real microgravity on orbital platforms. Even unmanned orbital (satellites) or sub-orbital platforms, such as sounding rocket flights, are very rare and extremely costly approaches. Further gravity research platforms like parabolic flights or drop towers cannot provide sufficient time under microgravity conditions to address questions regarding, e.g., developmental processes. Therefore, rotating bioreactors such as 2D clinostats, rotating wall vessels, or the random positioning machine (RPM, Figure 1A) have become essential tools to provide simulated microgravity environments for cellular biomedical research on Earth [7]. The rotational motion of the fluid environment allows suspension cells to experience simulated free-fall conditions avoiding sedimentation over longer durations. For some cell systems, therefore, these microgravity simulations can provide data comparable to experiments conducted on orbital platforms in real microgravity. Interestingly, exposure of certain types of adherent cells to simulated microgravity induces characteristic spheroid formation in some cell types (Figure 1B). However, it is not evident what induces the detachment of cells from the growth surface and their aggregation toward spheroid formation. The genomic, transcriptomic, and proteomic data even on a single cell type are heterogeneous across various platforms simulating microgravity or the respective culturing conditions [8,9]. Previously, it was argued that the effects of microgravity on individual cells are primarily indirect, and that the mass of a single cell is too low to directly sense changes in the gravity vector [10]. Instead, forces acting from the outside, such as the hydrostatic pressure of the medium or the local microenvironment, should change how the cell responds to the microgravity environment. The RPM induces biologically relevant shear forces [11–14] that affect human cancer cells in adherent cell layers. Suspension cancer cells in the same culture experience lower shear and are therefore affected differently. Currently, the studies on the RPM-based cellular behavior of human cancer-derived cell lines are not fully concise. Therefore, a generalized model of RPM-induced metastasis does not exist at the moment. In the current study, we aimed to understand which influences lead to cell detachment and spheroid formation under different modes of action on an RPM. The outcome might aid in the identification of metastasis traits at the onset of and in the course of cancer spheroid formation.

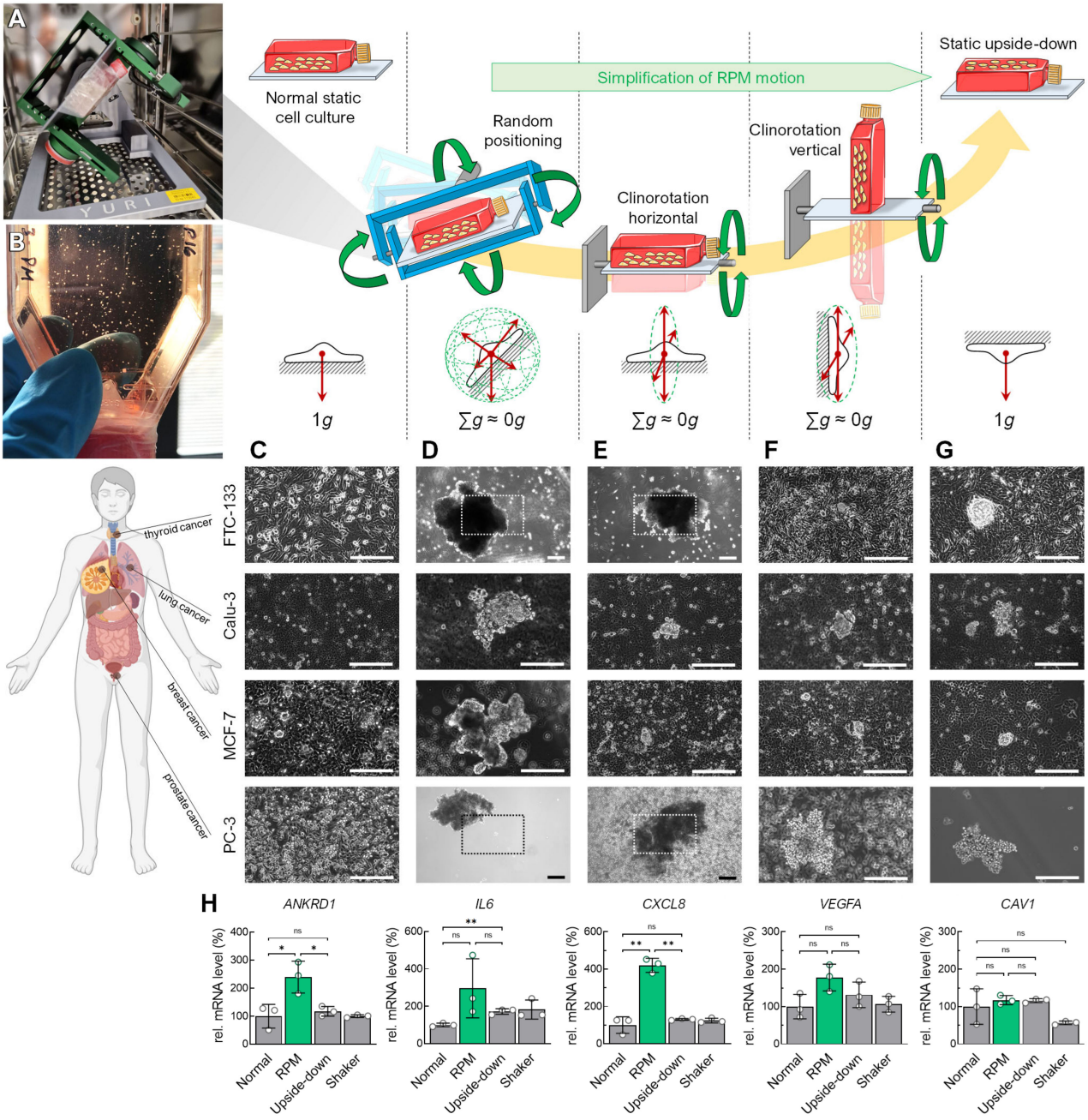

Figure 1. Spheroid formation of various adherent human carcinoma cell lines differently oriented with respect to Earth's gravity vector for 72 h. Rotational movements of the cell culture flasks are indicated with green arrows. (**A**) Benchtop RPM in an incubator during an experiment with a T25 flask attached. (**B**) Visible spheroids formed after 3 days of random positioning in a cell culture flask. (**C**) Standard static cell culture. (**D**) Random positioning in real random mode. (**E**) RPM clinorotation mode with horizontal orientation of the T25 flask. (**F**) RPM clinorotation mode with vertical orientation of the T25 flask. (**G**) Upside-down static cell culture. (**H**) RNA expression changes in specific genes in FTC-133 cells that have been described previously to play a role in spheroid formation on the RPM. The plots show the mean ± SD $\Delta\Delta C_T$ values of three cell cultures performed in triplicate together with the individual data points. Scale bars: 300 µm. The outlined areas reflect the magnification of the field of view in most images except for larger spheroids formed in FTC-133 and PC-3 cells in RPM and horizontal clinorotation mode. * Independent sample *t*-test $p \leq 0.05$, ** $p \leq 0.01$, ^{ns} non-significant. Parts of the figure were drawn by using pictures from Biorender.com and from Servier Medical Art.

2. Materials and Methods

2.1. Cell Lines and Cell Culture

The human follicular thyroid carcinoma FTC-133 cell line (passages 8–18) was purchased from Sigma-Aldrich (St. Louis, MO, USA). The MCF-7 mammary carcinoma cells (passages 5–9) and PC-3 prostate carcinoma cells (passages 36–40) were purchased from ATCC (Manassas, VA, USA). The Calu-3 lung carcinoma cell line (passage 19) was a kind gift from Prof. Heike Walles, the University of Magdeburg. The FTC-133, MCF-7, and PC-3 cells were cultured in the RPMI 1640 medium (Life Technologies, Carlsbad, CA, USA) supplemented with 10% fetal calf serum (FCS; Sigma-Aldrich, St. Louis, MO, USA) and 1% penicillin/streptomycin (Life Technologies) at 37 °C and 5% CO_2. The Calu-3 cells were cultured in the DMEM/F12 medium + 2.5 mM L-glutamine + 29 mM sodium bicarbonate (Life Technologies) supplemented with 10% FCS and 1% penicillin/streptomycin. The cells were routinely checked using visual inspection and maintained at a maximum confluence of 90% for up to 2 to 4 days before passaging. At 24 h before each experiment, a cell density of 1×10^6 cells (40,000 cells/cm^2) per flask was seeded in uncoated T25 cell culture flasks (Sarstedt, Nümbrecht, Germany) to allow cells to adhere. For immunofluorescence staining, uncoated glass coverslips (Carl Roth, Karlsruhe, Germany) were fixed using sterilized vaseline (Edeka, Hamburg, Germany) in a T25 flask before seeding a cell density of 1×10^6. For the cell cultures in channel slides, 20,000 cells/cm^2 (microscopy) or 40,000 cells/cm^2 (qPCR) were seeded in a µ-Slide I Luer Glass Bottom 0.8 (ibidi, Gräfelfing, Germany).

2.2. Rotating Cell Cultures

For the experiments (4 h, 24 h, 72 h), a desktop RPM 2.0 (Yuri, Meckenbeuren, Germany) was used in a HERAcell CO_2 incubator (Thermo Scientific) at 37 °C, 5% CO_2 without humidification. The medium was not specially pretreated. For random positioning, the RPM was operated in real random mode (two frames) at three different speed ranges: average speed 25°/s (range: 21–30°/s), average speed 60°/s (range: 50–70°/s), and average speed 90°/s (range: 80–100°/s). The RPM was operated in one frame mode for clinorotation with a constant speed of 60°/s. Before starting the rotation, the cell culture flasks were filled completely with medium, avoiding bubbles (any remaining bubbles were carefully removed using a pipette tip before closing the culture flask). Static controls were placed next to the RPM in the same incubator at the same environmental conditions.

2.3. Orbital Shaker Cell Cultures (FTC-133)

For the shaker experiments (72 h) with the FTC-133 cells, a Stuart SSM1 Orbital Shaker (Cole-Parmer, Vernon Hills, IL, USA) was used in a HERAcell CO_2 incubator at 37 °C, 5% CO_2 without humidification. The shaker was operated using fully filled T25 flasks at a speed of 60 rpm.

2.4. Flow Channel Cell Cultures (FTC-133)

An ISM827 Reglo peristaltic pump system (Ismatec, Grevenbroich, Germany) was used for the experiments (4 h, 24 h). The system consisted of a medium reservoir containing 70 mL of cell culture medium. Carbogen (5% CO_2 in O_2; Air Liquide, Düsseldorf, Germany) was continuously injected into the reservoir to supply CO_2 and O_2 to the cell culture. On top of the flask, a syringe attached to an empty flask served as a foam trap for the sterile filter of the exhaust gas. The medium was pumped in a closed loop from a reservoir via a channel slide with defined dimensions (50 × 5 × 0.8 mm) (ibidi) at a rate of 0.5 or 1 mL/min creating a calculated shear stress of 12.5 and 25 mPa [15]. To mimic the shear stress induced by bubbles, medium supplemented with defined bubbles was pumped via channel slides. A second peristaltic pump connected was added to the inlet tubing upstream the slide via a Y-adaptor. In this setup, one bubble was pumped every second.

The effect of an oscillating fluid flow was investigated in an oscillatory flow configuration ibidi pump system (ibidi), in which one cycle consisted of a change in flow direction

every 7.5 s and a flow rate of 1 mL/min (corresponding to 25 mPa of shear stress [15]). A brightfield image of the same slide area was acquired for live visualization every 5 min.

2.5. Serum Starvation and Pharmaceutical Treatment (FTC-133)

After 24 h of seeding, the FTC-133 cells were washed once using phosphate-buffered saline (PBS; Life Technologies), synchronized for 4 h in RPMI 1640 with 0.25% FCS and 1% penicillin/streptomycin, following cultivation with RPMI 1640 medium supplemented with 1 µM ethanol-soluble dexamethasone (Sigma-Aldrich) for 72 h, as described in [16]. The synchronization procedure was also used to reduce the amount of nutrients present before an experiment.

2.6. Phase Contrast Microscopy

The cells were routinely visually inspected and imaged using an Olympus CKX53 inverted microscope in phase contrast mode and a magnification of 10× (NA: 0.25) or 20× (NA: 0.4; Olympus, Tokyo, Japan). An Axiovert 200M microscope at brightfield mode at a magnification of 40× (NA: 0.6; Carl Zeiss, Oberkochen, Germany) was used for live visualization during the flow experiments in channel slides.

2.7. Cell Tracking and Migration Analysis (FTC-133)

For cell tracking, the Manual Tracking Plugin in Fiji v1.54f (ImageJ, imagej.net) was used. The exported file for tracking was processed using Chemotaxis and Migration Tool 2.0 (ibidi). For each condition, three independent FTC-133 cell cultures in the channel slides (see section Flow Channel Cell Cultures) were observed for 24 h. To determine the migratory ability of the cells, the average cell position at the end of the observation was determined for individual cells ($n > 40$ cells/condition), as well as the distance traveled in µm and the time to detachment in min.

2.8. Immunofluorescence Microscopy (FTC-133)

The cells were cultured as described above. For fixation, the cells were washed thrice using 0.1 M phosphate buffer (PB; Na_2HPO_4/NaH_2PO_4; Carl Roth), fixed for 15 min at 4 °C in 4% paraformaldehyde (PFA; Carl Roth), and then washed with PB for 3 × 15 min on a shaker. The cells were stored in 0.1 M PB at 4 °C for a maximum of one day before staining. The cell membrane was permeabilized using 0.2% Triton X-100 (Carl Roth) and washed thrice with 0.1 M PB. Non-specific binding sites were blocked using 3% bovine serum albumin (BSA, Carl Roth) in 0.1 M PB for 1 h at room temperature (RT). Subsequently, the cells were labeled with the primary antibodies diluted in 0.1 M PB containing 1% BSA (listed in Table S1) overnight at 4 °C. The next day, the cells were washed two times using 0.1 M PB. The cells were incubated with the secondary Alexa Fluor™ 488 (AF488)-conjugated (Invitrogen, Life Technologies) or Alexa Fluor™ 647 (AF647)-conjugated (Invitrogen, Life Technologies) antibodies (Table S1) at a dilution of 1:500 (MRTF-A) or 1:1000 at RT for 1 h. For F-actin staining, Alexa Fluor™ 568 Phalloidin (Invitrogen, Life Technologies) was added at a dilution of 1:400 for 1 h, and then the sample was washed thrice with 0.1 M PB. The cells were washed again three times using 0.1 M PB and mounted using Fluoroshield™ with DAPI (4′,6-diamidino-2-phenylindole) to stain the nuclear DNA (Sigma-Aldrich). The slides were examined using a ZEISS LSM 800 confocal laser scanning microscope (Carl Zeiss). To ensure comparability for intensity quantification, all the images were acquired with the same settings using the ZEISS Airyscan detector and ZEN 3.4 software (Carl Zeiss). The Airyscan processing settings were optimized for each antibody–wavelength combination and manually applied to the corresponding samples. To check for non-specific binding of the secondary antibody and thus a false negative signal, the secondary antibodies were applied to separate samples of the same condition without the primary antibody.

2.9. Immunofluorescence Analysis

To determine the localization of the transcription factors, we searched for the nuclear signal in the Z-position of the fluorescence image. The Z-position was used where the size of the nucleus was largest and the intensity of the nuclear signal was strongest. The cytoplasmic part of the signal was determined at the same Z-position. In this way, a correct measurement of the ratio between the nucleus and cytoplasm was ensured. Only 1 Z-position per file was used.

The resulting file was used in Fiji software v1.54f (ImageJ, imagej.net) to quantify the relative protein expression levels based on the sample's fluorescence intensity using the Image Calculator tool. The relative intensities were measured according to the method of Shihan et al. [17]. To determine the ratio of protein localization between the nucleus and cytoplasm (N/C ratio), the mean fluorescence intensities of the protein of interest were measured for the nuclear area and the cytoplasm area. Using the Freehand Selection tool, the nuclear area was determined based on the DAPI signal. The total cell area was determined by selecting the background without cells and subtracting it from the total area. The cytoplasmic area was determined by subtracting the nuclear area from the cell area. The intensity measured in the cytoplasmic area is the average signal from the cytoplasms of all cells in this image. The signal intensity from the nuclear area was divided by the signal intensity of the cytoplasmic area. This corresponds to the individual N/C ratio for the respective image.

2.10. mRNA Isolation and Quantitative Real-Time PCR (FTC-133)

The procedure was performed in the same way as described in [18]. To obtain sufficient mRNA out of the cells grown in channel slides, a higher cell number of 40,000 cells/cm^2 and a µ-Slide, 0.8 Luer, ibiTreat (ibidi) were used. The primer sequences used in the quantitative real-time PCR can be found in the Supplementary Materials (Table S2). The samples were measured in triplicate and evaluated by using the comparative threshold cycle ($\Delta\Delta C_T$) method. 18S rRNA was used as the housekeeper reference due to its stable expression in dynamic FTC-133 cell cultures [18].

2.11. Statistical Analysis

Statistical evaluation was performed using SPSS Statistics v29 (IBM, Armonk, NY, USA). The non-parametric Mann–Whitney U test was used to compare samples (biological replicates) from different culture conditions. For experiments in which only a few samples were available (<5 biological replicates), an independent sample *t*-test was used. All data are presented as mean ± standard deviation (SD). In most plots, the individual data points are shown additionally. The sample size for each experiment is provided in the figure legends.

3. Results

3.1. Alteration of the Gravity Vector

The operating principle of rotating microgravity simulators is based on a continuous change in the Earth's gravitational vector direction on the cells. We aligned diverse human carcinoma cell lines (FTC-133, Calu-3, MCF-7, PC-3) in various positions with respect to the Earth's gravitational vector field (Figure 1). In general, these cells grow as monolayers in standard (static) cell culture (Figure 1C). Although MCF-7 cells sometimes tend to form multiple cell layers, the cells remain adhered to their surface. Exposed to the RPM, the adherent cancer cells formed spheroids above the cell layer within 3 days (Figure 1D).

To determine which orientations or movements of the cell cultures contribute to spheroid formation during random positioning, and whether a particular gravity vector orientation is sufficient to form three-dimensional aggregates, we examined rotating cell cultures mounted horizontally (Figure 1E) or vertically (Figure 1F) on an RPM operated in 2D clinostat mode. After 3 days, the FTC-133 cells aligned parallel to the rotational axis formed spheroids, whereas the cells oriented perpendicular to the rotational axis remained

adherent. Calu-3, MCF-7, and PC-3 cells formed smaller spheroids in the perpendicularly oriented rotation than in the other rotations (Figure 1F). Interestingly, we also observed the formation of spheroids from all cell lines in a static, inverted cell culture (Figure 1G). These occurred in low-density cultures, making three-dimensional growth due to overgrowth an unlikely cause. Here, we detected new cell growth on the opposite (lower) side of the culture flask, caused by cell detachment from the cell layer and sedimentation. Spheroid formation from an inverted vessel suggested that the cells must hang "upside down" for a time for spheroids to form. The spheroids were more prominent in the rotating cell cultures, especially on the RPM. Accordingly, simply inverting the cell culture flasks only partially replaced random positioning for spheroid formation. This is also reflected in the upregulation of certain typical genes (e.g., *ANKRD1*, *IL6*, *CXCL8*) in FTC-133 cells that have been described previously as involved in RPM-induced spheroid formation (Figure 1H) [19–21]. To verify whether better mixing of the culture medium on the RPM (60°/s) compared to the static cell cultures could explain these RPM-specific gene regulatory effects, an additional experiment was performed using normal-orientated cell cultures on a rocket shaker (60 rpm). The shaker had only a minor effect on *CAV1* expression and cannot explain the molecular effects found in the RPM cultures (Figure 1H).

Since the FTC-133 cell line showed the greatest differences in spheroid formation at different orientations and is a well-characterized cell culture model in altered gravity conditions [3,22,23], we used this cell line for further studies. Next, we imitated the different orientations of cell culture flasks occurring on the RPM with static and rotating cell cultures (Figure 2). The RPM positions the cell culture flask via rotation in all spatial directions (Figure 2A). Both the cells and the culture medium surrounding them are subjected to gravity. In a completely filled T25 cell culture flask (h = 24 mm), the cell layer experiences 240 Pa ($p = \rho \times a \times h$) of hydrostatic pressure at a normal orientation. This pressure compresses the cells and the nuclei, which can also promote the nuclear transport of transcription factors (Figure 2B) [24]. In an upright cell culture flask, there is a gradient in hydrostatic pressure increasing from top to bottom.

In an inverted cell culture, there is no hydrostatic pressure from the cell culture medium on the cells, making this orientation the most "force-free". Cells in the inverted and at the top of the upright-oriented culture flasks showed lower F-actin filament density than in normal culture (Figure 2C). This could be related to the lower impact of mechanical forces lacking a large medium column, with corresponding hydrostatic pressure above the adherent cells. These results could support the idea that cells do not sense the gravity vector directly due to the low mass of their organelles but instead sense the indirect effects of gravity on larger structures, such as the surrounding culture medium [10]. There was minimal change in the nuclear or cytoplasmic distribution of the mechanosensitive transcription factors YAP1, p38 MAPK, or MRTF-A in the static cell cultures of different orientations (Figure 2D–F). These factors are important players in mechanosignaling, helping cells to recognize and respond to mechanical forces and adapt to changes in their microenvironment.

A cell culture on the RPM is not only subjected to different positions but also to different rotations, resulting in fluid shear forces and periodic compressions of the cell. These effects should be mimicked using two different types of 2D clinorotation produced by utilizing only one rotational axis of the RPM (Figure 2G). The F-actin density was similar in the clinorotation and RPM samples, indicated by some stress fibers (Figure 2H). A translocation to the cytoplasm was observed for YAP1 when the cells were exposed to random positioning (Figure 2I), and a statistically significant alteration in p38 MAPK subcellular localization when the cell culture flask was rotated with horizontal orientation (Figure 2J). We observed stark, but highly variable, differences in the nuclear/cytoplasmic fluorescence ratio for MRTF-A; compared to normal cell culture, more nuclear distribution was observed after clinorotation regardless of the flask orientation, and more cytoplasmic distribution was observed after random positioning (Figure 2K).

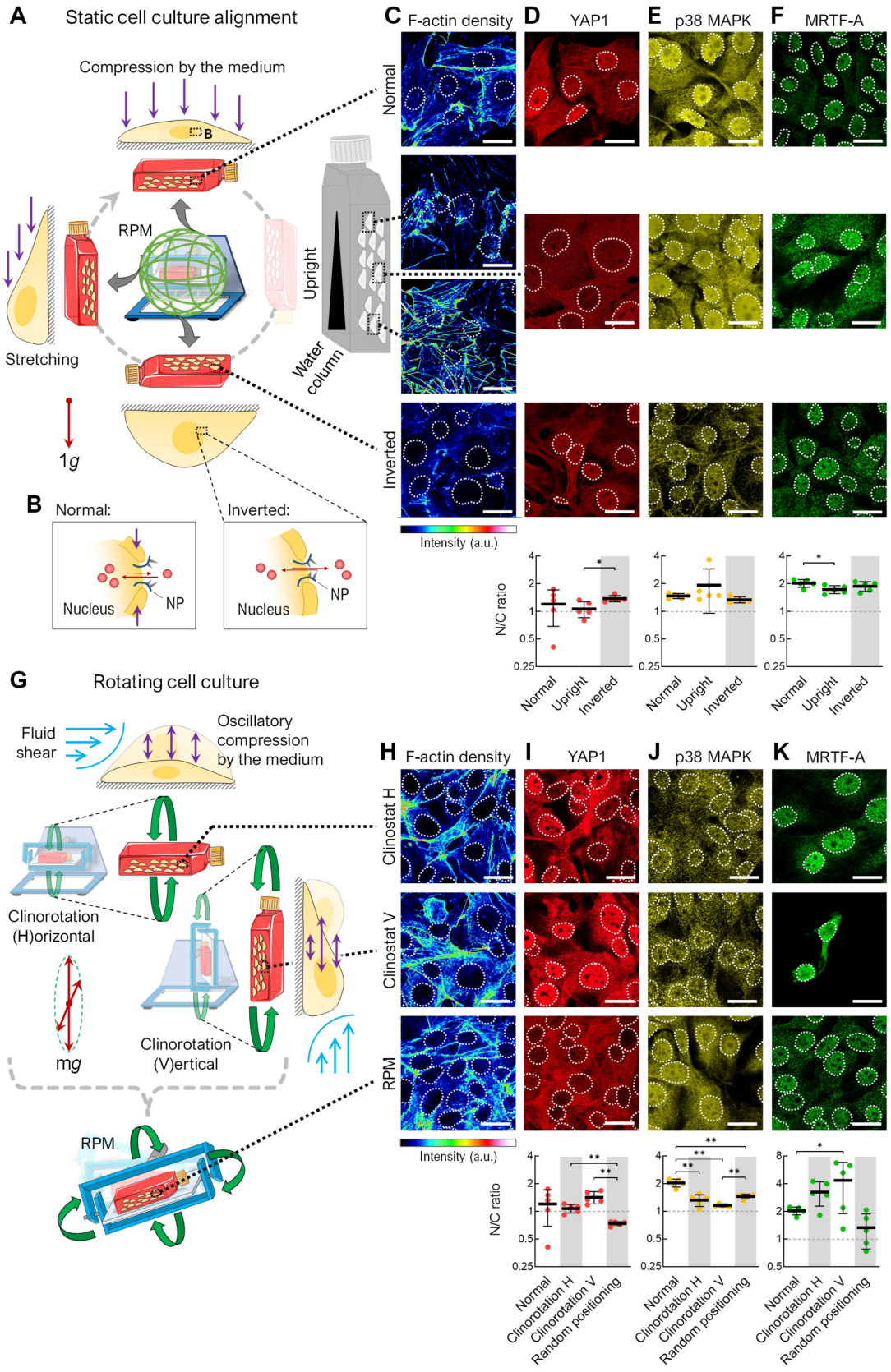

Figure 2. F-actin density and transcription factor localization in the remaining adherent cells in differently oriented and rotated cell culture flasks. (**A**) Static cell cultures in different orientations: normal cell culture, upright flasks, and inverted flasks. (**B**) Effect of cell compression on nuclear

transport of transcription factors (red circles) via nuclear pores (NP). (**C**) F-actin density (phalloidin staining) and immunofluorescence of the mechanoresponsive transcription factors (**D**) YAP1, (**E**) p38 MAPK, and (**F**) MRTF-A after 72 h (n = 5 for each condition; one representative picture is shown). Outlines of the nuclei as indicated using DAPI staining (not shown) depicted as dashed lines. (**G**) Rotating cell cultures: horizontal clinorotation (60°/s), vertical clinorotation (60°/s), and random positioning (average speed 60°/s). (**H**) F-actin density. (**I**) YAP1, (**J**) p38 MAPK, and (**K**) MRTF-A localization after 72 h (n = 5 for each condition; one representative picture is shown). Outlines of the nuclei are shown as dashed lines. (Below) The relative mean nuclear–cytoplasmic (N/C) ratio of transcription factors was measured for at least 15 cells (5 pictures per condition). Static cell culture was set as reference. The experimental conditions where the spheroid formation was observed are shaded gray. Scale bars: 300 µm. The fluorescence images in this figure were optimized to visualize protein localization and unsuitable for comparative protein level quantification. * Mann–Whitney $p \leq 0.05$, ** $p \leq 0.01$. Parts of the figure were drawn by using pictures from Servier Medical Art.

In summary, rotating cell cultures, including RPM cultures, have a stronger effect on transcription factor translocation than static cell cultures, further emphasizing the importance of flow shear on the RPM. However, it should be noted that in the cell cultures in which spheroids are formed (Figure 2, gray-shaded areas), there is no uniform nucleation of the transcription factors studied. This may indicate that these signaling pathways are not involved in spheroid formation or that the cells are already adapted to the culture conditions after 72 h.

An RPM experiment with different angular velocities showed that the time-averaged cancellation of the gravity vector alone could not form spheroids (Figure 3). In microgravity experiments, the RPM typically operates at an average frame speed of 60°/s, resulting in fluid flow in the cell culture flask [14,25] (Figure 3A). In addition to the usually applied real random mode at a velocity of 60°/s, we performed experiments at velocities of ~25°/s and ~90°/s. All operating speeds resulted in a calculated time-averaged milligravity (~0.01 g) within a few hours (Figure 3B–D). Slower random positioning of the FTC-133 cells (average speed 25°/s) failed to induce cell detachment or spheroid formation (Figure 3E). Using higher RPM speeds (average speed 90°/s), much smaller spheroids formed compared to the typical angular velocity of 60°/s.

Assuming that a balance between cell confluency and fluid flow was needed to efficiently induce spheroid formation, we let the cells attach for 24 or 48 h prior to RPM exposure in all three angular velocities. Indeed, a longer period of cell attachment before RPM exposure affected the spheroid formation ability. The FTC-133 cells that adhered for 48 h did not form spheroids at any RPM speed (Figure 3F), except for one single small spheroid (110 µm) found at 90°/s (Figure 3F, insert). This effect of a prolonged adhesion phase before the start of the experiment was also observed in the PC-3 cells (not shown) and during the CellBox-1 mission, in which the cells became confluent due to a delay in the rocket launch and did not form spheroids during the experiment on the ISS [26]. We demonstrated that only under spheroid-forming conditions on the RPM was the expression of certain genes upregulated (e.g., *IL6*, *CXCL8*, *ICAM1*, *KRT8*) that have previously been described as targets of various mechanosignaling pathways (including p38 MAPK, NFκB, MEK/ERK) in human cells, among others (Figure 3G) [19,20]. Hence, both the fluid flow generated by the RPM and the adhesion force of the cells are important parameters for spheroid formation.

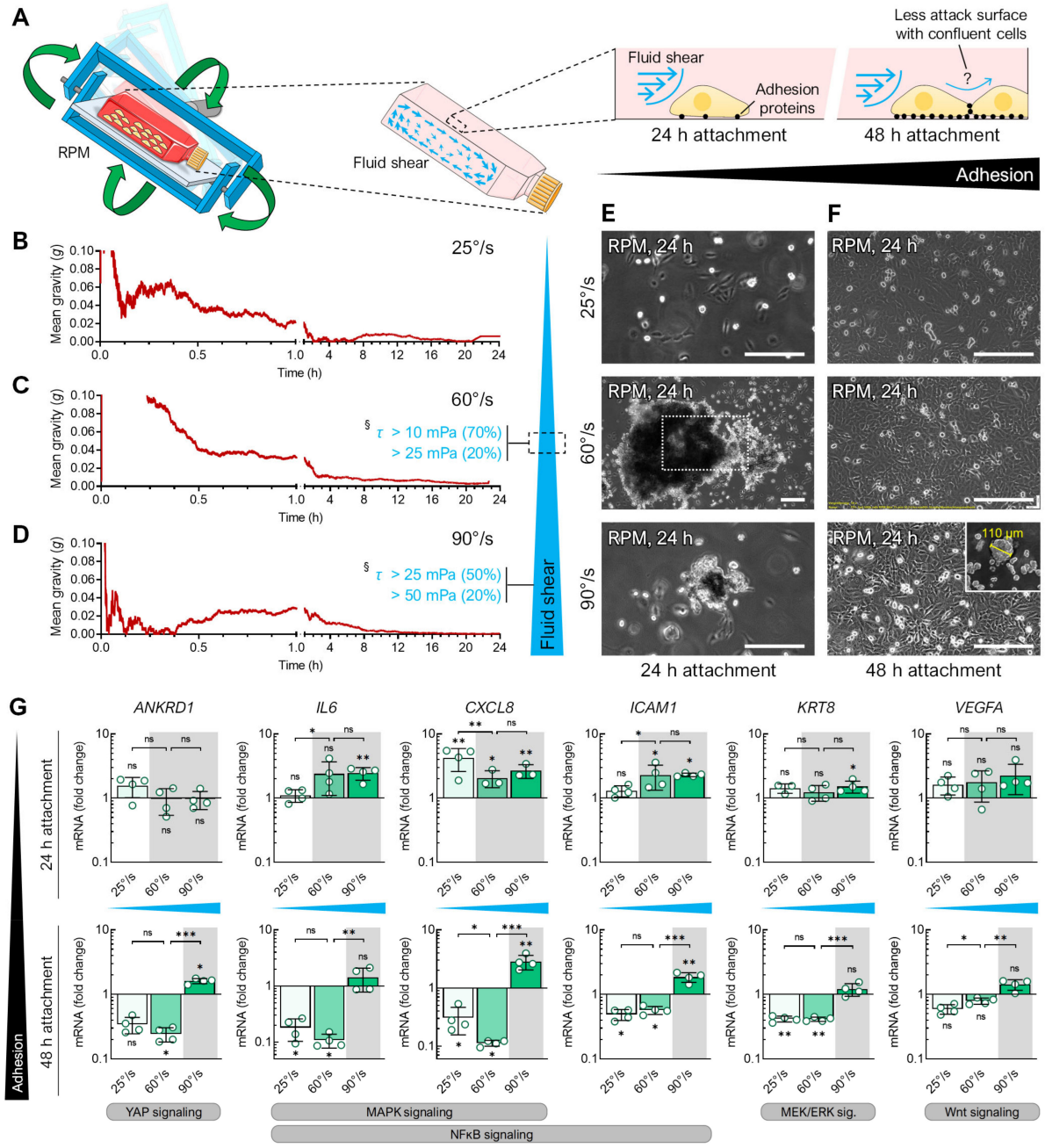

Figure 3. Spheroid formation of FTC-133 cells exposed to the RPM at different angular velocities for 24 h. (**A**) Illustration of fluid shear within cell culture flasks on the RPM. Time-averaged residual gravity levels and shear forces were calculated at RPM average velocities of (**B**) 25°/s, (**C**) 60°/s, and (**D**) 90°/s. Spheroid formation was examined in FTC-133 cultures that had previously been allowed to adhere to the bottom of the cell culture flask for (**E**) 24 h or (**F**) 48 h. The outlined area reflects the magnification of the field of view in most images except for larger spheroids compared at 60°/s after 24 h of normal cell growth followed by 24 h of exposure to the RPM. (**G**) Expression changes (compared to static cell culture) in gene transcripts known to be responsive to shear stress after 24 h exposure to the RPM operated with different velocities. The plots show the mean ± SD $\Delta\Delta C_T$ values of four cell cultures performed in triplicate together with the individual data points. The experimental conditions where spheroid formation was observed are shaded gray. Scale bars: 300 µm. * Independent sample *t*-test $p \leq 0.05$, ** $p \leq 0.01$, *** $p \leq 0.001$, ^{ns} non-significant vs. static control. § Shear stress τ according to Wuest et al. [14]. Parts of the figure were drawn by using pictures from Servier Medical Art.

3.2. Fluid Shear

Live-cell imaging on the RPM is not yet possible; therefore, we used a flow channel slide experiment to simulate the effects of RPM-induced fluid shear stress (Figure 4). Adherent FTC-133 cells were cultured in a channel slide connected to a peristaltic pump that perfused the medium through the channel at 0.5 and 1 mL/min speeds (Figure 4A,B). The fluid flow in the chosen dimensions of the channel slide (50 × 5 × 0.8 mm) produced shear stresses on the cells in the order of 12.5 and 25 mPa [15]. This stress was supposed to be similar to the fluid shear stress predicted to be observed on the walls of T25 cell culture flasks on the RPM at an average speed of 60°/s [14]. Both fluid flows significantly decreased the cell confluency within 20–24 h (confluency change at 0.5 mL/min: −11%, 1.0 mL/min: −38%) (Figure 4C). Time-lapse imaging showed cell detachment (Figure 4D, Video S1), migration, and rolling across the surface in the same direction as the media flow (Figure 4E). More cells detached at a flow rate of 1 mL/min, with initial cell detachment occurring after 12 h of flow exposure. This is consistent with prior observations of spheroid formation occurring after 16–24 h on the RPM [27–29]. Finally, the cells rounded off, detached, and were transported away by the flow. This observation over an extended period suggests that the detachment of the cell could be part of a biological process. In non-perfused cell cultures, no detachment was observed (Figure 4C), and the cell motility was significantly reduced (Figure 4F). Cell detachment is an essential step in RPM-induced spheroid formation; previous studies have shown that detached FTC-133 cells (i.e., suspension cultures) can form spheroids on the RPM. Interestingly, the proliferation of adherent cells was slightly higher at a flow rate of 1 mL/min compared with 0.5 mL/min, until approximately 12 h after the start of the experiment (Figure 4C,D).

3.3. Air Bubbles

From previous RPM experiments, we knew that the observation of air bubbles at the end of an RPM experiment (including their size and number, compare Figure S1) influences the number of adherent cells remaining, depending on the cell line and flask configuration used (Figure 5A). In a recent study, we described that FTC-133 cells cultured on the RPM in the presence of 1 μM dexamethasone (to avoid cell clustering) did not show spheroid formation [16]. However, when additional air bubbles were added to the cell culture flasks containing an FTC-133 cell culture (bubble diameter: 0.5–8.3 mm at the end of the experiment), spheroid formation occurred on the RPM even during treatment with 1 μM dexamethasone (Figure 5B). The air bubbles in a cell culture flask on the RPM thus appeared to be able to detach even "stickier" cells. RPM experiments usually are initiated using completely filled cell culture flasks devoid of air bubbles using de-gassed culture media. Therefore, it is challenging to determine when and where bubbles originate from (Figure S1). They occur sporadically, even without cells, which indicates an incomplete de-gassing of the medium and/or, e.g., temperature fluctuations during the filling of the flasks. Furthermore, repeated biological or technical replicates (identical cells, flasks, medium, treatment, and cell number) resulted in differing numbers and sizes of bubbles present at the end of the RPM experiment. In various experiments, we found a correlation between the formation of spheroids and the presence of bubbles in culture flasks. The size and geometry of the culture vessel also played a role in RPM-induced spheroid formation. For example, we have not observed air bubble movements and spheroid formation of adherent cancer cells in channel slides. In a μ-well slide experiment, only one single bubble was formed that moved around the interior edges of the cuboid chamber and did not disturb the cells (Figure 5A).

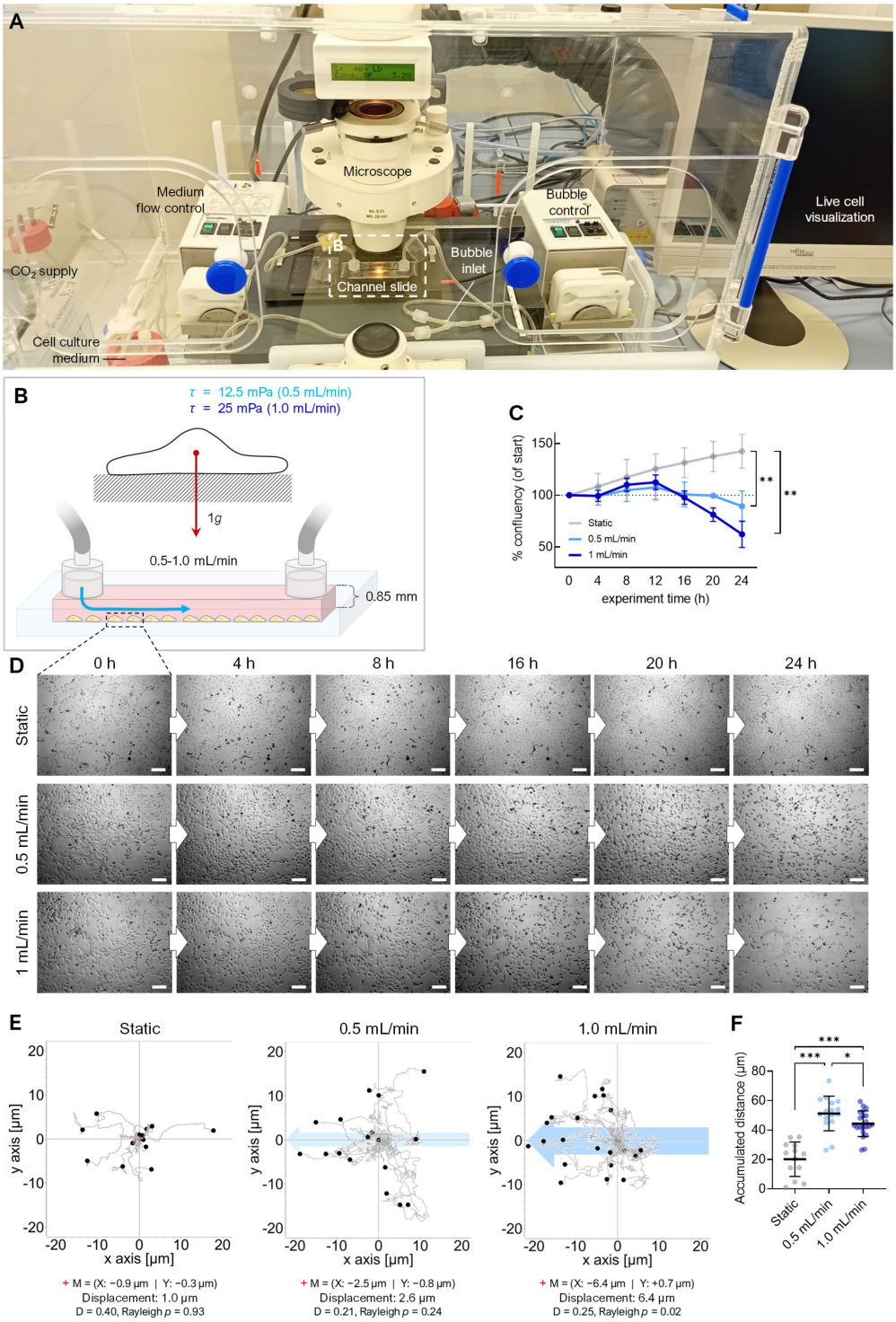

Figure 4. Effect of fluid flow on detachment of adherent FTC-133 cells. (**A**) Setup of the flow experiment. (**B**) Flow schematics. (**C**) Confluency of cell cultures over 24 h (n = 3). (**D**) Snapshots from the brightfield time-lapse recordings of one representative experiment with different flow speeds. (**E**) Migration traces of single cells in the flow channel perfused with different flow rates. The blue arrow indicates the direction of flow, and the position of cells (n > 40 cells for each condition) after 24 h is indicated by black circles. The red cross (+) indicates the mean value (M) of spatial cell migration (values are given below the plot). D: directness. (**F**) Cumulative migration distances of cells over 24 h at different flow rates. Scale bars: 300 µm. * Independent sample t-test (**C**) or Mann–Whitney (**F**) $p \leq 0.05$, ** $p \leq 0.01$, *** $p \leq 0.001$.

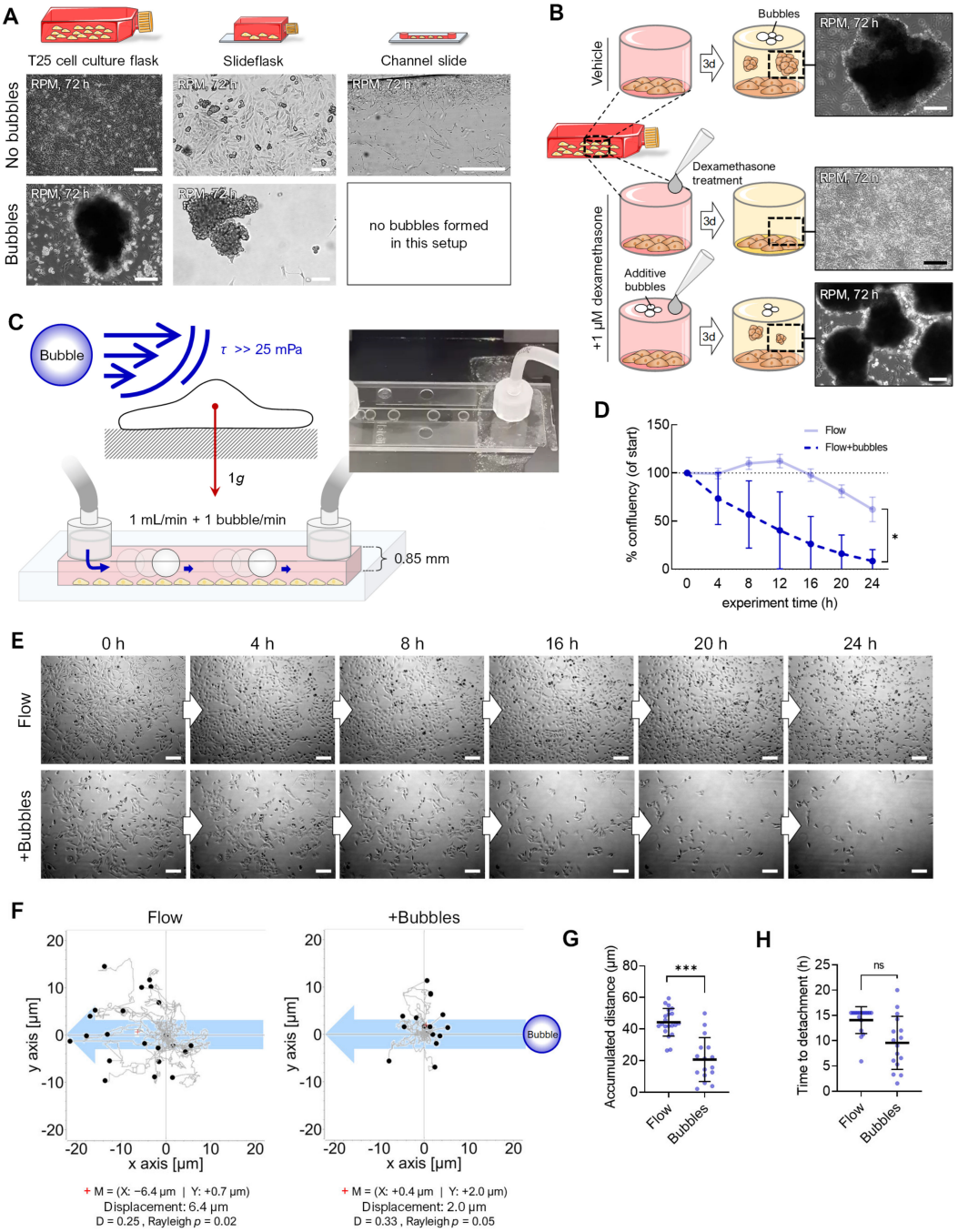

Figure 5. Enhancing effect of air bubbles on detachment of adherent FTC-133 cells. (**A**) Spheroid formation on the RPM depends on the culture flask geometry and the presence of air bubbles during the experiment. (**B**) Air bubbles were able to counteract the inhibitory effect of dexamethasone on the spheroid formation of FTC-133 cells on the RPM. (**C**) Setup of the bubble experiment. (**D**) Confluence of cell cultures over 24 h (n = 3). (**E**) Snapshots from the time-lapse recordings of one representative experiment with a flow rate of 1 mL/min without and with 1 bubble/min. (**F**) Migration traces of single cells in the flow channel. The blue arrow indicates the flow direction, and black circles indicate the position of cells after 24 h (n > 40 cells for each condition). The red cross (+) indicates the mean value (M) of spatial cell migration (values are given below the plot). D: directness. (**G**) Cumulative migration distances of cells over 24 h at a 1 mL/min flow rate with and without air bubbles. (**H**) Experiment time until initial cell detachment. Scale bars: 300 µm. * Independent sample t-test (**D**) or Mann–Whitney (**G**,**H**) $p \leq 0.05$, *** $p \leq 0.001$, ^{ns}, not significant. Parts of the figure were drawn by using pictures from Servier Medical Art.

Consequently, we modified the channel experiment, and air bubbles were pumped into the flowing medium at one bubble per second (bubble diameter: 5 mm; Figure 5C), using the same flow rate as in the shear flow experiments (1 mL/min). The cells detached at an earlier timepoint than without bubbles (Figure 5D,E; Video S2), suggesting bubble-enhanced cell detachment due to enhanced mechanical forces above 25 mPa (confluency change with bubbles: −92%, without bubbles: −38%). In addition, we observed significantly reduced cell migration (20.7 µm vs. 44.3 µm) when bubbles were present (Figure 5F,G). This could also be related to a faster detachment of the cells during migration (Figure 5H).

3.4. Flow Versus Random Positioning—Mechanobiology of Cell Detachment

After recognizing that fluid flow, as it occurs during the usual operation of the RPM in cell culture flasks, leads to the enhanced migration and detachment of adherent FTC-133 cells, we directly compared the mechanobiological responses of cells to flow- and RPM-induced shear forces (Figure 6). Because the number of cells in the channel slides decreased rapidly (compare Figure 5), we chose an examination time point 4 h after the start of the experiment. This also bypasses a possible adaptation of the cells that could be observed within 3 days. Shear forces might act differently on the same cell type depending on the culture vessel (T25 flasks and channel slides) and the corresponding possible exposure to fluid motions (Figure 6A). Nevertheless, in both culture conditions, we observed an increase in the F-actin density (Figure 6B) and altered localization (nuclear or cytoplasmic) of certain mechanosensitive transcription factors. Whilst both experimental approaches resulted in an altered nuclear protein content of RelA and p38 MAPK, the difference was only statistically significant for cells on the RPM (Figure 6C–E). Specifically, a decrease in nuclear p38 was observed on the RPM after 4 h, while an increase was observed in the flow channel (Figure 6D). MRTF-A nuclear localization was slightly decreased in the flow channel (Figure 6E). Subcellular localization of β-catenin remained unchanged. Conversely, the amount of β-catenin in the RPM cells was significantly increased (Figure 6F). Whilst there was no change in the nuclear levels of YAP1 on the RPM, YAP1 localization became more cytoplasmic in the cells under both exposure to RPM and flow (Figure 6G).

To investigate the mechanosignaling pathways, we investigated the mRNA expression of a panel of genes previously observed to be differentially expressed under simulated microgravity conditions [18]. The expression of these target genes was similar on the RPM and in the flow channel (Figure 6H). We found that *IL6*, *CXCL8*, and *ANKRD1* were upregulated in both RPM and flow conditions. We serum-starved T25 cell cultures for 4 h before starting the RPM. This procedure better mimicked the lower nutrient availability in the channel slides after the 24 h attachment phase and further approximated the gene expression changes to those of the cells from the flow channel experiment (Figure 6H, light grey bars). *CCN2*, *ICAM1*, *SNAI1*, *FN1*, and *VCL* showed similar regulatory behavior in both experimental setups.

The direction of the fluid flow in the RPM culture and the channel slide differs and changes continuously during random positioning. To test the effects of a discontinuous fluid flow on the cells, we utilized an oscillatory fluid flow of 1 mL/min and a flow direction change every 7.5 s (Figure 7A). Unlike a unidirectional flow, fewer cells detach when exposed to an oscillating flow (Figure 7B). In addition, β-catenin was significantly reduced in the nucleus after 4 h, whilst RelA, MRTF-A, and YAP1 were increasingly localized in the nucleus (Figure 7C). Thus, MRTF-A and YAP1 show a similar behavior as in cells exposed to the RPM, in contrast to β-catenin and RelA. qPCR confirmed that the SRF target gene *VCL* was upregulated, and the Wnt/β-catenin target genes *FN1*, *SNAI1*, and *VEGFA* were uniformly downregulated (Figure 7D).

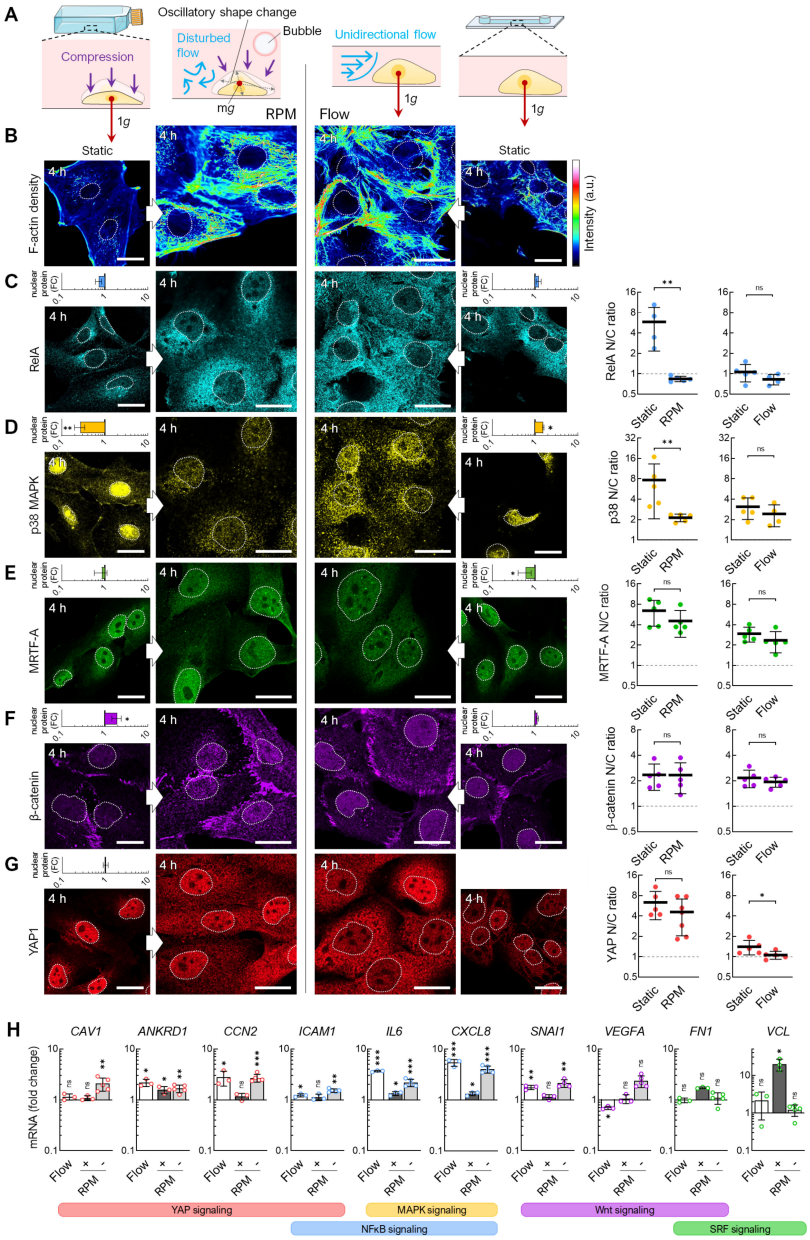

Figure 6. Transcription factor levels in random positioning compared to continuous flow. (**A**) Fluid motions acting on cells within different cell culture vessels. (**B**) Actin density and immunofluorescence of the mechanoresponsive transcription factors (**C**) RelA, (**D**) p38 MAPK, (**E**) MRTF-A, (**F**) β-catenin, and (**G**) YAP1 after 4 h. Outlines of the nuclei are shown as dashed lines. The small graphs indicate fold changes (FC) in nuclear protein levels compared to static cell cultures (n = 5 for each condition; one representative picture is shown). (Right) The mean nuclear/cytoplasmic (N/C) ratio of transcription factor localizations was measured for five overview images from independent experiments, each showing at least three cells. (**H**) Gene expression response after 4 h exposure to the RPM (60°/s) and continuous flow (1 mL/min). The plots show the mean ± SD ΔΔCt values of 3–5 independent experiments performed in triplicate. To mimic the channel slide's low medium and nutrient volume, the RPM experiment was performed once identically to the flow ("+", dark gray bars) experiment and once with a prior starvation phase ("−", light gray bars). Scale bars: 300 µm. The fluorescence images in this figure were optimized to visualize protein localization and unsuitable for comparative protein level quantification. * Mann–Whitney (**G**) or independent sample t-test (**H**) $p \leq 0.05$, ** $p \leq 0.01$, *** $p \leq 0.001$, ^{ns} non-significant vs. static control. Parts of the figure were drawn using pictures from Servier Medical Art.

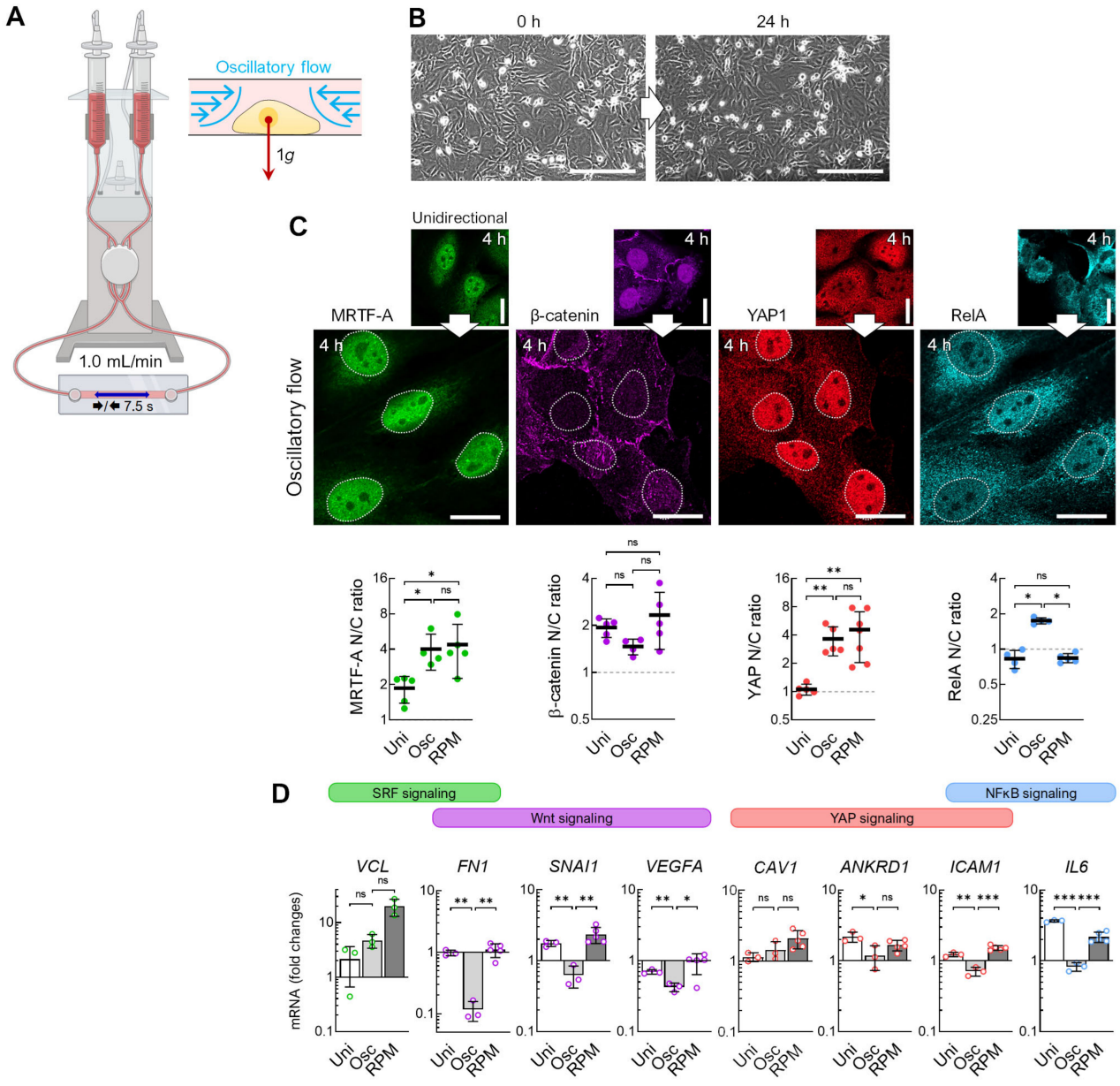

Figure 7. Transcription factor effects in response to oscillatory flow compared with continuous flow. (**A**) Setup for an oscillatory flow experiment (1 mL/min, direction change every 7.5 s). (**B**) Snapshots of cells in the channel before the start of the experiment and after 24 h of oscillating flow show reduced detachment of cells. (**C**) Nuclear transport of transcription factors after 4 h oscillatory flow ($n = 5$ for each condition; one representative picture is shown). (Below) Fold changes in nuclear protein levels compared to unidirectional flow. The mean nuclear/cytoplasmic (N/C) ratio of transcription factor localizations was measured for five overview images from independent experiments, each showing at least three cells. (**D**) Gene expression response after 4 h exposure to the oscillatory flow (Osc) compared to unidirectional flow (Uni) and to RPM culture ($n = 3$–5). Scale bars: 300 µm. The fluorescence images in this figure were optimized to visualize protein localization and unsuitable for comparative protein level quantification. * Mann–Whitney (**C**) or independent sample *t*-test (**D**) $p \leq 0.05$, ** $p \leq 0.01$, *** $p \leq 0.001$, ^{ns} non-significant. Parts of the figure were drawn using pictures from Biorender.com (accessed on 30 October 2023).

In summary, FTC-133 cells cultured on the RPM and those cultured in a flow channel show similar behavior regarding actin condensation, the translocation of mechanorespon-

sive transcription factors, and the expression of the target genes of the mechanosignaling pathways. An oscillatory flow showed greater similarity in the translocation of MRTF-A and YAP1 and lower similarity in the translocation of β-catenin and RelA to the cells on the RPM.

4. Discussion

Microgravity enables entirely new approaches to cell biology studies, including cancer research on a cellular level (reviewed in [5,30,31]). It is well established among gravitational researchers that it is impossible to simulate an exact microgravity environment in the laboratory. Nevertheless, depending on the device and the cell system chosen, ground-based facilities can produce results that closely resemble those of space experiments [32–34]. Therefore, simulated microgravity bioreactors may be a useful tool for space scientists. However, devices like the RPM have been a biological "black box", and most of the molecular and cellular processes that lead to exciting discoveries remain uncharacterized. In this study, we aimed to shed light on the cellular processes involved in cultivating adherent cancer cells on the RPM and understand how and why tumor spheroids form during culture in random positioning conditions.

4.1. Adherent Cells in Rotating Bioreactors

Investigation of gravitational biology is the most common reason for using rotating bioreactors. This requires that cells perceive changes in the direction of the gravity vector. While this property has already been proven for larger unicellular organisms (such as *Paramecium* or *Euglena*) [35–37], there has not been a clear answer for smaller human cells. Early calculations by Albrecht-Bühler suggest that the volume within a human cell is too small for the cell to sense gravitational changes [10]. Albrecht-Bühler instead assumed that the mass of the surrounding cell culture medium, which is also subject to gravity, triggers an indirect gravitational perception by exerting external pressure on the cell.

Restructuring of the cytoskeleton is often suggested as an early response to changes in the gravity vector [38]. Typical rearrangements of the cytoskeleton (reduced stress fibers, the formation of lamellipodia, etc.) were also observed by Ju et al. in their comparative study with different human cell types in response to simulated microgravity on a 3D clinostat. However, they observed the same cytoskeletal changes in an inverted cell culture, which they concluded must be a general response of mammalian cells to gravitational changes [39]. These effects could also be explained by the large column of culture medium above the cells in a standard orientated culture flask, which is not present in an inverted flask. However, it should be noted that the liquid column itself causes a hydrostatic pressure difference of 2.4 mbar in a 2.4 cm thick ($p = \rho \times a \times h$) completely filled T25 cell culture flask, which is in the order of magnitude of daily air pressure fluctuations. A possible (and maybe additive) influence of air pressure on cell culture observations should be investigated in a further study. Nevertheless, these results could explain the relaxation of tension the cell sensed, which may have induced the cytoskeletal changes observed. This could lead to the assumption that human cells in in vitro culture might sense only the indirect effects of gravity. In the meantime, however, other studies have appeared indicating that at least some human cells might be able to perceive gravity directly. Luna et al. [40] exposed human mesenchymal stem cells to different angular velocities on a clinostat and observed a rounder, less spread morphology as a function of the rotation speed. This angular frequency dependence suggested that the ability of a human cell to perceive the changing gravity vector depends on the rate of perturbation [40]. It is important to note that a slide, not a T25 culture flask, was used in this experiment to avoid the possible effects of shear forces and movement of the cell culture medium.

Clinorotation is usually associated with lower shear forces, which should result in a lower F-actin density in clinorotated cells compared with cells on the RPM. This was not observed in our experiments (Figure 2H); however, our goal was to study RPM motion and not to generate perfect clinorotation. One explanation for this discrepancy could be

the use of adherent cells instead of suspension cells. In addition, the rotation axis of an RPM operated in clinostat mode is much more offset compared with a slideflask/channel slide clinostat, resulting in low centrifugal forces (about 0.01 *g* on the cell layer, assuming a 10 cm offset and a rotation speed of 60°/s).

Even assuming that human cells are gravisensitive and can sense gravity directly, the question remains as to which subcellular structures are responsible. Vorselen's theory of the cytoskeleton as one of the first gravity responders in non-specialized cells [41] is still relevant, but is weakened by the fact that structural changes in the cytoskeleton happen in response to any mechanical influence on the cell, even with indirect perception of gravity. This is particularly evident as we observed changes in F-actin not only in response to the spatial orientation of the cell culture but also in response to the fluid flow without changing the gravitational vector (Figure 2). Also, the fact that MRTF-A and YAP1 are predominantly nuclear-localized in the rotating and flow cell cultures suggests that RhoA-dependent active actin remodeling occurred during fluid shear (Figures 2 and 6).

Zhang et al. [42] also compared different orientations of cell culture flasks for investigating the effect of the gravity vector on the mechanical remodeling of adherent murine MC3T3-E1 preosteoblast cells. Their results proposed a biomechanical model for integrating the mechanosensation of nucleus displacement with cytoskeletal remodeling and reorganization of the focal adhesion complex triggered by the gravity vector. If the mechanical stability of orientation-varied adherent cells could be explained, among other things, by the sedimentation of cell nuclei, this finding would suggest that gravisensing mechanisms in plant cells (sedimentation of statoliths) could also apply to mammalian cells in a distinct way. These results could explain why adherent cells adapt to a new physical culture condition after a period of time, which we saw in FTC-133 when comparing the results after 4 and 72 h (Figure 1). While we detected a significant translocation of p38 into the cytoplasm in RPM-exposed cells after 4 h, this was no longer the case after 72 h (Figure 2).

4.2. Flow Shear

Previous studies with thyroid cancer cells on the RPM show that the first spheroids form between 12 and 24 h. Our experiments have shown that FTC-133 cells begin to detach after about 12 h in a flow channel, which should have a similar fluid flow to a culture flask on the RPM. This process would be consistent with the timings observed on the RPM. We have also seen that the spheroid formation of FTC-133 cells depends on the RPM rotational speed, which should be proportional to the expected shear forces. Interestingly, by doubling the flow rate in the flow channel, we did not observe earlier detachment of the cells. Only in the presence of air bubbles did the cells' detachment occur from the beginning of the experiment.

We operated the RPM at different speeds to determine how shear stress affects biological experiments. After 8 h, the time-averaged gravity vector in all experimental setups was around 0.01 *g*, implying a "microgravity" condition. However, what distinguishes each setup from the others are the shear forces generated, which have already been calculated by Wuest et al. [14] for cell culture flasks on the RPM. Since the spheroid formation depended on the rotation speed, the microgravity simulation alone cannot be responsible for this process. When placed in a T25 flask at an average speed of 60°/s (commonly used in RPM microgravity simulation experiments), an estimated 70% of adherent cells experience a shear stress of at least 10 mPa. Further, 20% of the cells experience even higher rates of 25 mPa or more [14]. We mimicked these shear forces in a flow channel for ease of study and obtained a similar gene signature response to RPM experiments of the same length after 4 h.

Not all cells are exposed to the same shear forces on the RPM, which may have resulted in the lower fold changes in gene expression in the RPM-exposed cells compared to the cells from the flow channel. According to the simulations by Wuest et al. [14], only 20% of the cell monolayer was exposed to forces of the same magnitude as in the channel slide. There

were a few differences in the nuclear levels of the transcription factors p38, MRTF-A, and β-catenin, suggesting that the mechanosignaling of cells on the RPM cannot be replicated using a simple flow experiment. An oscillatory flow mimicked the changing shear stress direction found on the RPM better than a unidirectional flow but could not explain the difference. This further illustrates that the detachment of adherent cells, essential for spheroid formation on the RPM, can be mimicked by the shear forces from fluid flows and suggests that adherent cell layers on the RPM are subjected to higher mechanical stress before spheroids form. This is also supported by the fact that genes overexpressed in the adherent RPM cell population were upregulated in cancer cells exposed to shear stress (Figure 6F). Recently, advances in the study of the effects of low shear stress on cancer cells have been published [43–45]. Of particular interest for random positioning research are the low shear stress rates of 10–25 mPa that are expected during normal RPM operation. The physiological shear values of the lymphatic system (10–20 mPa), for example, can be found in this range [43], which is of critical importance for experiments with metastatic cancer cells or those isolated from lymphatic system metastases such as FTC-133. Work by Lee et al. [44] showed that low shear stress can activate YAP-dependent motility programs in metastatic cancer cell lines. In 2022, Kim et al. [45] showed that the cell motility in prostate cancer cell lines depends on the Piezo1–Src–YAP axis at low shear stress.

Triggered by the fluid flow inside the flow channel, we observed that the cells detach, migrate, and roll across the surface in the same direction as the media flow. At some point, the cells rounded out, detached, and were carried away by the flow. This observation over an extended period suggests that the increased detachment of the cells induced by flow is a biological process. Cells can sense flow-induced shear stress depending on its intensity and direction in a YAP-dependent manner that promotes cell motility [44]. We confirmed that the shear forces also contribute to the increased proliferation in RPM cell cultures [46,47]. We observed that cell confluency increased more rapidly at a higher flow rate of 1 mL/min compared with 0.5 mL/min until approximately 12 h after the start of the experiment.

Numerous research groups have reported alterations in gene and protein expression related to focal adhesion components, including integrins, as well as changes in the activity of focal adhesion kinase components, when employing rotating bioreactors to simulate microgravity [41]. These changes may be attributable to the cellular motility within this environment and can be more appropriately understood as a general cellular response to low shear stress.

4.3. Air Bubbles

First of all, it must be said that most studies pay enough attention to remove air bubbles in their experiments in order not to generate misleading results. It is therefore unusual to introduce additional air bubbles into a culture vessel. The bubble experiment (Figure 5) was primarily designed to investigate the effects of relatively large air bubbles on the cells. Despite particular care during filling, air bubbles in culture flasks on the RPM cannot be completely avoided, especially during longer experiments of $\geq$24 h. We have investigated a number of possible causes for the occurrence of bubbles in RPM experiments (compare Figure S1). However, it is most likely a combination of several effects. The correlation between the occurrence of air bubbles and the formation of spheroids, which we have seen in many RPM experiments, could be supported by the flow channel experiments in this study (Figure 5). The movement of air bubbles over the cell layer resulted in the rapid detachment of cells. This helps produce a larger amount of spheroids but results in much greater mechanical stress on the adherent cell population. Air bubbles also cause significant problems in microfluidic devices, and it is usually recommended to avoid them [48]. Bubbles in motion can have different effects depending on their size. They can interact directly with the cells and turbulent flow can be generated behind rising bubbles. Bubbles' effects on cell damage have been discussed for suspended cell populations. Cells can become trapped in the circulating fluid behind a rising bubble ("bubble wake") and are thereby dragged along by the bubble. For small bubbles, these microeddies can be

sufficiently intense to even create cell damage [49]. However, as soon as bubbles have formed in a culture flask on the RPM, they immediately hit the flask wall due to buoyancy and travel with rather high velocities along the wall with each revolution. These bubbles create high velocity gradients, and thereby high shear forces, in the liquid film between the bubble and cells [50].

4.4. Cell Density

Another interesting observation in our study was the influence of the cell pre-incubation time on RPM-induced spheroid formation. A longer pre-cultivation prior to RPM start resulted in a reduced formation to an absence of formation of 3D aggregates. It has previously been described that overgrown cell cultures no longer form spheroids under microgravity conditions [26]. In the case of a very dense cell culture, one possible explanation could be that there is no lateral surface of attack for shear forces due to the lack of space between the cells. Another explanation could be that cells detach during mitosis when they are less attached to the substrate (rounding of the cell). At low density, cells continue to divide and are at higher risk of detaching. At high density, the cells may go into a senescent state and stop dividing. Thus, the risk of detachment is lower. The results of the inverted flask experiments suggest that FTC-133 cells regularly detach from the surface, which would not be noticeable in a normally positioned cell culture (Figure 2). In cancer cells, this property can contribute to the formation of new metastases. However, further investigations are required to determine whether prior cell migration, cell–cell or cell–matrix contact formation, or mitosis is necessary for detachment (Figure 4). Our observations suggest that this is the case, as the detached cells migrated in the flow channel before their final detachment. The free space between the cells allows them to migrate according to the YAP nuclear status (Figure 2). YAP signaling is involved in contact inhibition of cell proliferation and growth [51] and allows the cell to maintain a motile environment by limiting the maturation of focal adhesions and restricting cytoskeletal tension [52]. Once a cell culture reaches confluence, YAP localization is completely cytoplasmic, and cells cease motility and possibly subsequent detachment in an RPM cell culture.

4.5. Spheroid Formation on the RPM

Our experiments indicated that the spheroid formation of adherent cells on the RPM is likely to be a two-step process (Figure 8A). In the first step, the cells are detached from their monolayer. Responsible for this are mainly fluid shear and the mechanical forces of migrating air bubbles during random positioning. Our fluid channel experiment mimicked fluid flow at a comparable scale to the RPM regular operation [14] and induced similar translocation of mechanosensitive transcription factors and a comparable signature of activated mechanoresponsive genes in FTC-133 cells. After detachment, the cells on the RPM are suspended in free-fall due to the appropriate rotational speed, preventing their sedimentation and two-dimensional outgrowth. In this phase, the cells aggregate into three-dimensional aggregates. The work of Melnik et al. [18] has shown that FTC-133 cells, when used as a suspension on the RPM, also form spheroids. Therefore, starting an RPM experiment with a layer of adherent cells is not essential for generating and studying spheroids. In other devices for microgravity research, such as the ClinoStar (CelVivo, Denmark) or the rotating wall vessel bioreactor (Synthecon, TX, USA), cells are also seeded in suspension before floating spheroids develop under rotation. However, using adherent cells in an RPM experiment allows for additional studies. For example, not all cells detach equally due to random positioning. A balance of adhesion and anti-adhesion proteins was discussed as responsible for this behavior [18]. In addition, metastatic cancer cells tolerate the suspension phase better due to the anoikis (cell death due to loss of cell–matrix contact) resistance they usually develop during the metastasis formation multistep process [53], as a prolonged culture phase before the start of random positioning inhibited the detachment of FTC-133 cells (Figure 3). After a two-day pre-attachment phase, the only conditions that obtained spheroids were higher angular velocities, which were only

able to induce the formation of a single small spheroid (ca. 110 µm) (Figure 3). The cells exhibited no transcriptional response to RPM treatment until higher velocities were applied. However, whether this inertia was related to increased "stickiness" due to a plentiful secreted extracellular matrix, to a higher level of adhesion proteins, or simply to the physical protection against flow shear caused by being embedded into a cell layer cannot be deduced from our data.

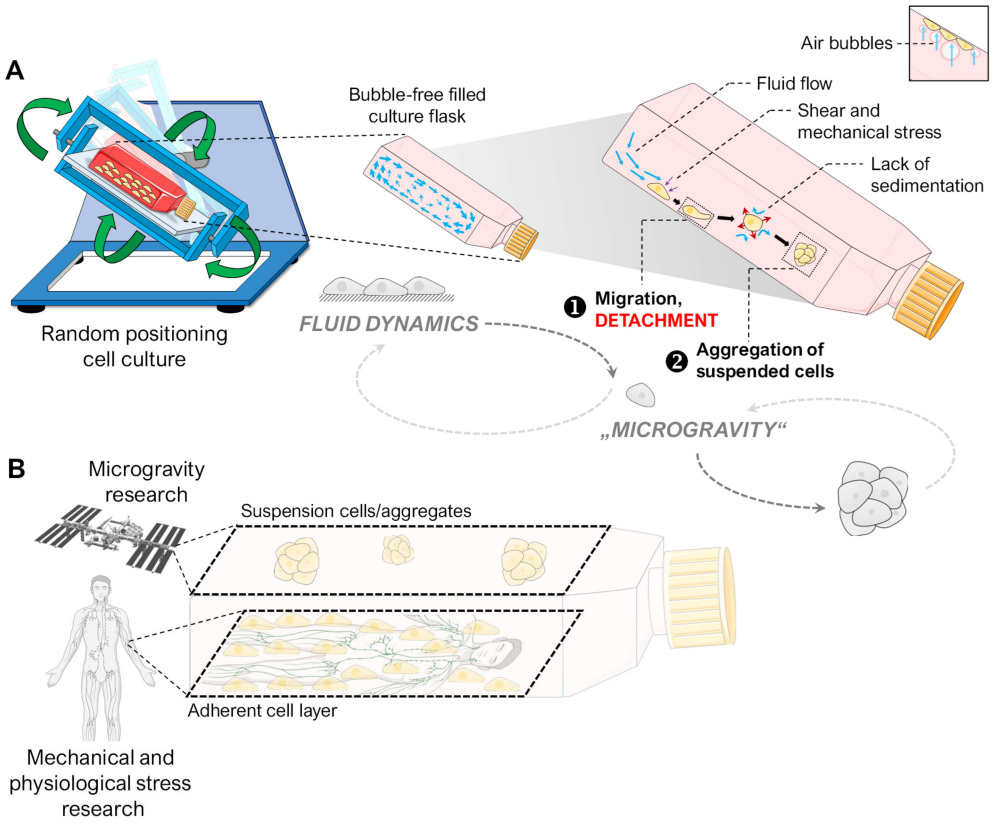

Figure 8. (**A**) Illustration of the hypothesized processes occurring with adherent cells in an initially air-bubble-free cell culture flask on the RPM, finally leading to spheroid formation. We observed that RPM-induced spheroid formation is a two-step process. First, the adherent cells detach due to mechanical stress (e.g., fluid flow, air bubbles). Then, "simulated microgravity" (free-fall) leads to the formation of three-dimensional spheroids by preventing the sedimentation of suspended cells. The small picture indicates the amplifying mechanical effect of air bubbles. (**B**) The two cell populations (adherent cell layer and suspension cells) of an RPM cell culture of adherent cells are subjected to different mechanical forces. While the suspension cells are held in a mostly stress-free suspension, the cell layer experiences shear forces similar to those in the human lymphatic system. Parts of the figure were drawn by using pictures from Biorender.com and from Servier Medical Art.

4.6. Implications for Future Experiments in Gravitational Biology

4.6.1. "Simulated Microgravity"

The RPM continues to be a suitable bioreactor to simulate microgravity effects for some cell model systems on Earth. To achieve optimal results in cell culture experiments, it is vital to have a thorough understanding of the internal dynamics of random positioning. Attention to these dynamics ensures that experiments are well planned and yield accurate and reliable results. For a suspended object, the RPM can simulate free-fall, the main effect experienced by astronauts and organisms on the ISS or during parabolic flights. An adherent cell population on the RPM is subject to shear forces that detach the cells after some time, leaving them to float free in the culture medium. Without sedimentation, if they can resist anoikis, they may aggregate and form spheroids.

It must be considered that the adherent cell layer and the suspension cells are exposed to very different mechanical forces, especially when air bubbles are present. Meaningful results will only be achieved with careful design of RPM-based experiments. The cellular effect triggered by fluid motion can be several orders of magnitude higher than the effect triggered by gravity alteration. Thus, it is not necessary to design a gravity-focused RPM experiment with a prior adhesion period leading to a two-dimensional cell layer. Instead, initiation with suspension cultures could prove a possible alternative. In 2022, Masini et al. [54] successfully performed a long-term experiment with suspended cancer cells on the RPM. They found that under the influence of the RPM, the behavior and metabolism of tumor cells led to the acquisition of an aggressive and metastatic stem cell-like phenotype.

The size and geometry of the cell culture vessel also play a role, as they directly influence the turbulence of the medium generated during random positioning. In the current study, we also observed this effect when using different culture flasks for the FTC-133 cells. In large flasks, the medium has a higher rotational energy. In small channel slides, the adhesive forces dominate, and the medium has hardly any chance to reach its full speed. Lower shear stress in the slide flasks or channel slides resulted in fewer or no spheroids, respectively, even though the RPM program or random speed and random direction velocities used were the same.

4.6.2. Real Microgravity

Spheroid formation of adherently growing human cells was also observed in several space experiments. In the ISS experiments SimBox [1], SPHEROIDS [2], and CellBox-2 [3], the formation of 3D aggregates in real microgravity has been reported. Since the detachment of cells has not yet been observed in microgravity, it cannot be completely ruled out that cells detach from their substrate during the microgravity phase. Nevertheless, it is possible that the appearance of these spheroids was triggered by a specific orientation of the flight hardware (e.g., by flipping) in combination with the formation of air bubbles (compare Figure S1). In our study, we were able to show that an upside-down-orientated cell culture flask with air bubbles led to the formation of spheroids after some time (Figure 2). Since it is unknown and not determinable in which orientation the flight hardware was stored between the handover and the rocket launch, a similar effect in the CellBox-2 experiment cannot be excluded. Accordingly, spheroids could have formed even before arrival on the ISS, e.g., due to accelerations or vibrations during the launch phase. FTC-133 cells were also used in the space experiment, and numerous air bubbles could be seen in the culture chamber at the end of the experiment (Figure S1B). Live cell observation during space experiments would help to determine when spheroids are formed during spaceflights. In future experiments on spheroid formation in real microgravity, special care must be taken to avoid air bubbles, e.g., using a bubble trap in the loop system or specific culture flask geometries that minimize the described bubble effect (e.g., channel or chamber slides).

4.6.3. Cell Models

While individual suspension cells are directly exposed to direct or indirect gravitational effects on the RPM, this is not necessarily true for cells inside cell clusters or multicellular organisms. While the cells of multicellular plants with statoliths still have intracellular perception mechanisms for gravity [55], mammalian cells have established perception of external structures exposed to gravity (e.g., otoliths). The cells used for the gravitational perception of environmental stimuli are mostly located on the internal or external surfaces of the organism, sometimes combined into sensory tissues or organs. The task of perceiving gravity is delegated to a higher organizational level (organ or system). Cells embedded into mostly non-gravity-sensitive tissue are likely to respond only to the mechanical deformation of the surrounding tissue but not to changes in the gravity vector. This may also be true for position-fixed adherent cells in a monolayer on the RPM. In 2022, ElGindi et al. [56] provided evidence of the more influential role of the local microenvironment in comparison to the general gravity vector. Their experiments showed that a 3D

microenvironment attenuated the changes in the transcriptome of T cells mediated by the RPM. The research group also exposed dendritic cells to the RPM in two different types of extracellular matrices (loose and stiff) [57]. The effects of random positioning at the transcriptome level were smaller when the cells were cultured in the denser matrix. Both studies indicate the major influence of the microenvironment on mammalian cell biology. This is also supported by the different effects at the transcriptional and protein levels found in numerous comparative analyses of the two cell populations (adherent cells, AD, and multicellular spheroids, MCS) in RPM experiments with human cells [8,19,46,58]; although both populations are by definition subjected to "simulated microgravity", the adherent cell layer is more exposed to mechanical fluid flow, whereas the spheroid cells float in a suspension with lower shear and are also primarily embedded into a protective stable tissue aggregate. Here, the cell microenvironment probably has a greater influence than the constantly changing gravitational vector and can influence cell signaling, proliferation, and apoptosis [59–61]. One possible approach to answering this ambiguous question is the planned project by Larose and colleagues to study spheroids and organoids under real microgravity conditions. This will open up the possibility of testing the extent to which microgravity affects the three-dimensional constructs of cancer cells [62].

Albrecht-Bühler [10] once commented that the microgravity simulation requires more than averaging the gravity vector in clinorotation. In addition, Einstein [63] stated that: "The gravitational field has only a relative existence in a way similar to the electric field generated by magnetoelectric induction. Because for an observer falling freely from the roof of a house there exists—at least in his immediate surroundings—no gravitational field". After more than 100 years, we can confirm this at least for human cells. While probably only isolated cells free-falling in vacuum could experience microgravity directly (a theoretical consideration), the indirect effects of altered gravity are perceived and processed differently by cells, depending on their type, origin, and cell culture conditions, and the characteristics of the "microgravity simulator" used. Conversely, this also means that a free-fall simulator is not always required to mimic the cellular effects of exposure to microgravity. A cell type-specific combination of mechanical stimuli could be sufficient.

4.7. Study Limitations

It should be noted that we have a heterogeneous cell population on the RPM (because not all cells are subjected to the same shear forces). Since we saw that not all cells detached simultaneously during flow exposure, we can hypothesize that cells may regulate some molecular factors before detaching from the surface. Unfortunately, we could only perform endpoint analyses from the localization of transcription factors and gene expression. Live cell observation of the cells on the RPM would provide more accurate information on spontaneous and/or short-term changes and adaptations. Some researchers suspect that the vibrations inside an incubator prevent/slow cell attachment to plastic flask surfaces. In the current study, we did not investigate the influence of vibrations, but started the experiments after a preceding 24(-48) h attachment phase of the cells.

5. Conclusions

Spheroid formation of adherently growing cells on the RPM is a two-step process. It requires detachment of the cells, caused mainly by fluid flow (triggered by the rotation of the cell culture flask), and air bubbles can enhance it. Once the cells are in suspension, random positioning prevents sedimentation, and 3D aggregate formation occurs.

The detachment itself seems to depend on the balance between the cell-specific adhesion forces (depending on the cell density, amount of matrix, and adhesion proteins) and the physical shear forces of the cell culture (flow rate, bubbles, surface conditions of the cell culture flask). In the current study, a fluid flow experiment mimicked several RPM-induced effects in adherent FTC-133 cells. During regular operation of the RPM, shear forces act in a range similar to that of the human lymphatic system. Thus, the RPM serves as a free-fall simulator for (detached) suspension cells in gravitational research, but it also

simulates the shear forces of the human organism on the adherent cell layer, providing a unique combination of study conditions for cancer research (Figure 8B). To ensure that, experiments with the RPM must be well planned and the results interpreted accordingly.

Supplementary Materials: The following supporting information can be downloaded at https://www.mdpi.com/article/10.3390/cells12222665/s1: Figure S1: Occurrence of air bubbles under different cell culture conditions and handling of cell culture flasks; Table S1: Antibodies used for immunofluorescence analyses; Table S2: Primer sequences for quantitative real-time PCR; Video S1: 24 h time-lapse video of FTC-133 cells exposed to a fluid flow of 1 mL/min inside a channel slide; Video S2: 24 h time-lapse video of FTC-133 cells exposed to a fluid flow of 1 mL/min with 1 bubble/min inside a channel slide.

Author Contributions: Conceptualization, J.L.C.-S. and M.K.; methodology, J.L.C.-S., V.S., S.K., D.M. and M.K.; software, J.L.C.-S.; formal analysis, J.L.C.-S. and M.K.; investigation, J.L.C.-S., D.M., V.S. and S.M.; resources, D.G.; writing—original draft preparation, J.L.C.-S. and M.K.; writing—review and editing, J.L.C.-S., S.L.W., C.L., I.R.D.J., M.C., S.K., S.M., D.M., D.G. and M.K.; visualization, J.L.C.-S. and M.K.; supervision, M.K.; funding acquisition, D.G. All authors have read and agreed to the published version of the manuscript.

Funding: This work was supported by the German Space Agency at DLR (Deutsches Zentrum für Luft- und Raumfahrt, grant number 50WB2219). J.L.C.-S. received financial support from the CONACyT-DAAD scholarship (CVU: 1059612).

Institutional Review Board Statement: Not applicable.

Informed Consent Statement: Not applicable.

Data Availability Statement: The data presented in this study are available in the electronic Supplementary Materials. The complete raw data are available on request.

Acknowledgments: We would like to thank ibidi GmbH, especially Charlotte Öri, for kindly providing the ibidi pump system as a demo test for the oscillatory flow. We would also like to thank Hermann-Josef Rothkötter (Institute of Anatomy, Magdeburg) for the opportunity to perform some experiments at his institute.

Conflicts of Interest: The authors declare no conflict of interest.

References

1. Pietsch, J.; Ma, X.; Wehland, M.; Aleshcheva, G.; Schwarzwälder, A.; Segerer, J.; Birlem, M.; Horn, A.; Bauer, J.; Infanger, M.; et al. Spheroid Formation of Human Thyroid Cancer Cells in an Automated Culturing System during the Shenzhou-8 Space Mission. *Biomaterials* **2013**, *34*, 7694–7705. [CrossRef] [PubMed]
2. Pietsch, J.; Gass, S.; Nebuloni, S.; Echegoyen, D.; Riwaldt, S.; Baake, C.; Bauer, J.; Corydon, T.J.; Egli, M.; Infanger, M.; et al. Three-Dimensional Growth of Human Endothelial Cells in an Automated Cell Culture Experiment Container during the SpaceX CRS-8 ISS Space Mission—The SPHEROIDS Project. *Biomaterials* **2017**, *124*, 126–156. [CrossRef] [PubMed]
3. Melnik, D.; Krüger, M.; Schulz, H.; Kopp, S.; Wehland, M.; Bauer, J.; Baselet, B.; Vermeesen, R.; Baatout, S.; Corydon, T.J.; et al. The CellBox-2 Mission to the International Space Station: Thyroid Cancer Cells in Space. *Int. J. Mol. Sci.* **2021**, *22*, 8777. [CrossRef] [PubMed]
4. Freed, L.E.; Langer, R.; Martin, I.; Pellis, N.R.; Vunjak-Novakovic, G. Tissue Engineering of Cartilage in Space. *Proc. Natl. Acad. Sci. USA* **1997**, *94*, 13885–13890. [CrossRef] [PubMed]
5. Kim, H.; Shin, Y.; Kim, D.-H. Mechanobiological Implications of Cancer Progression in Space. *Front. Cell Dev. Biol.* **2021**, *9*, 740009. [CrossRef] [PubMed]
6. Becker, J.L.; Souza, G.R. Using Space-Based Investigations to Inform Cancer Research on Earth. *Nat. Rev. Cancer* **2013**, *13*, 315–327. [CrossRef]
7. Brungs, S.; Egli, M.; Wuest, S.L.; Christianen, P.C.M.; van Loon, J.J.W.A.; Anh, T.J.N.; Hemmersbach, R. Facilities for Simulation of Microgravity in the ESA Ground-Based Facility Programme. *Microgravity Sci. Technol.* **2016**, *28*, 191–203. [CrossRef]
8. Kopp, S.; Slumstrup, L.; Corydon, T.J.; Sahana, J.; Aleshcheva, G.; Islam, T.; Magnusson, N.E.; Wehland, M.; Bauer, J.; Infanger, M.; et al. Identifications of Novel Mechanisms in Breast Cancer Cells Involving Duct-like Multicellular Spheroid Formation after Exposure to the Random Positioning Machine. *Sci. Rep.* **2016**, *6*, 26887. [CrossRef]
9. Shi, S.; Li, Q.; Cao, Q.; Diao, Y.; Zhang, Y.; Yue, L.; Wei, L. EMT Transcription Factors Are Involved in the Altered Cell Adhesion under Simulated Microgravity Effect or Overloading by Regulation of E-Cadherin. *Int. J. Mol. Sci.* **2020**, *21*, 1349. [CrossRef]
10. Albrecht-Buehler, G. Possible Mechanisms of Indirect Gravity Sensing by Cells. *ASGSB Bull.* **1991**, *4*, 25–34.

11. Hauslage, J.; Cevik, V.; Hemmersbach, R. Pyrocystis Noctiluca Represents an Excellent Bioassay for Shear Forces Induced in Ground-Based Microgravity Simulators (Clinostat and Random Positioning Machine). *NPJ Microgravity* **2017**, *3*, 12. [CrossRef] [PubMed]
12. Leguy, C.A.D.; Delfos, R.; Pourquie, M.J.B.M.; Poelma, C.; Westerweel, J.; van Loon, J.J.W.A. Fluid Dynamics during Random Positioning Machine Micro-Gravity Experiments. *Adv. Space Res.* **2017**, *59*, 3045–3057. [CrossRef]
13. Wuest, S.L.; Richard, S.; Kopp, S.; Grimm, D.; Egli, M. Simulated Microgravity: Critical Review on the Use of Random Positioning Machines for Mammalian Cell Culture. *BioMed Res. Int.* **2015**, *2015*, 971474. [CrossRef] [PubMed]
14. Wuest, S.L.; Stern, P.; Casartelli, E.; Egli, M. Fluid Dynamics Appearing during Simulated Microgravity Using Random Positioning Machines. *PLoS ONE* **2017**, *12*, e0170826. [CrossRef] [PubMed]
15. Ibidi GmbH. Application Note 11, Shear Stress and Shear Rates for Ibidi µ-Slides Based on Numerical Calculations. 2022. Available online: https://ibidi.com/img/cms/support/AN/AN11_Shear_stress.pdf (accessed on 29 October 2023).
16. Melnik, D.; Sahana, J.; Corydon, T.J.; Kopp, S.; Nassef, M.Z.; Wehland, M.; Infanger, M.; Grimm, D.; Krüger, M. Dexamethasone Inhibits Spheroid Formation of Thyroid Cancer Cells Exposed to Simulated Microgravity. *Cells* **2020**, *9*, 367. [CrossRef] [PubMed]
17. Shihan, M.H.; Novo, S.G.; Le Marchand, S.J.; Wang, Y.; Duncan, M.K. A Simple Method for Quantitating Confocal Fluorescent Images. *Biochem. Biophys. Rep.* **2021**, *25*, 100916. [CrossRef] [PubMed]
18. Melnik, D.; Cortés-Sánchez, J.L.; Sandt, V.; Kahlert, S.; Kopp, S.; Grimm, D.; Krüger, M. Dexamethasone Selectively Inhibits Detachment of Metastatic Thyroid Cancer Cells during Random Positioning. *Cancers* **2023**, *15*, 1641. [CrossRef]
19. Kopp, S.; Warnke, E.; Wehland, M.; Aleshcheva, G.; Magnusson, N.E.; Hemmersbach, R.; Corydon, T.J.; Bauer, J.; Infanger, M.; Grimm, D. Mechanisms of Three-Dimensional Growth of Thyroid Cells during Long-Term Simulated Microgravity. *Sci. Rep.* **2015**, *5*, 16691. [CrossRef]
20. Riwaldt, S.; Bauer, J.; Pietsch, J.; Braun, M.; Segerer, J.; Schwarzwälder, A.; Corydon, T.J.; Infanger, M.; Grimm, D. The Importance of Caveolin-1 as Key-Regulator of Three-Dimensional Growth in Thyroid Cancer Cells Cultured under Real and Simulated Microgravity Conditions. *Int. J. Mol. Sci.* **2015**, *16*, 28296–28310. [CrossRef]
21. Corydon, T.J.; Schulz, H.; Richter, P.; Strauch, S.M.; Böhmer, M.; Ricciardi, D.A.; Wehland, M.; Krüger, M.; Erzinger, G.S.; Lebert, M.; et al. Current Knowledge about the Impact of Microgravity on Gene Regulation. *Cells* **2023**, *12*, 1043. [CrossRef]
22. Ma, X.; Pietsch, J.; Wehland, M.; Schulz, H.; Saar, K.; Hübner, N.; Bauer, J.; Braun, M.; Schwarzwälder, A.; Segerer, J.; et al. Differential Gene Expression Profile and Altered Cytokine Secretion of Thyroid Cancer Cells in Space. *FASEB J.* **2014**, *28*, 813–835. [CrossRef] [PubMed]
23. Kopp, S.; Krüger, M.; Feldmann, S.; Oltmann, H.; Schütte, A.; Schmitz, B.; Bauer, J.; Schulz, H.; Saar, K.; Huebner, N.; et al. Thyroid Cancer Cells in Space during the TEXUS-53 Sounding Rocket Mission—The THYROID Project. *Sci. Rep.* **2018**, *8*, 10355. [CrossRef] [PubMed]
24. Kalukula, Y.; Stephens, A.D.; Lammerding, J.; Gabriele, S. Mechanics and Functional Consequences of Nuclear Deformations. *Nat. Rev. Mol. Cell Biol.* **2022**, *23*, 583–602. [CrossRef]
25. Brungs, S.; Hauslage, J.; Hemmersbach, R. Validation of Random Positioning Versus Clinorotation Using a Macrophage Model System. *Microgravity Sci. Technol.* **2019**, *31*, 223–230. [CrossRef]
26. Riwaldt, S.; Pietsch, J.; Sickmann, A.; Bauer, J.; Braun, M.; Segerer, J.; Schwarzwälder, A.; Aleshcheva, G.; Corydon, T.J.; Infanger, M.; et al. Identification of Proteins Involved in Inhibition of Spheroid Formation under Microgravity. *Proteomics* **2015**, *15*, 2945–2952. [CrossRef]
27. Kopp, S.; Sahana, J.; Islam, T.; Petersen, A.G.; Bauer, J.; Corydon, T.J.; Schulz, H.; Saar, K.; Huebner, N.; Slumstrup, L.; et al. The Role of NFκB in Spheroid Formation of Human Breast Cancer Cells Cultured on the Random Positioning Machine. *Sci. Rep.* **2018**, *8*, 921. [CrossRef]
28. Dietrichs, D.; Grimm, D.; Sahana, J.; Melnik, D.; Corydon, T.J.; Wehland, M.; Krüger, M.; Vermeesen, R.; Baselet, B.; Baatout, S.; et al. Three-Dimensional Growth of Prostate Cancer Cells Exposed to Simulated Microgravity. *Front. Cell Dev. Biol.* **2022**, *10*, 841017. [CrossRef]
29. Grosse, J.; Wehland, M.; Pietsch, J.; Schulz, H.; Saar, K.; Hübner, N.; Elles, C.; Bauer, J.; Abou-El-Ardat, K.; Baatout, S.; et al. Gravity-sensitive Signaling Drives 3-dimensional Formation of Multicellular Thyroid Cancer Spheroids. *FASEB J.* **2012**, *26*, 5124–5140. [CrossRef]
30. Sahebi, R.; Aghaei, M.; Halvaei, S.; Alizadeh, A. The Role of Microgravity in Cancer: A Dual-Edge Sword. *Multidiscip. Cancer Investig.* **2017**, *1*, 1–5. [CrossRef]
31. Medha, M.; Roy, A. Microgravity: New Aspect for Breast Cancer Treatment, a Review. *Acta Astronaut.* **2022**, *190*, 62–73. [CrossRef]
32. Herranz, R.; Anken, R.; Boonstra, J.; Braun, M.; Christianen, P.C.M.; de Geest, M.; Hauslage, J.; Hilbig, R.; Hill, R.J.A.; Lebert, M.; et al. Ground-Based Facilities for Simulation of Microgravity: Organism-Specific Recommendations for Their Use, and Recommended Terminology. *Astrobiology* **2013**, *13*, 1–17. [CrossRef] [PubMed]
33. Topal, U.; Zamur, C. Microgravity, Stem Cells, and Cancer: A New Hope for Cancer Treatment. *Stem Cells Int.* **2021**, *2021*, 5566872. [CrossRef] [PubMed]
34. Choi, D.H.; Jeon, B.; Lim, M.H.; Lee, D.H.; Ye, S.-K.; Jeong, S.-Y.; Kim, S. 3D Cell Culture Using a Clinostat Reproduces Microgravity-Induced Skin Changes. *NPJ Microgravity* **2021**, *7*, 20. [CrossRef] [PubMed]
35. Häder, D.-P.; Hemmersbach, R. Euglena, a Gravitactic Flagellate of Multiple Usages. *Life* **2022**, *12*, 1522. [CrossRef] [PubMed]
36. Roberts, A.M. The Mechanics of Gravitaxis in Paramecium. *J. Exp. Biol.* **2010**, *213*, 4158–4162. [CrossRef] [PubMed]

37. Hemmersbach, R.; Häder, D.P. Graviresponses of Certain Ciliates and Flagellates. *FASEB J.* **1999**, *13*, S69–S75. [CrossRef] [PubMed]
38. Lichterfeld, Y.; Kalinski, L.; Schunk, S.; Schmakeit, T.; Feles, S.; Frett, T.; Herrmann, H.; Hemmersbach, R.; Liemersdorf, C. Hypergravity Attenuates Reactivity in Primary Murine Astrocytes. *Biomedicines* **2022**, *10*, 1966. [CrossRef]
39. Ju, Z.; Thomas, T.N.; Chiu, Y.-J.; Yamanouchi, S.; Yoshida, Y.; Abe, J.-I.; Takahashi, A.; Wang, J.; Fujiwara, K.; Hada, M. Adaptation and Changes in Actin Dynamics and Cell Motility as Early Responses of Cultured Mammalian Cells to Altered Gravitational Vector. *Int. J. Mol. Sci.* **2022**, *23*, 6127. [CrossRef]
40. Luna, C.; Yew, A.G.; Hsieh, A.H. Effects of Angular Frequency during Clinorotation on Mesenchymal Stem Cell Morphology and Migration. *NPJ Microgravity* **2015**, *1*, 15007. [CrossRef]
41. Vorselen, D.; Roos, W.H.; MacKintosh, F.C.; Wuite, G.J.L.; van Loon, J.J.W.A. The Role of the Cytoskeleton in Sensing Changes in Gravity by Nonspecialized Cells. *FASEB J.* **2014**, *28*, 536–547. [CrossRef]
42. Zhang, C.; Zhou, L.; Zhang, F.; Lü, D.; Li, N.; Zheng, L.; Xu, Y.; Li, Z.; Sun, S.; Long, M. Mechanical Remodeling of Normally Sized Mammalian Cells under a Gravity Vector. *FASEB J.* **2017**, *31*, 802–813. [CrossRef] [PubMed]
43. Huang, Q.; Hu, X.; He, W.; Zhao, Y.; Hao, S.; Wu, Q.; Li, S.; Zhang, S.; Shi, M. Fluid Shear Stress and Tumor Metastasis. *Am. J. Cancer Res.* **2018**, *8*, 763–777. [PubMed]
44. Lee, H.J.; Diaz, M.F.; Price, K.M.; Ozuna, J.A.; Zhang, S.; Sevick-Muraca, E.M.; Hagan, J.P.; Wenzel, P.L. Fluid Shear Stress Activates YAP1 to Promote Cancer Cell Motility. *Nat. Commun.* **2017**, *8*, 14122. [CrossRef] [PubMed]
45. Kim, O.-H.; Choi, Y.W.; Park, J.H.; Hong, S.A.; Hong, M.; Chang, I.H.; Lee, H.J. Fluid Shear Stress Facilitates Prostate Cancer Metastasis through Piezo1-Src-YAP Axis. *Life Sci.* **2022**, *308*, 120936. [CrossRef] [PubMed]
46. Calvaruso, M.; Militello, C.; Minafra, L.; La Regina, V.; Torrisi, F.; Pucci, G.; Cammarata, F.P.; Bravatà, V.; Forte, G.I.; Russo, G. Biological and Mechanical Characterization of the Random Positioning Machine (RPM) for Microgravity Simulations. *Life* **2021**, *11*, 1190. [CrossRef] [PubMed]
47. Jha, R.; Wu, Q.; Singh, M.; Preininger, M.K.; Han, P.; Ding, G.; Cho, H.C.; Jo, H.; Maher, K.O.; Wagner, M.B.; et al. Simulated Microgravity and 3D Culture Enhance Induction, Viability, Proliferation and Differentiation of Cardiac Progenitors from Human Pluripotent Stem Cells. *Sci. Rep.* **2016**, *6*, 30956. [CrossRef] [PubMed]
48. Zhao, X.; Ma, C.; Park, D.S.; Soper, S.A.; Murphy, M.C. Air Bubble Removal: Wettability Contrast Enabled Microfluidic Interconnects. *Sens. Actuators B Chem.* **2022**, *361*, 131687. [CrossRef]
49. Chisti, Y. Animal-Cell Damage in Sparged Bioreactors. *Trends Biotechnol.* **2000**, *18*, 420–432. [CrossRef]
50. Huang, W.; Yun, H.; Huang, W.; Zhang, B.; Lyu, X. On the Influences of Air Bubbles on Water Flow in a Two-Dimensional Channel. *Math. Probl. Eng.* **2021**, *2021*, 6818673. [CrossRef]
51. Gumbiner, B.M.; Kim, N.-G. The Hippo-YAP Signaling Pathway and Contact Inhibition of Growth. *J. Cell Sci.* **2014**, *127*, 709–717. [CrossRef]
52. Mason, D.E.; Collins, J.M.; Dawahare, J.H.; Nguyen, T.D.; Lin, Y.; Voytik-Harbin, S.L.; Zorlutuna, P.; Yoder, M.C.; Boerckel, J.D. YAP and TAZ Limit Cytoskeletal and Focal Adhesion Maturation to Enable Persistent Cell Motility. *J. Cell Biol.* **2019**, *218*, 1369–1389. [CrossRef] [PubMed]
53. Khan, S.U.; Fatima, K.; Malik, F. Understanding the Cell Survival Mechanism of Anoikis-Resistant Cancer Cells during Different Steps of Metastasis. *Clin. Exp. Metastasis* **2022**, *39*, 715–726. [CrossRef] [PubMed]
54. Masini, M.A.; Bonetto, V.; Manfredi, M.; Pastò, A.; Barberis, E.; Timo, S.; Vanella, V.V.; Robotti, E.; Masetto, F.; Andreoli, F.; et al. Prolonged Exposure to Simulated Microgravity Promotes Stemness Impairing Morphological, Metabolic and Migratory Profile of Pancreatic Cancer Cells: A Comprehensive Proteomic, Lipidomic and Transcriptomic Analysis. *Cell. Mol. Life Sci.* **2022**, *79*, 226. [CrossRef] [PubMed]
55. Häder, D.-P.; Braun, M.; Hemmersbach, R. Gravity Sensing, Graviorientation and Microgravity. In *Gravitational Biology I*; SpringerBriefs in Space Life Sciences; Springer International Publishing: Cham, Switzerland, 2018; pp. 1–11, ISBN 9783319938936.
56. ElGindi, M.; Sapudom, J.; Laws, P.; Garcia-Sabaté, A.; Daqaq, M.F.; Teo, J. 3D Microenvironment Attenuates Simulated Microgravity-Mediated Changes in T Cell Transcriptome. *Cell. Mol. Life Sci.* **2022**, *79*, 508. [CrossRef] [PubMed]
57. ElGindi, M.; Sapudom, J.; Garcia Sabate, A.; Chesney Quartey, B.; Alatoom, A.; Al-Sayegh, M.; Li, R.; Chen, W.; Teo, J. Effects of an Aged Tissue Niche on the Immune Potency of Dendritic Cells Using Simulated Microgravity. *NPJ Aging* **2023**, *9*, 14. [CrossRef] [PubMed]
58. Svejgaard, B.; Wehland, M.; Ma, X.; Kopp, S.; Sahana, J.; Warnke, E.; Aleshcheva, G.; Hemmersbach, R.; Hauslage, J.; Grosse, J.; et al. Common Effects on Cancer Cells Exerted by a Random Positioning Machine and a 2D Clinostat. *PLoS ONE* **2015**, *10*, e0135157. [CrossRef] [PubMed]
59. Liu, Q.; Luo, Q.; Ju, Y.; Song, G. Role of the Mechanical Microenvironment in Cancer Development and Progression. *Cancer Biol. Med.* **2020**, *17*, 282–292. [CrossRef]
60. Jokela, T.A.; LaBarge, M.A. Integration of Mechanical and ECM Microenvironment Signals in the Determination of Cancer Stem Cell States. *Curr. Stem Cell Rep.* **2021**, *7*, 39–47. [CrossRef]
61. Mierke, C.T. Bidirectional Mechanical Response between Cells and Their Microenvironment. *Front. Phys.* **2021**, *9*, 749830. [CrossRef]

62. Larose, T.L. Tumors in Space: Preparation for Spaceflight. In *Preparation of Space Experiments*; Pletser, V., Ed.; IntechOpen: London, UK, 2020; ISBN 9781789851380.
63. Einstein, A. Grundgedanken Und Methoden Der Relativitätstheorie in Ihrer Entwicklung Dargestellt. In *The Berlin Years: Writings*; Janssen, M., Lehner, C., Buchwald, D., Eds.; Princeton University Press: Princeton, NJ, USA, 1918; Volume 7.